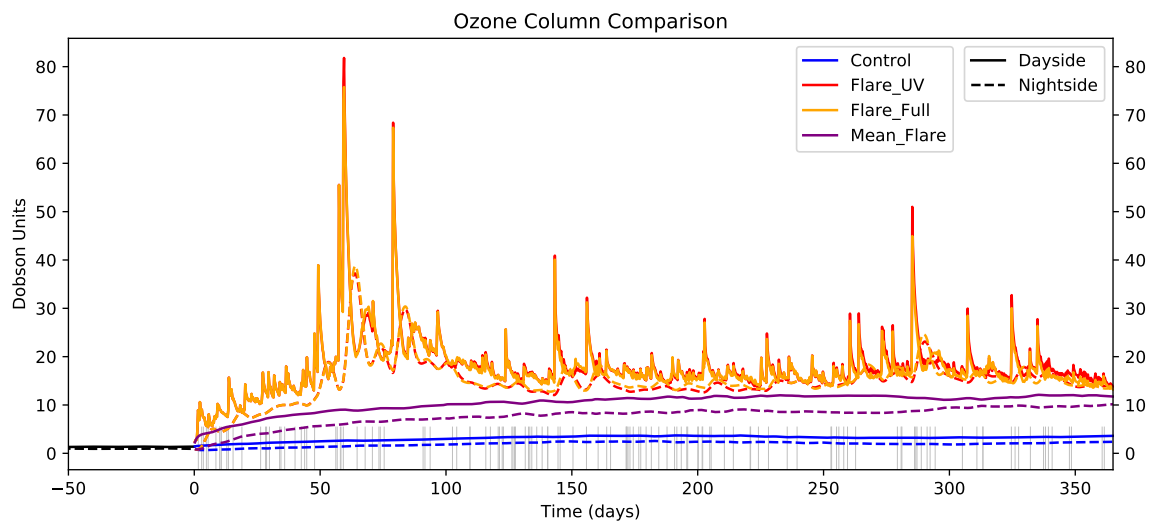# Simulating the impact of stellar flares on the climate and habitability of terrestrial Earth–like exoplanets

Robert James Ridgway

Submitted by Robert James Ridgway to the University of Exeter as a thesis for the degree of Doctor of Philosophy in Physics, May 2023.

I certify that all material in this thesis which is not my own work has been identified and that any material that has previously been submitted and approved for the award of a degree by this or any other University has been acknowledged.

Front page figure (Figure 5.12): The hemispherically averaged mean ozone column of the day–side and night–side from the simulations in this work, subjected to stellar flares. See Chapter 5 for details.

Abstract

Stellar flares present challenges to the potential habitability of terrestrial planets orbiting M dwarf stars through inducing changes in the atmospheric composition and irradiating the planet's surface in large amounts of ultraviolet light. To examine their impact, we have coupled a general circulation model called the Met Office Unified Model with a chemical kinetics scheme to examine the response and changes of an Earth-like atmosphere to stellar flares and coronal mass ejections. I have implemented enhancements to the chemical kinetics framework to include the effects of photolysis, stellar energetic protons, and deposition. This was tested with a series of chemical networks with increasing complexity. I find that a M dwarf with stellar flares increases the amount of ozone in the atmosphere by a factor of 20 compared to a quiescent M dwarf. I find that coronal mass ejections abiotically generate significant levels of potential bio-signatures such as N_2O, and do not have a large impact on the amount of ozone. The changes in atmospheric composition cause a moderate decrease in the amount of ultraviolet light that reaches the planet's surface, suggesting that while flares are potentially harmful to life, the changes in the atmosphere due to a stellar flare act to reduce the impact of the next stellar flare.

Table of Contents

List of Figures

List of Tables

Acknowledgements

Chapter 1

Introduction

Extrasolar planets, also known as exoplanets, are planets which orbit stars other than the Sun. Ever since the first detection of an exoplanet by Wolszczan & Frail (1992) and the first discovery of an exoplanet around a main-sequence star Mayor & Queloz (1995),

As of the time of writing, 5292 exoplanets are known to exist[1], with many more waiting to be detected by future instrumentation and missions. Recent missions such as Kepler (Borucki et al., 2010), and TESS (Ricker et al., 2014) have discovered thousands of exoplanets.

We have been able to study exoplanetary atmospheres for some time (Charbonneau et al., 2002), giving us the ability to characterise exoplanetary atmospheres, gaining some understanding into their compositions and chemistry. A recently launched mission that will greatly improve our understanding of exoplanetary atmosphere is the James Webb Space Telescope (JWST), which will help us shed light on exoplanets and their atmospheres.

For the foreseeable future terrestrial planets orbiting M dwarf stars represent our best opportunity of potentially identifying a habitable world beyond the solar system. As we currently have evidence of only one inhabited planet, Earth, we are

---

[1] http://exoplanet.eu/, obtained on December 6th, 2022

focusing efforts to identify potentially habitable worlds through the lens of life on Earth. However, although efforts are underway to identify targets amenable to follow–up characterisation as similar to the Earth as possible in terms of host star, orbital parameters etc.[2] these efforts are not expected to yield results in the near–future. Currently, our sample of potentially habitable planets, essentially defined as planets orbiting at a distance from their star such that liquid water could be present on their surface (i.e. in the 'habitable zone', or HZ, Kasting et al., 1993), are dominated by those orbiting M dwarfs. Planets orbiting M dwarfs in the HZ must have shorter periods than those orbiting Sun–like G dwarfs, due to the lower luminosity of the central star. This shorter period combined with the ubiquity of M dwarfs and the more favourable planet–to–star radius and mass ratios make detection and atmospheric characterisation much more feasible for these planets compared to their G dwarf counterparts. For some of these M dwarf hosted planets it may even be possible to obtain constraints on their atmospheric compositions in the near future, vital for determining potential climates (De Wit et al., 2018).

The study of potentially habitable terrestrial exoplanets orbiting M dwarfs is likely to play a pivotal role in answering one of the most significant and long–standing questions facing humankind: whether life on Earth is a unique and singular occurrence. This major, overarching, goal encompasses and requires contributions from a wide range of research disciplines. Exoplanet research has an opportunity to make a vital contribution to help unravel this puzzle.

However, there are several difficult challenges to our ability to understand and interpret the climates of any particular target. M dwarfs are cooler, smaller and often much more prone to stellar activity than G dwarfs. The M dwarf HZ is so close to the star that tidal forces are expected to rapidly force the planet into a circular orbit and becoming tidally locked (the same side of the planet always faces the star, Barnes, 2017). Being tidally locked has significant consequences for the planetary climate, primarily a large contrast in the day–night irradiation. This contrast leads to, for example, planetary–scale circulation through a super-rotating

---

[2]For example, the Terra Hunting Experiment, THE, https://www.terrahunting.org/

equatorial jet (Showman et al., 2013), and large day-night temperature contrasts.

In this thesis I will present relevant background in exoplanets, radiative transfer, atmospheric chemistry, and fluid mechanics, as they pertain to the models used in this work. This will lead into a description of the work I have done during my PhD:

1. Created a series of opacity files for several molecules

2. Extended a chemical kinetics framework to include photolysis, deposition, and a series of chemical networks describing the chemistry of ozone

3. Created a model describing stellar flares and coronal mass ejections

4. Ran simulations to observe the impact of stellar flares on the ozone chemistry on terrestrial planets

I will then conclude this thesis by describing several avenues for future work; improvements to the models I have developed and applications of my work to other areas of research within the field of planetary climates and exoplanets.

Chapter 2

Background

In this chapter I will describe necessary background for the work I have performed. I will describe how exoplanets are detected and how their atmospheres are characterised. I will then describe how 3D climate modelling works, radiative transfer, a description of atmospheric chemistry (specifically chemical kinetics), and a description of M dwarfs, the type of star used in this work. This will be aimed at a reader who is using a similar code–base as myself.

2.1 Exoplanet Detection

There are several methods that allow us to detect exoplanets, I will describe the two most common techniques, the transit method and the radial velocity method.

The transit method uses planetary transits to detect exoplanets. A planet transits its star if the planets orbital plane is aligned with an observer so that it travels across the face of the star from the observers perspective, and obscures the light from the star, lowering the star's brightness. The amount of dimming of the star (also known as the transit depth) is related to the ratio between the cross sectional area of the disk of the planet and the disk of the star and is given by

$$\text{depth} = \frac{\pi R_p^2}{\pi R_*^2} = \frac{R_p^2}{R_*^2},$$ (2.1)

where R_p is the radius of the planet and R_* is the radius of the star, respectively. Consequently, if the stellar radius is able to be measured or determined using stellar models, the planets radius can be determined.

There are some caveats regarding the transit method. Large planets (such as gas giants) or smaller stars (such as M dwarfs) will have a larger signal than smaller planets or larger stars. As well, planets on relatively short period orbits will be more likely to be observed transiting, as a larger fraction of time will be spent in-transit. Thus, this method tends to favour large planets orbiting smaller stars on short period orbits, and as such these planets represent a large fraction of the exoplanets that are known to exist at the time of writing, despite gas giants being expected to exist around only 1% of all stars (Marcy et al., 2005).

Another widely used technique is the radial velocity method. As the exoplanet orbits around the star, both the star and the planet are orbiting around the barycentre (centre of mass) of the star system. The orbit of the star around the barycentre causes the radial velocity (the velocity of the star in the direction of the observer) to change (Perryman, 2011). This is observed due to the Doppler effect. When the star is moving away from the observer, its light will be redshifted. When the star is moving towards the observer, its light will be blueshifted. By observing the period of the signal, the duration of the orbital period, and therefore the planet's mass, can be determined. However, without knowing the inclination of the planet's orbit, its mass cannot be determined, merely the apparent mass $M_p \sin(i)$, where M_p is the planets mass, and i is the inclination of the planet's orbit. The signal is stronger for more massive planets.

These techniques allow the determination of a planet's radius and mass, but have some limitations. If the planet does not transit its star, then the transit method is not usable. As well, if the planet has a low mass or has a long orbital period, the planet is much harder to detect. Future instrumentation with increased sensitivity will help alleviate this problem, but for the foreseeable future, exoplanet detections are dominated by high mass planets on short period orbits. However, in

the cases where both techniques are used, having the planet's apparent mass and the planet's radius allows you to estimate the planet's bulk density. This allows you to estimate whether it's likely to be a terrestrial planet or a gas giant, and allow some constraints on the composition of the planet (Seager et al., 2007; Rogers & Seager, 2010; Lopez & Fortney, 2014; Madhusudhan et al., 2020). If only the mass or the radius is known, then you must assume that the planet has a certain density in order to derive the other parameter. For example, Proxima Centauri b (Prox-Cen b) is a terrestrial planet in the Promixa Centauri system (Anglada-Escudé et al., 2016), and is the closest exoplanet to the solar system. It was discovered using the radial velocity method. However, it is not thought to transit (Jenkins et al., 2019). This means that while estimates exist for the mass of the planet, we do not know its radius or have any information regarding its atmosphere, including whether it has one. Despite this, ProxCen b has been the subject of several climate simulations (eg. Boutle et al., 2017, 2020; Braam et al., 2022; Ridgway et al., 2022). These works chose to assume that the planet has the same bulk density of Earth, and derived the radius using that assumption. They also assumed the existence of an Earth–like (N_2–O_2 dominated) atmosphere. This is acceptable, but should be noted when using derived values instead of measured quantities.

2.2   Atmospheric Characterisation

Along with estimating the planet's mass and size, it is possible to infer information regarding the planet's atmosphere, including whether it has one. This section will describe three techniques which have been used to retrieve information about exoplanetary atmospheres.

2.2.1   Transmission spectroscopy

In cases where the planet has an atmosphere and transits the star, transmission spectra can be retrieved. Light passing through a planetary atmosphere will be filtered by the atmosphere, and this will be dependent on the atmospheric compo-

sition of the planet, as well as the pressure and temperature profiles of the planet's atmosphere.

An example of transmission spectra is seen in Figure 2.1. These spectra were created by myself, using PandExo (Batalha et al., 2017), software created to simulate JWST observations of synthetic transmission spectra which were created by simulating the transmission of starlight through a model atmosphere created from climate simulations ran using the Met Office Unified Model. These were created for Boutle et al. (2020), which was examining the impact of dust and bio–marker gases on the transmission spectra of a planet representative of Proxima Centauri b with an 'Earth–like' atmosphere.

2.2.2   Emission spectroscopy

At longer wavelengths the ratio between planetary thermal emission (F_P) and the stellar emission (F_s) is higher, allowing a better signal and ease of observation. An emission spectrum is the spectrum of reflected and emitted light coming from the planet. This can be measured by separating the stellar emission from the combined stellar and planetary emission. This can be accomplished by observing the changes in the observed spectra when the planet is eclipsed by the star, when it passes behind it. Observing the emission spectra allows you to gain some information regarding the planet, such as the temperature profile and composition.

The emission spectrum can be obtained by separating the planetary thermal emission from the stellar emission. When the planet is behind the star, its contribution to the combined emission of the star system is removed, leaving just the stellar emission.

Figure 2.2 shows an example of emission spectra, created by myself as part of the results shown in Drummond et al. (2020).
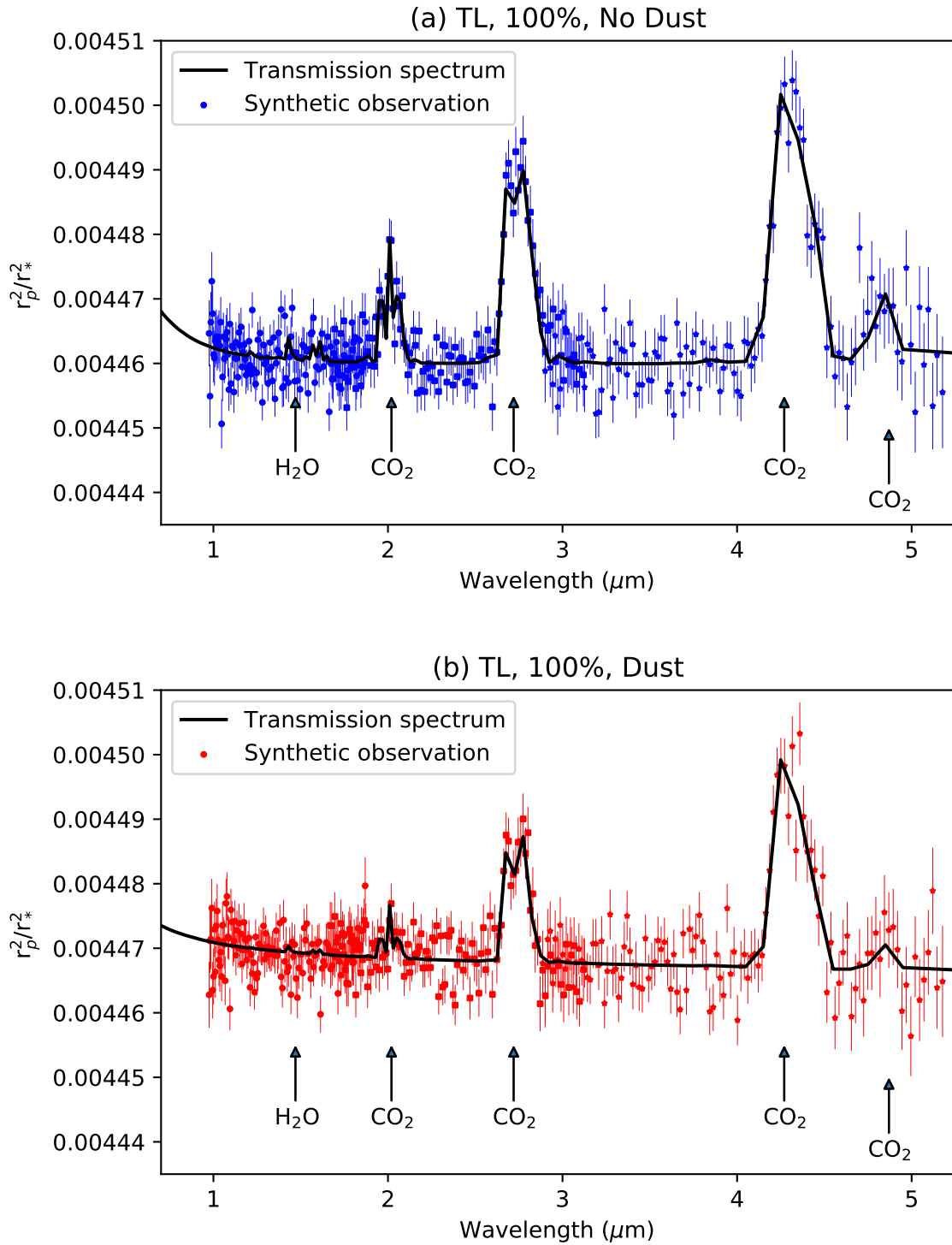
Figure 2.1: Transmission spectra created by PandExo simulating JWST observations of a planet similar to Proxima Centauri b, a terrestrial planet. These plots appeared in Figure 4 (a and b) of Boutle et al. (2020), and were created by myself.

2.2.3 Phase curves

A phase curve is an extension of the principles behind emission spectroscopy. By observing the planet throughout its entire orbit, you can determine how the emission spectra changes over the orbit. This allows you to obtain information
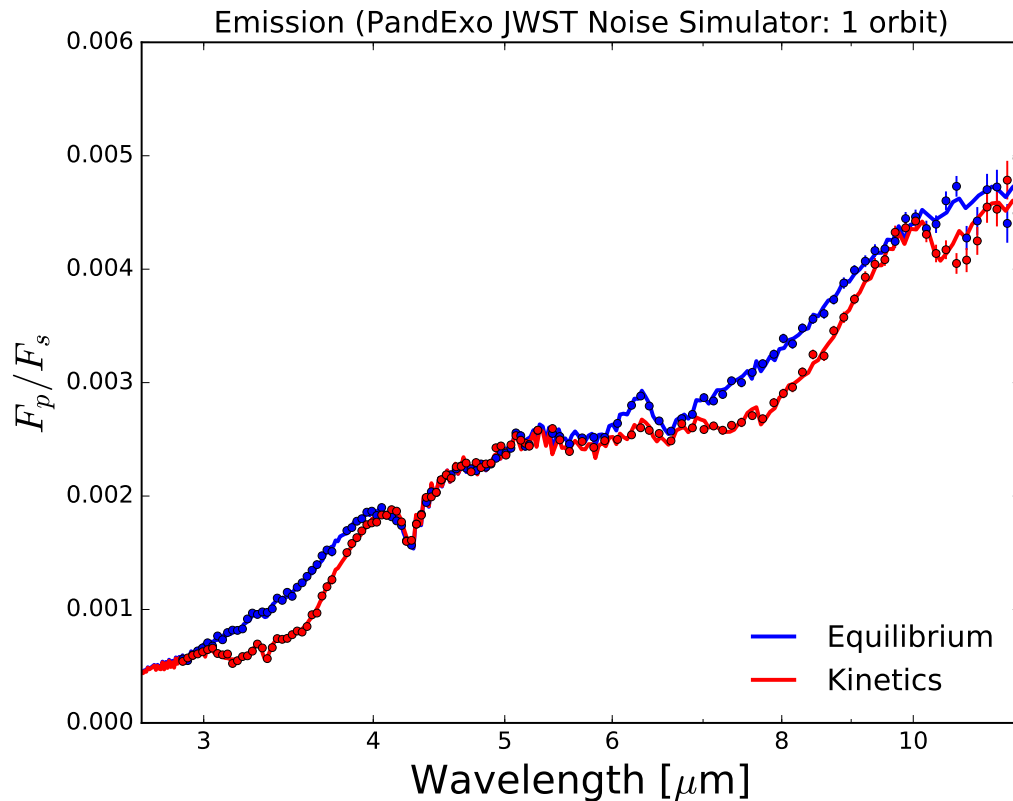
Figure 2.2: Emission spectra created by PandExo simulating JWST observations of a planet representative of HD 189733b, a hot Jupiter. The spectra were created assuming two models of atmospheric chemistry; equilibrium chemistry and chemical kinetics (see Section 2.5 for a description of those terms). The results from PandExo were created by myself, and this plot appeared in Figure 12 of Drummond et al. (2020).

across the entire planet, such as a temperature map. As an example, Demory et al. (2016) obtained a temperature map of the super–Earth 55 Cancri e, finding that the planet has strong day–side thermal emission, and a large temperature contrast between the day–side and night–side of the planet (also known as the day–night temperature contrast). This implies that the planet does not have strong circulation transporting hot material to the night–side.

2.2.4   Detection of life

Atmospheric characterisation is currently one of the most promising methods that is likely to lead to the discovery of extraterrestrial life. Currently, we can only use terrestrial life as an example of how life can affect planetary evolution. Life has had a strong effect on the Earth's atmosphere over its history. In Earth's early history, also known as the Archean period (3.8–2.5 billion years ago), is when the first

evidence for life is found (Nisbet & Sleep, 2001). The atmospheric had almost no O_2 and a large amount of CO_2. The advent of oxygenic photosynthesis during the Archean period slowly altered the atmospheric composition to have a much higher amount of O_2. This also changed what would be observed through transmission spectroscopy (Kaltenegger et al., 2007).

Biochemistry is a very complicated field, and life uses thousands of chemical species. Many of these molecules are released into the atmosphere, such as O_2, which is produced by photosynthesis. There are some species of molecules which are thought to be produced in large enough quantities that when observed, there would be a detectable spectral feature. Molecules which are thought to provide an observable signature of biological activity and are not explainable by abiotic activity are known as biosignatures. Examples of biosignatures include O_2, O_3, CH_4, N_2O, PH_3 (Sousa-Silva et al., 2020), CH_3SCH_3, $CH_3S_2CH_3$, and CH_3Cl. See reviews such as (Grenfell, 2018) and the references contained therein for more details. Work is ongoing to determine how well such molecules (and others) are indicative of biological activity, and eliminate false positives, such as O_2 being produced by photolysis in a CO_2 dominated atmosphere (eg. Meadows, 2017).

The recent Decadal Survey (National Academies of Sciences, Engineering, and Medicine, 2021) has identified that the discovery and identification of habitable planets is a priority goal for the next few decades. This includes the development of instrumentation capable of characterising the atmospheres of terrestrial planets. Due to their small size, terrestrial planets have not yet been characterised. Currently, the state of the art and upcoming instruments, such as the Giant Magellan Telescope (GMT), Thirty Meter Telescope (TMT), James Webb Space Telescope (JWST), European Extremely Large Telescope (E-ELT), or the Nancy Grace Roman Space Telescope (formerly known as the Wide Field Infrared Space Telescope) should allow the characterisation of nearby rocky exoplanets in the infrared. Looking into the future, proposed instruments such as LUVOIR should be able to characterise rocky exoplanets in the optical and ultraviolet.

2.3 Modelling of planetary climates

This section will describe how planetary climates have been simulated in this work using the Met Office Unified Model.

2.3.1 General circulation models

General circulation models (GCMs) are a powerful tool for the simulation of planetary atmospheres in 3D. These models solve a set of equations which describe fluid dynamics and radiative transfer, and describe planetary climates and weather. They are routinely used for numerical weather prediction, and studying climate change. They have also been used to study solar system planets and exoplanets. I will briefly describe the GCM that is used in this work.

2.3.2 The Unified Model

In this work I am using the Met Office Unified Model (UM). The UM is a GCM which has primarily been designed to simulate the Earth, to provide accurate weather forecasts and study climate change predictions (Walters et al., 2019). Over recent years, the UM has been adapted for the study of exoplanets. This was initially performed by Mayne et al. (2014b,a), which tested the UM for a few cases, including hot Jupiters. Amundsen et al. (2016) improved the accuracy of the radiative transfer to better describe planets which are much hotter than the Earth (temperature and pressure ranges where many sources for opacity are not well described). The UM has now been used for a range of exoplanet applications, such as investigating hot Jupiters (Mayne et al., 2014b; Drummond et al., 2016, 2018a, 2020; Zamyatina et al., 2022) and terrestrial planets such as Proxima Centauri b (Boutle et al., 2017, 2020; Eager et al., 2020; Yates et al., 2020; Braam et al., 2022; Ridgway et al., 2022) or Trappist-1e (Sergeev et al., 2022).

The atmospheric dynamics in the UM are calculated by a dynamical core known as ENDGame (Wood et al., 2014). ENDGame solves for the non–hydrostatic deep equations of motion which describe the flow of fluids on a rotating sphere. Ra-

diative transfer within the UM is calculated using a scheme called (Suite Of Community RAdiative Transfer codes based on Edwards & Slingo, 1996, SOCRATES). This will be described in more detail in Section 2.3.4.

2.3.3 Equations of motion of fluids

The equations of motion solved by ENDGame are equations which describe the evolution of zonal, meridional and vertical momentum, as well as a continuity equation, thermodynamic energy equation, as well as an equation of state. These equations are

$$\frac{Du}{Dt} = \frac{uv \tan \phi}{r} - \frac{uw}{r} + fv - f'w - \frac{c_P \theta}{r \cos \phi} \frac{\partial \Pi}{\partial \lambda} + D(u), \qquad (2.2)$$

$$\frac{Dv}{Dt} = -\frac{u^2 \tan \phi}{r} - \frac{vw}{r} - uf - \frac{c_P \theta}{r} \frac{\partial \Pi}{\partial \phi} + D(v), \qquad (2.3)$$

$$\delta \frac{Dw}{Dt} = -\frac{u^2 + v^2}{r} + uf' - g(r) - c_P \theta \frac{\partial \Pi}{\partial r}, \qquad (2.4)$$

$$\frac{D\phi}{Dt} = -\rho \left(\frac{1}{r \cos \phi} \frac{\partial u}{\partial \lambda} + \frac{1}{r \cos \phi} \frac{\partial (v \cos \phi)}{\partial \phi} + \frac{1}{r^2} \frac{\partial (r^2 w)}{\partial r} \right), \qquad (2.5)$$

$$\frac{D\theta}{Dt} = \frac{Q}{\Pi} + D(\theta), \qquad (2.6)$$

$$\Pi^{(1-\kappa)/\kappa} = \frac{R \rho \theta}{P_0}, \qquad (2.7)$$

where u, v, and w are the components of the wind velocity using the coordinate system of a zonal (East–West, λ), meridional (North–South, ϕ), and radial (r) directions, respectively. ρ is the density, δ is a switch (0 or 1) that is used to enable a quasi–hydrostatic form of these equations, Q is the heating rate determined by radiative transfer, c_P is the heat capacity, R is the specific gas constant, $\kappa = c_P/R$, P_0 is a reference pressure, and $g(r)$ is an altitude dependent gravity

$$g(r) = g_{\text{surf}}(\frac{R_{\text{p}}}{r})^2, \qquad (2.8)$$

where g_{surf} is the gravitational acceleration on the planets surface, and R_p is the planetary radius. θ is the potential temperature, which is defined as

$$\theta = T(\frac{P_0}{P})^{\frac{1}{\kappa}}, \tag{2.9}$$

and Π is the Exner pressure

$$\Pi = (\frac{P}{P_0})^{\frac{1}{\kappa}} \tag{2.10}$$

f and f' are the Coriolis parameters, and are defined as

$$f = 2\Omega \sin \phi, \tag{2.11}$$

$$f' = 2\Omega \cos \phi, \tag{2.12}$$

respectively, where Ω is the planetary rotation rate. $\frac{D}{Dt}$ refers to the material derivative, which describes how a quantity (a scalar or vector field) within a fluid changes over position and time, which has the following definitions depending on whether the quantity X is either a scalar or vector field

$$\frac{DX}{Dt} \equiv \frac{\partial X}{\partial t} + \vec{u} \cdot \nabla X, \tag{2.13}$$

$$\frac{D\vec{X}}{Dt} \equiv \frac{\partial \vec{X}}{\partial t} + (\vec{u} \cdot \vec{\nabla})\vec{X}, \tag{2.14}$$

where $\vec{u}$ is the fluid's velocity field. While quite similar, the form of the material derivative depends on whether the quantity X is either a scalar field X or a vector field $\vec{X}$. In the coordinate system the UM uses, the material derivative is defined as

$$\frac{D}{Dt} = \frac{\partial}{\partial t} + \frac{u}{r \cos \phi} \frac{\partial}{\partial \lambda} + \frac{v}{r} \frac{\partial}{\partial \phi} + w \frac{\partial}{\partial r}. \tag{2.15}$$

2.3.4 Radiative Transfer

Radiative transfer is the process where light interacts with some medium. This is a key component of climate modelling, and is necessary to atmospheric dynamics and photochemistry. The radiative transfer scheme used by the UM is called

(Suite Of Community RAdiative Transfer codes based on Edwards & Slingo, 1996, SOCRATES). During each radiative time-step in the UM, SOCRATES determines the heating rates throughout the atmosphere, which are then used to solve the dynamic equations. To calculate radiative transfer in a computationally efficient manner, SOCRATES uses the correlated–k method (Lacis & Oinas, 1991) to determine the opacity of each chemical species present in the atmosphere, which is combined to determine the overall opacity of the atmosphere. Opacities can vary drastically over small wavelength ranges (see the Figures in Section 2.4), which means that accurate radiative transfer would necessitate a high resolution, with high computational costs. The correlated–k method is quite useful as it reduces the computational load considerably while providing accurate results. A brief summary of the method follows. The range of wavelengths considered for radiative transfer are separated into a series of wavelength bands. These bands may differ between the incident radiation received from the star (shortwave radiation) and the thermal emission from the planet and atmosphere (longwave). For each molecule within each band, the opacity of the molecule within that band is rearranged into a profile which is much easier to compute than the original opacity. This allows the calculation of an averaged opacity for portions of the profile which are then used for the heating rate calculations.

SOCRATES applies the two–stream approximation, where the radiation is assumed to contain only an upward and downward component. As part of recent developments to incorporate the effects of space weather into the UM and SOCRATES (Jackson et al., 2020), a scheme for calculating photolysis (the destruction of chemical species due to light) has been included. The work presented in this thesis has helped validate the inclusion of photolysis and test its capabilities. SOCRATES has also recently included the option to account for spherical geometry, which was used in this work and Christie et al. (2021). Spherical geometry accounts for the 3D nature of planets, and changes the radiative transfer from a plane–parallel approximation (where the radiation is assumed to be only vertical) to a form where the radiation travels in a slanted path through the atmosphere.

This allows some shortwave heating and photolysis to occur on the planet's night–side.

2.3.5 The planetary surface

An important part of simulating planetary climates is the surface of planet. This is important for multiple reasons, as different types of surface or topography can have impacts on the climate and atmospheric circulation of the planet, as seen with the Earth. For terrestrial exoplanets with an atmosphere, their surface would also have some impact, but as there is no current technique for looking at the surface or topography of an exoplanet's surface, we must choose what to do to include a planet's surface in any climate simulation.

In this thesis and the work published in Ridgway et al. (2022), any simulated planet is assumed to be an 'aquaplanet', a planet which does not have any land, and is covered by a global ocean. For the surface, we use a slab ocean model (Frierson et al., 2006). The surface consists only of a single layer of ocean which has a fixed heat capacity of $10^7\,\mathrm{J\,K^{-1}\,m^{-2}}$), representing an ocean depth of approximately 2.4 m. There is no horizontal transport or heat transfer in this model. As well, this means that the surface is flat, with no topography. This is quite unrealistic, but is acceptable due to the lack of any ability to constrain the surface environment of ProxCen b. This choice of surface means that the day–side of the planet is covered in water, which has implications for the presence of the water cycle on this planet. A planet with a different land–ocean configuration will have a somewhat different climate. For example, if the planet has very little water on the day–side, and doesn't circulate enough heat to the night–side to sustain liquid water (if any water is present on the night–side), then the planet will have almost no water vapour in it's atmosphere. This has implications for the presence of clouds as well as impacts on the potential emergence of life and the composition of the atmosphere due to changes in atmospheric chemistry.

2.4   Opacities

Accurate molecular opacities are critical to understanding the climate of planets by allowing accurate radiative transfer. The opacity of a molecule controls how a molecule interacts with radiation, and is a key component to determining fluxes and atmospheric heating rates.

Opacities are determined by theoretical calculations and experiment (examples being Tolchenov & Tennyson, 2008; Campargue et al., 2015), and are ultimately a result of the different energy levels (both electronic and rovibrational) that a molecule has. If a molecule has a transition that corresponds to a change in energy of a 1 nm photon, then the molecule is at least partially opaque to 1 nm photons. Whether a particular transition is a strong absorber is dependent on the temperature and pressure of the molecule, as this determines the distribution of energy levels of molecules within a gas.

2.4.1   Line lists

A common term for a list of transitions for a molecule is known as a line list. Line lists are data which contain a series of electronic and rovibrational transitions for a given molecule, as well as Einstein coefficients. Einstein coefficients are a measure for the probability of a photon to be absorbed (or emitted) by a molecule due to a given transition. There are three types of transitions. Spontaneous emission occurs when a molecule spontaneously decays from a higher energy level to a lower energy level, and emits a photon. Absorption is the reverse process, where a molecule absorbs a photon and is excited to a higher energy level from a lower energy level. Stimulated emission occurs when (due to the presence of a photon) a molecule decays from a higher energy level to a lower energy level.

The HIgh–resolution TRANsmission (HITRAN) database (Gordon et al., 2022a) is a widely used source for line lists for molecules. In this work, I have used HITRAN extensively, except for shorter wavelength opacities, which are not supplied by HITRAN. This is important, as accurate photolysis calculations rely on shorter

wavelength opacities. The sources of short wavelength opacities are listed in Table A.1 in the Appendix.

2.4.2 Exocross

In order to create opacity files which are used by SOCRATES, I have used a script known as Exocross to calculate opacities from line lists. Exocross is a script developed by Yurchenko et al. (2018c) to calculate molecular opacities.

In order to work with Exocross for a range of pressures and temperatures, I created a Python-based wrapper for Exocross which automates the process of creating input files for Exocross, submitting jobs to a computing resource, and collating the output and creating opacity files for a molecule over a range of pressures and temperatures[1]. This has been used to create opacity files for a range of molecules and isotopologues.

Similar to the process described in Amundsen (2015), the absorption coefficients were determined for a fixed pressure and temperature grid, consisting of 20 temperature points (logarithmic between 70–3000 K) and 40 pressure points (logarithmic between 10^{-3}–10^8 Pa) for a series of 800 P–T points. The absorption coefficients are determined over a wave–number range (as given by the line–list reference information) with a resolution of $0.1\,\mathrm{m}^{-1}$, to match the resolution of absorption coefficients previously calculated by Amundsen (2015).

2.4.3 Isotopologues

It is worth noting that many of these species had data available for multiple isotopologues, a molecule composed of the same elements and the same structure but different isotopes of those elements, such as $H_2^{18}O$ or HDO, which are isotopologues of water. Different isotopologues have different physical properties, and accordingly different rovibrational and electronic transitions. That means that the opacity for one isotopologue will be different from another. When line lists were

---

[1]Available at https://github.com/exoclim/Exocross-Tools

available for multiple isotopologues, opacity files were created for each isotopologue. These were combined together and weighted by their relative abundance, using isotopic abundances listed by NIST[2], compiled by Berglund & Wieser (2011). See Figure 2.3 for an example of differing opacities between isotopologues of titanium oxide (TiO). This was chosen as titanium has non-negligible abundances of 5 isotopes. Figure 2.3 shows that while overall the opacities are similar between the isotopologues, there are some differences in opacity across all wave–numbers. There is some future work that could be done here with examining how planetary atmospheres formed with a different isotopic ratio (such as the D/H ratio, which could be different depending on where in a star system a planet formed) may have different climates, or what impact isotopic fractionation may have on climates and atmospheric chemistry.
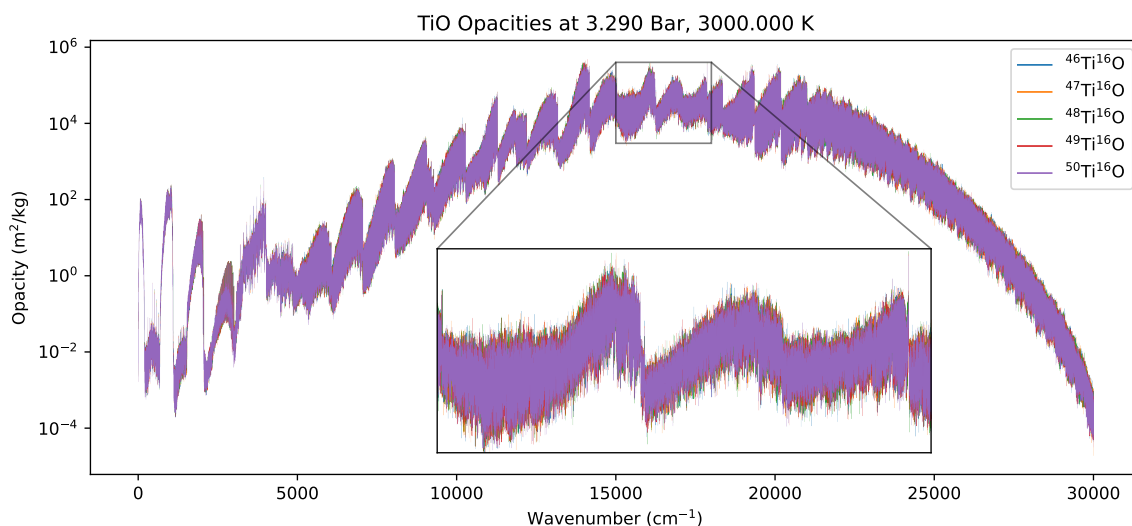
Figure 2.3: This demonstrates the different opacities for the available isotopologues of TiO, using the line lists created by McKemmish et al. (2019).

2.4.4 New opacity files

I have created opacity data for 14 molecules, which will be briefly described. Plots illustrating the opacity for the molecules will be shown for a single pressure, and three different temperatures to see how opacity changes with temperature. The opacities are shown in Figures 2.4–2.17. The list of molecules and citations are

1. H_2O, Polyansky et al. (2018)

---

[2]Available at https://physics.nist.gov/cgi-bin/Compositions/stand_alone.pl

2. AlH, Yurchenko et al. (2018b)

3. AlO, Patrascu et al. (2015)

4. CaH, Li et al. (2012); Bernath (2020)

5. CaO, Yurchenko et al. (2016)

6. MgH, GharibNezhad et al. (2013); Bernath (2020)

7. MgO, Li et al. (2019)

8. NaH, Rivlin et al. (2015)

9. SH, Gorman et al. (2019)

10. SiH, Yurchenko et al. (2018a)

11. SiO, Barton et al. (2013)

12. SiO_2, Owens et al. (2020)

13. SiS, Upadhyay et al. (2018)

14. TiO, McKemmish et al. (2019)

A new H_2O line list (POKAZATEL) was recently created by (Polyansky et al., 2018), supplanting an older BT2 line list created by (Barber et al., 2006). A comparison of the two line lists is shown in Figure 2.4, where we see that both line lists are similar below $20000\,cm^{-1}$, but the newer line list provides opacity information at a much higher wave-number.
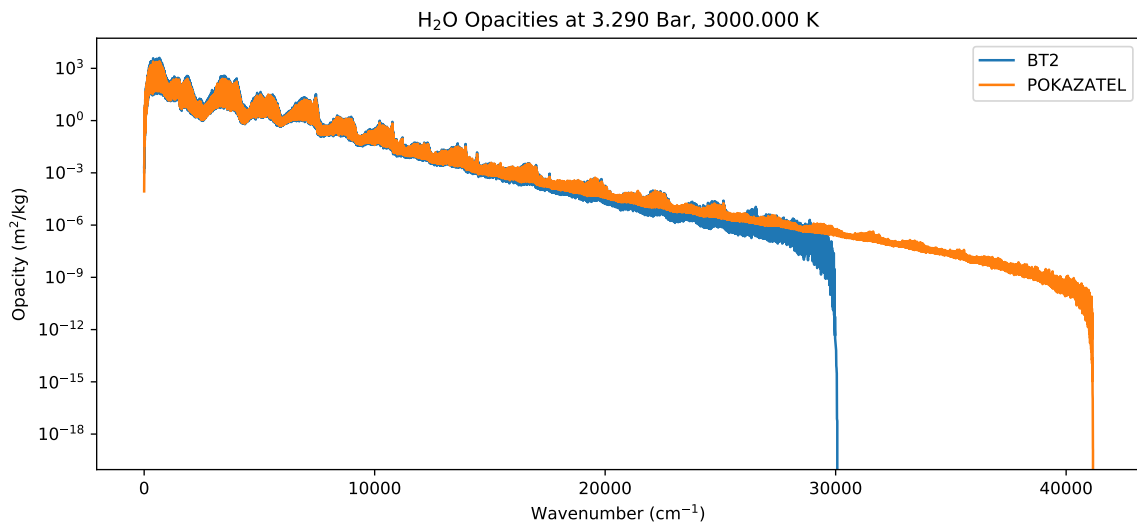
Figure 2.4: This demonstrates the difference in opacities for the older BT2 line-list and the newer POKAZATEL line-list.
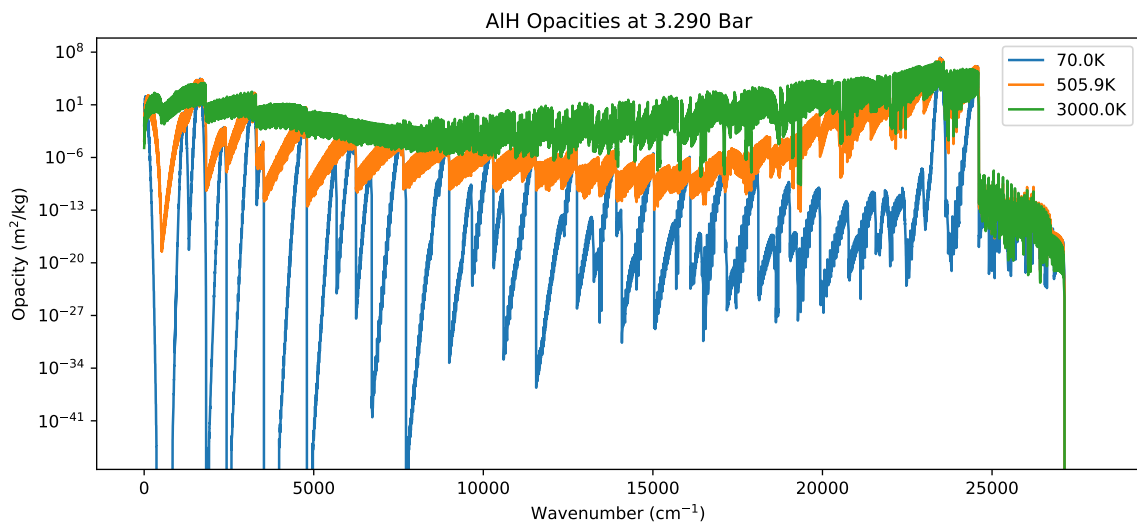
Figure 2.5: This demonstrates the opacity of AlH over several temperatures.
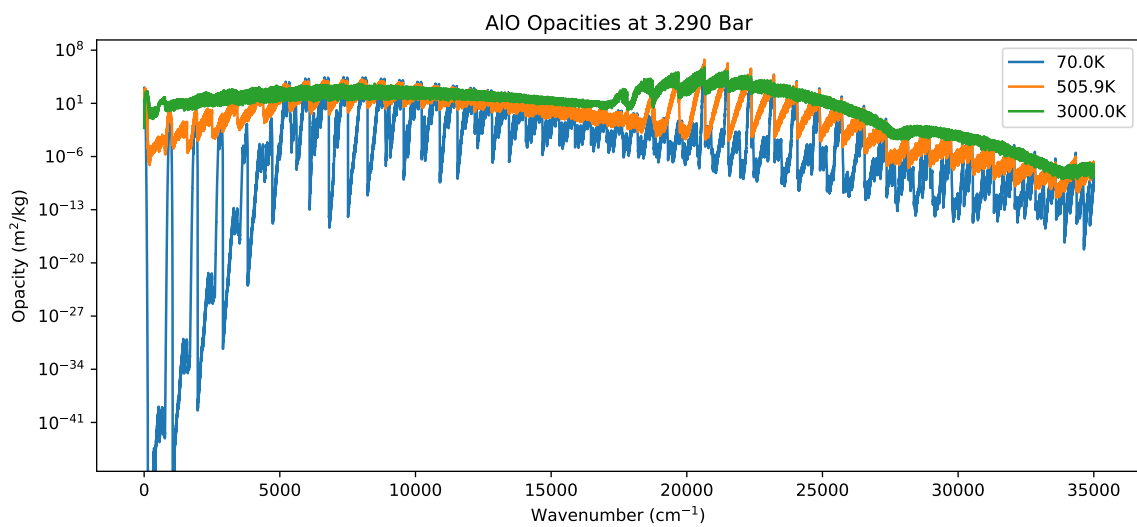
Figure 2.6: This demonstrates the opacity of AlO over several temperatures.
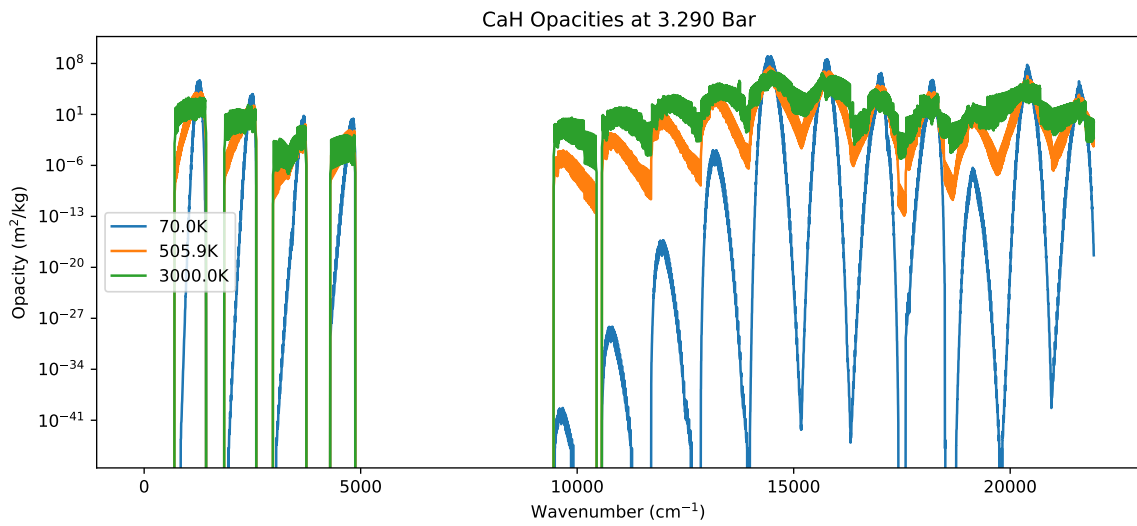
Figure 2.7: This demonstrates the opacity of CaH over several temperatures.
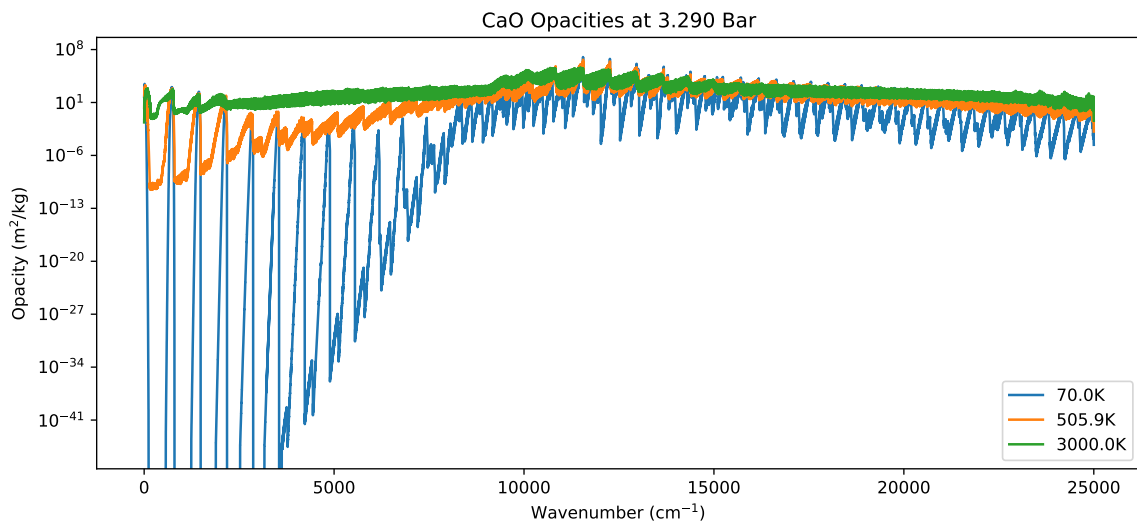
Figure 2.8: This demonstrates the opacity of CaO over several temperatures.
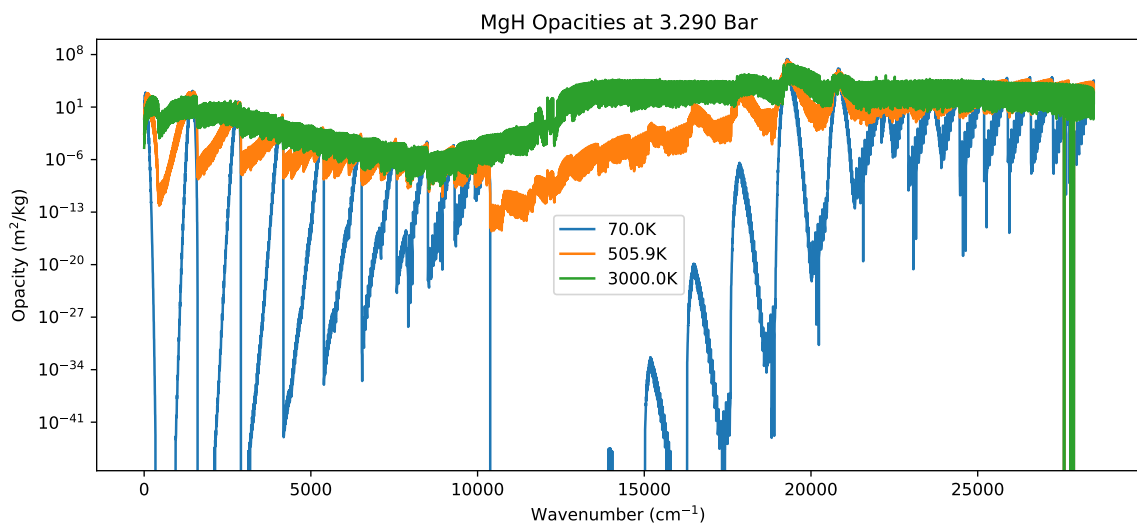
Figure 2.9: This demonstrates the opacity of MgH over several temperatures.
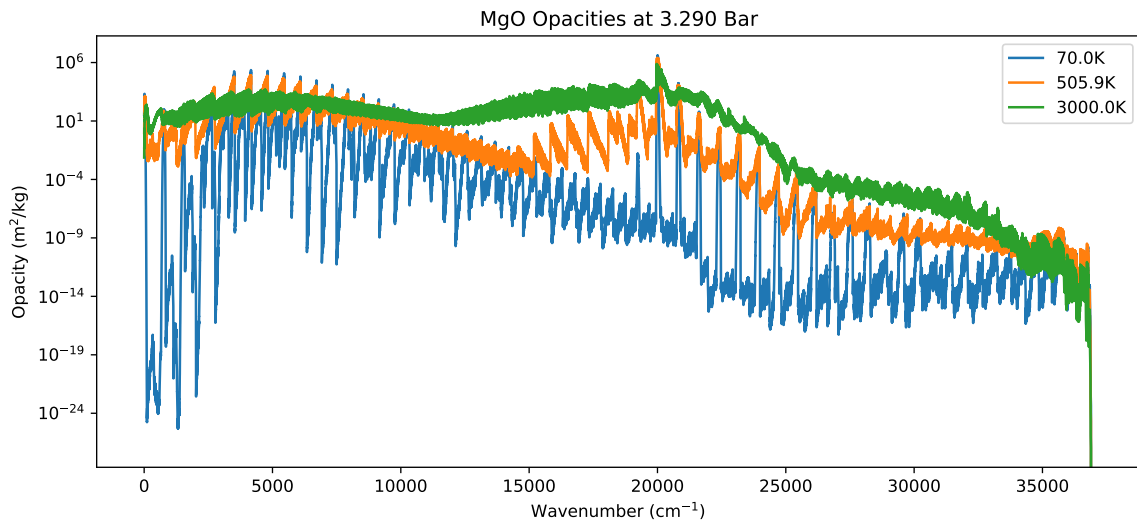
Figure 2.10: This demonstrates the opacity of MgO over several temperatures.
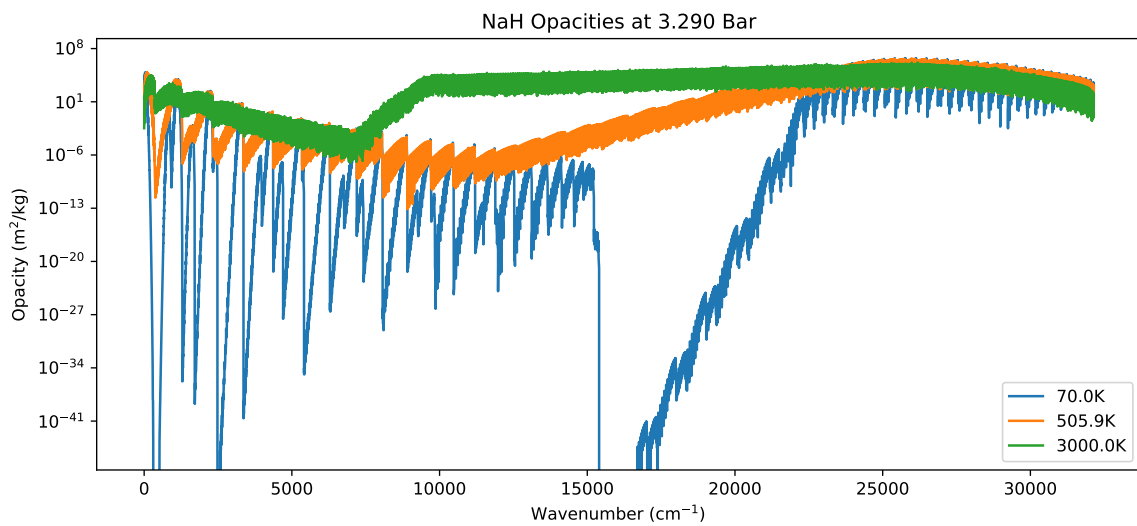
Figure 2.11: This demonstrates the opacity of NaH over several temperatures.
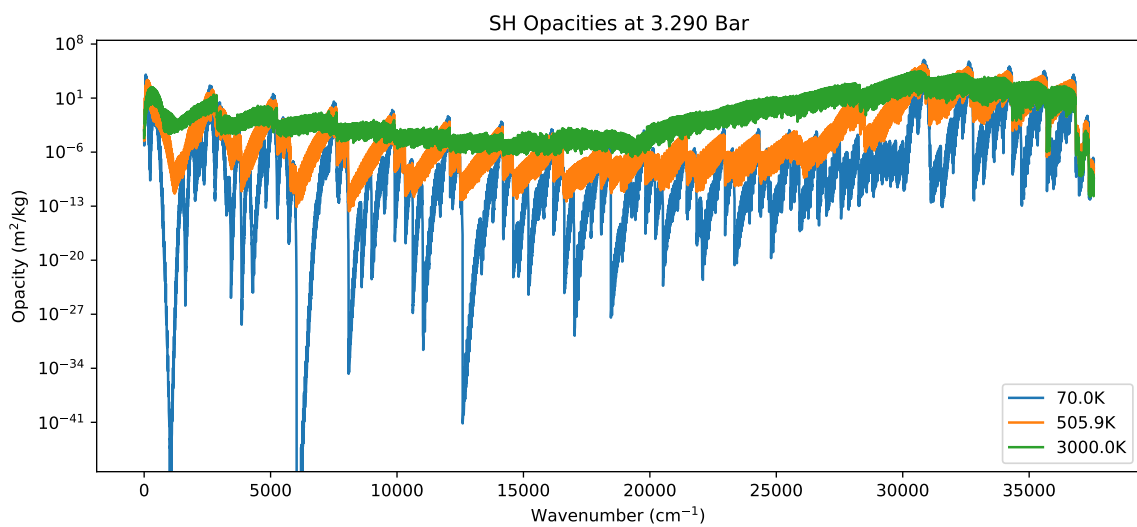
Figure 2.12: This demonstrates the opacity of SH over several temperatures.
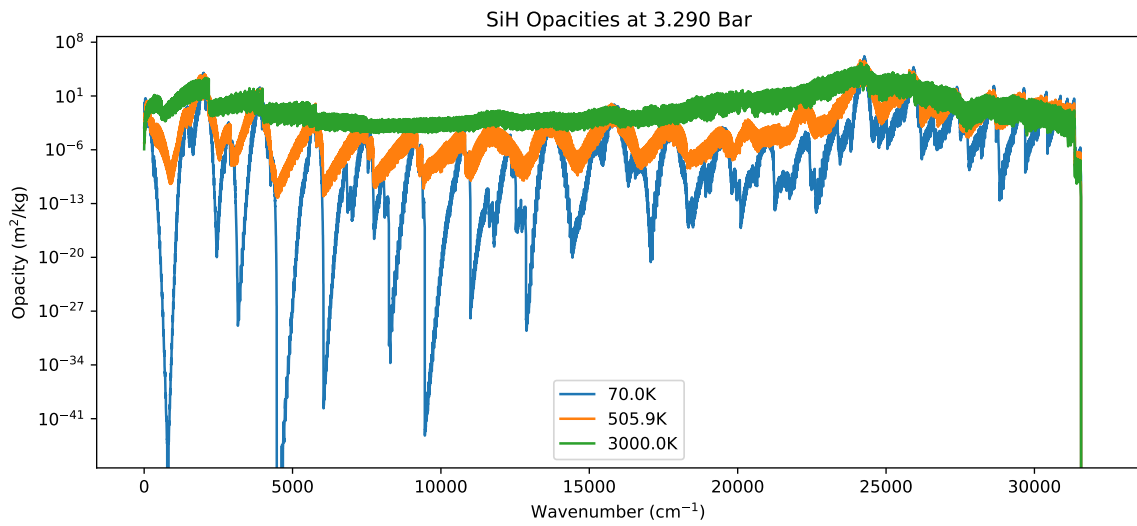
Figure 2.13: This demonstrates the opacity of SiH over several temperatures.
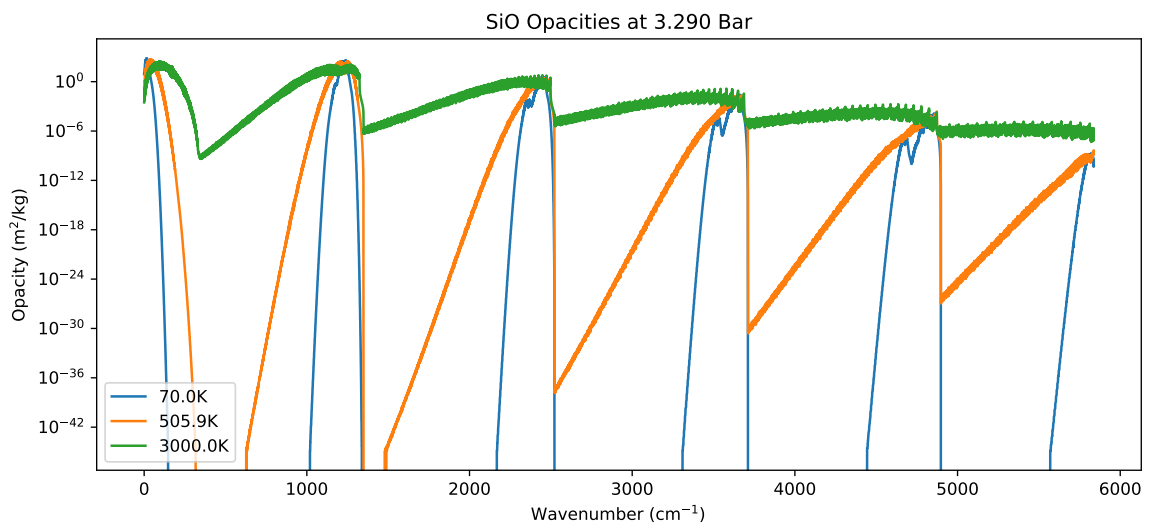
Figure 2.14: This demonstrates the opacity of SiO over several temperatures.
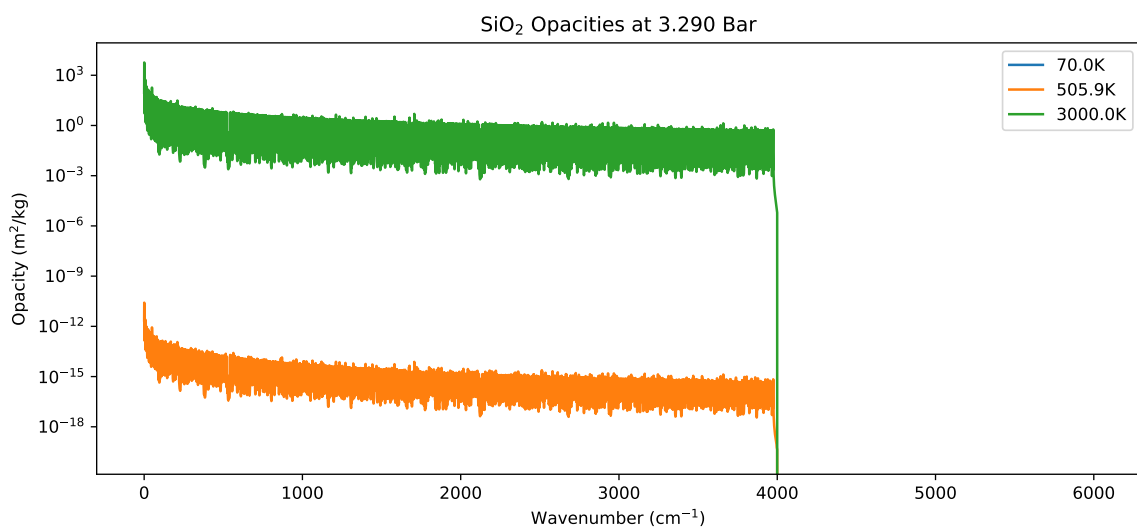
Figure 2.15: This demonstrates the opacity of SiO_2 over several temperatures.
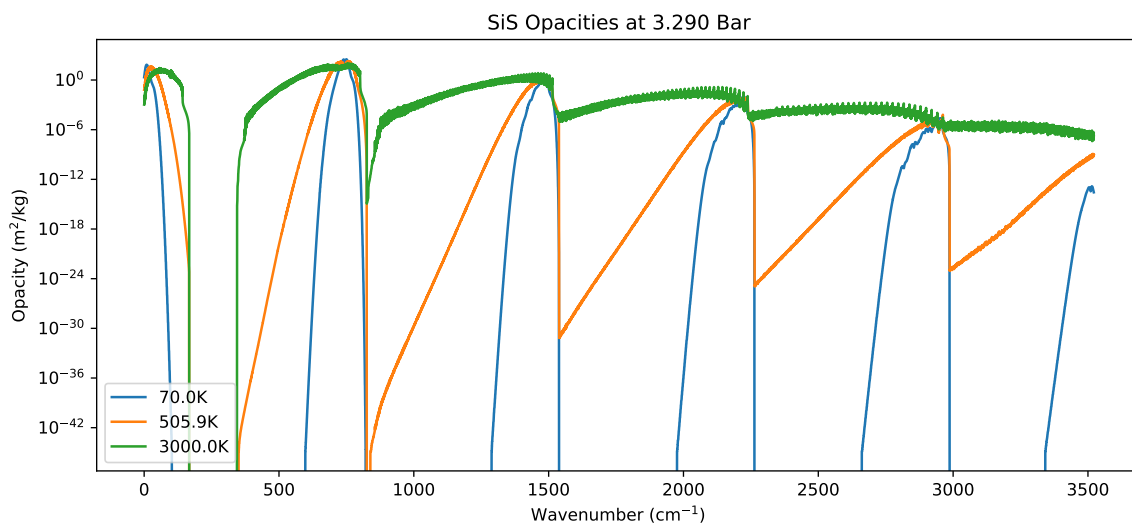
Figure 2.16: This demonstrates the opacity of SiS over several temperatures.
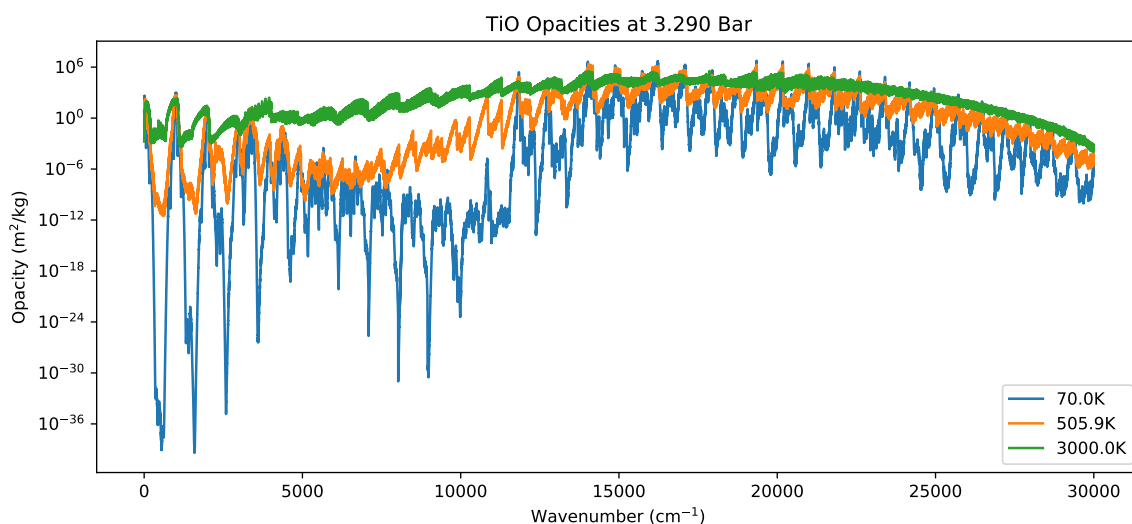
Figure 2.17: This demonstrates the opacity of TiO over several temperatures.

2.4.5 Disclaimer on their use

All of the opacity files for the described chemical species were created by myself, but do not factor into the work I am presenting in later chapters. These opacity files were created for use by Mark Phillips, Eric Hébrard, and Pascal Tremblin, amongst others. These files were created for use on simulating sulfur chemistry in gas giants (guided by the modelling performed by Visscher et al., 2006), the atmospheres of brown dwarfs, and the atmospheres of lava worlds (planets which are close enough to their star to have a molten surface on the day–side). They can be used for such cases, as well as perhaps planets with large amounts of volcanic activity.

An example of their use is shown in Figure 2.18. These plots were not created by myself but were supplied by Aurélien Falco for use in this thesis as an example of the opacity files being used. This figure shows an emission spectra of a planet, and includes contributions from SiO and MgO. The opacities created by myself have impacted the emission spectra (top) with (centre and bottom) the emission spectra created when these opacities are not included into the radiative transfer. We see the inclusion of SiO and MgO have created features at $10\,\mu$m and $17\,\mu$m, which are due to SiO and MgO respectively. As well, an increase in the continuum emission (between the emission peaks) between 1–$10\,\mu$m is due to the presence of MgO.

2.5   Atmospheric chemistry

Now that we have an understanding of fluid dynamics, radiative transfer, and how those are included within climate modelling, we can proceed to describing the final piece that completes the background, a description of atmospheric chemistry.

The UM has already been used to study the impact of the quiescent spectrum of an M dwarf on the atmospheric ozone distribution of a planet with an initial idealised Earth atmospheric composition (Yates et al., 2020). Yates et al. (2020) used the UM, coupled to the UKCA[3] chemical framework, to model ozone chemistry on a tidally locked planet (based on ProxCen b). They assumed the planet orbits a quiescent M dwarf, with a pre–industrial Earth-like atmosphere, with atmospheric chemistry consisting of the Chapman cycle and HO_x (in their case defined as OH, HO_2, without any H) chemistry. In parallel, we have developed an idealised chemistry framework (Drummond et al., 2016), coupled to the UM, designed to be flexible in terms of both the input chemical network and the level of sophistication ranging from simple equilibrium chemistry (Drummond et al., 2018a), to 'chemical relaxation' (Drummond et al., 2018b,c) and on to full chemical kinetics (Drummond et al., 2020; Ridgway et al., 2022; Zamyatina et al., 2022). Until recently this frame-

---

[3]https://www.ukca.ac.uk/wiki/index.php/UKCA
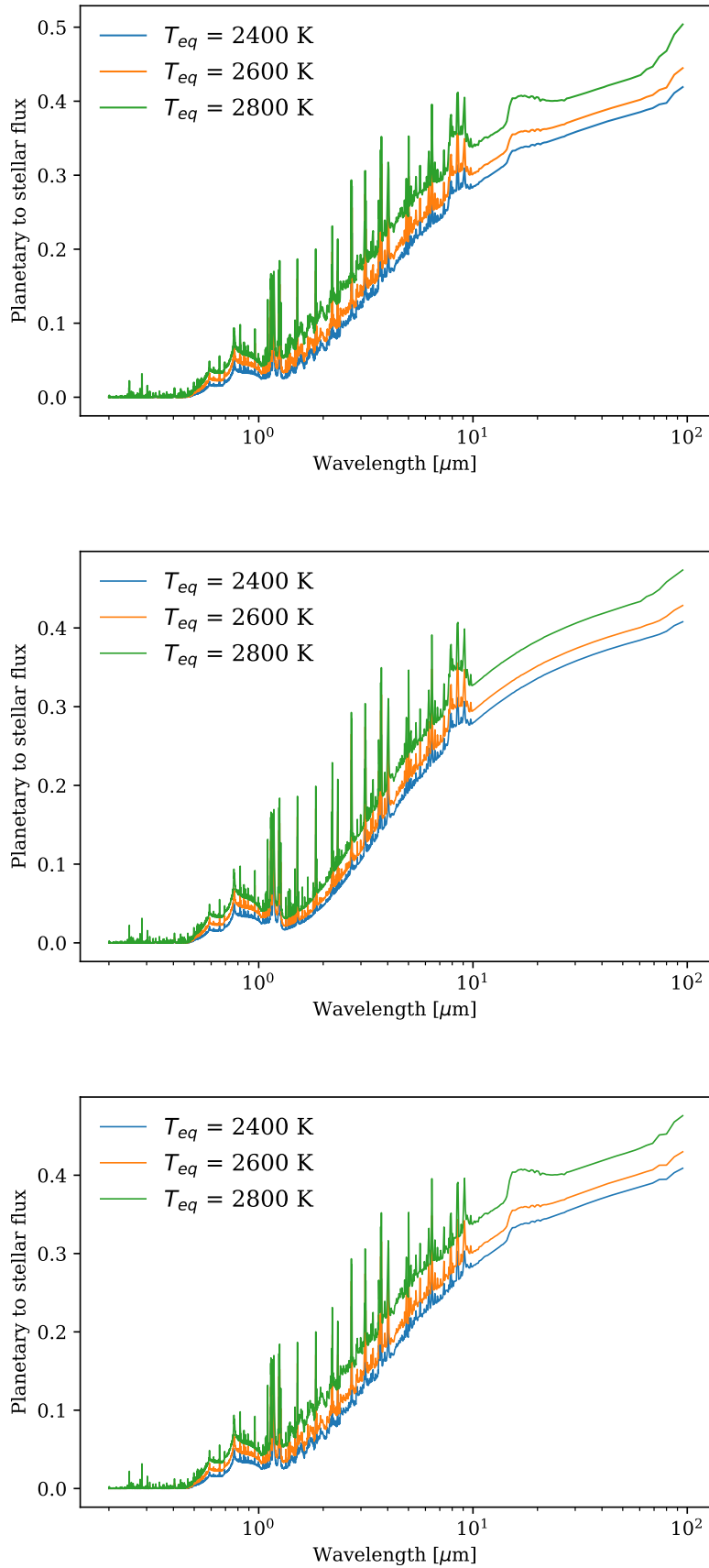
Figure 2.18: Emission spectra for a planet at three different equilibrium temperatures. Top panel contains both SiO and MgO features at 10 μm and 17 μm, middle panel lacks MgO, and the bottom panel lacks SiO. These plots were not created by myself but were supplied by Aurélien Falco for use in this thesis.

work had been applied only to hot Jupiter planets. In this work I have continued the development of this framework to give it the capability of describing photo-chemistry on terrestrial planets. This section will describe equilibrium chemistry, and transition into a description of the non–equilibrium chemical kinetics, and the types of chemical reactions that are included in this work.

2.5.1 Terminology

There are several terms used in this work that should be described before we can proceed.

The mole fraction (f_i) is a term which is used to describe the amount of a substance compared to the total amount of all material. Despite the name, it does not need to refer to the number of moles of a material, and can be defined as

$$f_i = \frac{N_i}{N} = \frac{P_i}{P} = \frac{n_i}{n} \tag{2.16}$$

Similarly, the mass fraction (w_i) is the ratio of the mass of species i compared to the total atmospheric mass, and can be written in terms of the mole fraction as

$$w_i = \frac{m_i}{\mu} f_i, \tag{2.17}$$

where m_i is the molar mass of species i and μ is the mean molar mass of the atmosphere.

2.5.2 Equilibrium chemistry

A system is in chemical equilibrium when the chemical composition has reached a steady–state and is no longer changing. This is dependent on a few factors such as pressure, temperature, and the molecules (and elements) that are included in the chemistry. In atmospheres, the temperature and pressure obviously vary, but assuming a local chemical equilibrium is applicable when the chemical timescale (the timescale for the composition to reach a steady–state) is much smaller than

the dynamic timescale (the timescale for a parcel of gas to move significantly). A technique used in chemical equilibrium to solve for the chemical abundances is Gibbs energy minimisation. Gibbs energy minimisation was implemented into the UM by Drummond et al. (2016). The Gibbs energy (G) is a measure of the amount of work which can be obtained from a closed system, and is described as

$$G = \sum^{i} \mu_i N_i, \tag{2.18}$$

where μ_i is the chemical potential of species i, and N_i is the number of moles of species i. The chemical potential is defined as

$$\mu_i = \left(\frac{\partial G}{\partial N_i}\right)_{T,P,N_j \neq i}. \tag{2.19}$$

The chemical potential can be written in terms of a standard chemical potential (determined at a reference pressure) and a term which depends on the partial pressure of the chemical species

$$\mu_i(T,P) = \mu_i^0(T) + RT \ln(P_i) = \mu_i^0(T) + RT(\ln(\frac{PN_i}{N})) = \mu_i^0(T) + RT \ln(P) + RT \ln(f_i) \tag{2.20}$$

where $\mu_i^0(T)$ is a standard chemical potential, R is the specific gas constant, T is the temperature, P_i and N_i are the partial pressure and amount of chemical species i, P and N are the pressure and total amount of all chemical species, and f_i is the mole fraction of species i. Gibbs minimisation represents chemical equilibrium, and is solved with the constraint of elemental conservation. That means that the total number of atoms of every element is conserved. See Drummond (2017) for more details on this implementation within the UM.

This technique is quite beneficial when it is applicable, as a detailed knowledge of the reaction pathways is not required to obtain the atmospheric composition, and as the technique is relatively efficient to compute, presents the ability to perform simulations relatively quickly. However, it is not applicable for the tidally

locked terrestrial planets that I will be simulating. There are several reasons why equilibrium chemistry is not applicable. Firstly, the assumption that the chemical timescale is much faster than the dynamic timescale is not globally true for a tidally locked planet. This will be described in more detail in Section 3.3.10 which examines the chemical lifetime of ozone, but we find that while the chemical timescale is considerably shorter than the dynamic timescale on large portions of the day–side, the opposite is true on the night–side. In particular, species which are heavily affected by photolysis (such as ozone), have an effectively infinite chemical timescale on the night–side. As well, photolysis reactions are a non–equilibrium process, and implementing photolysis is a key feature of this work.

2.5.3   Chemical Kinetics

For this work, I am using a chemical kinetics framework. Instead of assuming that the composition will reach a steady state of its own accord, chemical kinetics is dependent on an understanding on the chemical reactions occurring in the atmosphere, and other processes. Chemical kinetics is applicable when the chemical timescale (the timescale on which chemical species would approach a steady-state if left untouched) is greater than the dynamical timescale (the timescale on which a volume of gas moves around a planetary atmosphere), or there are non–equilibrium processes such as photolysis. When this occurs you cannot run an equilibrium chemistry code since the volume is being interfered with before it reaches a steady-state.

2.5.4   Continuity

In its simplest form, chemical kinetics uses a list of chemical reactions to build a series of coupled differential equations describing the change in number density n_i, which for species i can be written as

$$\frac{\partial n_i}{\partial t} = P_i - L_i + \nabla \Phi, \tag{2.21}$$

where n_i is the amount or concentration of species i, P_i is the total production of species i, L_i is the total destruction of species i, and $\nabla \Phi$ is a term representing transport within the atmosphere.

The list of chemical reactions is also referred to as a chemical network. More generally, a chemical network is a list of chemical species and reactions that is assumed to adequately describe the processes occurring within the atmosphere we want to simulate. We can begin to implement chemical kinetics by creating a series of coupled ODEs describing the change in number density of each species within the chemical network.

As a simple example, we can create a simple network consisting of three bimolecular reactions and three species A, B, and C

$$1.\ A + B \longrightarrow C,$$
$$2.\ A + C \longrightarrow B,$$
$$3.\ B + C \longrightarrow A.$$

Using the first reaction as an example, the formula for describing the reaction rate (in molecules cm^{-3} s^{-1}) of a bimolecular reaction is

$$k_1[A][B],$$

where k_1 is the reaction rate coefficient, a parameter that determines the reaction rates (and differs in calculation between types of reactions, as will be explained in Sections 2.5.6–2.5.9) and $[A]$ is the number density of A measured in molecules cm^{-3}. The rate of change of A due to this reaction is thus

$$k_1[A][B] = -\frac{\partial[A]}{\partial t} = -\frac{\partial[B]}{\partial t} = \frac{\partial[C]}{\partial t},$$

since A and B are reactants in the bimolecular reaction and are being destroyed by this reaction, while C is a product of the reaction and is being produced. A full

description of the network would be combining the reaction rates for all reactions together to create a series of coupled differential equations. In this example, the full series of equations describing the entire network is thus

$$\frac{\partial [A]}{\partial t} = -k_1[A][B] - k_2[A][C] + k_3[B][C],$$
$$\frac{\partial [B]}{\partial t} = -k_1[A][B] + k_2[A][C] - k_3[B][C],$$
$$\frac{\partial [C]}{\partial t} = \quad k_1[A][B] - k_2[A][C] - k_3[B][C],$$

where k_x is the reaction rate coefficient for reaction x, and the sign on each term depends on whether the species in a reaction is a reactant or product. Solving and integrating these equations will describe how the chemical network changes over time.

This work was done using a chemical framework that was adapted from the 1D chemical kinetics model ATMO, which has been used in hot Jupiter contexts previously, for both 1D radiative-convective equilibrium modelling (Amundsen et al., 2014; Tremblin et al., 2015, 2016) and forward modelling and retrieval (Evans et al., 2016, 2017; Wakeford et al., 2017). The framework was added into the UM as an alternative chemical kinetics scheme (Drummond et al., 2016). See Drummond (2017) for more details on the implementation and testing of the ATMO scheme within the UM.

2.5.5 Chemical transport

Chemical transport is especially important for a tidally locked planet. The UM allows us to add tracer particles which are advected throughout the atmosphere. The transport of the chemical species throughout the atmosphere is controlled by the UM, using a semi–Lagrangian advection scheme (Davies et al., 2005), where the tracers are advected with the flow of the atmosphere.

2.5.6 Chemical reactions

Reaction rate coefficients in general exhibit variations in magnitude at different temperatures and pressures. The exact amount of variations are typically unique to each reaction, but are generally a result of chemical reactions being initiated by collisions between the reactants. The reasons for this can be derived from gas kinetics (Brasseur & Jacob, 2017). We will use the reaction

$$A + B \longrightarrow C + D,$$
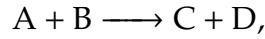
as an example. This reaction is initiated by a collision of a molecule of A and B which has enough kinetic energy to exceed the minimum energy required to start the reaction, the activation energy E_a. The collision rate between A and B (Z_{AB}) is dependent on two factors, the collisional cross section (σ_{col})

$$\sigma_{col} = \pi(r_A + r_B)^2, \tag{2.22}$$

where r_A and r_B are the radius of species A and B respectively, and the thermal velocity of the gas (v_{th})

$$v_{th} = \left(\frac{8kT}{\pi} \frac{m_A + m_B}{m_A m_B} \right)^{\frac{1}{2}}, \tag{2.23}$$

where k is the Boltzmann constant, T is the temperature, and m_A and m_B are the molecular masses of A and B respectively. This is assuming that the velocity distribution is described by a Maxwell-Boltzmann distribution. The collision rate is thus

$$Z_{ab} = \sigma_{col} v_{th}[A][B]. \tag{2.24}$$

The assumption of a Maxwell-Boltzmann distribution implies that the fraction of molecules with the required amount of energy to exceed the activation energy E_a is related to $\exp(-E_a/RT)$. From this we can obtain a form of the reaction rate of

$$\pi(r_A + r_B)^2 \left(\frac{8kT}{\pi} \frac{m_A + m_B}{m_A m_B} \right)^{\frac{1}{2}} \exp(-E_a/RT)[A][B], \tag{2.25}$$

with the reaction rate coefficient k_1 being

$$k_1 = \pi(r_A + r_B)^2 \left(\frac{8kT}{\pi} \frac{m_A + m_B}{m_A m_B} \right)^{\frac{1}{2}} \exp(-E_a/RT), \qquad (2.26)$$

From this we can rewrite k_1 in the form of the Arrhenius equation

$$k_1 = A \exp(-E_a/RT), \qquad (2.27)$$

where A is a pre–exponential factor

$$A = \pi(r_A + r_B)^2 \left(\frac{8k}{\pi} \left(\frac{m_A + m_B}{m_A m_B} \right)^{\frac{1}{2}} T^{\frac{1}{2}}, \qquad (2.28)$$

although the $T^{\frac{1}{2}}$ factor is typically neglected due to the difficulty in observing it, as the $\exp(-E_a/RT)$ term will dominate experiments to observe the reaction rate.

Transition state theory notes that this reaction is not instantaneous, and involves an activated complex $AB^\dagger$, which can either proceed into the reactions products, or return to the individual reactants. This changes the previous reaction to

$$A + B \rightleftharpoons AB^\dagger \longrightarrow C + D.$$

The energy required for the intermediate complex to form is called the activation energy (E_a). The reaction rate coefficient is derived to be (generally)

$$k_1 = AT^n \exp(-E_a/RT), \qquad (2.29)$$

where n is some constant, which is obtained by experiment and theory.

I will briefly describe the major types of reactions which are used in this work, and how the coefficients are calculated for each reaction.

2.5.7 Unimolecular reactions

Unimolecular reactions are reactions which consist of a single molecule. In this work, photolysis channels are considered to be unimolecular reactions, and the reaction rate coefficients are calculated using SOCRATES, which are then passed to the chemistry. See Section 3.1.1 for details on how we calculate our photolysis rates.

2.5.8 Bimolecular reactions

Bimolecular reactions are reactions consisting of two reactants. Generally, bimolecular reactions will look like A + B $\longrightarrow$ C + D. The reaction rate k_f, with units of molecule cm^{-3} s^{-1}, of a bimolecular chemical reaction (with reactants A and B) is calculated as

$$k_f = k[A][B], \tag{2.30}$$

where k is the reaction rate coefficient (cm^3 molecule^{-1} s^{-1}) and [A] is the number density of species A, and [B] the number density of species B (both expressed in molecule cm^{-3}). The reaction rate coefficient is calculated using the modified Arrhenius equation

$$k = A(T/300)^{\alpha} \exp(-E_a/RT), \tag{2.31}$$

where A is a pre-exponential factor (cm^3 molecule^{-1} s^{-1}), α is a parameter which controls temperature dependence, E_a is the activation energy of the reaction with units of J mol^{-1}, R is the universal gas constant (8.3144 J K^{-1} mol^{-1}), and T is the temperature. The parameters for every bimolecular reaction included in our model are included in Table A.2 in the Appendix.

2.5.9 Termolecular Reactions

A termolecular reaction is a reaction which involves three reactants. In this work, our termolecular reactions involve two main reactants and a third molecule (M) which symbolises a range of possible third-body molecules. Generally, this will be written as A + B + M $\longrightarrow$ C + D + M. The third-body facilitates the reaction

34

and stabilises the products. The reaction rate (k_f) for a termolecular reaction is

$$k_f = k[A][B][M],\tag{2.32}$$

where k is the reaction rate coefficient ($cm^6\,molecule^{-2}\,s^{-1}$) and [A] is the number density of species A, [B] is the number density of species B, and [M] is the combined number density of all possible third-body molecules M (all expressed in molecule cm^{-3}). Due to the dependence on the third-body molecule, the reaction rate coefficients of termolecular reactions are generally dependent on pressure. The low-pressure coefficient k_0 and the high-pressure coefficient k_∞ are defined as,

$$k_0 = k_1(T/300)^{\alpha_1}\exp(-\beta_1/T)\tag{2.33}$$

and

$$k_\infty = k_2(T/300)^{\alpha_2}\exp(-\beta_2/T),\tag{2.34}$$

respectively. We determine the overall rate coefficient k ($cm^6\,s^{-1}$) using

$$k = k_0(\frac{1}{1+P_r})F,\tag{2.35}$$

where P_r is the reduced pressure, which is calculated using

$$P_r = \frac{k_0[M]}{k_\infty},\tag{2.36}$$

where $[M]$ is the number density of the third-body molecule. F is a broadening factor determined by

$$F = F_c^{1/\left(1+\left(\frac{\log_{10}(P_r)+c}{N-d(\log_{10}(P_r)+c)}\right)^2\right)},\tag{2.37}$$

where $c = -0.4 - 0.67\log_{10}(F_c)$, $N = 0.75 - 1.27\log_{10}(F_c)$ and $d = 0.14$ and F_c is calculated using

$$F_c = (1-a)\exp(-T/b) + a\exp(-T/C) + \exp(-D/T),\tag{2.38}$$

where a, b, C, and D are parameters from the Troe formalism (Troe, 1983). In the case where all the Troe parameters are 0, $F = 1$, which is the Lindemann formalism (Lindemann et al., 1922). There are reactions which are accurately modelled just using the low pressure coefficient k_0, such as $O_2 + O(^3P) + M \longrightarrow O_3 + M$, an important reaction which governs the creation of ozone. In these cases, $k = k_0$. Tables A.3 and A.4 in the Appendix present the complete list of all the termolecular reactions included in this work, and the relevant parameters. For Table A.3, the reactions which are adequately described by the low pressure limit will only have the parameters for k_0 listed. Decomposition reactions, where one reactant decomposes into two products, require significantly different values of the parameters (as there is only a single reactant, which results in different units for k_1 and k_2) so we present these separately in Table A.4.

2.6 The effect of UV radiation on life

The UV flux received by the surface of Earth has a significant impact on life, and was also believed to play a significant role in the early evolution of organic compounds. On Earth, ever since the Great Oxygenation Event, an event in Earth's history that occurred approximately 2 billion years ago, where the amount of molecular oxygen increased from negligible levels to a concentration similar to modern amounts, the presence of ozone (O_3) (and potentially organic hazes in the case of the Archean Earth, Arney et al., 2016) in the upper atmosphere has acted to regulate the received surface UV flux (Gebauer et al., 2017). Understanding the potential surface UV flux for target M dwarf hosted planets with a similar atmospheric composition is, therefore, an important endeavour, linked to the presence of ozone. This is one of the motivations of this work, looking at how stellar flares can affect the surface UV radiation environment of such planets.

Studies exploring the chemistry of the early–Earth indicate that shallow pools undergoing varying, potentially diurnal fluctuations in UV radiation may well have been required to construct the building blocks of life (Powner et al., 2009; Patel

et al., 2015). UV radiation is required to form hydrogen cyanide (HCN), potentially a key building block for the creation of amino acids, but too much UV radiation can halt the process and effectively sterilise the planetary surface (Kitadai & Maruyama, 2018).

UV radiation and energetic particles alter the chemistry, and therefore composition, of planetary atmospheres. For the case of modern Earth, most UV radiation is absorbed by ozone in the stratosphere (10–50 km), with ozone generated and regulated through an ozone–oxygen cycle commonly called the Chapman cycle (Chapman, 1930). Ozone chemistry also depends on the generation of short–lived free radical species termed HO_x (H, OH, and HO_2) and NO_x (N, NO, and NO_2), which play an important role in regulating the abundance of ozone. Alongside the impacts of the UV flux the energetic particles emitted from the star ionise the gases in the atmosphere, creating additional HO_x and NO_x species which contribute to the depletion of atmospheric ozone (Segura et al., 2010; Tilley et al., 2019). The changes in the atmospheric composition will also change the planetary surface to some degree, by making it cooler or warmer, or changing the stellar spectra which reaches the surface Any changes in the planetary surface conditions due to flares may have an important role to play in shaping whether life is formed or allowed to flourish.

2.7 M dwarf stars

Before we proceed to discussing the chemistry used in this work in greater detail, I will describe the current understanding of M dwarfs, and how this connects to my work.

2.7.1 Background

M dwarfs are the smallest type of star, just massive enough to sustain nuclear fusion, ranging in mass from 0.075–0.6 $M_\odot$, where $M_\odot$ is a Solar mass, and have an effective temperature from 2300-4000 K (Pecaut & Mamajek, 2013; Rajpurohit et al.,

2018). Within the local stellar population (within 25 parsecs of the Solar System), M dwarfs comprise approximately 75% of all known stars, and are thought to be the most common type of star to exist (Bochanski et al., 2010; Winters et al., 2019). This has already been mentioned, but is repeated here to underline how common they are.

Depending on the mass of the M dwarf, the internal structure can either be partly or fully convective, with lower mass stars ($< 0.35\,\mathrm{M_\odot}$) being fully convective. Fully convective M dwarfs allow almost all of the hydrogen in the star's envelope to be fused, which translates to a very long stellar lifetime, with the smallest M dwarfs having an estimated lifetime of trillions of years. Due to this, they present an opportunity that may be favourable for the emergence of life due to their long lifetimes.

Observationally, M dwarfs are fairly distinct. Due to their relatively cool temperature for a star, it is possible for molecular compounds to exist in the atmosphere of M dwarfs, such as H_2O and TiO (Allard & Hauschildt, 1995). This complicates analysis of the spectral features of M dwarfs when observed using spectroscopy, as the transition structure of molecules is more complicated than atoms, making it computationally much more difficult.

Like other stars, M dwarfs have a magnetic field, which is driven by a stellar dynamo due to convection in the star as well as stellar rotation. Modern instrumentation has been able to observe signatures of M dwarf magnetic fields (eg. Johns-Krull & Valenti, 1996; Lavail et al., 2018; Shulyak et al., 2019), such as Zeeman splitting of spectral features, allowing the field strength to be determined. This provides a strong tool for understanding the development of stellar magnetic fields. For a review of the magnetic fields of M dwarfs, and their observational history, peruse Kochukhov (2021) and the references contained therein for more details. The presence of a magnetic field drives stellar activity.

Similarly to the Sun, M dwarfs are known to exhibit stellar activity (eg. Joy & Hu-

mason, 1949; Hawley & Pettersen, 1991). Stellar activity refers to phenomena exhibited by stars which change its electromagnetic output from its quiescent (quiet, or inactive) state or involve the release of highly energetic particles. Examples of stellar activity on the Sun include solar flares, sunspots, and coronal mass ejections. The activity of M dwarfs have been studied as part of studies to detect and monitor flaring stars (such as Günther et al., 2020).

2.7.2 Simulating the climates of planets orbiting M dwarfs

Our understanding, and therefore predictive capability, of the basic climate of terrestrial planets hosted by M dwarfs is rapidly improving. Models of varying complexity have been applied to such planets, starting with the pioneering study of Joshi et al. (1997) and recently with the THAI model inter-comparison project (TRAPPIST Habitable Atmospheres Intercomparison, Fauchez et al., 2021; Turbet et al., 2022; Sergeev et al., 2022; Fauchez et al., 2022). Due to being similar in size to Earth and orbiting their host stars in the HZ, many simulations have focused on two major targets of interest, Proxima Centauri b (ProxCen b, Anglada-Escudé et al., 2016) and the TRAPPIST–1 planets (Gillon et al., 2017) such as Turbet et al. (2016) and Turbet et al. (2018), respectively.

Stellar activity is thought to play a significant role on the climates of many planets (with an atmosphere) orbiting M dwarfs. Günther et al. (2020) performed a study of the first data release from TESS (Transiting Exoplanet Survey Satellite) to look at the population of flaring stars. They found that the majority of flaring stars observed by TESS were M dwarfs. Hawley et al. (2014) and Davenport et al. (2014) found that flares on M dwarfs can occur over a wide range of durations and magnitudes. One of the largest solar flares ever observed, the 1859 Carrington event (Carrington, 1859), was estimated to have released $\approx 5 \times 10^{32}$ ergs (Cliver & Dietrich, 2013). Hawley et al. (2014) found that for active M dwarfs such as GJ 1243, flares of comparable magnitude can occur approximately once a month. Flares and stellar activity give rise to an increase in the high–energy and short–wavelength emission from the star, alongside releases of energetic particles known

as a Coronal Mass Ejection (CME) (Yashiro et al., 2006). These particles are highly energetic, and are capable of inducing changes in the atmospheric composition of terrestrial planets. Yashiro et al. (2006) found that energetic solar flares are almost always accompanied by a CME.

2.7.3 Stellar spectrum of M dwarfs

In previous simulations of ProxCen b, Boutle et al. (2017) and Yates et al. (2020) used a stellar spectrum for ProxCen from BT-Settl (a model of stellar atmospheres) (Rajpurohit et al., 2013) assuming an effective temperature $T_{eff} = 3000\,K$, a stellar surface gravity of $g = 1000\,m\,s^{-2}$, and a metallicity of $0.3\,dex$. This spectrum includes essentially no UV light below 200 nm, as the BT-Settl models capture stellar photospheric emission but do not account for chromospheric emission. The stellar chromosphere is the region of the star between the photosphere and the corona, and due to its high temperature is a source of short wavelength radiation emission. The study of Boutle et al. (2017) employed a fixed ozone layer, and focused on altitudes below those employed here, meaning the impacts of the missing very short wavelength flux would have been negligible in their study. However, with our focus on the ozone chemistry and higher altitude atmosphere, it is vital we improve on this aspect. Simulations of Earth–like planets over a range of M dwarfs for active and inactive stellar models (Rugheimer et al., 2015) show that inactive stellar models will produce significantly different ozone compositions than more active stellar spectra models, and spectra derived from observations of M dwarf stars.

We have constructed a stellar spectrum from a combination of the MUSCLES survey (France et al., 2016; Youngblood et al., 2016; P. Loyd et al., 2016)[4] and Ribas et al. (2017) describing ProxCen. This spectrum has significantly higher fluxes in the UV to X-ray than the equivalent BT–Settl model, a significantly different radiation environment. Figure 2.19 illustrates the differences in stellar spectra by showing the top–of–atmosphere stellar irradiance received by the Earth, the BT–

---

[4]The *adapt-const-res-sed.fits* version of the spectra
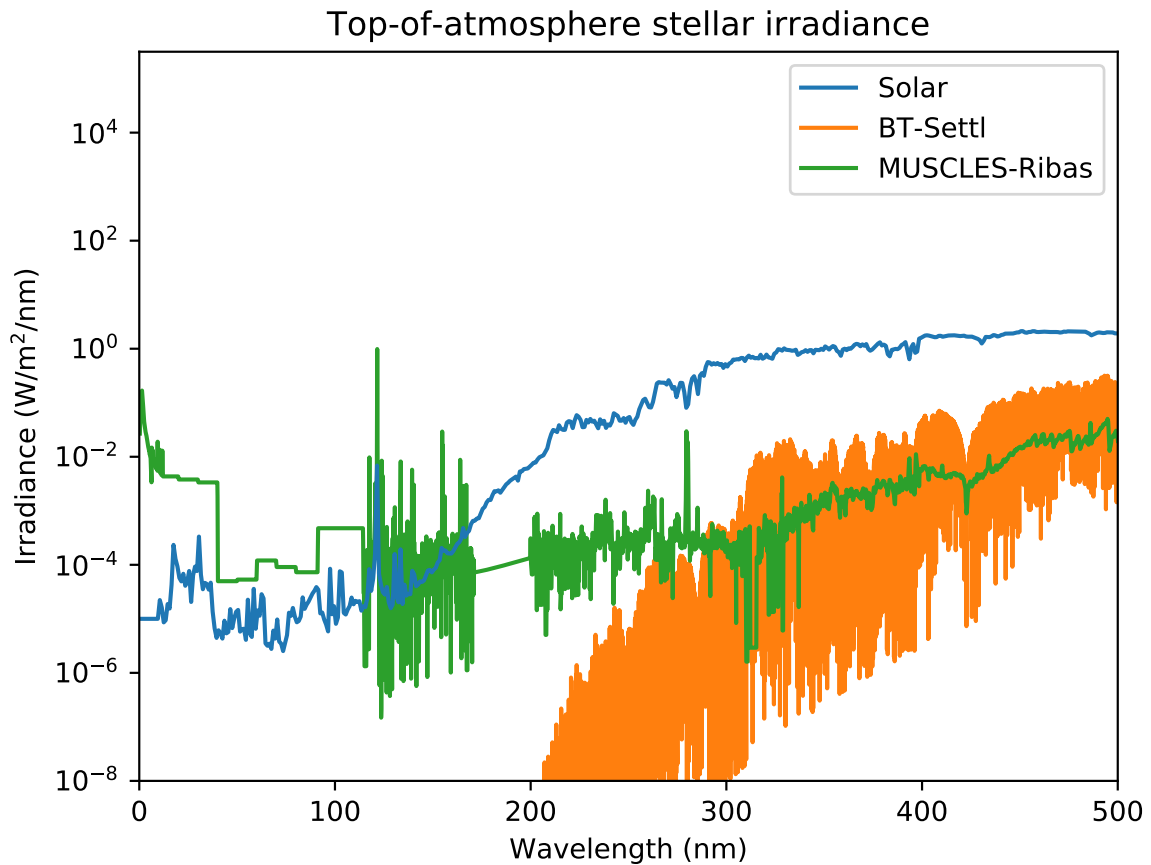
Figure 2.19: The top-of-atmosphere stellar irradiance for Earth, the BT-Settl spectrum for Prox-Cen b, and the combined MUSCLES-Ribas spectrum for ProxCen b. We note that the irradiance below 300 nm differs significantly between the two ProxCen b spectra.

Settl model at ProxCen b, and the spectrum used in this work. The combined spectrum has significantly higher UV radiation than the BT-Settl model below 300 nm, and in fact has higher levels of extreme UV/X–ray than the Solar spectrum below 120 nm. The enhancement of UV leads to increased O_2 photolysis (which occurs below 242 nm). The increased rate of photolysis leads to significantly higher abundances of atomic oxygen, which leads to significantly faster growth in ozone through the three-body reaction $O_2 + O(^3P) + M \longrightarrow O_3 + M$, where M denotes a third body. Braam et al. (2022) used the same spectrum as this work to simulate a similar 'Earth–like' planet as Yates et al. (2020), and found that when compared to Yates et al. (2020) (who used the BT-Settl spectrum) they had significantly higher amounts of ozone. This was due to two factors, the change in spectrum to one which has higher UV increases the amount of ozone significantly, and an improved calculation of photolysis rates as compared to the work done by Yates et al. (2020).

2.7.4   M dwarfs and flares

The impact of stellar flares and CMEs on terrestrial exoplanets has been addressed in only a small number of studies. Such studies have, however, shown the significant changes they can cause in the chemical processes and composition. For example, Segura et al. (2010) found that according to their results from a 1D photochemical model, for an unmagnetised 'Earth-like' planet orbiting an M dwarf star the amount of ozone in the atmosphere was not significantly impacted by a single stellar flare, when only including the increase in electromagnetic radiation. However, they also showed that ozone was initially significantly depleted by the proton flux associated with the stellar flare and CME, before recovering to the original levels of ozone abundance. Tilley et al. (2019) extended on the work of Segura et al. (2010) using the same model but including multiple flares, suggesting that the recovery of the ozone after the period of activity was unlikely. Quite recently, Louca et al. (2022) used a 1D model to examine the impact of stellar activity on a range of atmospheres, from hydrogen (H_2)-dominated to nitrogen (N_2)-dominated, and found potentially permanent changes in the atmospheric composition due to flares. Their N_2 dominated atmosphere simulations showed that flares can cause a gradual increase in the amount of ozone.

Extension from 1D is required, however, given that the target planets are expected to be tidally–locked, with one hemisphere constantly irradiated, and in the likely absence of a significant magnetic field (Christensen et al., 2009), a hemisphere which is not directly impacted by any stellar activity. Chen et al. (2021) performed a 3D study exploring the impact of stellar flares from a range of stellar types (M, K, G) on an Earth-like planet. They found that in the case of K/M dwarfs the planet retained a significantly perturbed atmospheric composition due to flaring (planets around a G dwarf quickly returned to their pre–flare atmospheric composition). This presents questions regarding interpreting exoplanetary atmospheres determined using atmospheric retrieval, as nitrous oxide (N_2O) was significantly enhanced compared to the same planet subject to a non–flaring star's irradiation. On the modern Earth, nitrous oxide's abundance is heavily controlled by biolog-

ical activity (Syakila & Kroeze, 2011) (although not entirely, N_2O can be created abiotically), and is thought to be a bio–signature (Des Marais et al., 2002). Finding a plausible abiotic source of significant nitrous oxide would raise doubts about the potential of N_2O as a bio–signature.

2.8 Chapter summary

In this chapter I have described the relevant background of the work that I have been doing. I have introduced methods of exoplanet detection and atmospheric characterisation, and how this relates to the search for extraterrestrial life. As well, I have detailed the components of radiative transfer, molecular opacity calculations, atmospheric dynamics, and atmospheric chemistry, and how they have been captured in a 3D climate modelling framework. Finally, I have described M dwarf stars and how planets orbiting M dwarfs have been simulated in previous work.

In the following chapter, I will further detail the atmospheric chemistry used in this work, as well as show the results of UM simulations looking at the chemistry.

Chapter 3

Chemical kinetics and ozone chemistry

In this chapter, I will describe atmospheric chemistry as it pertains to ozone chemistry in an abiotic context. After describing chemical kinetics, several types of chemical reactions and how I use atmospheric chemistry in the UM, I will describe the Chapman cycle, hydrogen oxide (HO_x) chemistry, and nitrogen oxide (NO_x) chemistry. I will show the results of quiescent (no stellar variability or activity) simulations using chemical networks of varying complexity on the ProxCen b aquaplanet for 12,000 days of simulation, and how the atmospheric composition changes as the complexity of the chemical networks increases. A description of how stellar flares and stellar energetic particles were included in the chemistry and UM simulations is described in Chapter 4. The results presented here were reported in Ridgway et al. (2022), and the description in this thesis was expanded from the text in that paper.

3.1   Additions to the chemistry framework

For this project I have continued the development of the chemical kinetics framework in order to allow the framework to model terrestrial planets. These addi-

tions include photolysis, dry deposition, coupling the UM's hydrological cycle to the chemical framework, and the creation of a series of chemical networks which describe ozone chemistry. The development of the chemistry framework is described in this section. Section 3.2 will describe the three chemical networks that were created to test how the abundance of ozone changes as chemical network complexity increases. Section 3.3 will describe the climate of our ProxCen b, and the evolution of ozone in these networks.

I have also developed a framework for modelling the impact of Stellar Energetic Protons (SEPs) and Coronal Mass Ejections (CMEs) that also interact with the chemistry scheme. These are described in Section 4.5 in the next chapter.

3.1.1 Photolysis

The reaction rates of photolysis reactions or channels (J, s^{-1}), are determined using

$$J = \int_0^\infty Q(\lambda)\sigma(\lambda)F(\lambda)d\lambda, \tag{3.1}$$

where $Q(\lambda)$ is the wavelength dependent quantum yield, $\sigma(\lambda)$ is the wavelength dependent cross section of the dissociating species, and $F(\lambda)$ is the actinic flux. These rates are calculated by the SOCRATES radiative transfer code (Manners et al., 2022; Jackson et al., 2020), and passed to our chemical solver (Drummond et al., 2016). Quantum yields describe the relative likelihood that a particular photolysis reaction will occur. When only considering first-order effects, the maximum quantum yield is one, as a quantum yield of less than one means that not every absorbed photon will cause the particle to dissociate, this is mostly relevant near the threshold wavelength (the wavelength corresponding to a photon with the minimum energy needed to dissociate the molecule). In the cases where a species has multiple possible channels (such as O_2 or O_3, for example), their quantum yields determine the relative proportion of each channel. As an example, Figure 3.1 shows how the quantum yields for the two O_3 photolysis channels used in this work change with wavelength. We see that the $O(^3P)$ channel is the domi-
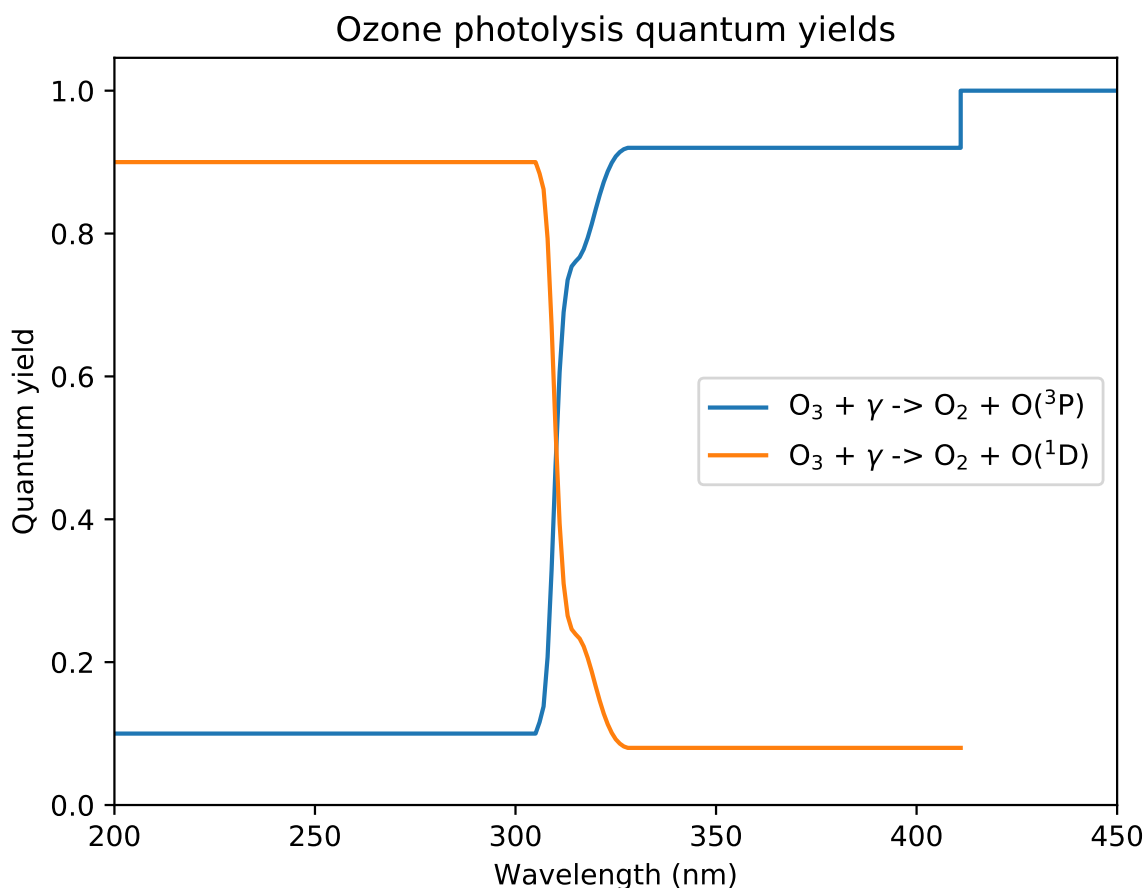
Figure 3.1: The wavelength dependent quantum yields for $O_3 + h\nu \longrightarrow O_2 + O(^3P)$ and $O_3 + h\nu \longrightarrow O_2 + O(^1D)$ used in this work.

nant channel at longer wavelengths, and the $O(^1D)$ channel is dominant at shorter wavelengths. When available, the recommended quantum yields from JPL2019 (Burkholder et al., 2019) were the primary source used in this work. When there were no recommended quantum yields, we assumed a quantum yield of 1 for all wavelengths below the threshold wavelength. Table 3.1 lists all the photolysis channels captured in our model, repeated here for completeness. The threshold wavelength and the sources for the quantum yields are also included.

The model for photolysis included in SOCRATES includes photodissociation directly caused by radiation, and secondary dissociations caused by photoelectrons (free electrons released by photoionisations). Photoelectrons are sufficiently high energy as to cause ionisations/dissociations. The photoelectrons themselves are generated by high-energy photons causing ionisations, but we do not directly capture their generation in our chemistry scheme (including the effects of ionisation into the chemistry scheme is an idea for future work). Instead, we adopt the pa-

Photolysis	Threshold wavelength (nm)	Quantum yield source
$O_2 + h\nu \longrightarrow O(^3P) + O(^3P)$	242.3	JPL2019
$O_2 + h\nu \longrightarrow O(^3P) + O(^1D)$	175	JPL2019
$O_3 + h\nu \longrightarrow O(^3P) + O_2$	1180	JPL2019
$O_3 + h\nu \longrightarrow O(^1D) + O_2$	411	JPL2019
$HO_2 + h\nu \longrightarrow OH + O(^3P)$	438	Assumed to be 1
$HO_2 + h\nu \longrightarrow OH + O(^1D)$	259	Assumed to be 1
$H_2O + h\nu \longrightarrow H + OH$	242	JPL2019
$H_2O + h\nu \longrightarrow H_2 + O(^1D)$	175	JPL2019
$H_2O + h\nu \longrightarrow H + H + O(^3P)$	129	JPL2019
$H_2O_2 + h\nu \longrightarrow OH + OH$	557	JPL2019
$H_2O_2 + h\nu \longrightarrow H + HO_2$	329	JPL2019
$NO_2 + h\nu \longrightarrow NO + O(^3P)$	422	JPL2019
$NO_3 + h\nu \longrightarrow NO_2 + O(^3P)$	7320	JPL2019
$NO_3 + h\nu \longrightarrow NO + O_2$	640	JPL2019
$N_2O + h\nu \longrightarrow N_2 + O(^1D)$	336	JPL2019
$N_2O_5 + h\nu \longrightarrow NO_3 + NO_2$	1255	JPL2019
$N_2O_5 + h\nu \longrightarrow NO_3 + NO + O(^3P)$	298	JPL2019
$HONO + h\nu \longrightarrow OH + NO$	579	Assumed to be 1
$HNO_3 + h\nu \longrightarrow NO_2 + OH$	581	Assumed to be 1
$HO_2NO_2 + h\nu \longrightarrow HO_2 + NO_2$	1207	JPL2019
$HO_2NO_2 + h\nu \longrightarrow OH + NO_3$	726	JPL2019

Table 3.1: The list of photolysis reactions (channels) used in the chemical network, the threshold wavelength for each reaction, and the sources for the quantum yields.

rameterisation and coefficients of Solomon (2005) for the ionisation due to photo-electrons of O_2. As a result of including the effects of photoelectrons and the significantly higher amount of UV in the stellar spectra than used in previous works (see Section 2.7.3), we find significantly higher amounts of ozone in the planets atmosphere than compared to previous works when using similar chemical networks, such as the results reported in Yates et al. (2020). This is also caused by the treatment of irradiation and an issue with the distribution of the stellar flux across wavelength bins causing erroneous photolysis rates in Yates et al. (2020), see Braam et al. (2022) for a further discussion.

Now that the calculation of photolysis has been described, we will describe how the photolysis rates are included into the chemistry scheme. The chemistry framework was updated to accept a list of photolysis reactions as an input. This list is expected to match the photolysis reactions included in the SOCRATES configuration file (spectral file). Once the photolysis rates are calculated in SOCRATES (see 3.1.1 for an explanation for how those are calculated), they are passed to the chemical kinetics code and used as the reaction rate coefficients for the reactions.

Internally, these are treated as a unimolecular reaction, where the reaction rate is $k_f = J[A]$ in order to calculate the resulting change in the number density of said molecule. The chemical abundances are then passed to SOCRATES for future radiative transfer calculations. This creates a coupling between the chemistry framework and the photolysis scheme.

3.1.2 Coupling of water vapour to the rest of the UM

Beyond relying on the temperature and pressure fields of the UM and coupling the radiative transfer to the chemistry by using the atmospheric composition determined by the chemistry framework, the chemistry scheme was initially not coupled to the rest of the systems in the UM, such as precipitation and the water cycle. This was not a problem when the UM was being used to simulate gas giants without a hydrological cycle (Drummond, 2017), but it did present a problem for when we wanted to use the chemistry on terrestrial planets with a water cycle. I coupled the chemistry scheme to the UM's water cycle. To accommodate the coupling, at the beginning of each chemical time-step the mass mixing ratios of every non-water chemical species in each grid-box is adjusted to keep the sum of the mass mixing ratio for each species equal to one,

$$\frac{1 - m_{\mathrm{v}}}{1 - mmr_{H2O}},\tag{3.2}$$

where m_v is the moisture variable ($\mathrm{kg\,kg^{-1}}$) in each grid-cell, and mmr_{H2O} is the mass mixing ratio of water in each grid-cell before the weighting. The moisture variable is the amount of water vapour which comes from the UM. The mass mixing ratio of water is then set to the value of the moisture variable supplied by the UM. After the kinetics calculations, the updated value for the water vapour abundance is passed back to the UM. This allows us to couple the chemistry scheme to the precipitation scheme. In practice, the impact of the coupling was rather limited, with the concentrations of water vapour being mostly unaffected by the chemistry except at high altitudes. This may be improved by the inclusion of water

vapour generation into the chemistry framework, similar to recent developments in UKCA (Archibald et al., 2020).

3.1.3 Deposition

Deposition is the process where material in the atmosphere (gas-phase or aerosol particles) is deposited on the surface of the planet and removed from the atmosphere. There are two types of deposition that were considered for this work, dry deposition and wet deposition. Dry deposition occurs when (through gravitational settling or turbulence) particles are deposited onto the surface. Wet deposition occurs when gases dissolve into raindrops. Dry deposition is an important sink for molecules such as ozone, and is included in the chemistry. During development, wet deposition was not considered as it was not expected to change ozone concentrations significantly, as ozone was expected to be mostly prevalent in the stratosphere and have a limited amount in the troposphere when using the full chemical network. While this is true, a lack of wet deposition creates some problems when discussing the surface radiation environment, as a lack of wet deposition results in a large reservoir being created of HNO_3, a species which should effectively be removed by wet deposition. The existence of the reservoir results in a significant reduction in the surface UV, which would not occur if HNO_3 was not present. This will be discussed further in Section 5.4. This section will describe how dry deposition was implemented into the chemistry.

3.1.4 Dry deposition

In this work dry deposition was implemented in the simple form described by Giannakopoulos et al. (1999) for the following seven species: O_3, NO_2, NO_3, N_2O_5, HO_2NO_2, HNO_3, and H_2O_2. We chose to parameterise dry deposition through a single deposition velocity V_{dep}. $V_{dep} \equiv F_c/n_i$, is the ratio of the flux density of particles (F_c) onto the surface to the number density of particles in the air above the surface (n_i). V_{dep} varies for different terrains (Giannakopoulos et al., 1999), but as we are simulating an aquaplanet we adopt values of V_{dep} representing dry

deposition onto an ocean which is used for the entire planetary surface. Using the definition of deposition velocity we can derive the first–order loss rates due to dry deposition. Starting from the definition of deposition velocity, a quantity describing the ratio between the flux of material being deposited on a surface and the concentration of that material in the air

$$V_{\text{dep}} = \text{Flux}/\text{Concentration} = (\text{Kg}/\text{m}^2\text{s})/(\text{Kg}/\text{m}^3) = \text{m/s}. \tag{3.3}$$

Deposition velocity depends on the chemical species and the type of terrain. For this work, as the planet is an aquaplanet, we can use a deposition velocity which is applicable for oceans. More advanced dry deposition schemes determine the deposition velocity using a resistance-based approach (Wesely, 1989) accounting for several factors such as the winds near the surface and the effect of the type of surface (ocean, forests, urban environments, etc.) to accept the molecule. Incorporating this into our model is the aim of future work.

Knowing that we are using a 3D grid to simulate our atmosphere, we can rewrite Equation 3.3 in terms of the number of molecules of species i (N_i), the surface area (A) of the surface level grid cell, and the volume (V) of the surface level grid cell

$$V_{\text{dep}} = -(\text{N}_i/A\text{t})/(\text{N}_i/V) = (-\text{N}_i/A\text{t})/n_i, \tag{3.4}$$

where n_i is the number density of species i and t is an arbitrary period of time. The right-hand side is negative as the molecules being deposited are a sink for the species.

$$V_{\text{dep}}n_i = -\text{N}_i/A\text{t}, \tag{3.5}$$

$$V_{\text{dep}}n_iA = -\frac{\partial \text{N}_i}{\partial t}. \tag{3.6}$$

Finally, dividing by V gives us the a formula for determining the change in the

number density of species i due to deposition

$$V_{\text{dep}} \frac{n_i A}{V} = -\frac{\partial n_i}{\partial t}. \tag{3.7}$$

We thus have

$$\frac{\partial n_i}{\partial t} = -\frac{V_{\text{dep}} A}{V} n_i, \tag{3.8}$$

which gives us the following formula for the change in number density of species i due to dry deposition over an elapsed time t

$$n_i(t) = n_i(t = 0) e^{-\frac{V_{\text{dep}} A}{V} t}. \tag{3.9}$$

The next step is the correct choice of V_{dep}. Table 3.2 contains the deposition velocities for selected species as measured at 1m from the surface. They were obtained from the values used by UKCA for deposition onto open ocean (O'Connor et al., 2014). Our lowest model layer is typically 20m thick. We need to extrapolate the deposition velocity to a value that is more accurate for the midpoint of the cell. The 1m values were extrapolated to the midpoint of the lowest layer, following the formula of Berntsen & Isaksen (1997)

$$V_{\text{dep}}(10\,\text{m}) = V_{\text{dep}}(1\,\text{m}) \frac{1}{1 + \frac{V_{\text{dep}}(1\,\text{m})}{DC}}, \tag{3.10}$$

where DC is the vertical diffusion coefficient, approximated as

$$DC \approx \frac{\log_{10}(z_1)/2}{\kappa u_*}, \tag{3.11}$$

where z_1 is the height of the surface level grid cell, κ is the von Karman constant, and u_* is the surface friction velocity.

Species	V_{dep} (cm/s)
O_3	0.05
NO_2	0.02
NO_3	0.02
N_2O_5	1.00
HO_2NO_2	1.00
HNO_3	1.00
H_2O_2	1.00

Table 3.2: A list of the species in the chemical networks which exhibit dry deposition, and the deposition velocities measured 1 meter from the surface.

3.2 Chemical networks controlling Ozone in terrestrial atmospheres

Now that the technical developments have been described, we can proceed to looking at the development of chemical networks describing ozone chemistry. The chemical networks describe a range of complexity and help qualify how ozone behaves in our model.

3.2.1 Chapman Cycle

During the early 20th century, Chapman (1930) proposed a series of reactions which describes the production, destruction, and regulation of ozone. In its simplest form, this consists of a series of 4 reactions. The process is initiated by the photolysis of O_2 which produces atomic oxygen, O (in this simplified view we do not distinguish between energy states of atomic oxygen). Atomic oxygen can react with molecular oxygen in a termolecular reaction to produce ozone. Ozone can be photolysed as well, returning back to atomic and molecular oxygen. The products of ozone photolysis could reform into ozone via the termolecular reaction without additional reactions which deplete atomic oxygen. To complete the cycle, a final reaction is required which converts ozone and atomic oxygen into molecular oxygen. This series of chemical reactions is known as the Chapman mechanism

or the Chapman cycle, and is described as

$$O_2 + h\nu \longrightarrow O + O,$$

$$O + O_2 + M \longrightarrow O_3 + M,$$

$$O_3 + h\nu \longrightarrow O_2 + O,$$

$$O_3 + O \longrightarrow O_2 + O_2.$$
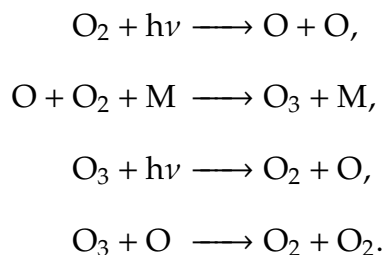
While useful, this view of the Chapman cycle does not capture several components, such as the existence of atomic energy states. The energy states of chemicals species such as atomic oxygen, are important to note, as they can cause additional chemical reactions to occur. For our purposes, we need to be aware of the ground state of atomic oxygen, $O(^3P)$, and an excited state, $O(^1D)$. The excited state is created by photolysis with more energetic photons, and plays a key role in initiating the HO_x cycle, as will be described in the following section.

A list of the chemical species involved in the simulation of the Chapman cycle are listed in Table 3.3. Note that several species (N_2, CO_2) are included in the simulation but are not reactive (as in they are not changed into other chemical species). They are included as they are involved in de–excitation reactions of atomic oxygen, converting $O(^1D)$ into $O(^3P)$.

Species	Formula
Molecular oxygen	O_2
Ozone	O_3
Molecular Nitrogen	N_2
Carbon dioxide	CO_2
Atomic oxygen (ground state)	$O(^3P)$
Atomic oxygen (first excited state)	$O(^1D)$

Table 3.3: The species included in the 'Chapman cycle' simulations used in this work.

This network, which is designated as the Chapman network, consists of the fol-

lowing reactions

$$O_2 + h\nu \longrightarrow O(^3P) + O(^3P) \qquad (\lambda <242 \text{ nm}) \qquad (R1)$$

$$O_2 + h\nu \longrightarrow O(^3P) + O(^1D) \qquad (\lambda <175 \text{ nm}) \qquad (R2)$$

$$O_2 + O(^3P) + M \longrightarrow O_3 + M \qquad (R3)$$

$$O_3 + h\nu \longrightarrow O_2 + O(^3P) \qquad (\lambda <1180 \text{ nm}) \qquad (R4)$$

$$O_3 + h\nu \longrightarrow O_2 + O(^1D) \qquad (\lambda <411 \text{ nm}) \qquad (R5)$$

$$O_3 + O(^3P) \longrightarrow O_2 + O_2 \qquad (R6)$$

$$O_3 + O(^1D) \longrightarrow O_2 + O_2 \qquad (R7)$$

$$O_3 + O(^1D) \longrightarrow O_2 + O(^3P) + O(^3P) \qquad (R8)$$

$$O_2 + O(^1D) \longrightarrow O_2 + O(^3P) \qquad (R9)$$

$$N_2 + O(^1D) \longrightarrow N_2 + O(^3P) \qquad (R10)$$

$$CO_2 + O(^1D) \longrightarrow CO_2 + O(^3P) \qquad (R11)$$
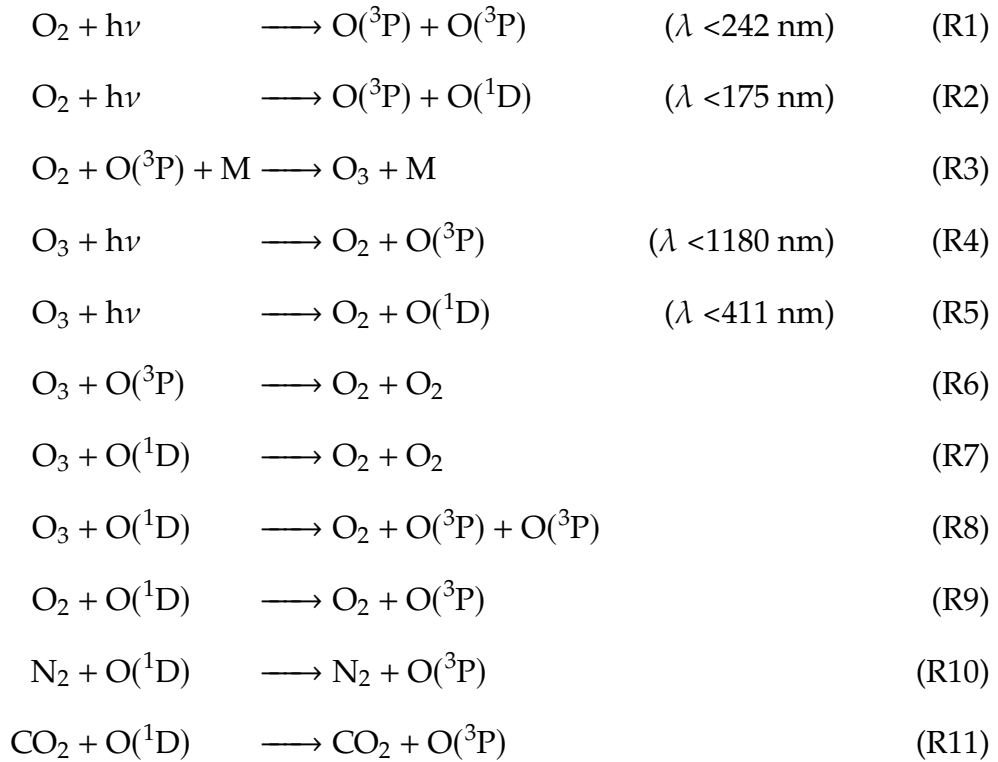
The Chapman cycle does not accurately capture the stratosphere however, and tends to overestimate the concentrations of ozone. In particular, it neglects two families of molecules which act as ozone sinks, hydrogen oxides, and nitrogen oxides. The inclusion of these families will reduce the concentration of ozone substantially. These two families will now be described.

3.2.2 Hydrogen oxides

Hydrogen oxides, also referred to as HO_x, refer to H, OH, and HO_2, a series of molecules which are generated from the destruction of water vapour by photolysis, atomic oxygen, and Stellar Energetic Protons (SEPs). These species react with each other and ozone to create a catalytic cycle, which depletes ozone substantially. The HO_x catalytic cycle is initiated by the destruction of water vapour into HO_x molecules, which react with ozone and destroy it. A typical view of the reactions

which comprise the catalytic cycle is

$$O(^1D) + H_2O \longrightarrow OH + OH,$$

$$OH + O_3 \longrightarrow HO_2 + O_2,$$

$$HO_2 + O_3 \longrightarrow OH + O_2 + O_2,$$

$$OH + HO_2 \longrightarrow H_2O + O_2,$$
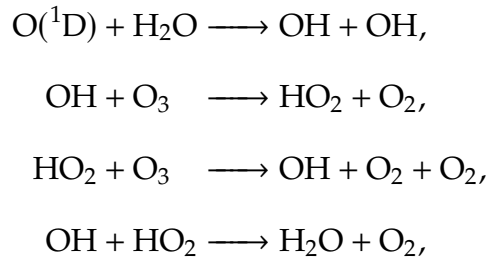
where OH is initially generated from water vapour. OH is converted into HO_2, and HO_2 can convert back into OH, also by destroying ozone. The cycle is terminated by OH and HO_2 reacting together and turning into water vapour. There are other sources of HO_x, such as the photolysis of water vapour

$$H_2O + h\nu \longrightarrow H + OH \qquad (\lambda < 242 \text{ nm}),$$

$$H_2O + h\nu \longrightarrow H + H + O(^3P) \quad (\lambda < 129 \text{ nm}),$$

$$H + O_3 \longrightarrow OH + O_2,$$
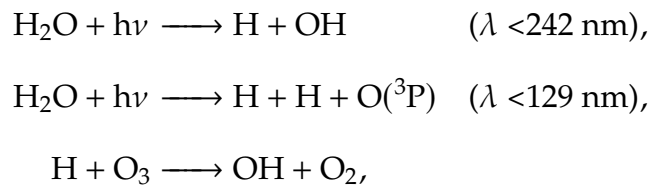
as well as SEPs, which will be described in Section 4.5. The additional chemical species involved with the inclusion of HO_x chemistry in this work are listed in Table 3.4.

Species	Formula
Hydroxyl radical	OH
Hydroperoxyl radical	HO_2
Molecular hydrogen	H_2
Atomic hydrogen	H
Hydrogen peroxide	H_2O_2

Table 3.4: The species added to the network to include HO_x chemistry.

This network, hereafter designated as the HO_x network, consists of all the reactions from the Chapman network, as well as the following list of reactions:

$$O(^1D) + H_2O \longrightarrow OH + OH \tag{R12}$$

$$OH + O_3 \longrightarrow HO_2 + O_2 \tag{R13}$$

$$HO_2 + O_3 \longrightarrow OH + O_2 + O_2 \tag{R14}$$

$$\text{OH} + \text{HO}_2 \longrightarrow \text{H}_2\text{O} + \text{O}_2 \tag{R15}$$

$$\text{H} + \text{O}_3 \longrightarrow \text{OH} + \text{O}_2 \tag{R16}$$

$$\text{H} + \text{HO}_2 \longrightarrow \text{OH} + \text{OH} \tag{R17}$$

$$\text{H} + \text{HO}_2 \longrightarrow \text{O}(^3\text{P}) + \text{H}_2\text{O} \tag{R18}$$

$$\text{H} + \text{HO}_2 \longrightarrow \text{H}_2 + \text{O}_2 \tag{R19}$$

$$\text{OH} + \text{H}_2 \longrightarrow \text{H}_2\text{O} + \text{H} \tag{R20}$$

$$\text{OH} + \text{OH} \longrightarrow \text{H}_2\text{O} + \text{O}(^3\text{P}) \tag{R21}$$

$$\text{OH} + \text{H}_2\text{O}_2 \longrightarrow \text{H}_2\text{O} + \text{HO}_2 \tag{R22}$$

$$\text{HO}_2 + \text{HO}_2 \longrightarrow \text{H}_2\text{O}_2 + \text{O}_2 \tag{R23}$$

$$\text{O}(^1\text{D}) + \text{H}_2 \longrightarrow \text{OH} + \text{H} \tag{R24}$$

$$\text{O}(^3\text{P}) + \text{OH} \longrightarrow \text{O}_2 + \text{H} \tag{R25}$$

$$\text{O}(^3\text{P}) + \text{HO}_2 \longrightarrow \text{O}_2 + \text{OH} \tag{R26}$$

$$\text{O}(^3\text{P}) + \text{H}_2\text{O}_2 \longrightarrow \text{OH} + \text{HO}_2 \tag{R27}$$

$$\text{H}_2\text{O} + h\nu \longrightarrow \text{H} + \text{OH} \quad (\lambda < 242 \text{ nm}) \tag{R28}$$

$$\text{H}_2\text{O} + h\nu \longrightarrow \text{H}_2 + \text{O}(^1\text{D}) \quad (\lambda < 175 \text{ nm}) \tag{R29}$$

$$\text{H}_2\text{O} + h\nu \longrightarrow \text{H} + \text{H} + \text{O}(^3\text{P}) \quad (\lambda < 129 \text{ nm}) \tag{R30}$$

$$\text{HO}_2 + h\nu \longrightarrow \text{OH} + \text{O}(^3\text{P}) \quad (\lambda < 438 \text{ nm}) \tag{R31}$$

$$\text{HO}_2 + h\nu \longrightarrow \text{OH} + \text{O}(^1\text{D}) \quad (\lambda < 259 \text{ nm}) \tag{R32}$$

$$\text{H}_2\text{O}_2 + h\nu \longrightarrow \text{OH} + \text{OH} \quad (\lambda < 557 \text{ nm}) \tag{R33}$$

$$\text{H}_2\text{O}_2 + h\nu \longrightarrow \text{H} + \text{HO}_2 \quad (\lambda < 324 \text{ nm}) \tag{R34}$$

$$\text{H} + \text{O}_2 + \text{M} \longrightarrow \text{HO}_2 + \text{M} \tag{R35}$$

$$\text{OH} + \text{OH} + \text{M} \longrightarrow \text{H}_2\text{O}_2 + \text{M} \tag{R36}$$

$$\text{HO}_2 + \text{HO}_2 + \text{M} \longrightarrow \text{H}_2\text{O}_2 + \text{O}_2 + \text{M} \tag{R37}$$

A list of the reaction rate coefficients for each chemical reaction included as part of the HO$_\text{x}$ network is listed in Table A in the Appendix. The inclusion of HO$_\text{x}$

chemistry is an improvement over just the Chapman Cycle, but is further improved by the introduction of nitrogen oxide chemistry, which will now be described.

3.2.3 Nitrogen oxide chemistry

Nitrogen oxides, also called NO_x, refer to NO and NO_2. The NO_x cycle behaves similarly to the HO_x cycle. The NO_x cycle depletes ozone via the following reactions

$$NO + O_3 \longrightarrow NO_2 + O_2,$$
$$O(^3P) + NO_2 \longrightarrow NO + O_2,$$
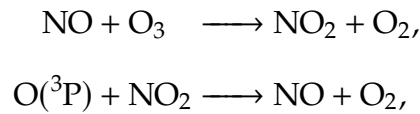
which has the effect of $O_3 + O(^3P) \longrightarrow 2\,O_2$ while recycling NO and NO_2.

On Earth, a large source of NO_x and nitrous oxide (N_2O) is biological activity in soils (Tables 4.8 and 4.1 respectively, from Ehhalt et al., 2001). Without any estimation or knowledge of a hypothetical ProxCen b biosphere, we restrict ourselves to abiotic sources of NO_x. In this model, the amount of NO_x is heavily controlled by the presence of SEPs. Without any SEPs, NO is generated by

$$N_2 + O(^1D) + M \longrightarrow N_2O + M,$$
$$N_2O + O(^1D) \longrightarrow NO + NO.$$
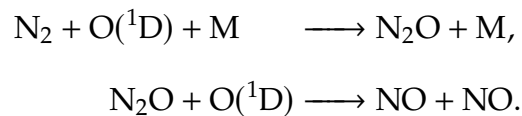
With the presence of SEPs, NO is modified by the generation of atomic nitrogen

$$N_2 + p^+/e^- \longrightarrow N(^4S) + N(^4S),$$
$$N_2 + p^+/e^- \longrightarrow N(^2D) + N(^2D),$$
$$O_2 + N(^4S) \longrightarrow NO + O(^3P),$$
$$O_2 + N(^2D) \longrightarrow NO + O(^3P),$$
$$NO + N(^4S) \longrightarrow N_2 + O(^3P),$$
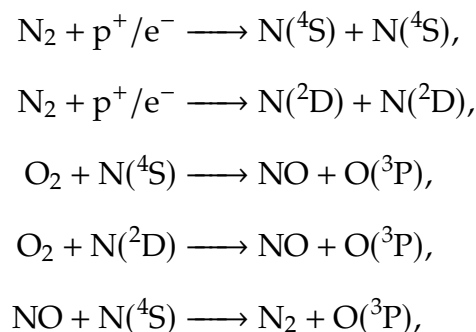
where p^+/e^- denotes that the reaction is caused by SEPs.

The method in which this was included in the chemistry and how it impacts ozone concentrations will be discussed in more detail in Sections 4.5 and 5.2, respectively.

In this work, we include NO_x species, as well as several important NO_x reservoirs, which are collectively referred to as NO_y. The included species are listed in Table 3.5.

Species	Formula
Nitric oxide	NO
Nitrogen dioxide	NO_2
Nitrate radical	NO_3
Dinitrogen pentoxide	N_2O_5
Peroxynitric acid	HO_2NO_2
Nitrous acid	HONO
Nitric acid	HNO_3
Nitrous oxide	N_2O
Atomic nitrogen (ground state)	$N(^4S)$
Atomic nitrogen (excited state)	$N(^2D)$

Table 3.5: The species added to the network to include NO_x chemistry.

To model the impacts of SEPs on the atmospheric composition, reactions involving atomic nitrogen were included in the chemical network. One of the main reaction pathways of SEPs is the destruction of molecular nitrogen into atomic nitrogen. Reactions for the excited state of atomic nitrogen, $N(^2D)$, were obtained from Herron (1999). The list of reactions that were deemed as potentially relevant are listed in Table 3.6.

Reaction	A (cm^3 molecule^{-1} s^{-1})	E_a/R (K)	k(298) (cm^3 molecule^{-1} s^{-1})	Notes
$N(^2D) + H_2O \longrightarrow$ products	–	–	4×10^{-11}	–
$N(^2D) + O(^3P) \longrightarrow N(^4S) + O(^3P)$	3.3×10^{-12}	260	5.2×10^{-12}	300-400 K
$N(^2D) + O_2 \longrightarrow NO + O(^3P)$	9.7×10^{-12}	185	6×10^{-11}	200-500 K
$N(^2D) + NO \longrightarrow N_2 + O(^3P)$	–	–	6×10^{-11}	–
$N(^2D) + N_2O \longrightarrow N_2 + NO$	1.5×10^{-11}	570	2.2×10^{-12}	200-400 K
$N(^2D) + N_2 \longrightarrow N(^4S) + N_2$	–	–	1.7×10^{-14}	–

Table 3.6: Reaction rate coefficients from Herron (1999) for reactions involving $N(^2D)$. As described in Section 2.5.8), A is a pre–exponential factor, E_a/R is the activation temperature (dividing the activation energy by the universal gas constant), k(298) is the reaction rate coefficient at 298 K, and Notes lists the temperature range tested for the reaction rate coefficients.

Of these reactions, we decided to include the following reactions

$$N(^2D) + O(^3P) \longrightarrow N(^4S) + O(^3P),$$

$$N(^2D) + O_2 \longrightarrow NO + O(^3P),$$

$$N(^2D) + N_2O \longrightarrow N_2 + NO,$$

$$N(^2D) + N_2 \longrightarrow N(^4S) + N_2,$$
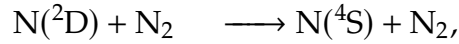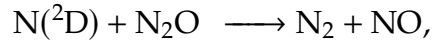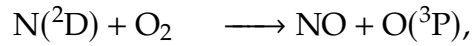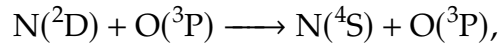
as the first three reactions have defined reaction rate coefficients, and the latter reaction provides a de–excitation channel for $N(^2D)$ to convert to $N(^4S)$, despite only having a reaction rate coefficient defined for 298 K. Without a temperature dependent reaction rate there is the risk of under or over–estimating the loss rate of $N(^2D)$ which has implications on how strong the effect of the SEPs will be. Future work in this area is needed to improve our modelling of atomic nitrogen chemistry.

The network, designated as the NO_x network, consists of every reaction from the Chapman and HO_x networks, as well as the following reactions:

$O(^1D) + N_2 + M$	$\longrightarrow N_2O + M$		(R38)
$N_2O + h\nu$	$\longrightarrow N_2 + O(^1D)$	($\lambda < 336$ nm)	(R39)
$O(^1D) + N_2O$	$\longrightarrow N_2 + O_2$		(R40)
$O(^1D) + N_2O$	$\longrightarrow NO + NO$		(R41)
$NO + O_3$	$\longrightarrow NO_2 + O_2$		(R42)
$NO_2 + h\nu$	$\longrightarrow NO + O(^3P)$	($\lambda < 422$ nm)	(R43)
$O(^3P) + NO_2$	$\longrightarrow NO + O_2$		(R44)
$O(^3P) + NO + M$	$\longrightarrow NO_2 + M$		(R45)
$NO_2 + O_3$	$\longrightarrow NO_3 + O_2$		(R46)
$O(^3P) + NO_2 + M$	$\longrightarrow NO_3 + M$		(R47)
$O(^3P) + NO_3$	$\longrightarrow NO_2 + O_2$		(R48)
$H + NO_2$	$\longrightarrow OH + NO$		(R49)
$OH + NO_3$	$\longrightarrow HO_2 + NO_2$		(R50)

$$\text{HO}_2 + \text{NO} \longrightarrow \text{NO}_2 + \text{OH} \tag{R51}$$

$$\text{HO}_2 + \text{NO}_3 \longrightarrow \text{OH} + \text{NO}_2 + \text{O}_2 \tag{R52}$$

$$\text{NO} + \text{NO}_3 \longrightarrow \text{NO}_2 + \text{NO}_2 \tag{R53}$$

$$\text{NO}_3 + h\nu \longrightarrow \text{NO}_2 + \text{O}(^3\text{P}) \qquad (\lambda < 7320 \text{ nm}) \tag{R54}$$

$$\text{NO}_3 + h\nu \longrightarrow \text{NO} + \text{O}_2 \qquad (\lambda < 640 \text{ nm}) \tag{R55}$$

$$\text{NO}_2 + \text{NO}_3 \longrightarrow \text{NO} + \text{NO}_2 + \text{O}_2 \tag{R56}$$

$$\text{NO}_3 + \text{NO}_3 \longrightarrow \text{NO}_2 + \text{NO}_2 + \text{O}_2 \tag{R57}$$

$$\text{NO}_2 + \text{NO}_3 + \text{M} \longrightarrow \text{N}_2\text{O}_5 + \text{M} \tag{R58}$$

$$\text{N}_2\text{O}_5 + h\nu \longrightarrow \text{NO}_3 + \text{NO}_2 \qquad (\lambda < 1255 \text{ nm}) \tag{R59}$$

$$\text{N}_2\text{O}_5 + h\nu \longrightarrow \text{NO}_3 + \text{NO} + \text{O}(^3\text{P}) \qquad (\lambda < 298 \text{ nm}) \tag{R60}$$

$$\text{N}_2\text{O}_5 + \text{M} \longrightarrow \text{NO}_2 + \text{NO}_3 + \text{M} \tag{R61}$$

$$\text{N}_2\text{O}_5 + \text{H}_2\text{O} \longrightarrow \text{HNO}_3 + \text{HNO}_3 \tag{R62}$$

$$\text{OH} + \text{NO}_2 + \text{M} \longrightarrow \text{HNO}_3 + \text{M} \tag{R63}$$

$$\text{HNO}_3 + h\nu \longrightarrow \text{NO}_2 + \text{OH} \qquad (\lambda < 581 \text{ nm}) \tag{R64}$$

$$\text{OH} + \text{HNO}_3 \longrightarrow \text{H}_2\text{O} + \text{NO}_3 \tag{R65}$$

$$\text{OH} + \text{NO} + \text{M} \longrightarrow \text{HONO} + \text{M} \tag{R66}$$

$$\text{OH} + \text{HONO} \longrightarrow \text{H}_2\text{O} + \text{NO}_2 \tag{R67}$$

$$\text{HONO} + h\nu \longrightarrow \text{OH} + \text{NO} \qquad (\lambda < 579 \text{ nm}) \tag{R68}$$

$$\text{HO}_2 + \text{NO}_2 + \text{M} \longrightarrow \text{HO}_2\text{NO}_2 + \text{M} \tag{R69}$$

$$\text{HO}_2\text{NO}_2 + h\nu \longrightarrow \text{HO}_2 + \text{NO}_2 \qquad (\lambda < 1207 \text{ nm}) \tag{R70}$$

$$\text{HO}_2\text{NO}_2 + h\nu \longrightarrow \text{OH} + \text{NO}_3 \qquad (\lambda < 726 \text{ nm}) \tag{R71}$$

$$\text{OH} + \text{HO}_2\text{NO}_2 \longrightarrow \text{H}_2\text{O} + \text{NO}_2 + \text{O}_2 \tag{R72}$$

$$\text{HO}_2\text{NO}_2 + \text{M} \longrightarrow \text{HO}_2 + \text{NO}_2 + \text{M} \tag{R73}$$

$$\text{N}(^4\text{S}) + \text{O}_2 \longrightarrow \text{NO} + \text{O}(^3\text{P}) \tag{R74}$$

$$\text{N}(^4\text{S}) + \text{NO} \longrightarrow \text{N}_2 + \text{O}(^3\text{P}) \tag{R75}$$

$$\text{N}(^4\text{S}) + \text{NO}_2 \longrightarrow \text{N}_2\text{O} + \text{O}(^3\text{P}) \tag{R76}$$

$$\text{N}(^2\text{D}) + \text{N}_2 \longrightarrow \text{N}(^4\text{S}) + \text{N}_2 \tag{R77}$$

$$\text{N}(^2\text{D}) + \text{O}(^3\text{P}) \quad \longrightarrow \text{N}(^4\text{S}) + \text{O}(^3\text{P}) \qquad\qquad\qquad \text{(R78)}$$

$$\text{N}(^2\text{D}) + \text{O}_2 \quad \longrightarrow \text{NO} + \text{O}(^3\text{P}) \qquad\qquad\qquad\qquad \text{(R79)}$$

$$\text{N}(^2\text{D}) + \text{N}_2\text{O} \quad \longrightarrow \text{N}_2 + \text{NO} \qquad\qquad\qquad\qquad\quad \text{(R80)}$$

3.3   Chemical network validation

Now that we have described the chemical networks that comprise this work, we can test how they work using the UM. These simulations were run assuming no stellar activity, no flares or SEPs. Table 3.7 lists the simulations we have performed for this work, the stellar irradiation, the time-steps for the dynamics, radiation and chemistry for each simulation. The aim of these simulations is to qualify how the chemical framework and the amount of ozone changes with increasing complexity, and not to test the impact of the inclusion of each portion of the network. Due to this, there is no simulation which only includes the Chapman mechanism and NO_x chemistry. Simulations were run to gauge the impact of quiescent SEPs, which are described in Section 5.2. Aside from slightly different initial chemical compositions depending on the chemical network, every simulation starts from the same atmospheric conditions, derived from an initial spin–up simulation. To verify that the simulations are stable for long periods of time, an initial simulation was run for 3000 Earth days without chemistry, and the fixed 'Earth–like' atmospheric composition as prescribed in Table 2 of Boutle et al. (2017). The end point of this simulation, which was in a climatic steady–state (near constant mean surface temperatures and top–of–atmosphere radiative flux balance) was then used as the start point for the quiescent phase simulations with chemistry. Likewise, the end state of the quiescent simulation containing the full chemical network and quiescent SEPs was used as the start point for the flaring simulations. Before we can explore the effects of the choice of chemical network on the concentration of ozone, the climate and dynamics of the planet's atmosphere should be described.

Phase	Name	Spectrum	Chemistry	Time–steps (minutes)		
				Dynamic	Radiation	Chemistry
	Quiet_Ch	Quiescent	ChC			
Quiescent	Quiet_Ch_HOx	Quiescent	ChC & HO_x	10	60	60
	Quiet_Ch_HOx_NOx	Quiescent	ChC, HO_x & NO_x			

Table 3.7: All quiescent simulations without stellar energetic protons performed for this work, with short names and a description of the components included.

Band	Wavelength range (nm)
1	0.5–75
2	75–100
3	100–125
4	125–150
5	150–175
6	175–200
7	200–225
8	225–250
9	275–300
10	300–320
11	320–505
12	505–690
13	690–1190
15	1190–2380
16	2380–10000

Table 3.8: The shortwave wavelength bands used by the radiation scheme for this work.

For this work, the spectral file (configuration file used by SOCRATES for the radiative transfer) that is used to represent ProxCen b contains 16 wavelength bands, which are listed in Table 3.8.

3.3.1 Qualification of the photolysis scheme

Due to time constraints, a full simulation of a planet representative of the Earth was not performed. Instead, the photolysis scheme was tested to understand how the scheme compares to other schemes. This will provide some justification for not simulating the Earth.

Without the ability to measure photolysis rates on exoplanets to directly compare to our photolysis rate calculations, I tested how calculated terrestrial photolysis rates compare to other photolysis models, using the photolysis rate data supplied for PhotoComp 2008[1] as part of the Chemistry-Climate model intercomparison

---

[1]Available from https://homepages.see.leeds.ac.uk/~lecmc/ccmvalj/

performed for Xu et al. (2017), comparing the rates from the P1a experiment (a clear-sky with Rayleigh scattering, see their Table 6.2). In order to test how well SOCRATES captures terrestrial photolysis rates, a version of my spectral file that was used in this work for the ProxCen b simulations was created using the Solar spectrum for the shortwave with the same band structure seen in Table 3.8. The following three photolysis reactions were tested

$$O_2 + h\nu \longrightarrow O + O, \tag{R81}$$

$$O_3 + h\nu \longrightarrow O_2 + O, \tag{R82}$$

$$O_3 + h\nu \longrightarrow O_2 + O(^1D), \tag{R83}$$
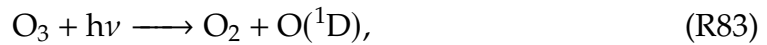
as these reactions are important reactions that regulate and control ozone chemistry in the atmospheres of terrestrial planets. This will be explained further in Sections 3.2.1–3.2.3 which will explain the chemistry involved in this work.

Two versions of the Solar spectral are shown in the following figures. The first was created in 2020 and uses the same opacity data as the ProxCen b spectral file, see Table A.1 in the Appendix for a list of all opacity sources. The second file was created with more recently compiled ozone opacity data (courtesy of James Manners) and is labelled 2023. To compare the photolysis rates, I used the single column model of SOCRATES, which computes radiative transfer for a column of a given atmospheric composition, temperature, and pressure profiles. Figure 3.2 shows a comparison of the rates of $O_2 + h\nu \longrightarrow O + O$. The computed rates from SOCRATES for the 2020 and 2023 spectral files are quite similar to the reference data for most pressure, but does show higher photolysis rates at pressures of less than $10\,\text{Pa}$ and pressures greater than $10^4\,\text{Pa}$.

Figures 3.3 and 3.4 show the computed rates for ozone photolysis, total atomic oxygen production, and the production of $O(^1D)$ (an excited state of atomic oxygen). We see that the results using the 2020 spectral file matches the reference data well for pressures above $100\,\text{Pa}$, but does have lower photolysis rates for pressures below $100\,\text{Pa}$. The results from the newer 2023 spectral file are significantly im-
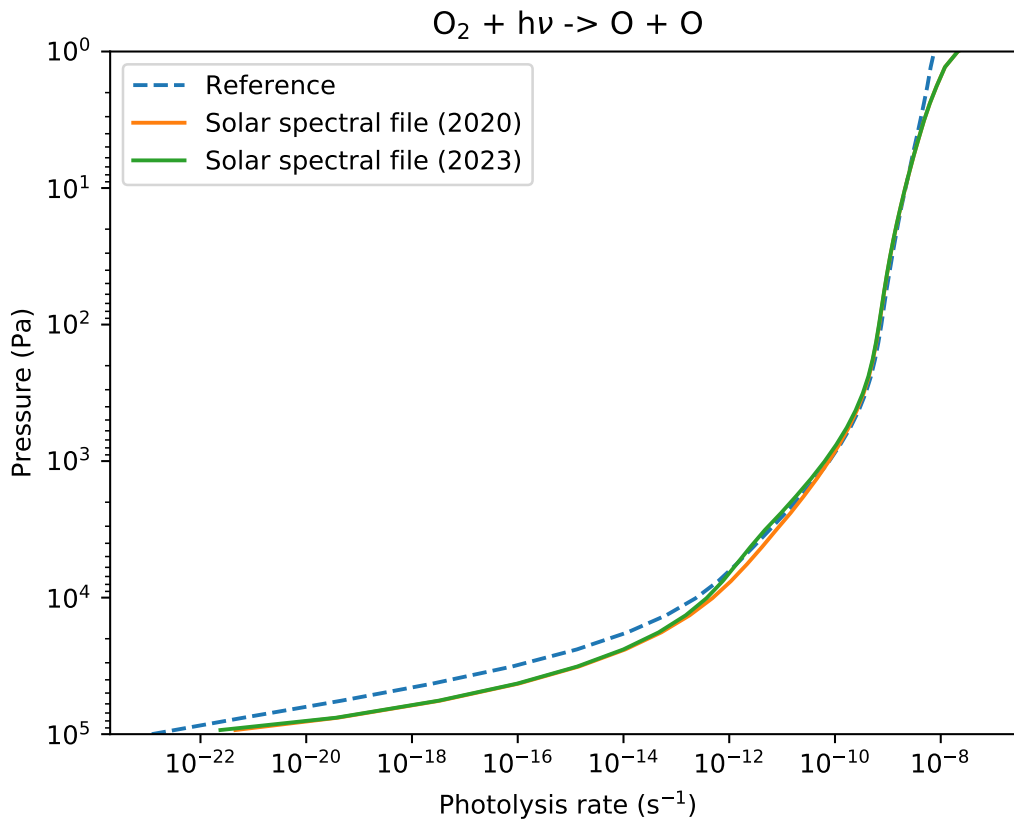
Figure 3.2: A single column SOCRATES simulation comparing oxygen photolysis rates.

proved at lower pressures.

The results of these figures are similar to the reference data and the range of photolysis rates shown in Xu et al. (2017),This demonstrates that the photolysis scheme used in this work is capable of calculating similar photolysis rates to other photolysis schemes. As the process to create the ProxCen b spectral file was very similar, merely using a different stellar spectra to create the *k*–coefficients used for the radiative transfer, this gives us justification for using the photolysis scheme for non–Earth planets. Further testing and qualification of the photolysis scheme in non–Earth–like atmospheres would be appreciated.

Due to time constraints, UM simulations examining the results of the differing chemical networks were not performed for a representation of the modern Earth. However, the photolysis scheme performed well in describing photolysis in an Earth representation. As the photolysis scheme is flexible, this gives confidence that as long as the data provided for use in the photolysis scheme is accurate (the stellar spectrum, opacities, quantum yields, the reactions being considered) for
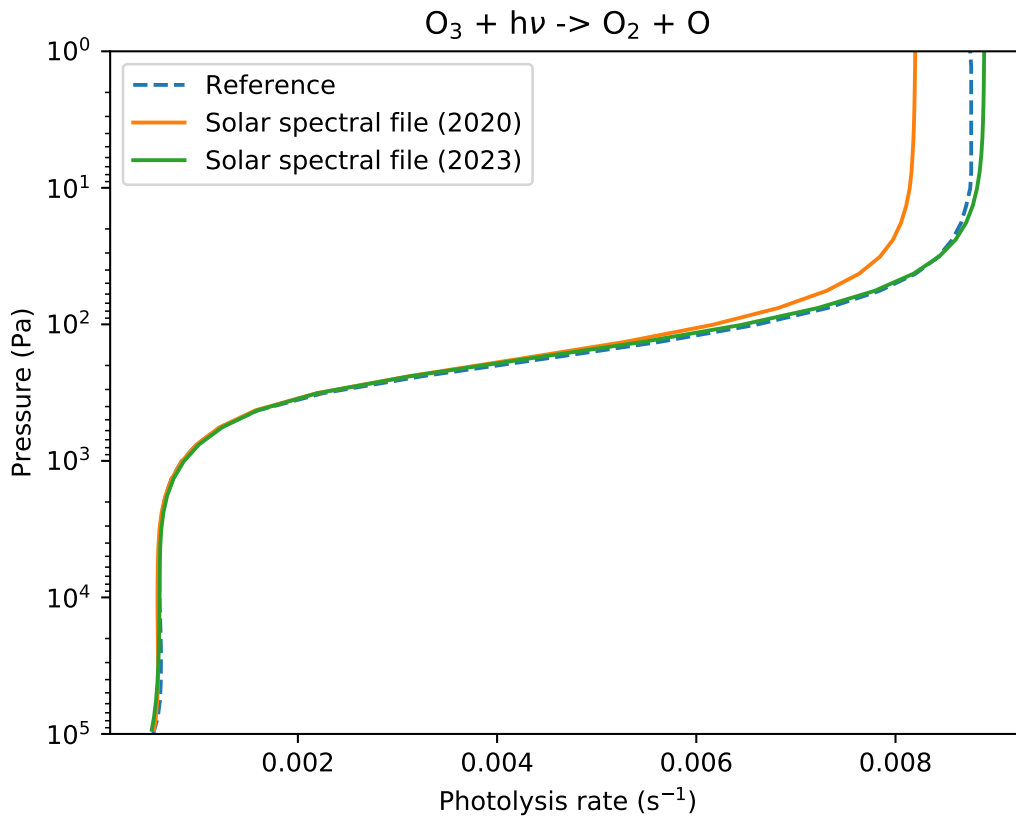
Figure 3.3: A single column SOCRATES simulation comparing the total production of atomic oxygen from ozone photolysis.
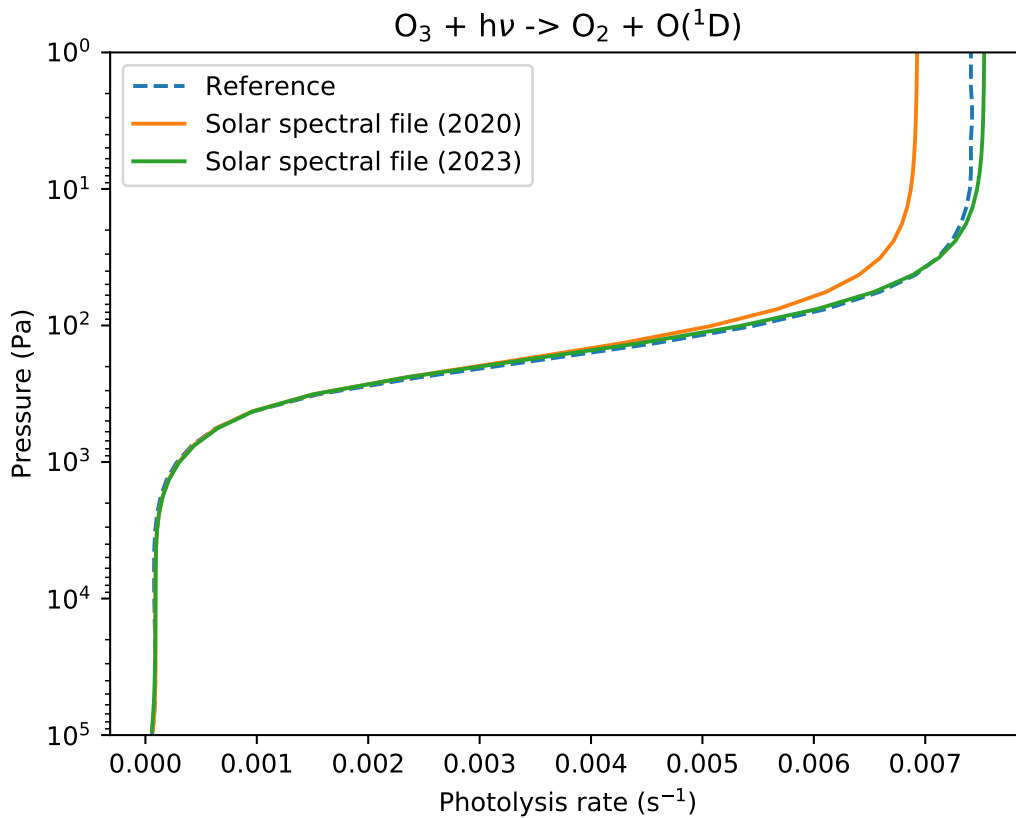
Figure 3.4: A single column SOCRATES simulation comparing the production rate of O(^{1}D) from ozone photolysis.

the gases, temperatures, and pressures expected to be seen in the simulation, the photolysis rates calculated by the photolysis scheme will be accurate.

Having some justification for accurate photolysis rates, we can say that we have an accurate photochemical scheme. The data for the thermochemical reactions (and deposition) has been validated for use in terrestrial chemistry, and is dependent on the temperature and pressures in the atmosphere. From this, there is some confidence in the results reported by this work that the chemistry scheme will return accurate results.

Simulations of the Earth should be the subject of future work, particularly in the context of describing the response of the terrestrial atmosphere to powerful flares or coronal mass ejections.

3.3.2   The climate of a tidally locked terrestrial planet

The planet in this work is based on Proxima Centauri b. Our setup is built upon that presented in Boutle et al. (2017), and consists of a terrestrial planet with an 'Earth-like' atmosphere as well as a global ocean. We have adopted their planetary parameters, which are listed in Table 3.9, and their 'Earth–like' initial atmospheric composition (see Table 2 of Boutle et al., 2017).

Planet Constants	Proxima Centauri b
Planet radius (km)	7160
Stellar constant (W/m^2)	2.07
Rotation rate (radians/s)	6.501×10^{-6}
Semi-major axis (AU)	0.0485
Top-of-atmosphere incident stellar flux (W/m^2)	880
Surface gravity (m/s^2)	10.9
Eccentricity	0
Obliquity	0
Height of atmosphere (km)	78.75
Tidally locked?	Yes

Table 3.9: The planetary and orbital parameters used in this work. The planet is assumed to be tidally locked.

The initial atmospheric composition for each simulation is described in Table 3.10. The orbital parameters are the values measured by Anglada-Escudé et al. (2016).

The planet is assumed to be tidally locked. The quiescent stellar constant is calculated using the same inputs and methodology as in Boutle et al. (2017). The planetary radius and surface gravity are those estimated by Turbet et al. (2016) assuming a mass of 1.4 Earth masses and a density similar to Earth of 5500 kg m^{-3}. The atmosphere is assumed to be N_2-O_2 dominated, with CO_2, and an active water cycle generating water vapour. The atmosphere extends to 78.75 km (at a pressure of approximately 3×10^{-2} Pa), as the high temperatures seen at high altitudes in this model caused model instabilities if the model height was kept at higher altitudes. This is not seen when using the same BT-Settl spectrum as Boutle et al. (2017) and is due to the change in spectra to the MUSCLES spectra (see Section 2.7.3).

Species	Initial mass fraction (kg kg^{-1})	Quiet_Ch	Quiet_Ch_HOx	Quiet_Ch_HOx_NOx
CO_2	5.941×10^{-4}	X	X	X
O_2	0.2314	X	X	X
$O(^3P)$	0	X	X	X
$O(^1D)$	0	X	X	X
O_3	10^{-9}	X	X	X
H_2O	$10^{-6} - 10^{-2}$	X	X	X
N_2	~ 0.76	X	X	X
OH	10^{-12}	–	X	X
HO_2	10^{-12}	–	X	X
H	10^{-12}	–	X	X
H_2	0	–	X	X
H_2O_2	10^{-12}	–	X	X
$N(^4S)$	10^{-12}	–	–	X
$N(^2D)$	10^{-12}	–	–	X
NO	10^{-12}	–	–	X
NO_2	10^{-12}	–	–	X
NO_3	10^{-12}	–	–	X
HNO_3	10^{-12}	–	–	X
N_2O	10^{-12}	–	–	X
N_2O_5	10^{-12}	–	–	X
HONO	10^{-12}	–	–	X
HO_2NO_2	10^{-12}	–	–	X

Table 3.10: The species included in each of the quiescent simulations, and the initial mass fractions (IMF) of each species. As the water mass fraction was controlled by the UM, its initial value was not constant but was a range of values. Due to this, and the differing number of species in the network, the initial mass fraction of N_2 differs slightly between networks.
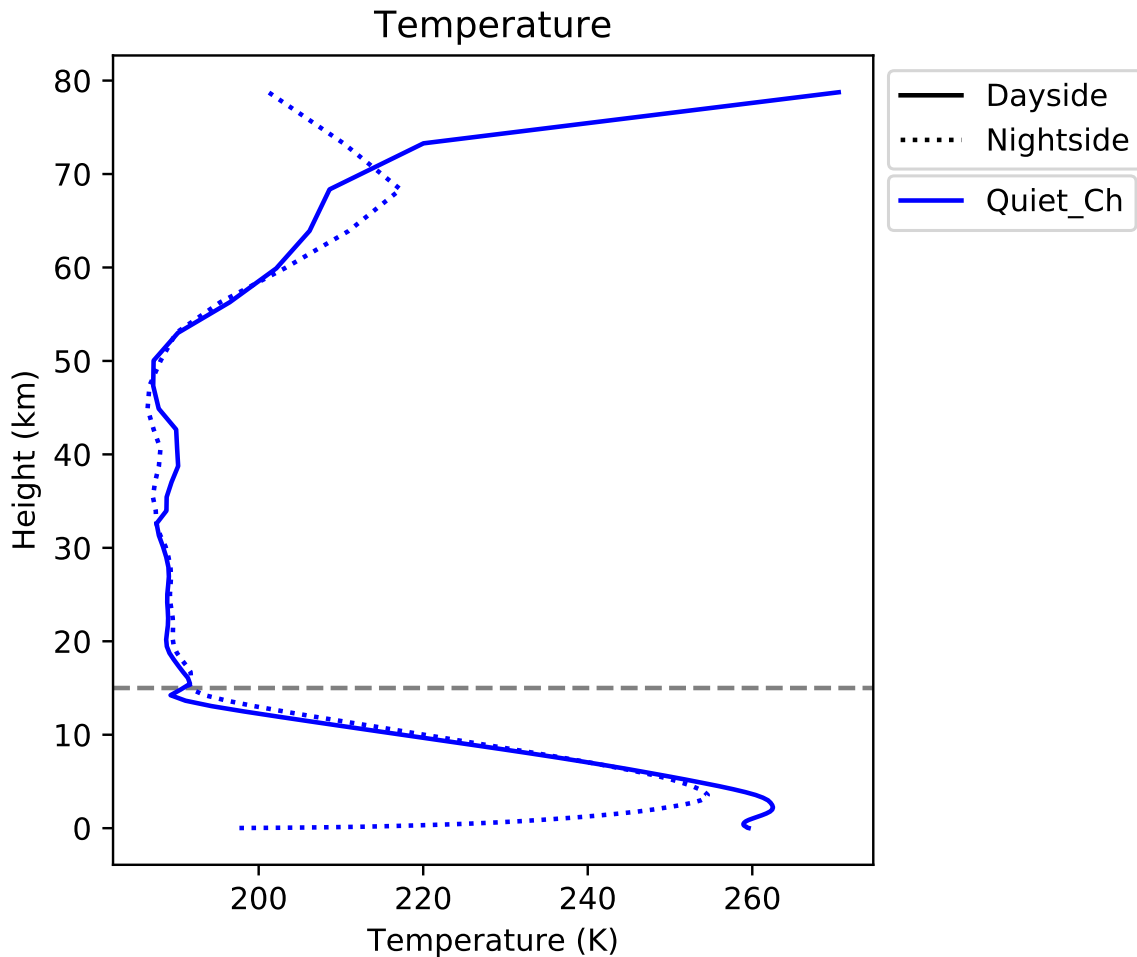
Figure 3.5: The hemispherically averaged day–side and night–side vertical temperature profiles from the last 100 days of Quiet_Ch.

To describe the planet climate and dynamics, we will use the results from the last 100 days of the Quiet_Ch simulation. This provides a baseline which will be compared with the changes in climate and planetary circulation due to the different chemical networks, which will be explored as part of Section 3.3.3. The planetary climate is dominated by the conditions imposed by the permanent day–side and night–side. Figure 3.5 shows a vertical profile of the averaged day–side and night–side temperature. We can see that at low altitudes there is a large day–night temperature difference of over 60 K. This difference decreases with altitude and becomes small above 5 km. The tropopause is at an altitude of about 15 km, where the temperature is roughly constant between 15–50 km at a value of 190 K. Above 50 km the temperatures increase, due to the absorption of shorter wavelength UV light.

The wind speed and direction in the troposphere is shown in Figure 3.6, and in
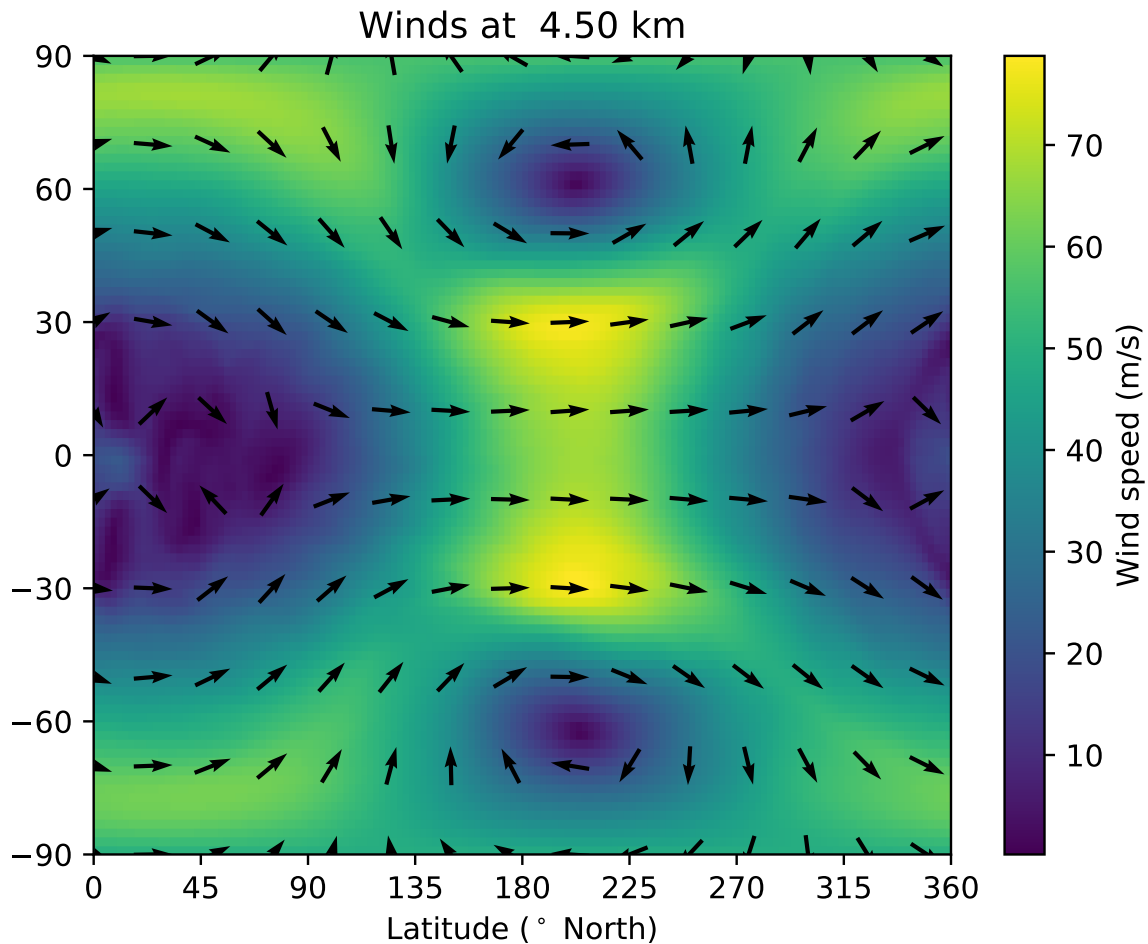
Figure 3.6: The wind speed and direction averaged over the last 200 days of Quiet_Ch at a height of approximately 4.5 km.

the lower stratosphere in Figure 3.7. We can see that circulation is dominated by zonal flow, aside from winds flowing away from the substellar point and the winds forming the cold traps at high latitudes on the night–side. The cold traps are thought to be a potential reservoir of ozone (Yates et al., 2020; Chen et al., 2021), as ozone contained in the cold traps (also called gyres) is shielded from destruction through photolysis and chemical loss processes occurring predominately on the day–side.

Above the troposphere, the planetary circulation is dominated by a super–rotating (moving faster than the planets rotational velocity) jet between 15-30 km. Figure 3.8 shows the zonal average (averaged over all longitudes) zonal wind velocity using data from the last 100 days of Quiet_Ch.
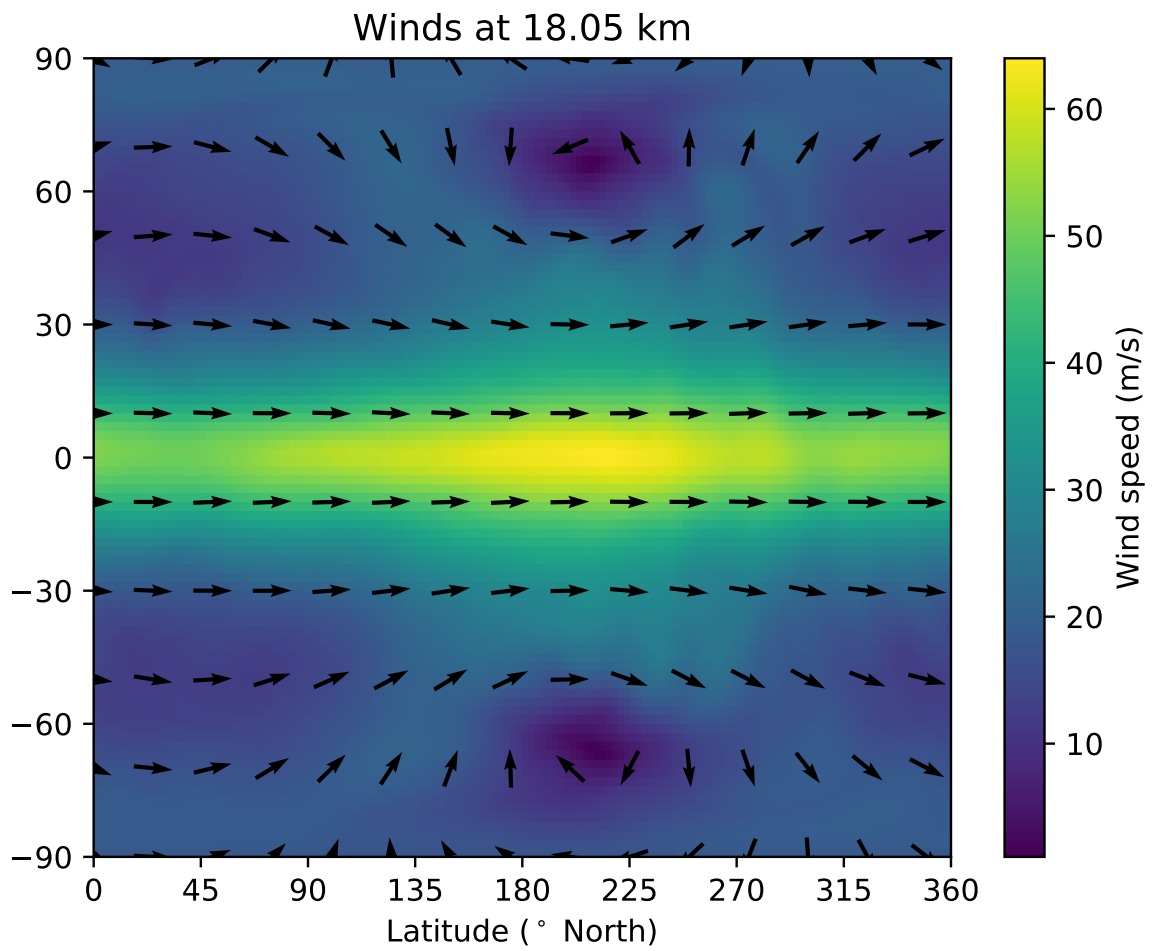
Figure 3.7: The wind speed and direction averaged over the last 200 days of Quiet_Ch at a height of approximately 18 km.
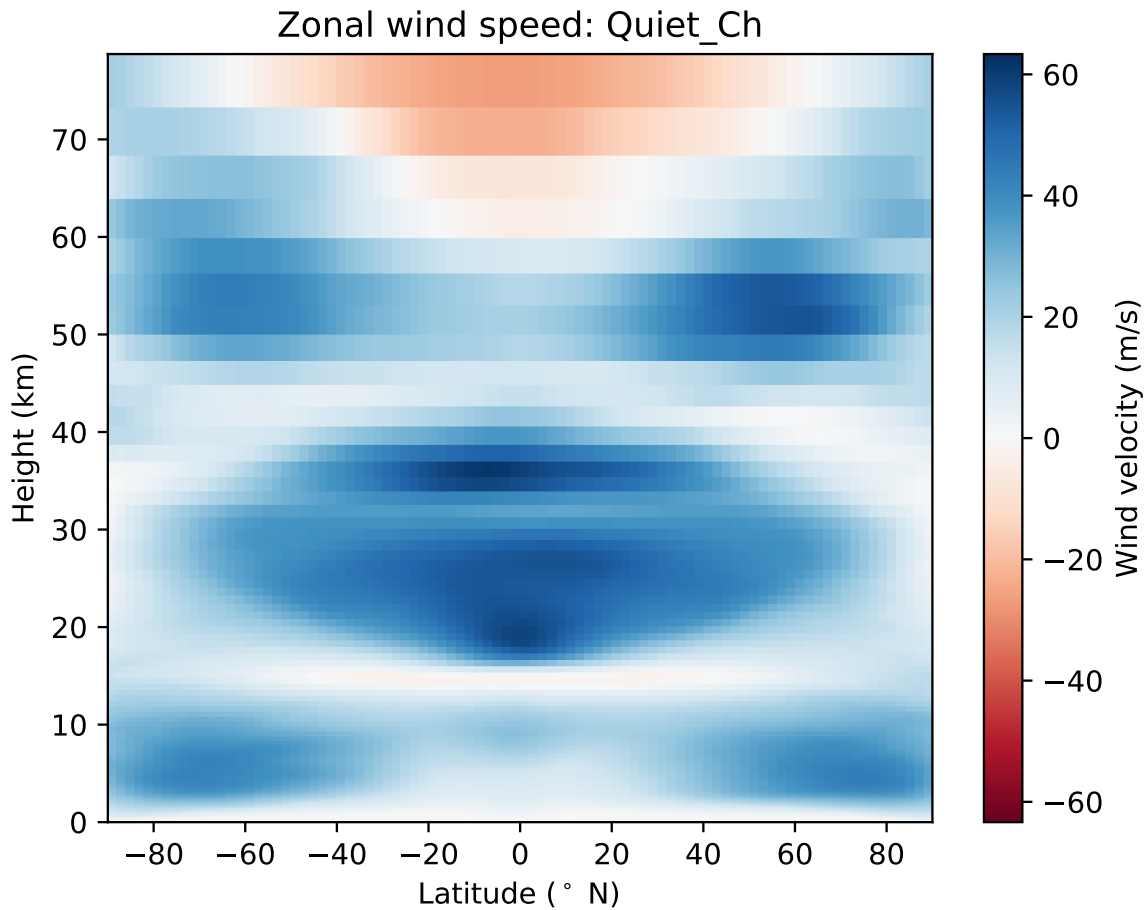
Figure 3.8: The zonally averaged zonal wind velocity from the last 100 days of Quiet_Ch.

3.3.3 Effects of the chemical network on ozone

This section describes the evolution in the abundance and distribution of ozone as the chemical networks become more complex. We will start with the Chapman cycle and show how the inclusion of HO_x and NO_x chemistry causes a large decrease in the amount of ozone.

3.3.4 Dobson unit

The total amount of ozone in the atmosphere will be described in Dobson units (DU), which are a common unit (with units of molecules m^{-2}) when discussing amounts of ozone in planetary atmospheres. It is defined as the amount of ozone molecules in a layer of ozone 0.01 mm thick at a temperature of 273 K and a pressure of 101325 Pa (STP conditions). The value of a Dobson unit can be derived from the ideal gas law

$$P = nk_bT, \tag{3.12}$$
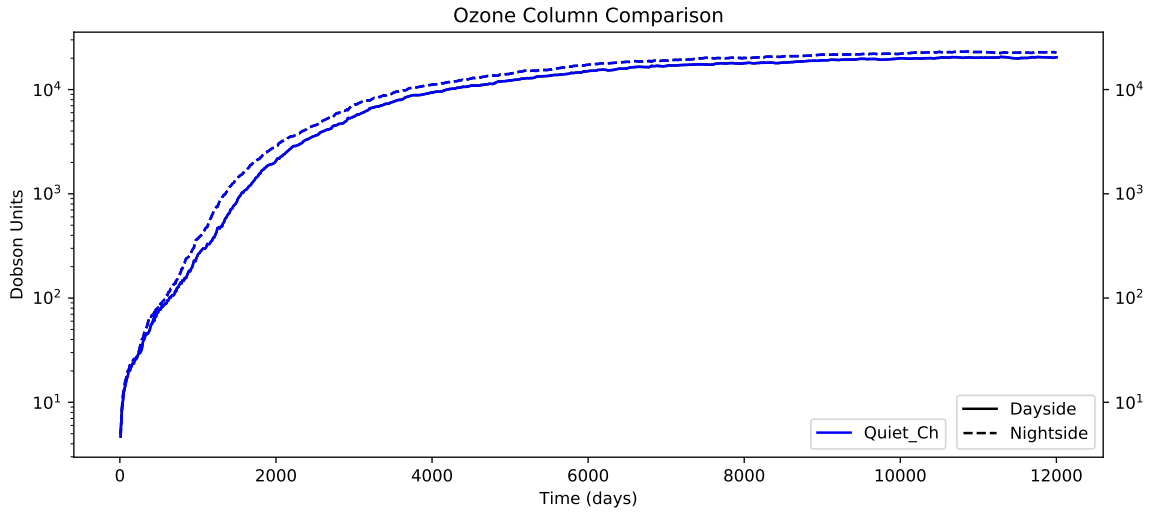
Figure 3.9: The average day–side and night–side ozone column in Dobson units for Quiet_Ch.

where P is the atmospheric pressure, n is the number density, k_b is the Boltzmann constant, and T is the temperature. A quick rearrangement gives us

$$n = \frac{P}{k_b T}. \tag{3.13}$$

The value of a Dobson unit is thus

$$1 \text{ DU} = n \times 10^{-5} \text{ m} = \frac{101325 \text{ Pa } 10^{-5} \text{ m}}{1.38 \times 10^{-23} \frac{\text{J}}{\text{K}} \ 273 \text{ K}} = 2.69 \times 10^{20} \text{ molecules m}^{-2}. \tag{3.14}$$

As a Dobson unit is a measure of the ozone column density, it is used to describe the ozone column in an atmosphere. The ozone column on Earth typically ranges from 200-500 DU (Gulev et al., 2021).

3.3.5 Chapman cycle

The Quiet_Ch simulation allows us to isolate the ozone production through the Chapman cycle, and effectively test the model performance. Figure 3.9 shows the evolution of the day–side and night–side ozone columns. The simulation generates a very large ozone column, exceeding 20,000 DU across the entire planet. This is significantly higher than observed on Earth, where it is typically 200-500 DU. We can see that night–side ozone has a larger ozone column than the day–side. The reason for this is shown in Figure 3.10.
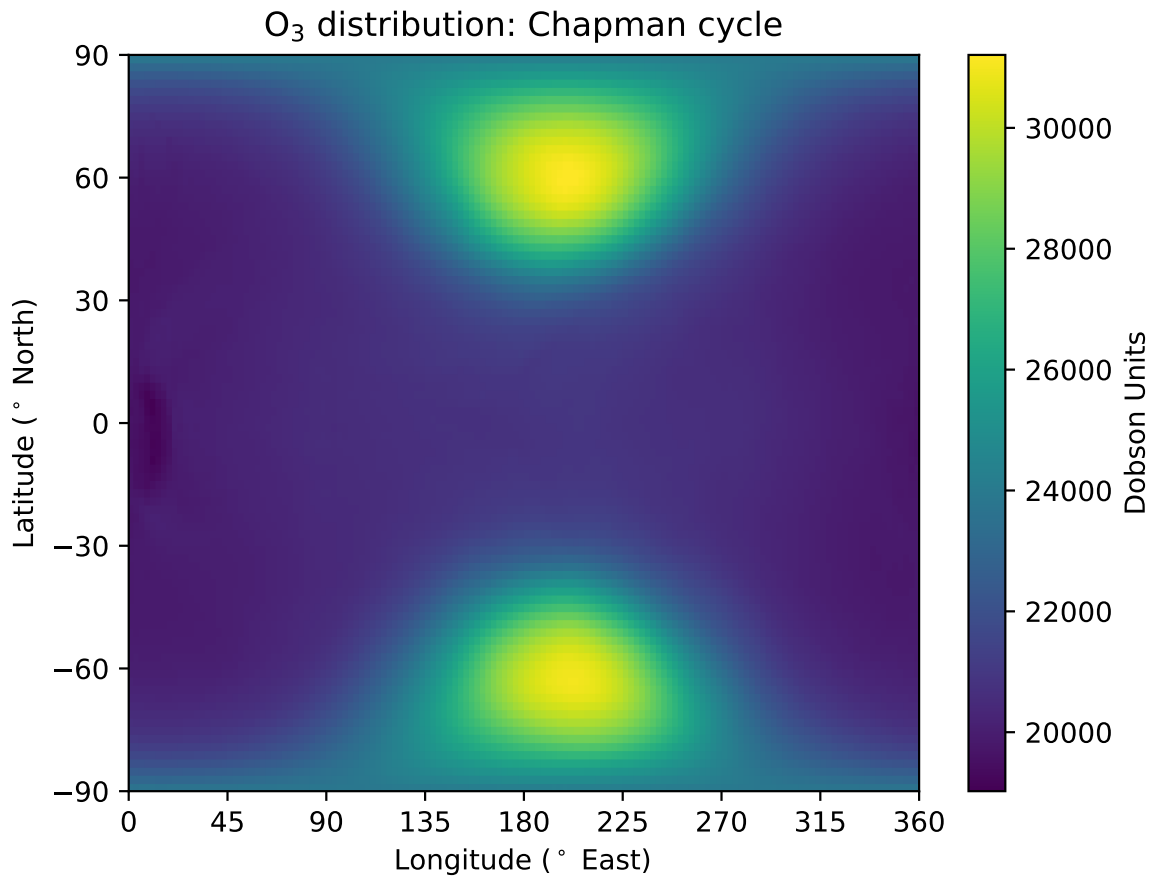
Figure 3.10: A map of the ozone column across the entire planet from Quiet_Ch, using data from the last 200 days of the simulation. Note that this plot is centered on the night–side.

Figure 3.10 shows a map of the ozone column across the planet averaged over the last 200 days of the simulation. We see a relatively uniform distribution of ozone throughout the planet, except for in the high–latitude gyres where the ozone column is much thicker than the rest of the planet, exceeding 31000 DU. This occurs due to high levels of O_2 photolysis, which provides a large source of atomic oxygen, allowing a very large amount of ozone to be created. Ozone created on the day–side that is transported to the night–side accumulates in the gyres, due to the atmospheric circulation on the night–side as well as a limited impact of the loss processes present in the Chapman network.

Figure 3.11 shows the vertical profiles of the mole fraction of day–side and night–side ozone from the Quiet_Ch simulation. We see that the Quiet_Ch simulation has a substantial amount of tropospheric ozone, ~ 25 parts–per–million (ppm) on the day–side and ~ 30 ppm on the night–side, and a large amount of ozone in the stratosphere, ranging between $\sim 30 - 110$ ppm. This is substantially higher than
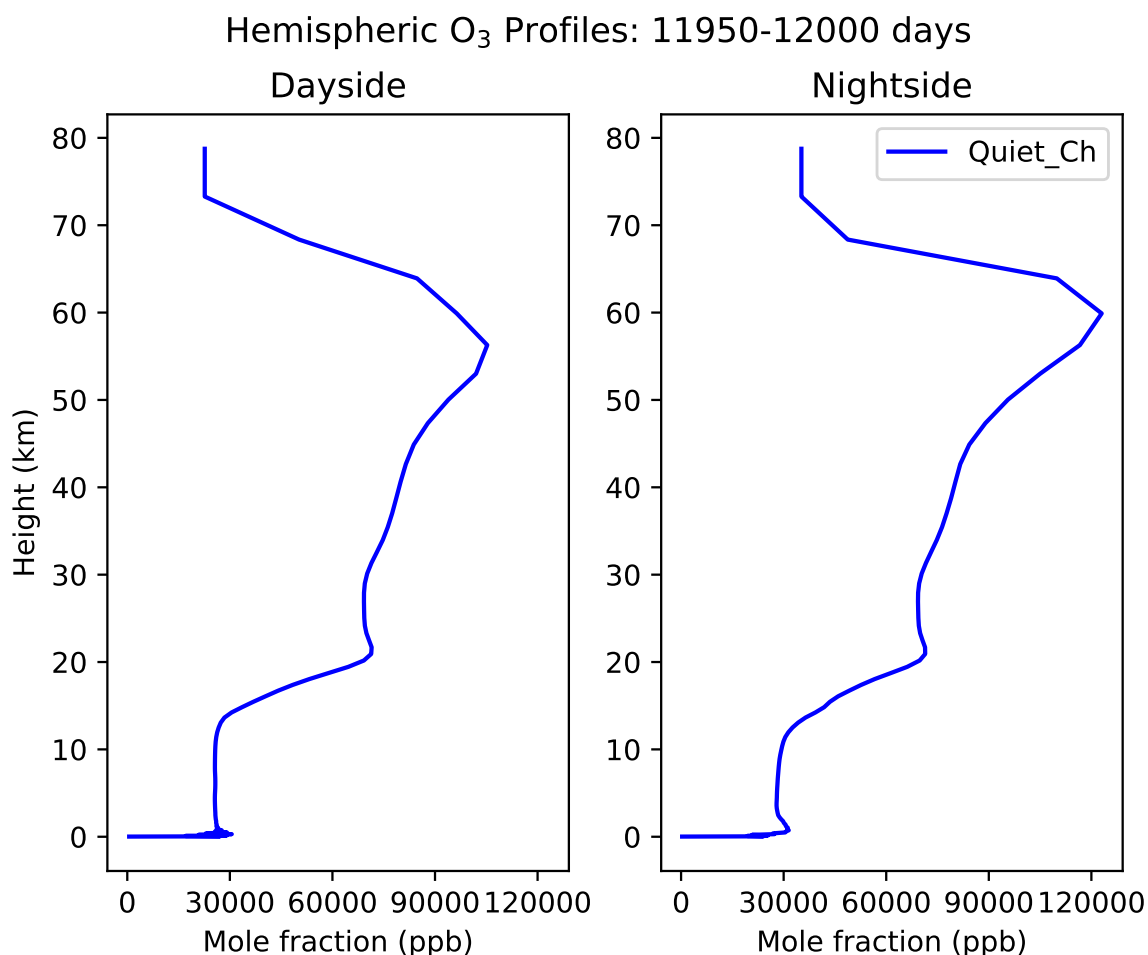
Figure 3.11: The average vertical day–side and night–side ozone concentration profile for Quiet_Ch from the last 50 days of the simulation.

the abundances of ozone seen on Earth, which is typically around 10 ppm (Fraser, 1997).

Figure 3.12 shows the averaged reaction rates of the reactions comprising the Chapman mechanism on the day–side and night–side. As a result of the pseudo–spherical approximation recently implemented in SOCRATES (Jackson et al., 2020) and used in this work, photolysis rates are not zero on the night–side. Unsurprisingly though, photolysis rates are much weaker on the night–side. Other reactions are weaker as well, due to the lack of available atomic oxygen, which arises due to the weaker photolysis rates and limited advection onto the night–side, except at high altitudes. The reaction rates tell us several things about the chemistry. We see that R3 and R4 (ozone photolysis and the termolecular reaction forming ozone) are very rapid and very similar in magnitude, except at high altitudes. R1 falls off with altitude much faster then ozone photolysis. This can be attributed to a couple

factors. As oxygen photolysis requires higher energy photons, it depends much more on shorter wavelengths, which are absorbed and scattered much more than longer wavelengths. As well, the absorption cross–sections of oxygen and ozone are different, with the ozone cross–section peaking at a longer wavelength than oxygen. We see that in contrast, the rate of ozone photolysis is strongest near the planet's surface. The termination reaction of the Chapman cycle, R6, is strongest in the troposphere as well, due to the additional atomic oxygen created by ozone photolysis.
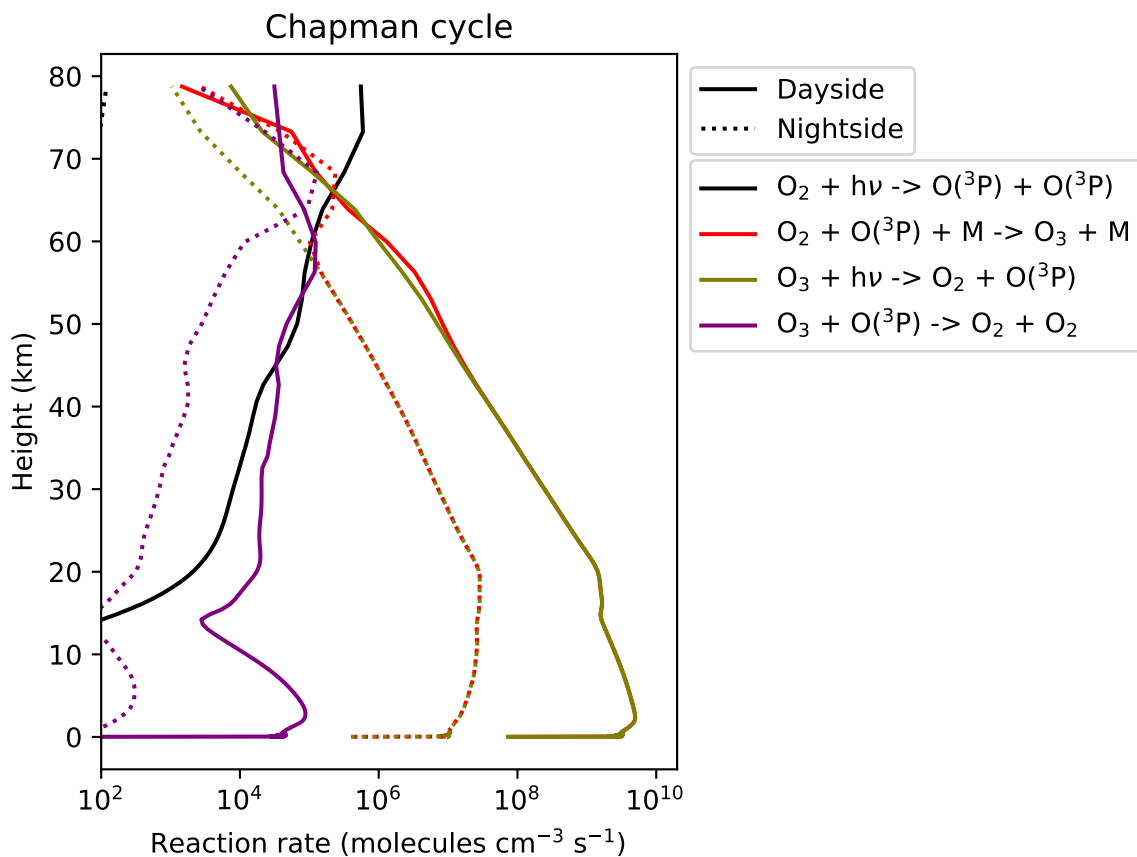
Figure 3.12: Reaction rates of the reactions comprising the core of the Chapman cycle, using data from the last 100 days of Quiet_Ch. The rates are averaged to give values for the day–side and night–side.

We can extend our analysis to looking at all reactions which impact ozone in some way. Figure 3.13 shows the averaged day–side and night–side reaction rates for all chemical reactions which destroy ozone as well as the termolecular formation reaction. In particular, reactions R2 and R5, which are photolysis reactions which generate $O(^1D)$. We see that R2 falls off significantly below 50 km, but is comparable to R1 above this altitude. Below 60 km, R5 is much weaker than R4, and also
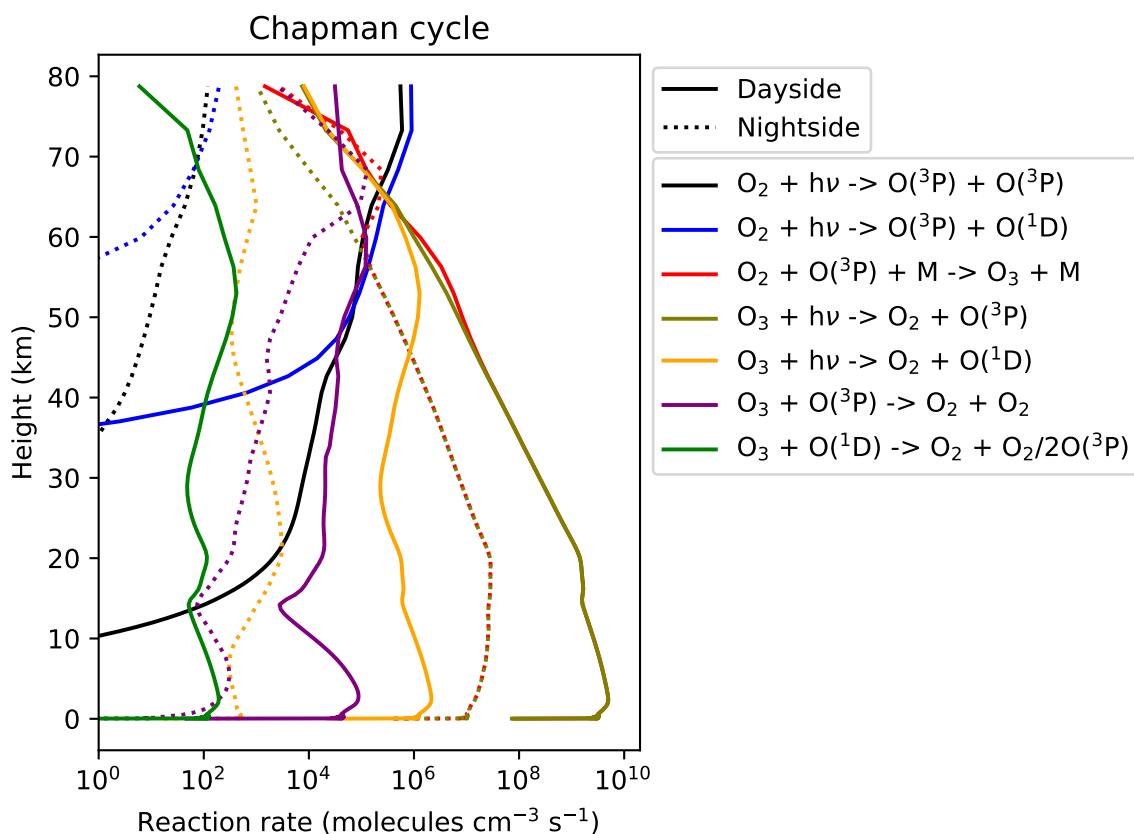
Figure 3.13: The reaction rates of the reactions comprising the extended Chapman cycle used in this work. The reaction rates for both $O_3 + O(^1D)$ reactions are the same, so they have been combined for this figure.

does not significantly change with altitude. This creates a comparatively large source of $O(^1D)$ in the troposphere, which becomes important when discussing the reactions which comprise the HO_x cycle.

3.3.6 Hydrogen oxide chemistry

The introduction of HO_x chemistry causes a large reduction in the amount of ozone. Figure 3.14 shows the evolution of the day–side and night–side ozone column once HO_x chemistry is included, showing the ozone column from the previously described simulation, as well as the Quiet_Ch_HOx simulation. Comparing to Quiet_Ch, the ozone column has been reduced by about 75%, dropping to about 5000 DU from ~ 20000 DU. This is still higher than the amount seen on Earth, but has been substantially reduced.

The resulting changes in the abundances of ozone are shown in Figure 3.15, which shows the day–side and night–side ozone profiles, similarly to Figure 3.11. The
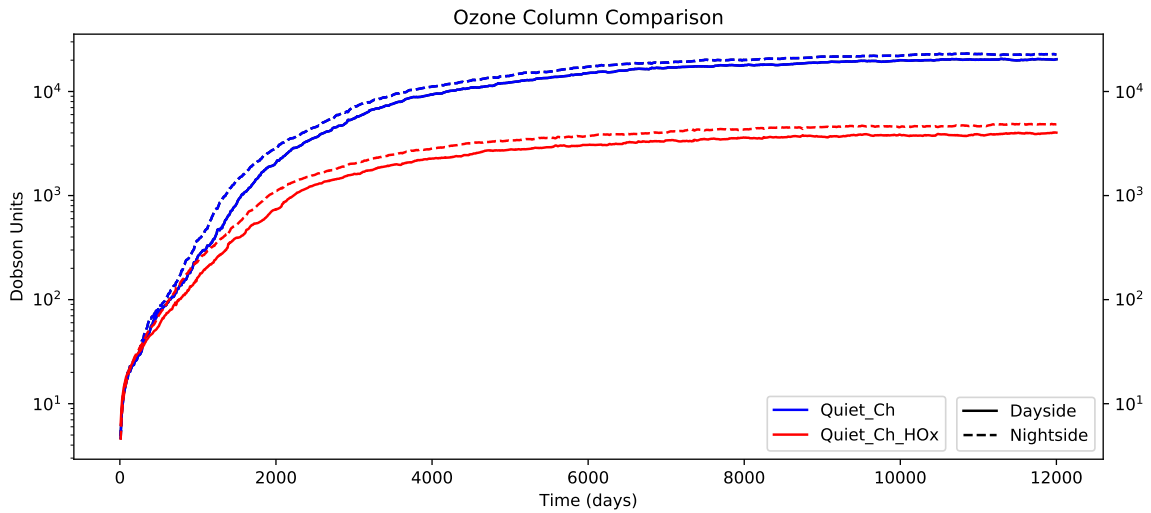
Figure 3.14: The average day–side and night–side ozone column in Dobson units for Quiet_Ch and Quiet_Ch_HOx.

stratosphere is more heavily depleted than the troposphere, having been reduced to 15 ppm in the stratosphere, and 5 ppm in the troposhere. The absolute change is largest in the stratosphere, but due to the increased density of the air in the troposphere, the depletion of the troposphere contributes much more to the changes in the total ozone column.

A map of the ozone column is shown in Figure 3.16. The overall distribution is very similar to Figure 3.10, as the ozone column is fairly evenly distributed, except in the gyres where it is significantly thicker. In the gyres the ozone column is roughly 7000 DU, and the ozone column is about 4000 DU for the rest of the planet. The drop in the ozone column is roughly the same factor everywhere, a reduction of about 75%. Comparing this result with the top left panel of Figure 4 from Yates et al. (2020) reveals the differences caused by updating the stellar spectrum and, to a lesser extent, the inclusion of shorter wavelengths in the treatment of photolysis, as these are the main differences between our treatment for the Quiet_Ch_HOx simulation and that of Yates et al. (2020). The update to the MUSCLES-Ribas stellar spectrum leads to much higher levels of ozone, however the change is mainly due to the increased UV flux as this result was not found when using the BT-Settl spectrum. This illustrates the importance of including low (<200 nm) wavelength fluxes into chemistry models.
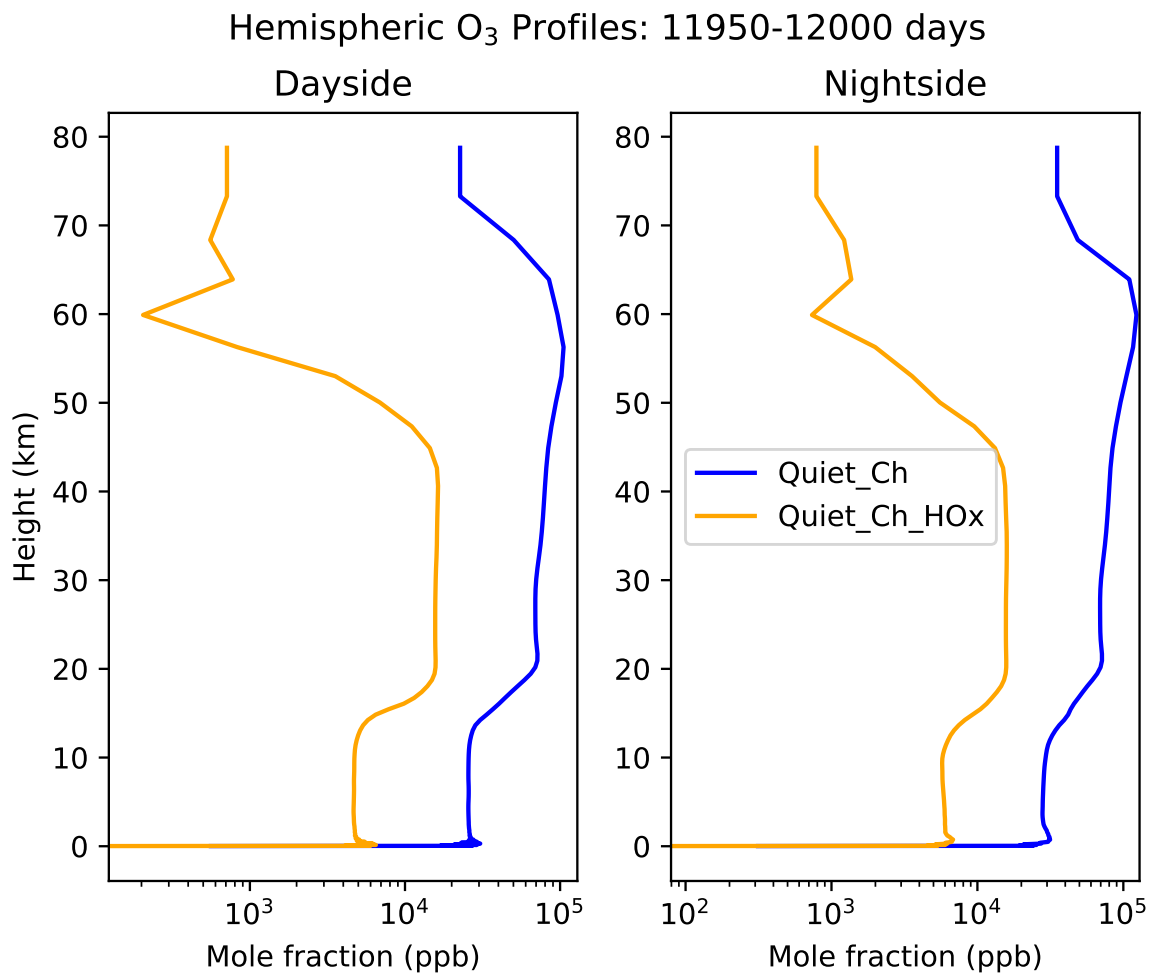
Figure 3.15: The average vertical day–side and night–side ozone concentration profile for Quiet_Ch and Quiet_Ch_HOx.
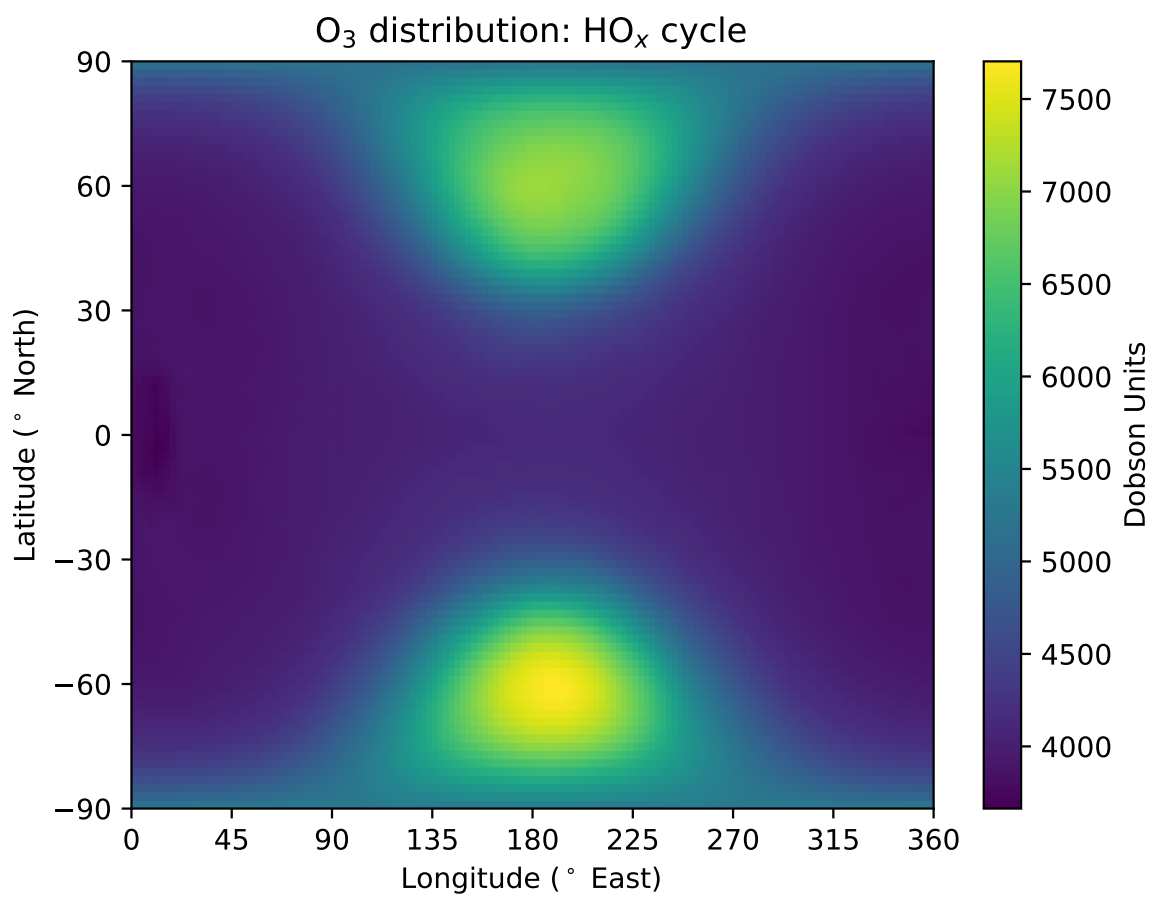
Figure 3.16: A map of the ozone column across the entire planet from Quiet_Ch_HOx, using data from the last 200 days of the simulation. Note that this plot is centered on the night–side.
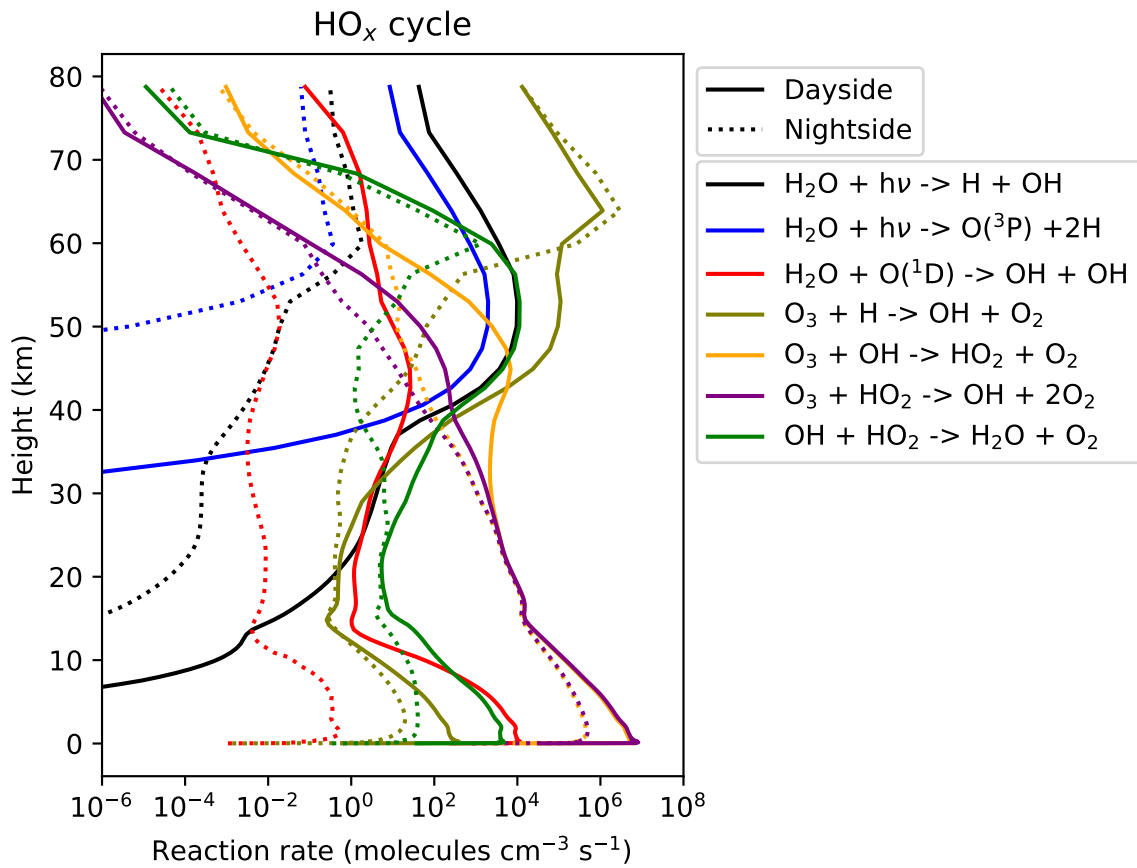
Figure 3.17: The averaged day–side and night–side reaction rates of the HO$_x$ cycle as they pertain to ozone loss, averaged over the last 100 days of Quiet_Ch_HOx.

Figure 3.17 shows the averaged reaction rates that comprise the HO$_x$ cycle. We see that there are two regimes of reactions which dominate ozone destruction. Below 40 km, ozone loss is dominated by R13 and R14 (destruction by OH and HO$_2$). Above 40 km, ozone loss is dominated by R16, destruction by H. This also helps illustrate that H$_2$O photolysis is a large source of HO$_x$, although this is much weaker than R12 (HO$_x$ production via O(^{1}D)) below 20 km. As mentioned previously, the source of O(^{1}D) is R5.

This can be seen in Figure 3.18, which shows the reaction rates of every reaction in the HO$_x$ network that impacts ozone. We see that below 40 km ozone photolysis is still the dominant loss process for ozone, although it is still quickly reformed by R3. Above 40 km, R16 is the dominant loss process for ozone. Loss of ozone due to R13 and R14 is significantly higher than R6 below 35 km. The increased loss of ozone in the lower stratosphere and troposphere results in the vertical ozone profile seen in Figure 3.11.
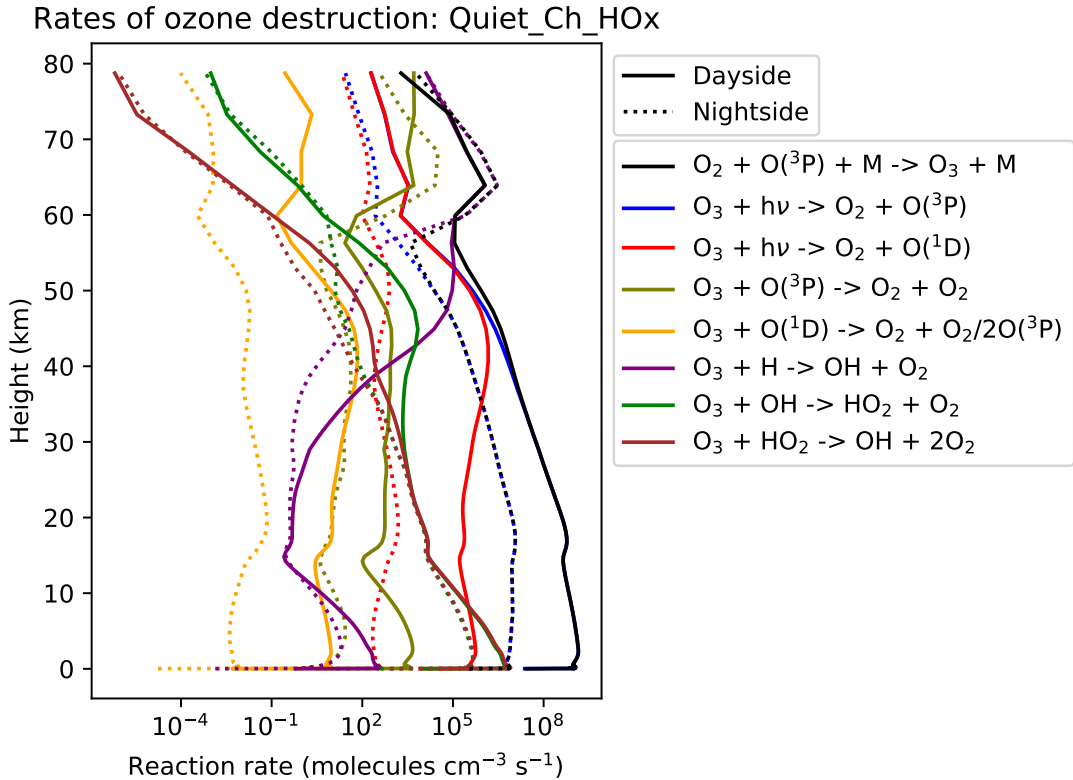
Figure 3.18: Reaction rates of reactions which generate or destroy ozone, averaged over the last 100 days of Quiet_Ch_HOx.

3.3.7 Nitrogen oxide chemistry

Finally, we come to the inclusion of NO_x chemistry. The inclusion of NO_x reduces the ozone column to a much thinner column than seen on Earth. Figure 3.19 shows the evolution of the day–side and night–side ozone column. Due to time constraints, I was not able to run this simulation until it had converged. The decision to stop the simulations was determined by when the simulation with the full chemical network (containing all three chemical cycles as well as the effects of SEPs) converged, which it had after 12000 days. As that was meant to be the focus of this work, the decision was made to stop all quiescent simulations once that simulation had converged. This does present some uncertainties regarding the results presented here. The ozone in Quiet_Ch_HOx_NOx has a significantly different evolution than the results seen from the two previous simulations. After peaking in value after ~3000 days with an average ozone column of 2000 DU, the amount of ozone slowly decreases, reaching a value lower than 100 DU by the end of the simulation. This is about 40 times lower than the ozone column seen in
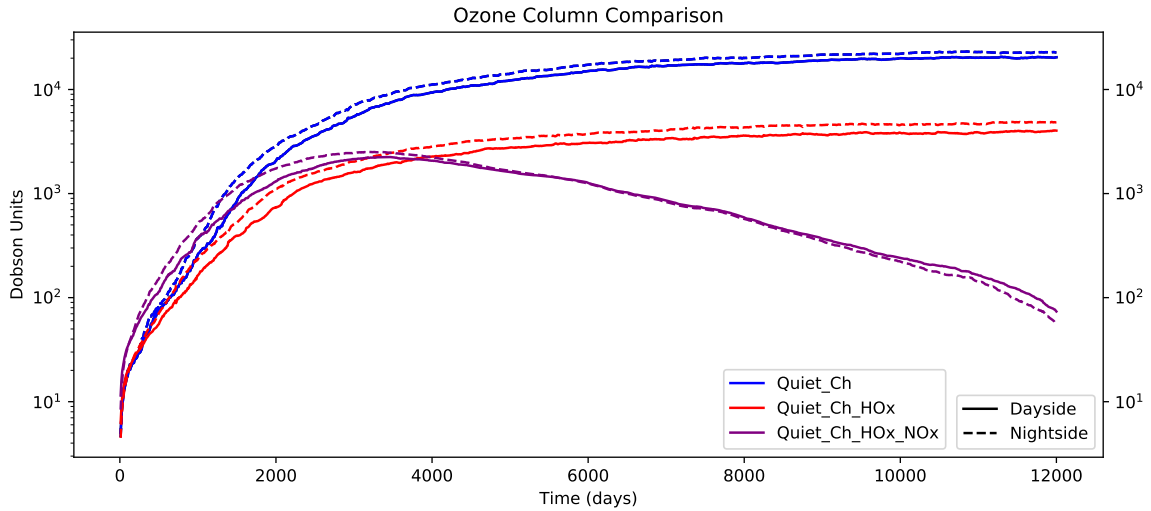
Figure 3.19: The average day–side and night–side ozone columns from the three quiescent simulations without SEPs. Refer to Table 3.7 for the details of the different networks.

Quiet_Ch_HOx, telling us that the NO_x cycle is a major ozone sink. The map of the ozone column is shown in Figure 3.20. The distribution has changed significantly from what was seen in Figures 3.10 and 3.16, as the gyres are not a large reservoir of ozone, and are now depleted relative to the rest of the planet.

Figure 3.21 shows the spatially averaged day–side and night–side vertical profiles of the ozone mole fraction. In comparison to the HO_x network, we see that below 60 km ozone has been heavily reduced, with a thin layer of ozone at 50 km of ~2 ppm. Below 40 km the concentration of ozone has been reduced to 100 ppb.

Figure 3.22 shows the average day–side and night–side reaction rates for the NO_x cycle. We see that destruction of ozone by the NO_x cycle (R42 and R44) is dominant above 15 km, while R46, $NO_2 + O_3 \longrightarrow NO_3 + O_2$, is dominant below 15 km. The NO_x cycle relies on the recycling of NO_2 back into NO. We see that NO_2 photolysis and destruction by atomic oxygen (R43 and R44) is fairly rapid, comparable to or exceeding R42 except at low altitudes. The NO_3 produced is either converted into N_2O_5 or is quickly destroyed by photolysis.

Figure 3.23 now shows the NO_x cycle in context with the HO_x cycle, ozone generation, and ozone photolysis. We see that R16 is still the dominant loss process at high altitudes, but is weaker than R42 below 45 km, which remains the dominant loss process for ozone until below 15 km where $NO_2 + O_3 \longrightarrow NO_3 + O_2$ becomes

82
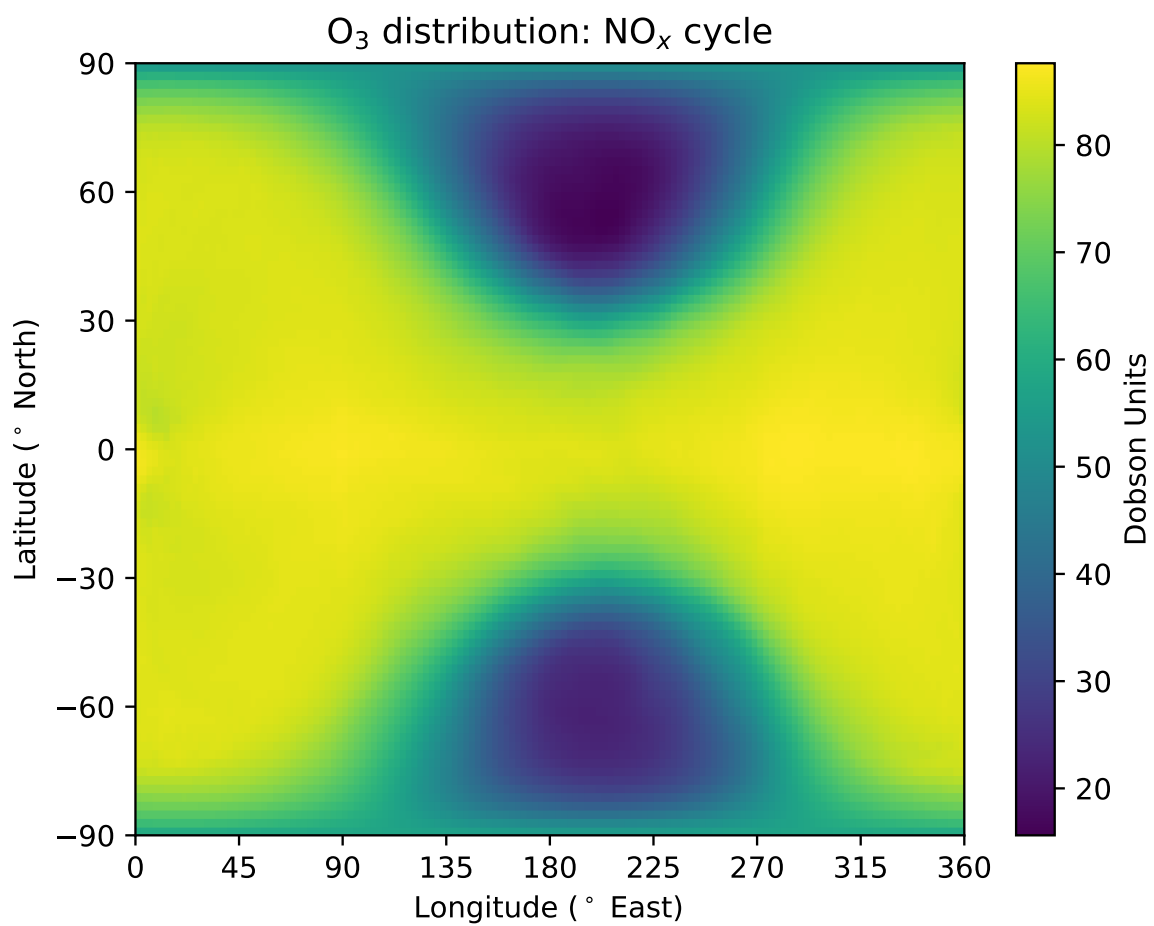
Figure 3.20: A map of the ozone column across the entire planet from Quiet_Ch_HOx_NOx, using data from the last 200 days of the simulation. Note that this plot is centered on the night–side.
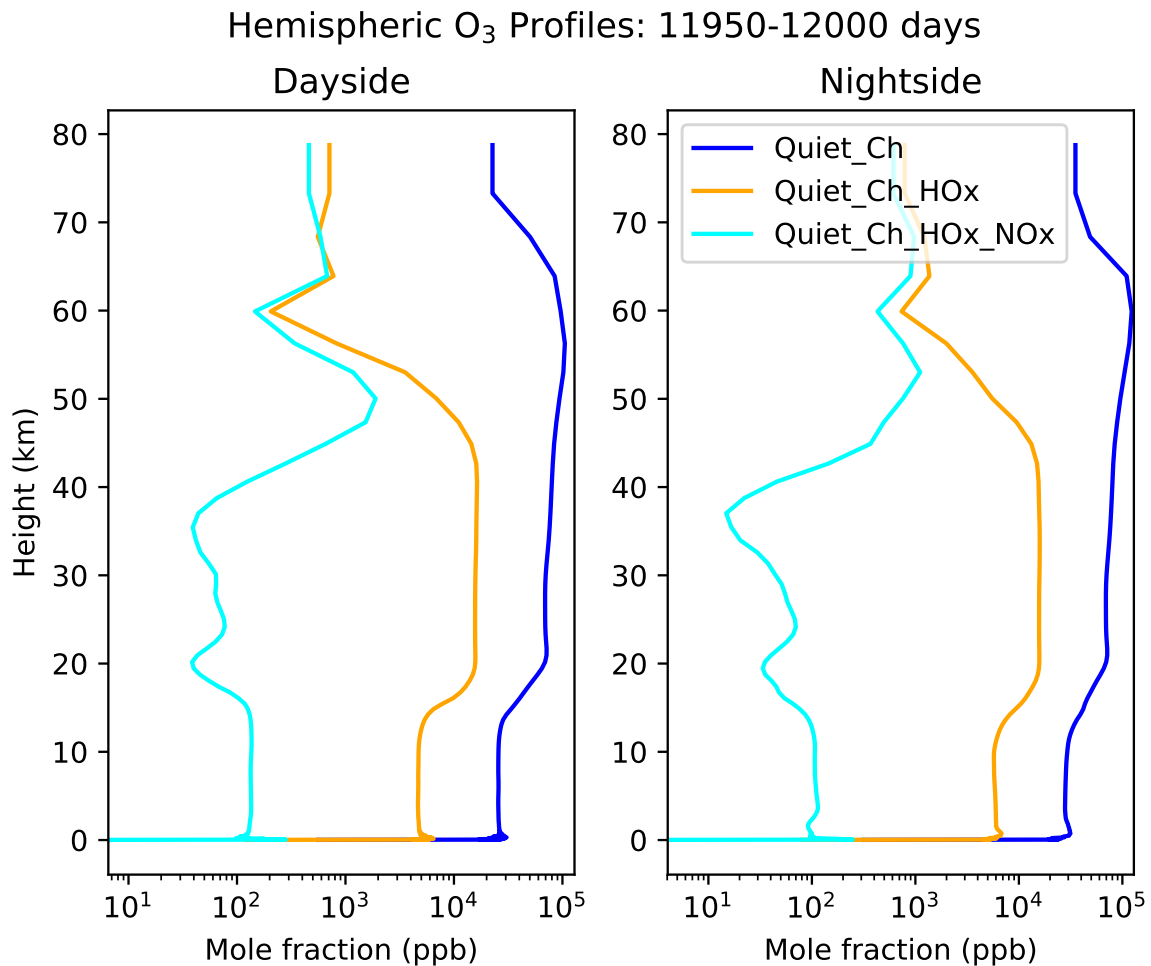
Figure 3.21: The spatially averaged vertical profile of the ozone mole fractions from the planets day–side and night–side for the three chemical networks under quiescent conditions without SEPs. Refer to Table 3.7 for the details of the different networks.

dominant as previously described. Below 40 km the loss of ozone due to the NO_x cycle is much stronger than the HO_x cycle. We can also see that R13 and R14 now differ significantly at all altitudes, which was not seen in Quiet_Ch_HOx.

To summarise the results seen in the quiescent networks without SEPs, as network complexity increases we move from a simulation which has a very thick ozone column to a simulation which has a very thin ozone column. The simplest network consisting only of the Chapman cycle has the largest ozone column (≈ 22000 DU), and the introduction of HO_x and NO_x chemistry heavily diminishes the ozone column, particularly in the latter case. The introduction of HO_x and NO_x chemistry heavily depletes tropospheric and stratospheric ozone (through the reactions listed in Sections 3.2.2 and 3.2.3).
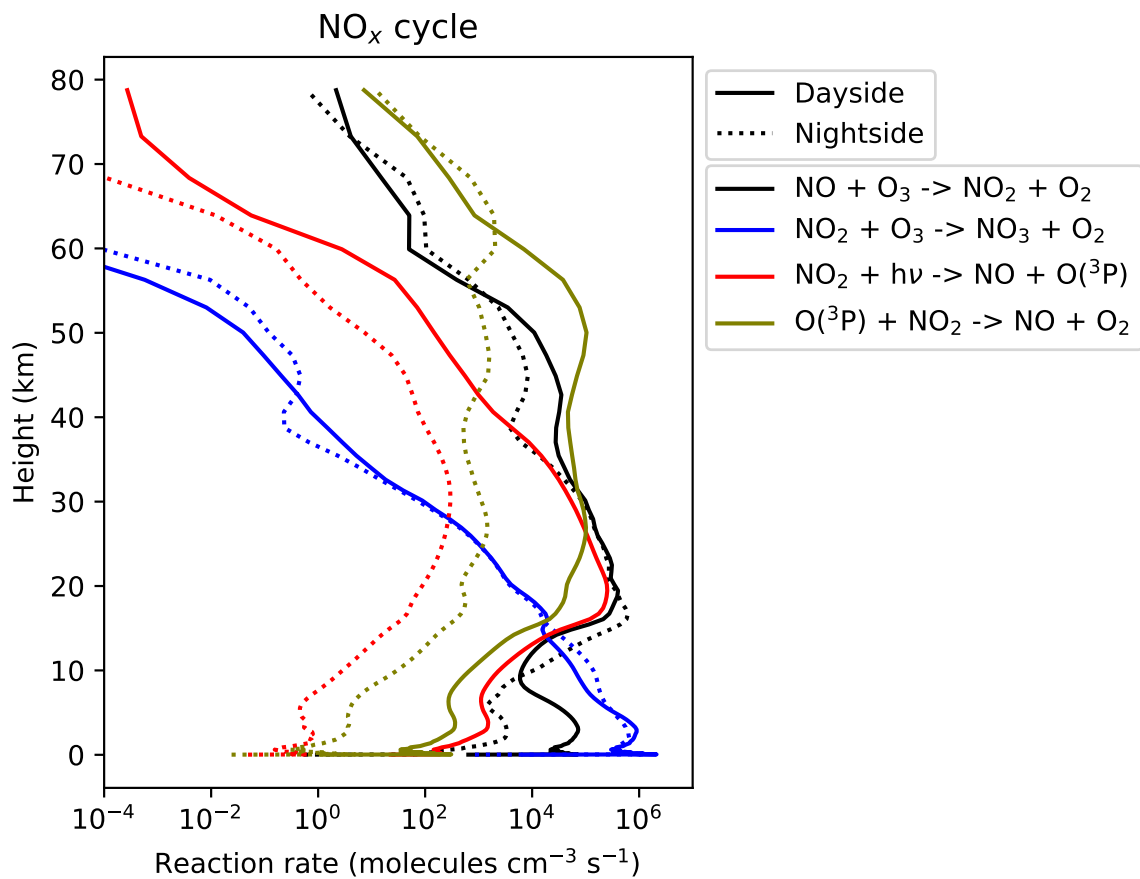
Figure 3.22: The averaged day–side and night–side reaction rates of the NO$_x$ cycle as they pertain to ozone loss, averaged over the last 100 days of Quiet_Ch_HOx_NOx.
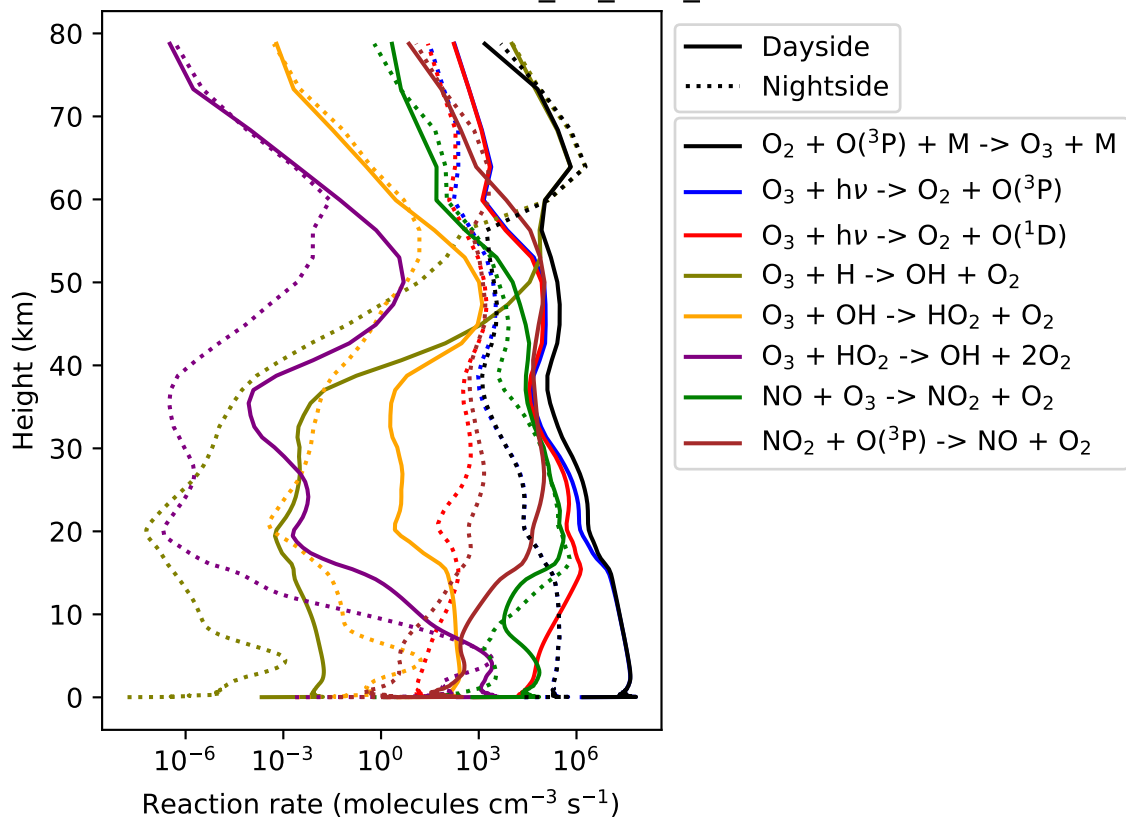
Figure 3.23: Reaction rates of reactions which generate or destroy ozone, averaged over the last 100 days of Quiet_Ch_HOx_NOx.

3.3.8   Temperature effects of the changes in ozone

The differing atmospheric compositions from the different chemical networks result in some changes in the planet's climate. Figure 3.24 shows the average day–side and night–side vertical temperature profiles from the three quiescent simulations. We see that the same characteristics are present in each simulation, a large day–night temperature contrast in the lower troposphere near the surface, and a small (if any) difference in the stratosphere. As the chemical network expands, the resulting reduction in ozone causes less heating to occur in the stratosphere. This is occurring due to less UV being absorbed as there is less ozone to absorb it. This has the effect of lowering the temperature from ~190 K in Quiet_Ch to ~180 K in Quiet_Ch_HOx_NOx. The increased UV radiation in the troposphere causes an increase in the day–side tropospheric temperatures by a small amount. The effects on circulation were found to be minimal.
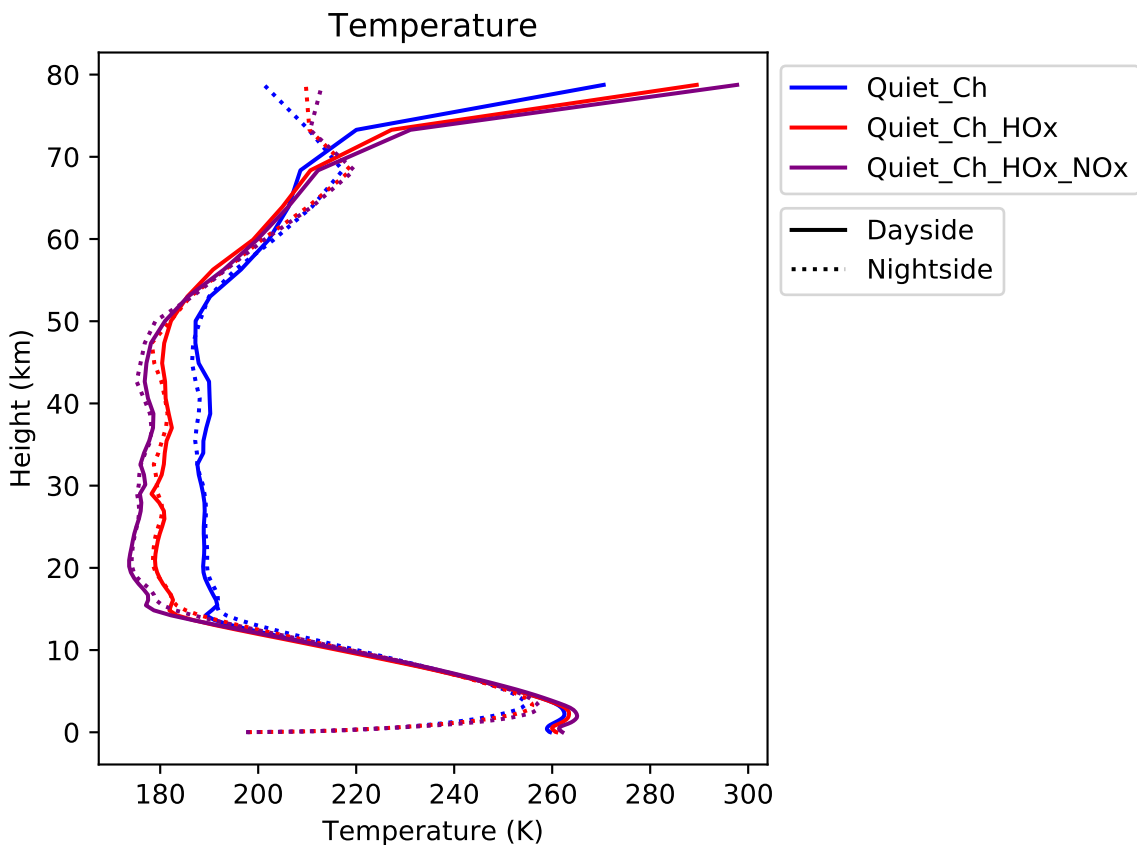
Figure 3.24: The hemispherically averaged vertical day–side and night–side temperature profiles from the three quiescent simulations without the inclusion of SEPs.

Even though Quiet_Ch and Quiet_Ch_HOx have significantly more ozone than seen on Earth, the stratospheric temperatures lower than seen on Earth. This can

be attributed to several factors. The stellar spectrum of ProxCen and the location of ProxCen b mean that the planet receives less total radiation than the Earth does. At the top-of-atmosphere, the Earth receives approximately $1360\,\mathrm{W\,m^{-2}}$, whereas ProxCen b receives $880\,\mathrm{W\,m^{-2}}$, approximately 35% less energy per unit area than the Earth does. The different stellar spectra also affects stratospheric heating. As seen in Figure 3.25, the ProxCen spectrum is much weaker between 150–900 nm. From Gorshelev et al. (Figure 3 of 2014), we see that the opacity of ozone peaks at approximately 250 nm with a second local maxima at 600 nm, the opacity of ozone decreases significantly above 600 nm. This means that the atmosphere is fairly transparent for this range of wavelengths, meaning that while there is a lot of ozone, it may not significantly absorb radiation. This is seen in the relatively small change in stratospheric temperatures between Quiet_Ch and Quiet_Ch_HOx_NOx. Another factor is the lack of atmospheric heating or cooling due to the chemical reactions themselves. The ozone formation reaction R3 is exothermic (releases energy) and contributes to heating the atmosphere. When this is combined with ozone photolysis this creates an additional heating source for the stratosphere. From the records of Atkinson et al. (2004), we can see that these reactions have the following data regarding the amount of energy released

$$O_3 + h\nu \longrightarrow O_2 + O(^3P) \quad \Delta H^O = 101\,\mathrm{kJ\,mol^{-1}},$$

$$O + O_2 + M \longrightarrow O_3 + M \quad \Delta H^O = -106.5\,\mathrm{kJ\,mol^{-1}},$$
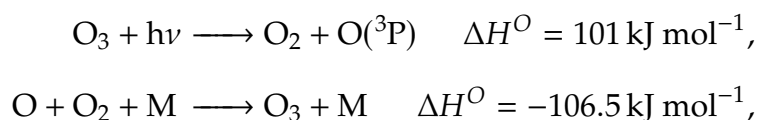
where ΔH^O is the enthalpy of reaction, which describes the amount of heat released due to a chemical reaction. A positive value denotes an endothermic reaction, and a negative value denotes an exothermic reaction. The combined enthalpy of reaction is -5.6 kJ mol^{-1}, which means that it is a net release of heat to destroy ozone via photolysis and regenerate it. As seen in Figure 3.12, these reactions are quite rapid. This provides an additional heating source to the stratosphere which is not captured in this work. The photolysis scheme used in SOCRATES does account for thermalisation, where any excess energy from the photolysis reaction (the kinetic energy of the products) is transferred into the rest of the atmosphere,

but any heating from chemical reactions is not included. This is an area which should be improved by future work.
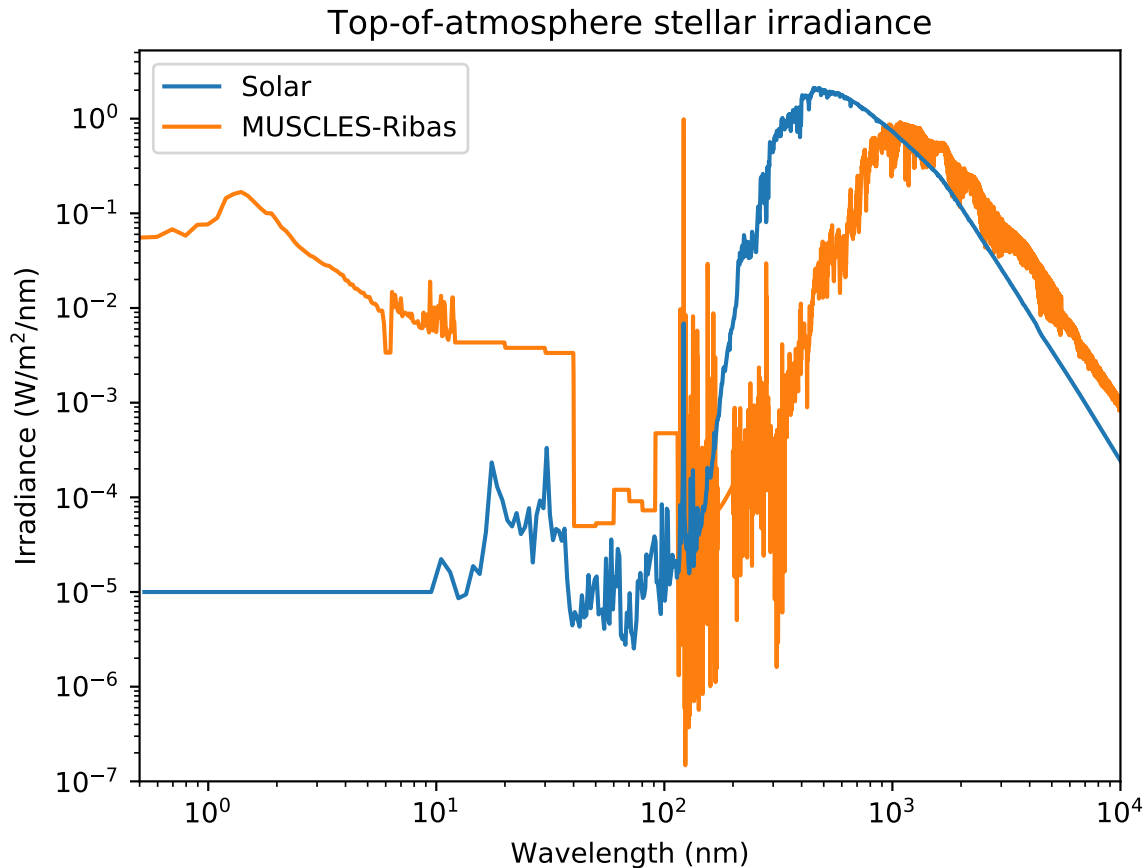
Figure 3.25: The top-of-atmosphere stellar irradiance for Earth and the MUSCLES-Ribas spectrum for ProxCen b over the entire wavelength range used in this work.

The stratosphere is also cooler than the results seen in Meadows et al. (2018), which found (for a pre–industrial Earth orbiting ProxCen) a warmer troposphere and day–side. While a detailed comparison is warranted and should the aim of future work, this is possibly attributable to a few factors. While our stellar spectra is very similar, there are differences in atmospheric composition that would change the temperature profile. Referring to their atmospheric composition profiles and temperature profile shown in Figure 8 (right), we see that the amounts of CO_2 is much higher in their model (approximately 5% compared to 5.941×10^{-4}, see Table 3.10), as well as large amounts of CO and CH_4. The high amount of CO_2 was included to raise the surface temperature to 273 K. As well, their model includes surface fluxes for several gases, CH_4, CO, N_2O, H_2S, and SO_2. The additional warming in the troposphere is likely not observed in our results due to the differences in model design. Future work is needed to examine this in more detail.

3.3.9 Comparison to previous works

These results can be compared to the simulations performed by Chen et al. (2018), which used a 3D chemistry-climate model to look at hemispheric anisotropies of biosignatures on tidally locked M dwarf planets. There are some differences which complicate a comparison. While they did simulate a tidally locked planet orbiting an active M dwarf, their planet receives significantly more energy than our planet does. Their planet received an incident top–of–atmosphere stellar flux of $1360\,\mathrm{W}$ m^{-2}, compared to $880\,\mathrm{W\,m}^{-2}$ in this work (see Table 3.9), meaning that their planet receives 54% more energy than our planet does. This will result in higher photolysis rates and atmospheric heating which will cause differences in atmospheric composition. Their planet is also rotating much slower than our planet, with a rotational period of 50 days compared to the 11.2 days used in this work. This results in their planet having a weaker Coriolis force, which has implications for atmospheric circulation. Lefèvre et al. (2021) found that differences in rotation rate for a tidally locked planet will result in differences to the location and amount of clouds, which has implications for planetary circulation and photolysis rates (the high optical depth of clouds will reduce the amount of photolysis below them). Tan & Showman (2020) found that changes in the rotation rate of tidally locked gas giants cause changes in the height and shape of the equatorial jet. This would result in a change in the amount of material able to be transported in the jet.

Chen et al. (2018) found that there is a hemispheric anistropy of stratospheric ozone of 18.7%, with more ozone on the night–side than the day–side, and very little ozone in the troposphere, with a day–side mixing ratio of 10^{-11}. This is quite different from the ozone from my simulations, which has a tropospheric mixing ratio of 10^{-7}. Their ozone mixing ratio in the stratosphere approaches 5×10^{-6} at $48\,\mathrm{km}$. This is much close to my results, which have a mixing ratio of 2×10^{-6} at the same altitude. This is a large discrepancy, which merits some explanations.

From their ozone production rates between 20–48 km for an active M dwarf shown in Figure 2 (top–centre), we see a maximum ozone production rate of approx-

imately 10^5 molecules cm^{-3} s^{-1} at 48 km, with minimal ozone production below 32 km. This differs substantially from my ozone production rates (see Figure 3.13), which are several orders of magnitude larger (between 10^7–10^9 molecules cm^{-3} s^{-1} over the same altitude range) and are substantial for all altitudes, with a maximum in ozone production rate near the surface. I believe this is attributable to increased O_2 photolysis rates in my work driving an increase in the amount of atomic oxygen, which drives ozone formation. As well, there may be some differences in ozone deposition which result in a difference in the amounts of tropospheric ozone. Their model also includes surface fluxes of several trace gases which may impact tropospheric ozone, namely chlorine and bromine oxides. They have a similar role as HO_x and NO_x and have a negative impact on ozone concentrations. This merits future work to further explore these differences.

As well, while there are some important differences as previously described, the results from Meadows et al. (2018) are a source of comparison as well. Both works have a similar stellar spectrum, but different chemical networks. Their results show an ozone profile which is more similar to my results, but differs substantially in the troposphere. The maximum of their ozone profile is 3×10^{-6} at approximately 40 km which is similar to the results shown here. The profile in the troposphere shows large differences, with their profile reaching a minimum of a 10^{-8} at 10 km (the mixing ratio below this altitude is not visible. This work shows a tropospheric profile which is approximately 10^{-7} throughout the troposphere. This may be explained by differences in composition arising from their inclusion of surface fluxes which may negatively impact ozone concentrations. This also merits future work.

I would suggest that these comparisons should be performed as part of a wide comparison of 1D and 3D chemical–climate models, analogous to the GCM comparisons performed for THAI (Fauchez et al., 2021; Turbet et al., 2022; Sergeev et al., 2022; Fauchez et al., 2022) or the radial velocity fitting challenge proposed by Dumusque (2016) and analysed in Dumusque et al. (2017). Without establish-

ing baselines for how each model behaves under a similar set of inputs, explaining differences is challenging. When components of the model are quite different, explaining differences becomes even more challenging.

3.3.10 Ozone lifetime

The chemical lifetime (τ_{chem}) of ozone is calculated by dividing the concentration of ozone by the loss rate of ozone (Brasseur & Jacob, 2017). For example, if chemical species A is only lost through a single first-order process, the loss rate of A can be written as

$$\frac{\partial [A]}{\partial t} = -k[A], \tag{3.15}$$

where k is a reaction rate coefficient. This has the solution

$$[A](t) = [A]_0 e^{-kt} = [A]_0 e^{-t/\tau_{\mathrm{chem}}}, \tag{3.16}$$

where $[A]_0$ is an initial concentration of A and $\tau_{\mathrm{chem}} = 1/k$ is the timescale where the concentration is reduced to a factor of $1/e$ of the original concentration. This is the chemical lifetime of the species. In the case of ozone, we have multiple loss processes

$$k[O_3] = \frac{[O_3]}{\tau_{\mathrm{chem}}} = \sum_i k_i [A_i][O_3] + \sum_j k_j [O_3], \tag{3.17}$$

which combines the loss rates of all bimolecular reactions (with other reactants A_i) and unimolecular reactions. The chemical lifetime of ozone is calculated as

$$\tau_{\mathrm{chem}} = \left(\frac{\sum_i k_i [A_i][O_3] + \sum_j k_j [O_3]}{[O_3]} \right)^{-1}. \tag{3.18}$$

The hemispherically averaged day–side chemical lifetimes of ozone are shown in Figure 3.26. We observe that the addition of the HO_x and NO_x cycles have reduced the lifetime of ozone. The lifetime of day–side ozone at the planets surface (neglecting the impact of deposition) decreases from 4×10^5 seconds in Quiet_Ch to 1×10^5 seconds (4.63 days to 1.16 days) in Quiet_Ch_HOx_NOx. The lifetimes gen-

erally decrease with increasing altitude, as the increase in ozone photolysis and other loss processes causes a faster destruction of ozone. The sharp decrease in ozone lifetimes for Quiet_Ch_HOx and Quiet_Ch_HOx_NOx above 50 km is due to the presence of atomic hydrogen, as the high reaction rate of $H + O_3 \longrightarrow OH + O_2$ makes it the dominant loss process of ozone above 50 km, see Figure 3.18 and 3.23.
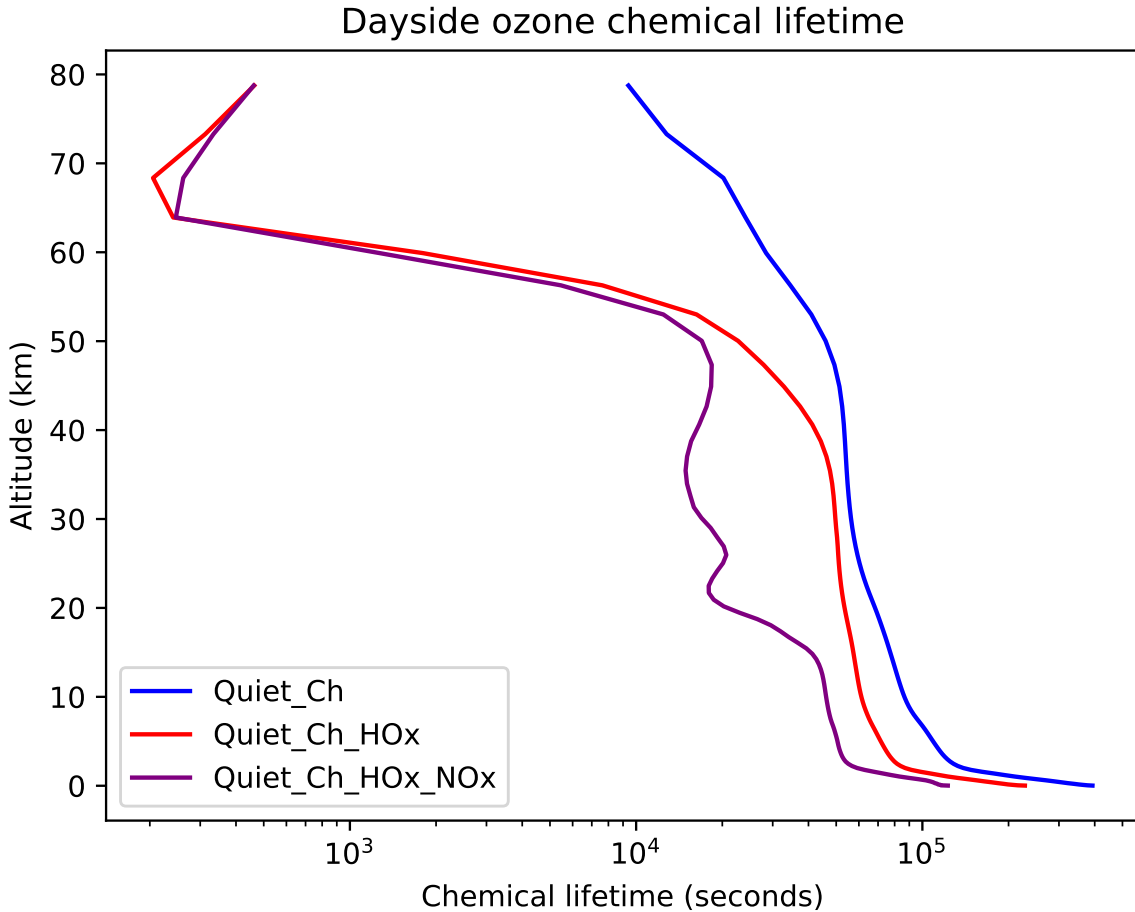
Figure 3.26: The vertical profile of the hemispherically averaged day–side chemical lifetimes of ozone calculated from the quiescent simulations without any SEPs. The effect of deposition on the chemical lifetime is not included.

We can compare the chemical lifetimes of ozone to the time it takes for a parcel of air to cross the day–side (the day–side advection timescale, τ_{day}). This timescale can be estimated by

$$\tau_{\text{day}} \approx \frac{\pi(r_p + h)\cos(\text{latitude})}{\bar{u}_{\text{day}}}, \tag{3.19}$$

where the term in the numerator is the latitude and altitude dependent distance across the day–side and $\bar{u}_{\text{day}}$ is the average day–side zonal velocity. This does not account for meridional or vertical transport, but is a reasonable approximation
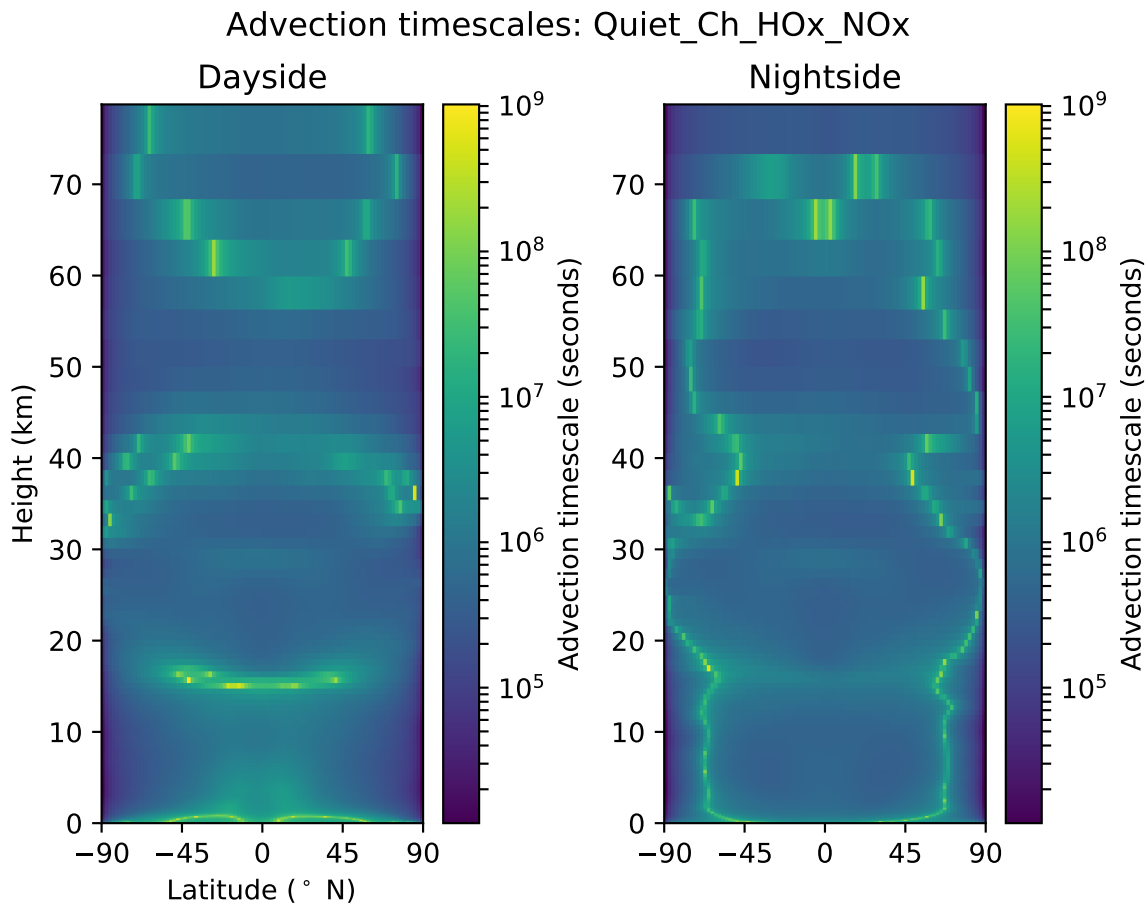
Figure 3.27: Approximations for the day–side and night–side advection timescales using winds from Quiet_Ch_HOx_NOx.

for the timescale for a parcel of air to cross the day–side. This estimation of the day–side and night–side advection timescales (calculated in the same manner) are shown in Figure 3.27 using the winds from the Quiet_Ch_HOx_NOx simulation.

The advection timescales are higher than the chemical lifetimes, mostly around 10^6 seconds, which is much larger than the chemical lifetime of ozone, which range from 10^5 seconds near the surface to 400 seconds at high altitudes. The chemical lifetimes are only comparable to the advection timescale in the polar regions in the troposphere, where the relatively short distance needed to cross the hemisphere at high latitudes reduces the timescale considerably. This tells us that an ozone molecule is not likely to survive a journey across the day–side, but will instead be destroyed and recreated several times. The lack of ozone photolysis and only a limited amount of ozone–destroying molecules being advected onto the night–side means that the night–side lifetime is much higher than the day–side. The lifetime of night–side ozone is controlled by planetary circulation and dynamics

rather than chemical loss.

Examining the lifetime of other molecules can tell us which species are acting as reservoirs. In this context, a reservoir is a molecule which acts as a store of other molecules such as HO_x or NO_x. For example, on the day–side, NO_2 is destroyed by

$$O(^3P) + NO_2 \longrightarrow NO + O_2,$$

$$OH + NO_2 + M \longrightarrow HNO_3 + M,$$
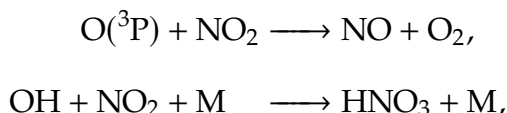
but on the night–side these reactions cannot occur (due to the lack of photolysis limiting $O(^3P)$ and OH), and instead NO_2 is converted by

$$NO_2 + O_3 \longrightarrow NO_3 + O_2.$$
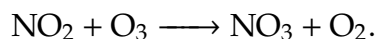
NO_3 is very easily destroyed in sunlight, but if it persists, can be turned into N_2O_5 by

$$NO_2 + NO_3 + M \longrightarrow N_2O_5 + M,$$
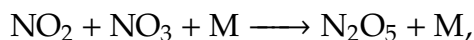
N_2O_5 and HNO_3 are fairly unreactive on the night–side, but on the dayside are photolysed and release the stored NO_x by

$$N_2O_5 + h\nu \longrightarrow NO_3 + NO_2 \ (\lambda < 1255 \text{ nm}),$$

$$HNO_3 + h\nu \longrightarrow NO_2 + OH \quad (\lambda < 581 \text{ nm}),$$

$$OH + HNO_3 \longrightarrow H_2O + NO_3,$$

$$NO_3 + h\nu \longrightarrow NO_2 + O(^3P)(\lambda < 7320 \text{ nm}).$$
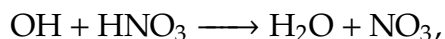
Figure 3.28 shows the mole fractions of several molecules comprising the HO_x and NO_x cycles. We see that there are no major reservoirs of HO_x molecules on the

night–side. We see that N_2O_5 and HNO_3 are major reservoirs of NO_x molecules on the night–side.
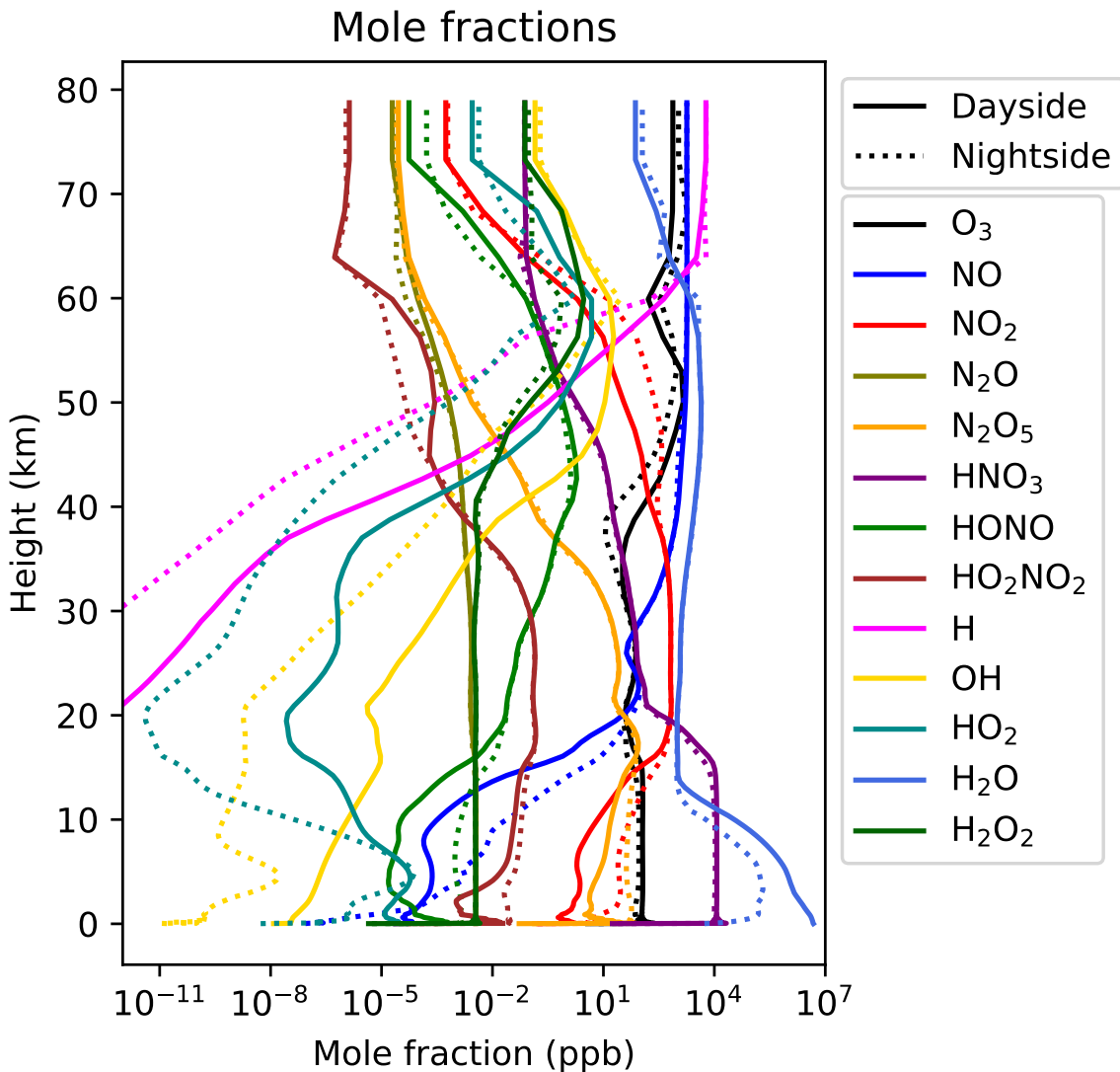
Figure 3.28: Hemispherically averaged day–side and night–side vertical profiles of molecules comprising the HO_x and NO_x cycles. This is taken from the last 100 days of Quiet_Ch_HOx_NOx.

We can examine the chemical lifetimes of the species to see them acting as reservoirs. A comparison of the day–side and night–side chemical lifetimes of ozone, NO_x, NO_y, and H_2O_2 from the Quiet_Ch_HOx_NOx simulation is shown in Figure 3.29. We can see that the ozone chemical lifetime is significantly longer on the night–side at most altitudes, which is due to two factors. As shown in Figure 3.13, photolysis (the main source of ozone destruction on the day–side and night–side) is naturally much lower on the night–side. Non–zero photolysis rates do not extend far beyond the dusk and dawn terminators, which has the result of significantly reducing the rate of ozone destruction. Additionally, there is a lim-

ited amount of transport of ozone–destroying molecules (atomic oxygen, HO_x) transported onto the night–side. Without generation of these molecules due to photolysis, they are much less abundant, which leaves ozone that is away from the terminators relatively untouched.
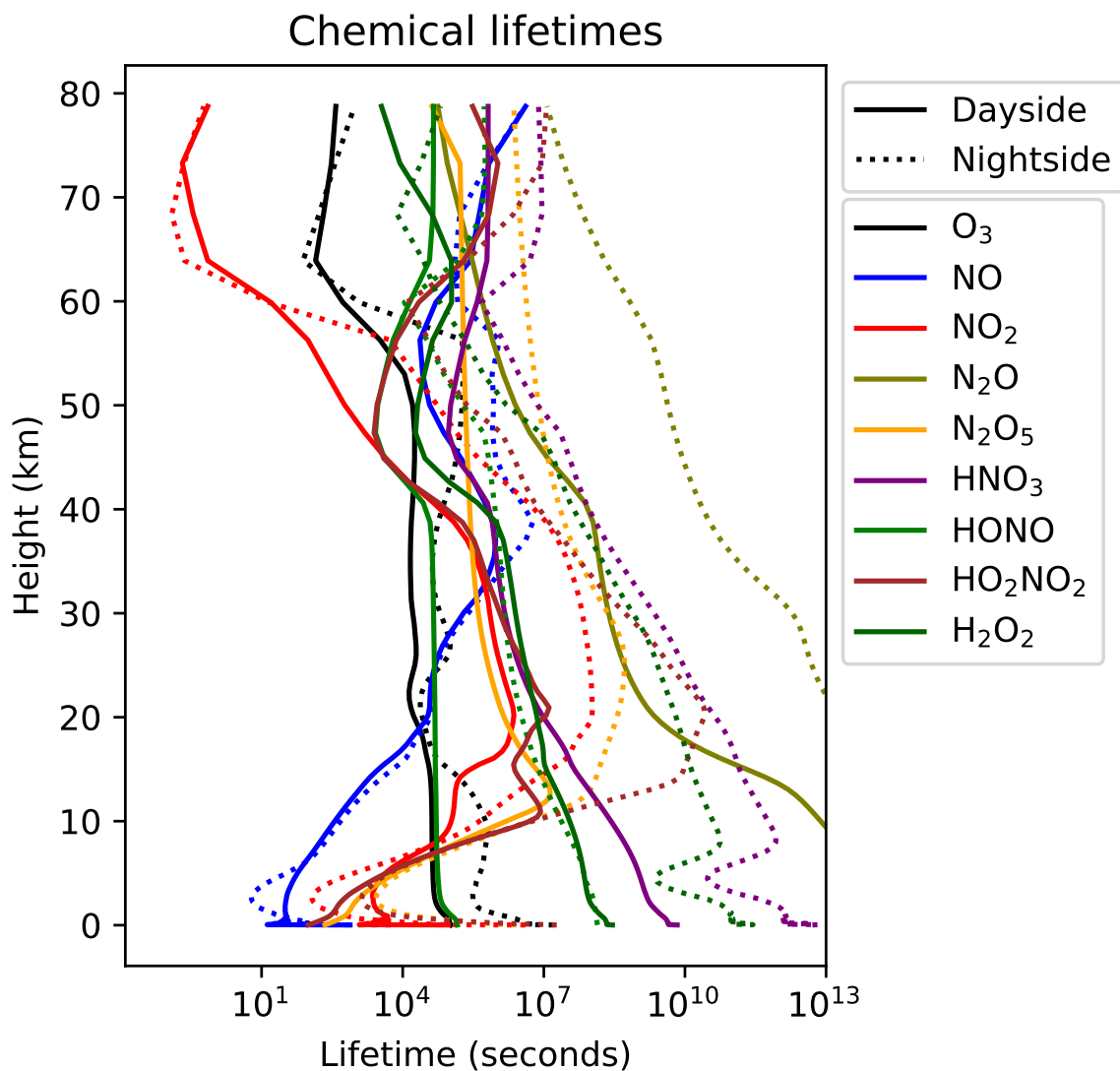
Figure 3.29: The vertical profile of the averaged day–side and night–side chemical lifetimes of ozone, NO_x, and NO_y molecules calculated from the last 100 days of the Quiet_Ch_HOx_NOx simulation. The effect of dry deposition on the chemical lifetime is not included.

Figure 3.29 also shows the chemical lifetimes of NO_x and NO_y molecules. We see that N_2O and HNO_3 have very large chemical lifetimes (ranging from years to many thousands of years), many times longer than the advection timescale shown in Figure 3.27. We see that N_2O_5 and HO_2NO_2 are destroyed fairly rapidly, and do not show day–night asymmetry below 10 km. Above 10 km the molecules show a much longer lifetime on the night-side, ranging from 10^7–10^9 seconds for

N_2O_5 and 10^7–10^{11} seconds for HO_2NO_2. Due to their high abundances and long chemical lifetimes, we find that N_2O_5 and HNO_3 are the main reservoirs of NO_x molecules on the planet's night–side. This is a similar result to terrestrial chemistry. However, there is terrestrial atmospheric chemistry which is not captured by this model that does complicate a comparison. We have not included chlorine and bromine oxides (ClO_x and BrO_x, respectively) which have a large impact on ozone chemistry in the terrestrial stratosphere (Fraser, 1997). They were not included due to their main source being biological emissions, which I did not include in this work. Testing the effects of such emissions should be the aim of future work. As such, we do not capture behaviour such as polar springtime reactive halogen events, events that occur in the polar night which produce oxidisers such as BrO (Simpson et al., 2018). Abiotic polar ClO_x and BrO_x sources are thought to include sea salt aerosols, and interactions with the snow pack (Lopez-Hilfiker et al., 2012; Krnavek et al., 2012). N_2O_5 has been identified as an important molecule for the generation of ClO_x and BrO_x, and the formation of N_2O_5 is favoured during the polar night (Chang et al., 2011; McNamara et al., 2019). For this reason, future work should aim to incorporate additional types of chemical reactions such as heterogeneous reactions as well as emissions which would allow the inclusion of these species.

3.4   Chapter Summary

In this chapter I have introduced the atmospheric chemistry that we are including in this work, and demonstrated how models of increasing complexity change the abundances and distribution of species such as ozone. In the following chapter, I will describe how stellar flares and coronal mass ejections were implemented. This will lead into Chapter 5 where I describe my simulations showing their impact on atmospheric ozone.

Chapter 4

Stellar Flares

In this chapter I will explain some of the previous work exploring the impact of stellar flares on planetary atmospheres, and then describe how I implemented flares into my simulations. This will describe how I have created a model for the creation of flares for ProxCen. Finally, I detail my implementation of SEPs and CMEs into the model framework.

4.1   Background

Our understanding of stellar flares should begin with solar flares. Solar flares are events which are caused by the release of stored magnetic energy in the solar corona (the outermost layer of the Sun) (Benz & Güdel, 2010). The energy is released in a process known as magnetic reconnection, which arises when magnetic field lines merge within a plasma. The merging of field lines releases energy, accelerating the plasma on the field line, rapidly heating the plasma in the solar corona. Some of the energy is radiated away as X rays, while the heated plasma is transported along magnetic field lines. The heated plasma deposited into the chromosphere releases a large amount of energy as well.

This is observed as a strong brightening of the Sun at shorter wavelengths, particularly gamma ray, X ray, and ultraviolet light. Solar flares occur over a range of

energies, and are more common during periods of high magnetic activity on the Sun, particularly around Solar Maximum.

Solar flares are associated with events known as Coronal Mass Ejections (CMEs), an event where large amounts of energetic particles erupt from the surface of the Sun and are sent into interplanetary space. Yashiro et al. (2006) reports that for very energetic solar flares, there is typically an associated CME that occurs that is associated with the flare, although this is dependent on solar flare energy.

Flares are known to occur on stars other than the Sun, and are known as stellar flares. Stellar flares have been observed on low-mass stars such as M dwarfs. Stellar flares on M dwarfs are thought to occur by the same process as solar flares (Benz & Güdel, 2010; Mullan, 2010). Günther et al. (2020) examined the catalog of stars (looking at F/G/K/M dwarfs) from the first two months of the TESS (Transiting Exoplanet Survey Satellite) mission, and found that the majority of flaring stars were M dwarfs. Depending on spectral class, between 5–30% of the M dwarfs observed exhibited flares, while only 1% of the observed F/G/K dwarfs flare.

Günther et al. (2020) found that when the stellar rotation period was fast (less than 10 days), stars were much more likely to flare. 60% of the fast rotating M dwarfs exhibited flaring, when only 10% of the M dwarfs with unknown rotation periods exhibited flaring. This is similar to the results reported by Kepler (Davenport, 2016). This might be due to changes in the stellar dynamo on slowly rotating stars, with slowly rotating stars lacking sufficient energy within their magnetic fields to sustain flaring, but may be also explainable by the flare rate or flare amplitude being smaller on slowly rotating stars, which may be difficult to observe.

They also show flare frequency distributions for F/G/K dwarfs, early M dwarfs, and late M dwarfs. They found that higher flare rates was associated with a longer flare duration and higher maximum flare amplitude. Early M dwarfs are shown to have more energetic flares than late M dwarfs. F/G/K dwarfs show higher flare energies than M dwarfs. While the range of energies of flares is similar between M

dwarfs and other stars, their significantly lower luminosity makes flares relatively much more powerful than the same flares on a more luminous star like the Sun.

4.2 Simulating flares in climate models

Simulating flares in a GCM requires a treatment of two aspects of the flare, the changes in stellar irradiation due to the flare, as well as any changes in the stellar proton flux due to the flare. In the following sections I will briefly describe previous work in this area, which will lead into the explanation of my approach to this problem.

4.2.1 Previous work

I have already described previous work looking at photochemistry on M dwarf planets in Section 3.3.9. I will now describe several works which have looked at the effects of flares on exoplanets.

4.2.2 Modelling the impact of flares in 1D

Segura et al. (2010) examined the impact of flares on an Earth–like planet that was assumed to be orbiting the M dwarf AD Leonis (AD Leo), a star which is known to exhibit strong flares. Hawley & Pettersen (1991) describes the 'great flare of 1985' that occurred on AD Leo, a flare which released more than 10^{34} ergs over a period lasting more than 4 hours, representing a large increase in UV and visible emission. The planet was assumed to be Earth-like, and orbiting AD Leo at a distance where it received the same amount of stellar radiation as the Earth receives. They looked at the effects of both the increased UV radiation from the flare, as well as the impacts of including stellar protons. They found that the UV radiation from the flare only caused a small temporary variation of less than 1% in the ozone column. When the effects of solar protons were included, the ozone column was severely reduced, reaching a maximum of 94% depletion compared to the pre–flare atmosphere. The atmosphere returned to its original composition

after ~ 48 years. The amount of UV light that reached the surface during the peak of the flares was found to be higher than the UV flux received on Earth for only 100 seconds. They concluded that flares may not present a direct danger for life that may exist on planets that were similar to their hypothetical planet.

A few years later, Venot et al. (2016) looked at the impact of stellar flares on two planets, these were a super–Earth/sub–Neptune that were also assumed to be orbiting AD Leo, at two different distances, so that the effective temperature of the planets was 412 K and 1303 K. Their atmospheric composition is similar to a gas giant, with high abundances of H_2, H_2O, CH_4, N_2, CO, CO_2, NH_3, and HCN.

They found that flares were capable of inducing changes in the planet's atmospheric composition. Species such as CO_2 changed their distribution significantly, becoming much more depleted at high altitudes. Interestingly, they found that the atmospheric composition was permanently altered by flares and did not return to its original composition, even after flares stopped affecting the planet. The post–flare atmospheric composition remained significantly different from the pre–flare composition, even after 10^{12} seconds (approximately 31,710 years) after the flare.

As well, Venot et al. (2016) also found that the transmission spectra of their simulated planets were significantly altered due to the flare. The most significantly changed features were those of CO_2 and CO. The cooler 412 K planet had smaller changes in the transmission spectrum, changing by $1 - 10$ ppm during the flare, and approximately 40 ppm by 10^{12} seconds after the flare. The hotter 1303 K had larger changes, changing the transit depth by $75 - 125$ ppm. 10^{12} seconds after the flare, the transit depth of the CO and CO_2 features was reduced by over 500 ppm.

Tilley et al. (2019) improved on the study of Segura et al. (2010). The approach is similar to Segura et al. (2010) (although some details are different, such as the flare template), but improves the way that flares were included. Instead of a single flare or a series of the same flare, flares were derived from a realistic distribution of flares, using the flare occurrence-energy distribution of flares on GJ 1243 as

reported by Hawley et al. (2014). This meant that flares could vary in magnitude and duration. They also incorporated a realistic impact probability for whether a CME would impact the planet. Similarly to Segura et al. (2010), they found that the electromagnetic portion of flares does not affect the ozone column, but when the effects of CMEs were included, the ozone column was reduced severely, depleting by 94% after 10 years of simulation.

Another recent work looking at flares by Louca et al. (2022) simulated the impact of flares on hydrogen–dominated and nitrogen–dominated atmospheres. This work does include atmospheric escape, but does not include the impact of stellar protons. Similar to this work, the quiescent stellar spectra in their work is obtained from the MUSCLES collaboration. Their planets were simulated for 11 days, and subjected to 515 flares. They do not include any heating effects by the flares.

Despite the relatively short length of the simulation, they observed trends indicating a permanent change in the atmospheric composition due to the flares. In contrast to previous results shown in Tilley et al. (2019) and Chen et al. (2021), they found that for nitrogen–dominated atmospheres the abundance of ozone in the upper atmosphere slowly increases. The changes to atmospheric composition do not sufficiently alter the emission and transmission spectra to make observable changes using current instrumentation.

4.2.3   Modelling the impact of flares in 3D

Chen et al. (2021) modelled the impact of flares and CMEs using the Whole Atmosphere Community Climate Model (WACCM). They simulated planets with a pre–industrial Earth–like atmosphere orbiting several types of stars, G dwarfs, K dwarfs, and M dwarfs. For each stellar type, they tested a different planetary configuration. For the G dwarf star, they tested a strongly magnetized rapidly rotating (P = 1 Earth day) planet, with the magnetic field being a dipole oriented with the rotation axis of the planet. For the K dwarf, they tested a weakly magnetised slowly rotating (P = 92 Earth days) planet. For the M dwarf, they simulated

an unmagnetised rapidly rotating (P = 4.32 Earth days) planet. The K dwarf and M dwarf planets were assumed to be tidally locked. The The effect of magnetism in their model altered how the stellar protons are included into the atmosphere. For the unmagnetised case, there is no deflection so the stellar protons are injected into the atmosphere at all latitudes across the day–side of the planet. If the planet is strongly magnetised, it is assumed that the stellar protons are guided along the magnetic field lines to the magnetic poles, so the protons are only injected at high latitudes (> 60°) across all longitudes. The weakly magnetised planet is assumed to have a "patchy" magnetic field similar to Mars, so the protons are injected into three different regions of the planet, both on the day–side and night–side. Their inclusion of stellar protons scales observations of solar proton events with the strength of the flare. This is used to scale the rate of ionisation in the atmosphere producing atomic nitrogen and HO_x molecules.

For their simulations, they assumed that the planet has the same integrated top–of–atmosphere stellar flux, the amount received by the Earth. The size of the planet is 1 Earth radii and had a mass of 1 Earth mass. The surface was composed of the modern Earth's continental configuration, topography, and albedo. The planets were simulated for 300 Earth days. In all three simulations, they found that the amount of ozone present at 1 hPa (1 hPa = 100 Pa) decreased due to flares. The effect was smallest for the G dwarf, decreasing the mixing ratio by a small amount. The impact of flares was found to be stronger for the K and M dwarf planets, decreasing the mixing ratio at 1 hPa by an order of magnitude. The effects of flares were limited below 50 km. For the K dwarf and M dwarf cases, the amount of ozone (averaged over the 300 days of simulation) above 50 km was reduced by an order of magnitude, reaching 2–3 orders of magnitude during the peak of the flare on day 60. Large changes in the amount of N_2O, HNO_3, and water vapour were also observed. The effects of the magnetic field assumptions heavily controlled where the products created by the stellar protons, and produced significantly different patterns of OH production, and drives changes in ozone destruction. They suggest that if the spatial distribution of nitrogen–bearing and hydrogen–bearing

species can be determined, this may provide a method for determining the presence and structure of a exoplanetary magnetosphere.

4.3 Creation of Flare Spectra

I constructed a time–varying stellar irradiance that represents a flare, that is applied whenever a flare occurs. To create a series of flares for the simulations, I used the flare template of Venot et al. (2016) that represents the 'great flare on April 12th 1985' of AD Leonis (AD Leo), reported and characterised by Hawley & Pettersen (1991). This was used after modifying the input stellar irradiance to make it more appropriate for ProxCen.

4.3.1 ProxCen flare template

The flare template used by Venot et al. (2016) only uses flare data from 100–444 nm. As such, outside of this wavelength range the spectrum is constant and does not change during the flare. In the future the flare template could be extended to longer wavelengths, however, the increased flux from the flaring decreases rapidly beyond 444 nm. The flare template was converted so the flare would represent a flare occurring on ProxCen. From the AD Leo flare template we obtained scaling factors of the irradiance for the duration of the flare using

$$F_{\text{Prox,Flare}}(\lambda, t) = F_{\text{Prox,Qui}}(\lambda, t) \frac{F_{\text{ADLeo,Flare}}(\lambda, t)}{F_{\text{ADLeo,Qui}}(\lambda, t)}, \tag{4.1}$$

where $F_{\text{Prox,Qui}}$ and $F_{\text{Prox,Flare}}$ are the stellar irradiances of ProxCen during quiescent conditions and during a given stellar flare respectively, and $F_{\text{ADLeo,Qui}}$ and $F_{\text{ADLeo,Flare}}$ are the stellar irradiances of AD Leo during quiescent conditions and during a given stellar flare, respectively.

The Venot et al. (2016) flare template is separated into three phases spanning 2586 seconds:

- First impulsive phase: 0–800 s, rapid growth in stellar flux

- Second impulsive phase: 912–1497 s, fast decrease in stellar flux, still much higher than quiescent at end of the phase

- Gradual phase: 1589-2586 s, a slow decrease in stellar flux towards quiescent values
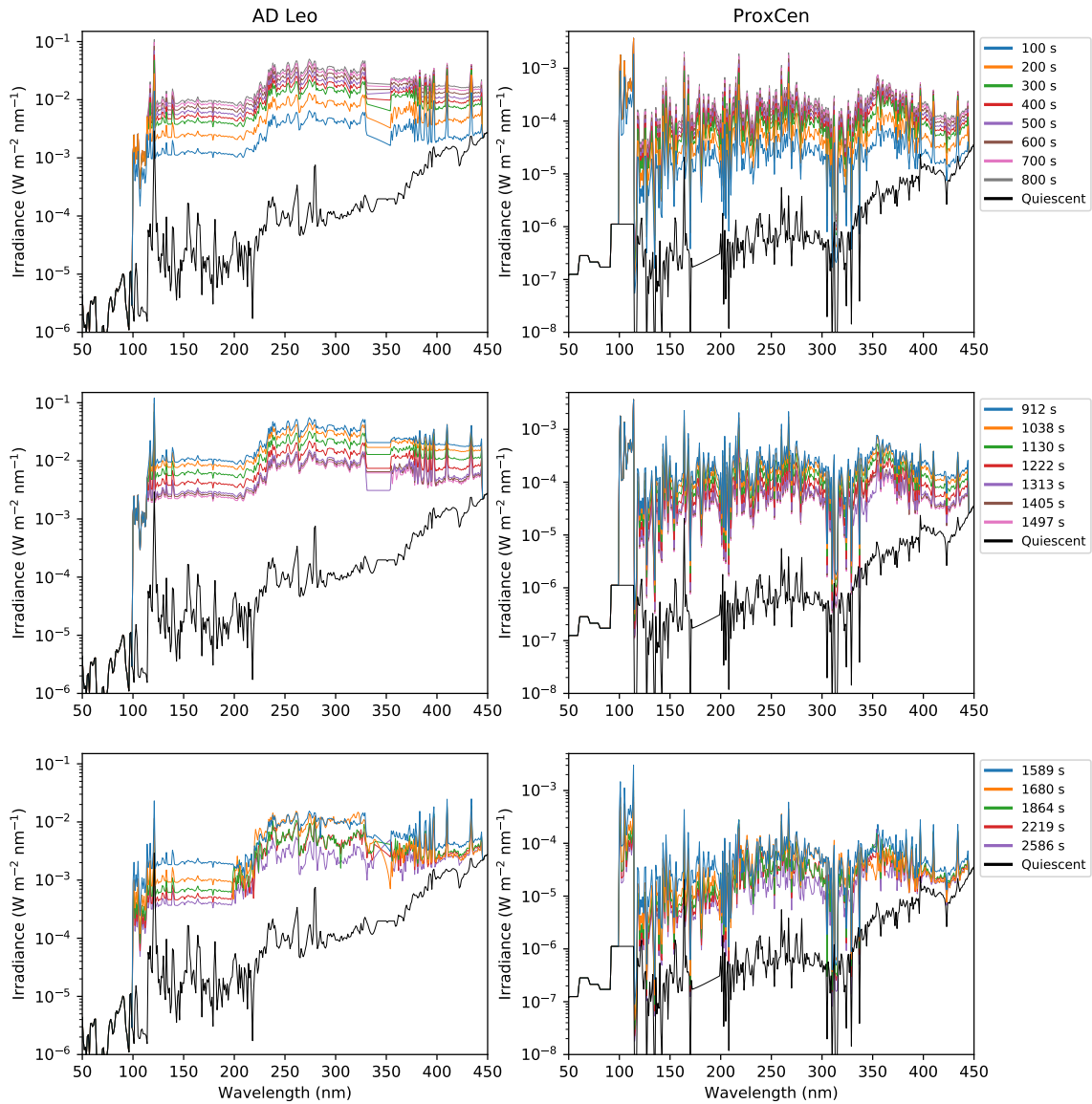
Figure 4.1: Stellar spectra of the template flare of AD Leo at a distance of 1 AU (left), and the converted values for the template of a ProxCen flare (right). The figure is separated into three phases, first impulsive (top), second impulsive (middle), and gradual (bottom).

Figure 4.1 shows the AD Leo flare over time, and the adapted ProxCen flare, separated into the three phases. We see that the stellar irradiance for both stars is still much higher at the end of the flare than their quiescent irradiance, although it is closer to quiescent values at higher wavelengths. The rest of the stellar spectrum (less than 100 nm, and greater than 444 nm) is kept constant and does not change
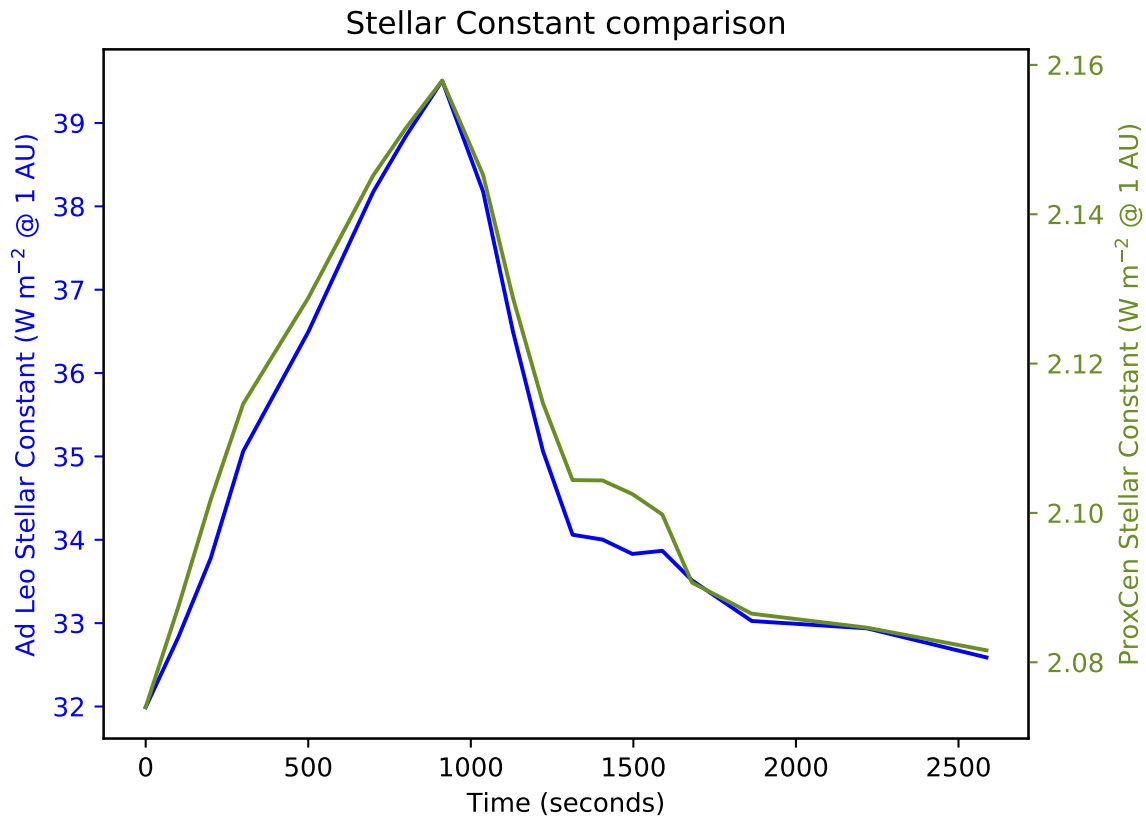
Figure 4.2: The change in stellar constants for the AdLeo flare (left) and the adapted ProxCen flare (right).

during the flare. As a result, despite a large increase in UV and visible radiation by several orders of magnitude, the overall brightness of the star does not increase by the same amount. Figure 4.2 shows the change in stellar constants for the Ad Leo and ProxCen flares during the flare. The AD Leo flare increases the stellar constant from a quiescent value of $32\,\mathrm{W/m^2}$ to a maximum of $39.5\,\mathrm{W/m^2}$. The Prox-Cen flare increases the stellar constant from the quiescent value of $2.074\,\mathrm{W/m^2}$ to a maximum of $2.158\,\mathrm{W/m^2}$. This translates to a maximum change of $\sim 23.5\%$ from the quiescent value.

Now that we understand how the template for a ProxCen flare was created, we can continue onto how this template is used to simulate flares of a range of energies and durations.

4.3.2 Scalable flare template

The ProxCen flare template is scaled based on two factors, the flare energy and the duration. The flare energy is the energy released by the flare in the form of

electromagnetic radiation. Given a flare energy E_f, the energy released from the flare can be calculated as

$$E_f = \int \int \int h(F_f(\lambda, t) - F_*(\lambda, t))d\lambda dt dA, \qquad (4.2)$$

where h is a scaling factor, F_f is the stellar spectral irradiance released from the star during the flare, and F_* is the quiescent stellar spectral irradiance. If the irradiance is scaled for the irradiance received at 1 AU from the star, we can change Equation 4.2 to

$$E_f = 4\pi d^2 h \int \int F_f(\lambda, t) - F_*(\lambda, t)d\lambda dt, \qquad (4.3)$$

where d=1 AU (1.496×10^{11} m). We want a tool which can generate complex flares, which occur when multiple flares occur at the same time. That changes Equation 4.3 to

$$E_f = 4\pi d^2 h \int \int F'_f(\lambda, t)d\lambda dt, \qquad (4.4)$$

where F'_f is the additional flux emitted from the star during the flare, calculated as

$$F'_f = F_f - F_*. \qquad (4.5)$$

The scaling factor h is used to create flares, and scales the magnitude of the Prox-Cen flare template, and is calculated as

$$h = \frac{E_f}{4\pi 1 AU^2 \int \int F'_f(\lambda, t)d\lambda dt}. \qquad (4.6)$$

The flare duration is dependent on flare energy. More energetic flares last longer. For this work, we used the flare duration formula from Tilley et al. (2019), derived from Hawley et al. (2014), which is

$$\log_{10} t = 0.395 \log_{10} E - 9.269, \qquad (4.7)$$

where t is the duration of the flare in seconds and E is the energy of the flare in ergs

(1 erg=10^{-7} J). The duration of the flare template is scaled to match the duration from Equation 4.7, and is then used to calculate h to scale the magnitude of the flare. All phases are scaled by the same amount.

This scalable template was used to generate flares over a range of different energies.

4.4 Flare Generation

The goal of this work was to subject our simulated planet to a series of flares. Like Tilley et al. (2019), we subjected the planet to a realistic range of flare energies instead of flares at the same energy. This produces a more realistic result. To accomplish this, two problems needed to be solved; creating time-varying spectral data for flares, and generating a series of flares over a realistic range of energies.

The previous section described the first step, how we can create a time-varying spectral profile for a flare, once a flare energy is determined. This section will describe how the series of flares were generated for use in the UM.

4.4.1 Inverse Transform Sampling

This section will describe the technique I used to generate a sample of flares from a pre–determined frequency distribution. Given a cumulative distribution function (CDF) relating flare energy and flare occurrence frequency F(x), we want to generate a sample of flare energies that is representative of the CDF. I chose to use Inverse Transform Sampling to generate these samples. We can use the flare energy occurrence distribution for GJ 1243 (Hawley et al., 2014) for flare energies between $10^{30.5} - 10^{34}$ ergs (1 erg = 10^{-7} Joules). Equation 4.8 describes how the occurrence of flares correlates with the energy released during the flare

$$\log_{10}(\nu) = -1.01 \log_{10}(E) + 31.65, \tag{4.8}$$

where E is the energy released from the flare in ergs and nu is the number of flares occurring per day of at least energy E. In other words, ν is the absolute

108
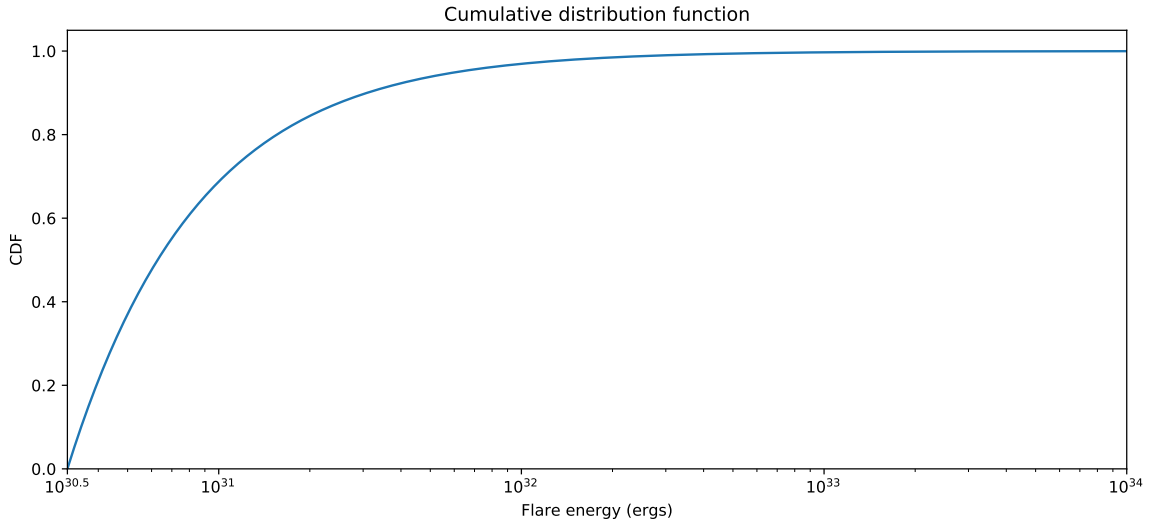
Figure 4.3: The constructed CDF of the flare occurrence-energy distribution.

inverse cumulative frequency. Let us use the generalized form of Equation 4.8, $\log_{10}(\nu) = \alpha \log_{10}(E) + \beta$. To construct the CDF (F(E)), we first need to normalise the inverse cumulative frequency ν' so it now ranges from 0 to 1 (issues arising from ν not being 0 at 10^{34} ergs will be explained shortly). We normalize this by

$$\nu' = \nu(\log_{10}(E))/\nu(30.5), \tag{4.9}$$

which is constructed as

$$\nu' = \frac{\nu(\log_{10}(E))}{\nu(30.5)} = \frac{10^{\beta} \times 10^{\alpha \log_{10}(E)}}{10^{\beta} \times 10^{\alpha 30.5}}, \tag{4.10}$$

$$= \frac{10^{\alpha} \log_{10}(E)}{10^{\alpha 30.5}}, \tag{4.11}$$

$$= 10^{\alpha(\log_{10}(E) - 30.5)}. \tag{4.12}$$

The CDF is simply 1-ν', so

$$F(E) = 1 - \nu' = 1 - 10^{\alpha(\log_{10}(E) - 30.5)}. \tag{4.13}$$

Figure 4.3 shows the CDF for this distribution.

Now that we have an equation for the CDF, we need to invert the CDF to let us create a sample of energies. Let $y = [0, 1]$ be a uniform distribution of values that

would correspond to a distribution of energies E such that

$$y = F(E), \tag{4.14}$$

so to find the distribution of energies E in terms of y, we need to invert the CDF to find

$$E = F^{-1}(y), \tag{4.15}$$

where F^{-1} is the inverted CDF. This is found by

$$y = F(E) = 1 - 10^{\alpha(\log_{10}(E) - 30.5)},$$

$$1 - y = 10^{\alpha(\log_{10}(E) - 30.5)},$$

$$\log_{10}(1 - y) = \alpha(\log_{10}(E) - 30.5),$$

$$\log_{10}(E) = \frac{\log_{10}(1 - y)}{\alpha} + 30.5. \tag{4.16}$$

Finally, we note that since y is a uniform distribution from $[0, 1]$, $1 - y = y$, so we can slightly simplify Equation 4.16 to

$$\log_{10}(E) = \frac{\log_{10}(y)}{\alpha} + 30.5. \tag{4.17}$$

This gives us our population of flares which is drawn from the energy-occurrence distribution. There is one final caveat that we need to note before we can proceed to generating flares. The distribution is only defined between $10^{30.5}$–10^{34} ergs, but the distribution has a non-zero probability of flares with an energy $> 10^{34}$ ergs. Figure. 4.4 shows the differences between two methods for generating flares from this distribution and how sample populations compare to the actual distribution (black). 30 years of flares were sampled, and the resulting inverse cumulative frequencies were compared to the analytic distribution that they were drawing from. The first option (blue) is capping the energy of flares which were generated with an energy of $E > 10^{34}$ ergs to 10^{34} ergs. The second option is rejecting any flares which are too large and redrawing the energy until they have an acceptable
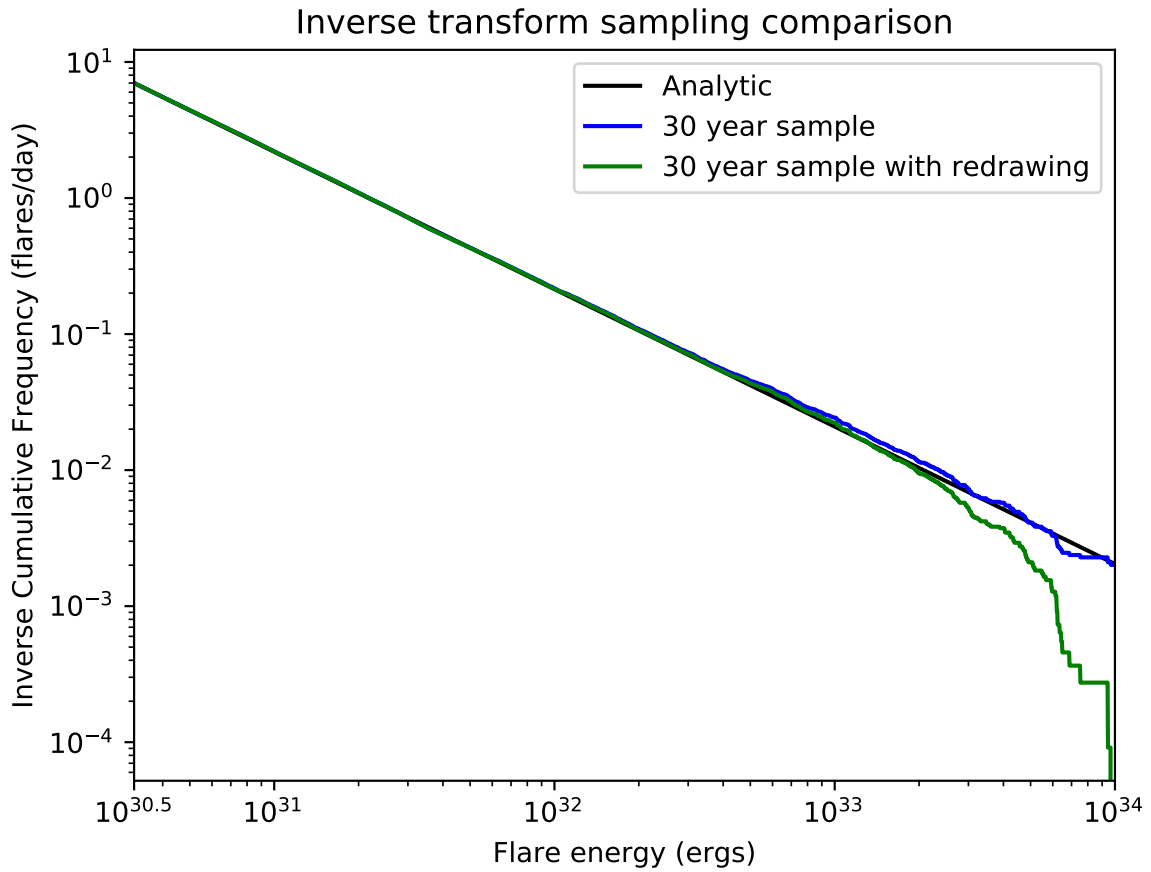
Figure 4.4: Two samples of 30 years of flares drawn from the distribution with and without redrawing flare energies which are outside the defined range of flare energies, and how they compare to the analytic distribution.

energy. We settled on the former, as the distribution of flares using the latter technique does not capture the prevalence of the highest energy flares. As seen in Figure 4.4, by redrawing the flare energies, the resulting inverse cumulative frequency seriously diverges from the distribution for flare energies above 2×10^{33} ergs.

Using the adapted flare template and the techniques explained here, we can now generate flares with a realistic distribution of energies and durations. We can now proceed to describing how Stellar Energetic Protons and Coronal Mass Ejections were modelled.

4.5 Stellar Energetic Protons

This section will explain how I have included the effects of stellar energetic protons (SEPs) into my chemical networks, what reactions are induced by SEPs, and how

I have coupled SEPs to Coronal Mass Ejections (CMEs) caused by stellar flares. Energetic particles are constantly released by the Sun, which is known as the solar wind. During periods of solar activity the Sun can release larger bursts of energetic particles. Events where large amounts of solar protons are released and the solar proton flux is elevated are known as Solar Proton Events (SPEs). During a solar flare, they can be released by solar events such as coronal mass ejections, also known as CMEs. If SPEs are released at the right time and the right direction, they can impact the terrestrial magnetosphere and reach the Earth's atmosphere.

When the protons precipitate into the atmosphere, collisions with neutral particles in the atmosphere create pairs of ions. The proton causes an electron to be removed from the neutral atom or molecule, producing a positively charged ion. These electrons are also known as secondary electrons. Some energy from the proton is transferred into the ion pair, which is capable of causing additional ionisations.

To parameterise the effects of stellar protons (or stellar energetic particles, SEPs), we used ion pair production rates observed in Earth's atmosphere, and scaled them with ProxCen flare strength. We take a similar approach to previous work (Chen et al., 2021), using the solar proton data provided for use[1] in the sixth Coupled Model Intercomparison Project (CMIP6) (Matthes et al., 2017). These data consist of proton fluxes measured from various space–based instruments and provides ion pair production rates in the atmosphere due to solar protons. The rates are used to determine the reaction rates of the following reactions

$$H_2O + p^+/e^- \longrightarrow H + OH, \tag{R84}$$

$$N_2 + p^+/e^- \longrightarrow N(^4S) + N(^4S), \tag{R85}$$

$$N_2 + p^+/e^- \longrightarrow N(^2D) + N(^2D), \tag{R86}$$
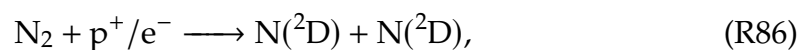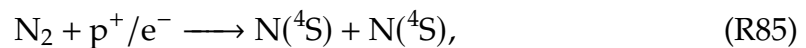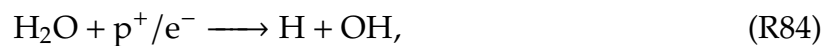
where $N(^4S)$ is ground state atomic nitrogen, and $N(^2D)$ is an excited state of atomic nitrogen. Following Solomon et al. (1981) and Porter et al. (1976), we assume that $2\,HO_x$ molecules (one H and one OH molecule) and 1.25 nitrogen atoms

---

[1]obtainable from SOLARIS-HEPPA: https://solarisheppa.geomar.de/solarprotonfluxes

Reaction	Production efficiency	Scheme
$H_2O + p^+/e \longrightarrow H + OH$	2	HO_x
$N_2 + p^+/e \longrightarrow N(^4S) + N(^4S)$	0.55	NO_x
$N_2 + p^+/e \longrightarrow N(^2D) + N(^2D)$	0.7	NO_x

Table 4.1: The list of reactions caused by stellar proton (or stellar energetic particles, SEPs) forcing used in the chemical networks and the total amount of molecules produced per ion pair for each reaction.

$(0.7 \, N(^2D)$ and $0.55 \, N(^4S)$ atoms) are created per ion pair. The reactions and production efficiencies are listed in Table 4.1.

4.5.1 Planetary magnetic field

As SEPs are charged particles, the presence of a planetary magnetic field would alter how and where SEPs enter the atmosphere. If the planet has a magnetic field, the SEPs would be deflected/funnelled towards the magnetic poles. This is observable on Earth, as SEPs are deflected towards the magnetic poles (Jackman & McPeters, 2004). This is dependent on the energy of the proton, as higher energy protons would be deflected less. In this work we assume the planet does not have a significant magnetic field. Due to a slow rotation rate, the planet is not expected to have a significant geodynamo so any magnetic field would be relatively weak (Christensen et al., 2009) and would cause little deflection. Without any deflection from the magnetic field, the protons are assumed to impact across the entire illuminated side of the planet.

4.5.2 Quiescent and flaring conditions

The amount of ion pair production depends on the energy distribution of the SEPs. During solar storms, a larger amount of higher energy (> 10 MeV) protons are released by the Sun. Higher energy protons penetrate further into the atmosphere and cause higher levels of ion pair production (Reid, 1986). Due to differences in proton energy distributions and fluxes during CMEs, the magnitude and profile of the ion pair production rate will differ between quiescent conditions and during a CME. We chose a profile to use during quiescent conditions, and a scalable profile that is used to simulates CMEs.The quiescent profile was created by averaging
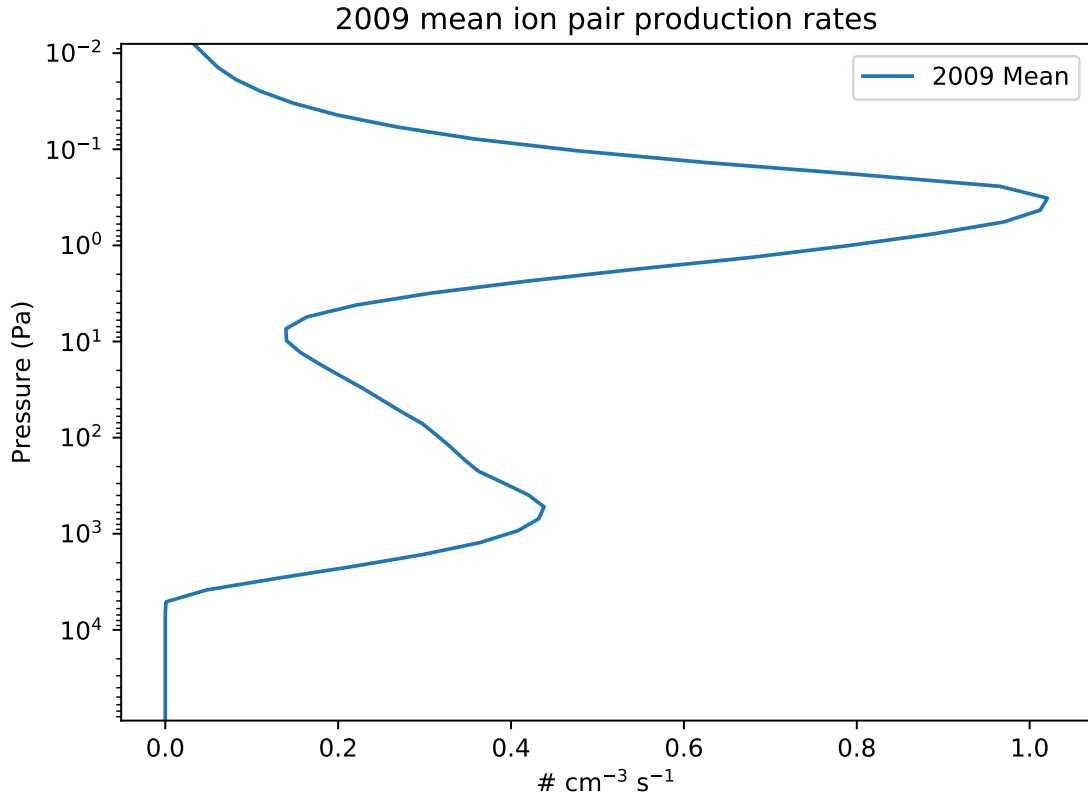
Figure 4.5: The reaction rate profile used for SEPs during quiescent conditions, obtained from averaging ionisation rates observed during the 2009 solar minimum.

the Earth–based ion pair production rates from 2009, near Solar Minimum. This serves as a low-activity baseline for quiescent conditions. Figure 4.5 shows a view of the quiescent ion pair production profile. We see that the production rate peaks at just over $1\,\mathrm{cm^{-3}\,s^{-1}}$, with a secondary peak at a lower pressure of $\sim 0.45\,\mathrm{cm^{-3}\,s^{-1}}$.

The ion pair production rate used to simulate CMEs was created from observations during the October 2003 solar storm. The production rates from October 27th 2003-November 1st 2003 are shown in Figure 4.6, which shows the evolution in production rates as the solar storm grew in strength before reaching a maximum on October 29th, and eventually decreasing in strength. The October 29th profile was used since it was the maximum magnitude and represents the zenith in solar storm strength. We see that ion pair production was much higher than the quiescent profile, almost reaching $10^4\,\mathrm{cm^{-3}\,s^{-1}}$. The location of the peak production rate is also at a much higher pressure, indicating the presence of high-energy protons.
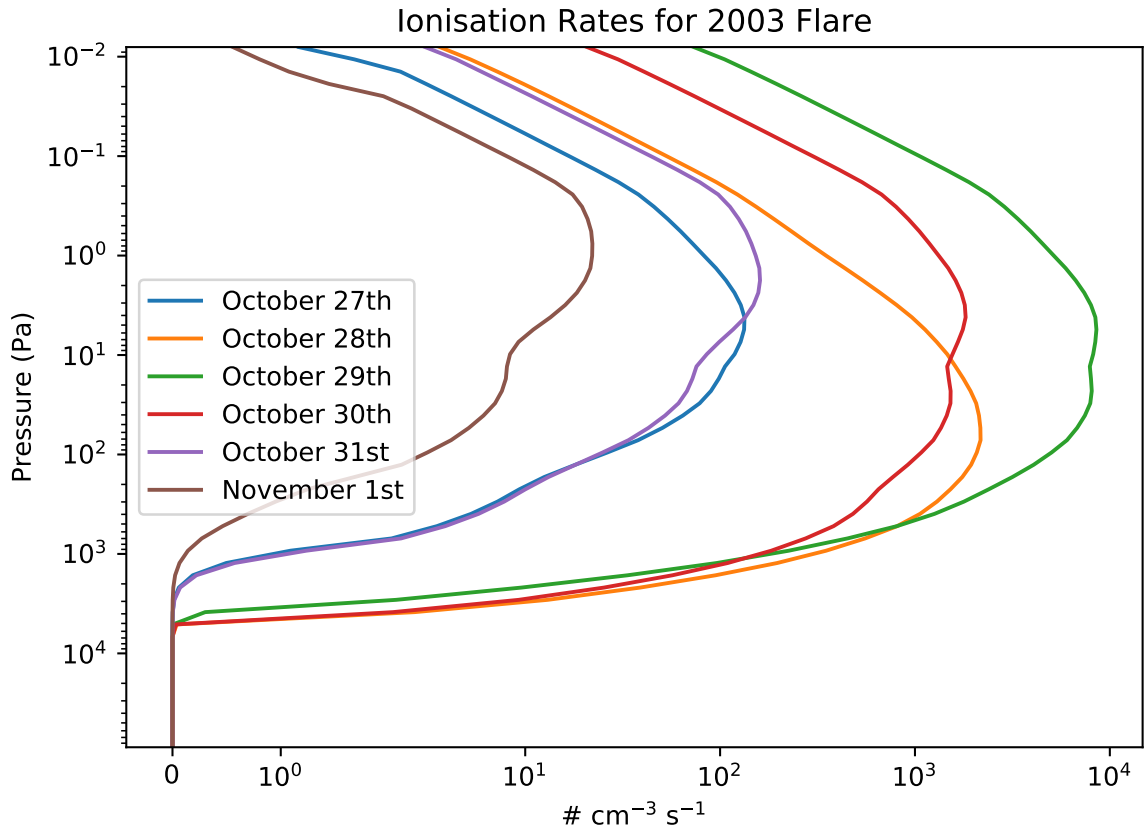
Figure 4.6: The ion pair production rates observed during the Halloween 2003 solar storm.

To determine how to scale the production rate with flare strength, we use the relation of flare strength to proton flux from Belov et al. (2005) which relates proton flux to the peak X–ray intensity during the flare. As described in Tilley et al. (2019) the proton flux (in proton flux units, or pfu) for protons with an energy greater than 10 MeV, with units of protons/cm^2/s/sr, (sr is steradian) is given by

$$I_p(> 10\text{MeV}) = k_0 \left(\frac{\phi^{1.08}}{a^2} \right)^{1.14}, \tag{4.18}$$

where ϕ is the relative flux increase in the Johnson U band, a is the semi-major axis in astronomical units. We represent the transient nature of CMEs by only applying the scalable CME profile during the flare (if a CME impacts the planet), otherwise the planet only receives the quiescent profile. This is scaled using the proton fluence measured from GOES–11 during the October 29th 2003 solar storm, which measured a rate of 7.7×10^8 protons/cm^2/day/sr, or 8912 pfu[2]. This is applied as a constant for the duration of the flare, with no correction for a delay between

---

[2]obtained from `ftp://ftp.swpc.noaa.gov/pub/warehouse/`
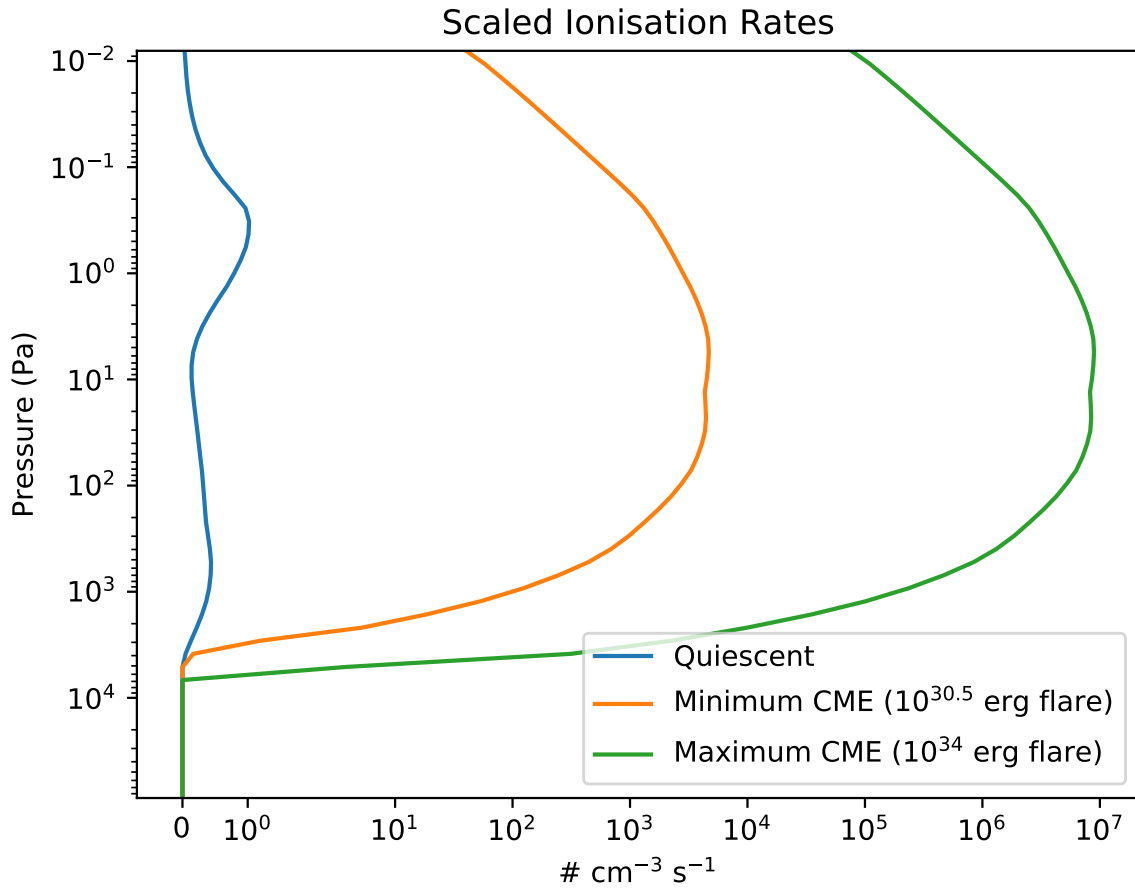
Figure 4.7: The ion pair production rates during quiescent conditions (blue), the ionisation rates during a $10^{30.5}$ erg flare (orange), and a 10^{34} erg flare (green).

the onset of the flare and the onset of the CME. Solar CMEs range in velocities from $\sim 30 - 2600\,\text{km s}^{-1}$, with an average velocity of $428\,\text{km s}^{-1}$ (Yashiro, 2004). For our simulations assuming the planet is orbiting at a distance of 0.0485 AU, that would mean an average delay of ~ 4.7 hours, ranging from ~ 0.77-67.2 hours. The response of the atmosphere when the CMEs are delayed is a topic for future research. The range in ion pair production rates is shown in Figure 4.7, which compares rates during quiescent conditions to the rates during a $10^{30.5}$ erg flare, and a 10^{34} erg flare. We see that even the weakest CME has a much higher production rate than the quiescent conditions.

4.6 Modelling Coronal Mass Ejections

Coronal Mass Ejections are modelled as occurring concurrently with flares. In this work we assume that every flare has an associated CME. This is similar to Tilley et al. (2019) and Chen et al. (2021). However, recent work by Muheki et al. (2020);

Alvarado-Gómez et al. (2022) indicates that the relationship between solar flares and CMEs is not appropriate for M dwarf stars, where there is less CME activity. Therefore, our results will effectively act as the upper limit of the effects of CMEs. However, as will be described in the following chapter, the effects of CMEs were quite limited, and would be even smaller with less CMEs occurring.

It should be noted that not every CME is expected to impact the planet. This is due to several factors, such as the angular size of the CME, and where on the star the CME was released. We incorporate a few assumptions regarding the geometry of CMEs that allow us to obtain a plausible probability regarding whether a CME will impact the planet.

4.6.1 CME impact probability

The probability of a CME impacting the planet (P) is determined using the relation derived in Khodachenko et al. (2007) for CMEs occurring on the Sun. The factors controlling the likelihood of a CME impacting the planet depends on a few factors, the stellar co-latitude and longitude (θ and ϕ) where the CME originates, the angular width of the Δ_{CME}, and the angular width of the planet δ_{pl}. The angular width of the planet is simply calculated as

$$\delta_{pl} = 2\arctan(r/a), \tag{4.19}$$

which for a planet of radius $r = 7160\,\text{km}$ orbiting the star at a distance of $a = 0.0485\,\text{AU}$ is calculated as 1.974×10^{-3} radians. The angular width of CMEs is assumed to be similar to solar CMEs. Yashiro (2004) reports that the average width of solar CMEs (Δ_{CME}) ranges from 45–61°, being smallest near solar minimum and peaking just before solar maximum. I chose to use an average CME width of $\Delta_{CME} = 47°$, the average CME width observed between 1996-2003 (Gopalswamy, 2004). I also assume that CMEs can only originate between a maximum latitude (Θ), which is assumed to be ±60°. While CMEs can occur at any solar latitude, they typically originate at lower latitudes, particularly during solar minimum (Yashiro,

2004; Gopalswamy et al., 2008). Figure 4.8 shows a schematic illustrating the geometry of CME impacts. The impact probability P can be separated into two components

$$P = P_1 P_2, \tag{4.20}$$

where P_1 is the probability of the CME being ejected at an acceptable range of solar latitudes, and P_2 the probability of the CME being ejected at an acceptable range of solar longitudes. The CME being ejected at an acceptable range of latitudes means that the polar launch angle θ is (assuming the planet is orbiting the star in the stellar equatorial plane $\theta = \frac{\pi}{2}$) in the interval of

$$\frac{\pi}{2} - (\Delta_{\mathrm{CME}} + \delta_{\mathrm{pl}})/2 < \theta < \frac{\pi}{2} + (\Delta_{\mathrm{CME}} + \delta_{\mathrm{pl}})/2. \tag{4.21}$$

The interval is the range of angles where the angular width of the CME and the angular width of the planet will partially overlap and Using the approach of Khodachenko et al. (2007), we assume that the CME latitude distribution is approximately $\sin(\theta)$. P_1 is thus calculated as the fraction of CMEs that originate from within the previously mentioned interval

$$P_1 = \frac{\int_{\pi/2-(\Delta_{\mathrm{CME}}+\delta_{\mathrm{pl}})/2}^{\pi/2+(\Delta_{\mathrm{CME}}+\delta_{\mathrm{pl}})/2} \sin(\theta)d\theta}{\int_{\pi/2-\Theta}^{\pi/2+\Theta} \sin(\theta)d\theta} = \frac{\sin((\Delta_{\mathrm{CME}} + \delta_{\mathrm{pl}})/2)}{\sin(\Theta)}. \tag{4.22}$$

P_2 is determined in a similar manner. The meridional launch angle ϕ needs to be within the range of

$$-(\Delta_{\mathrm{CME}} + \delta_{\mathrm{pl}})/2 < \phi < (\Delta_{\mathrm{CME}} + \delta_{\mathrm{pl}})/2, \tag{4.23}$$

where ϕ is the azimuthal angle, assuming the planet is located at $\phi = 0$ for convenience. The longitudinal distribution of solar CMEs is approximately uniform
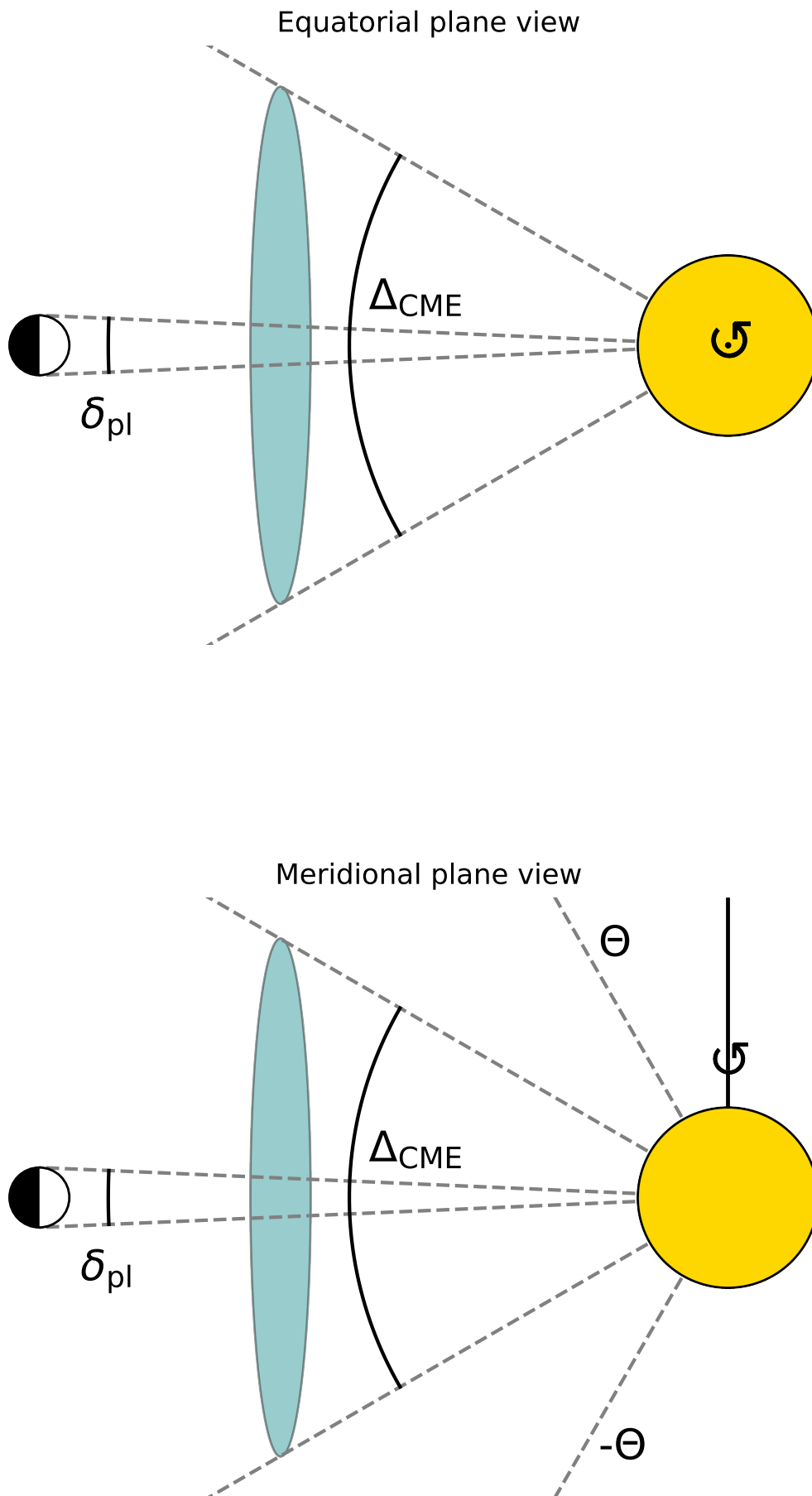
Figure 4.8: A schematic illustrating the geometry governing the CME impact probability. Δ_{CME} is the angular width of the CME, δ_{pl} is the angular size of the planet, and Θ is the maximum latitude where CMEs can originate from. This is an adaptation of Figure 3a from Khodachenko et al. (2007).

(Gopalswamy et al., 2008) so we can calculate P_2 as

$$P_2 = \frac{\int_{-(\Delta_{CME}+\delta_{pl})/2}^{(\Delta_{CME}+\delta_{pl})/2} d\phi}{\int_0^{2\pi} d\phi} = \frac{\Delta_{CME} + \delta_{pl}}{2\pi}. \tag{4.24}$$

The probability for a CME impact is thus

$$P = P_1 P_2 = \frac{(\Delta_{CME} + \delta_{pl}) \sin((\Delta_{CME} + \delta_{pl})/2)}{2\pi \sin(\Theta)}. \tag{4.25}$$

Under the previous assumptions of $\Delta_{CME} = 47°$, $\Theta = 60°$, and $\delta_{pl} \approx 2 \times 10^{-3}$, the probability that a CME impacts the planet is 0.06, or 6%. This tells us that CMEs that impact the planet are quite infrequent. Referring back to Equation 4.8, the number of flares that hit the planet in this model are ~ 6.995 flares/day. This gives us a CME impact frequency of 0.42/day, or that we would expect a CME to impact the planet approximately once every ~ 2.38 days.

4.7 Chapter Summary

In this chapter I have described previous work which looked at the impact of stellar flares on planetary atmospheres, both in 1D and in 3D. The method I have used to generate flares for the UM simulations has been described in detail. The introduction of SEPs (stellar energetic particles) into the chemical networks has been described, as well as assumptions regarding how CMEs and SEPs will impact the planet.

In the following chapter I will describe the addition of quiescent SEPs to the quiescent simulations (comparing with the quiescent simulations described in Chapter 3) and how those impact the atmosphere. As well, I include flares into the UM simulations and describe how flares and CMEs have shaped the atmosphere after a single year of simulation.

Chapter 5

Atmospheric response to stellar energetic protons, flares, and coronal mass ejections

In this chapter I will describe the results of the inclusion of stellar energetic protons into quiescent simulations, and then how I have incorporated stellar flares and coronal mass ejections into the UM simulations and atmospheric chemistry.

5.1   Simulations with SEPs and Flaring

Before we proceed to the results from the inclusion of flares, it would be useful to understand the effects that quiescent SEPs have before it is complicated by stellar activity. This section will describe two more quiescent simulations before we describe the simulations involved in simulating the impact of flares and CMEs.

In addition to the three quiescent simulations described in Chapter 3, two more simulations were performed, Quiet_Ch_HOx_SEP and Quiet_Full, which describe HO_x chemistry with the inclusion of R84, and describe NO_x chemistry with the inclusion of R84–R86 respectively. The simulations and their details are listed in Table 5.1. The climate, dynamics, and atmospheric composition of Quiet_Full is

Phase	Name	Spectrum	Chemistry	SEPs (affected species)	Time–steps (minutes)		
					Dynamic	Radiation	Chemistry
Quiescent	Quiet_Ch	Quiescent	ChC	–	10	60	60
	Quiet_Ch_HOx	Quiescent	ChC & HO_x	–			
	Quiet_Ch_HOx_SEP	Quiescent	ChC, HO_x	Quiescent (H_2O)			
	Quiet_Ch_HOx_NOx	Quiescent	ChC, HO_x & NO_x	–			
	Quiet_Full	Quiescent	ChC, HO_x & NO_x	Quiescent (H_2O, N_2)			
Flaring	Control	Quiescent	ChC, HO_x & NO_x	Quiescent (H_2O, N_2)	2	2	2
	Flare_UV	Flaring	ChC, HO_x & NO_x	Quiescent (H_2O, N_2)			
	Flare_Full	Flaring	ChC, HO_x & NO_x	Flaring (H_2O, N_2)			
	Mean_Flaring	Mean flaring	ChC, HO_x & NO_x	Quiescent (H_2O, N_2)			

Table 5.1: All simulations performed for this work, with short names, description of the components included, and the time–steps used.

used as the initial state for all simulations involved in the simulation of flares.

To simulate flares and CMEs four simulations were performed, a control simulation without any flares or CMEs (Control), a simulation with flares but without any change in SEPs due to CMEs (Flare_UV), a simulation with flares and CMEs (Flare_Full), and a simulation that has a different stellar spectrum that was created from the temporal average of the time-varying stellar spectra used in the flaring simulation (Mean_flaring). These four simulations allow us to examine the effects of flares separately from the effects of CMEs, as well as examine whether a non-time-varying stellar spectrum (which results in the planet receiving the same amount of energy) is potentially able to adequately describe the impact of stellar flares at a significantly lower computational cost and ease of use.

Due to the increased temporal resolution required to capture the stellar flares, the time–steps for the dynamics, radiative transfer, and the chemistry were shortened to 2 minutes, with the radiative transfer and chemistry being calculated on every time–step instead of every hour. This presents a much larger computational cost, slowing the simulation speed severely. As a result, while the quiescent simulations were simulated for 12000 days, the flaring simulations were run for only a single year (365 Earth days). The simulations and their details are listed in Table 5.1.

Figure 5.1 shows how the flare spectrum changes from quiescent to the peak of a $10^{30.5}$ erg and 10^{34} erg flare, as well as the 'mean flaring' stellar spectrum. The 'mean flaring' spectrum is much weaker than the peak 10^{34} erg flare spectrum, as expected, and is between 0.5–1 orders of magnitude higher than the quiescent spectrum over the flaring templates wavelength range. This tells us that the at-
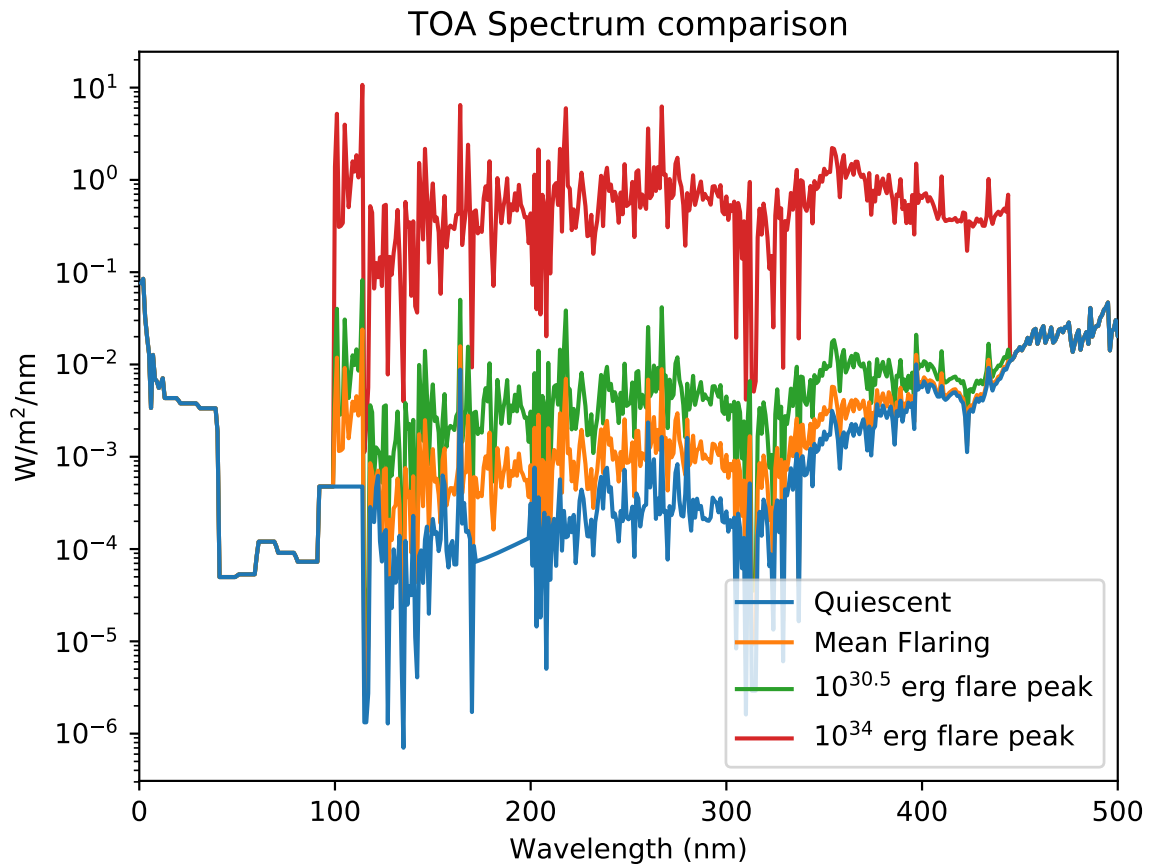
Figure 5.1: The top–of–atmosphere 'mean flaring' stellar spectrum compared to the quiescent stellar spectrum and the spectrum at the peak of a $10^{30.5}$ and 10^{34} erg flare. The 'mean flaring' spectrum was created by calculating the mean spectrum over the year of simulated flares.

mosphere's response to a 'mean flaring' spectrum will diverge from the quiescent spectrum, due to the UV radiation driving higher photolysis rates. Although the planet receives the same total amount of energy over the simulated period from the 'mean flaring' spectrum as the time-varying spectrum with flares, we will see that this does not necessarily capture the changes in dynamics due to the heating and long–term atmospheric composition changes arising from the temporary abundance changes occurring during flares. The impacts of the resolved flares are examined in Section 5.3.

5.1.1 Simulation computation time and resources

Before the results are discussed, it is worth describing the computational resources used to produce the results presented in the preceding chapter and this chapter. The UM simulations were computed on Monsoon, a high-performance computing system hosted by the Met Office (The United Kingdom's national weather service)

using 216 cores per simulation.

For the five quiescent simulations, the varying complexity of the chemical network had a very large impact on the rate of simulation. Quiet_Ch (the smallest chemical network) took approximately 75 minutes per 50 days of simulation, while Quiet_Full (the largest chemical network) took approximately 170 minutes per 50 days of simulation. The combined computational cost of the quiescent simulations is calculated as approximately 458,000 CPU–hours. The longest simulations took approximately 4 weeks to compute.

For the four flaring simulations, I used a much higher temporal resolution for the dynamics, chemistry, and radiative transfer. As the UM currently lacks the ability to include a dynamic time–step, a much smaller time–step had to be used for all times. This resulted in a significant slowdown in the rate of simulation. A single day of simulation took ≈ 75 minutes. The computational cost of the four flaring simulations is calculated as approximately 394,000 CPU–hours, and approximately 3 weeks to compute.

Combining the computational cost of the quiescent and flaring simulations gives a total of approximately 852,000 CPU–hours, and approximately 7 weeks to fully compute.

5.2   Quiescent Simulations with SEPs

In this section we will describe the effects that quiescent SEPs (using the quiescent ion pair production profile described in Section 4.5.2) have on the atmospheric composition. This will help us understand what effects a quiescent stellar wind would have on planets around M dwarfs, and would also be useful to understand planets around inactive M dwarfs that are not prone to stellar activity.

5.2.1 Impact of quiescent SEPs on atmospheric composition

Figure 5.2 shows the evolution of the ozone column (refer to Section 3.3.4 for a description of the term) for all five quiescent simulations. We see that SEPs do not cause a meaningful change in the ozone column when only considering HO_x chemistry. We see that NO_x chemistry is heavily affected by SEPs, reducing the ozone column by over an order of magnitude. The sharp decrease in the ozone column of Quiet_Full at 11,000 days warrants further investigation.
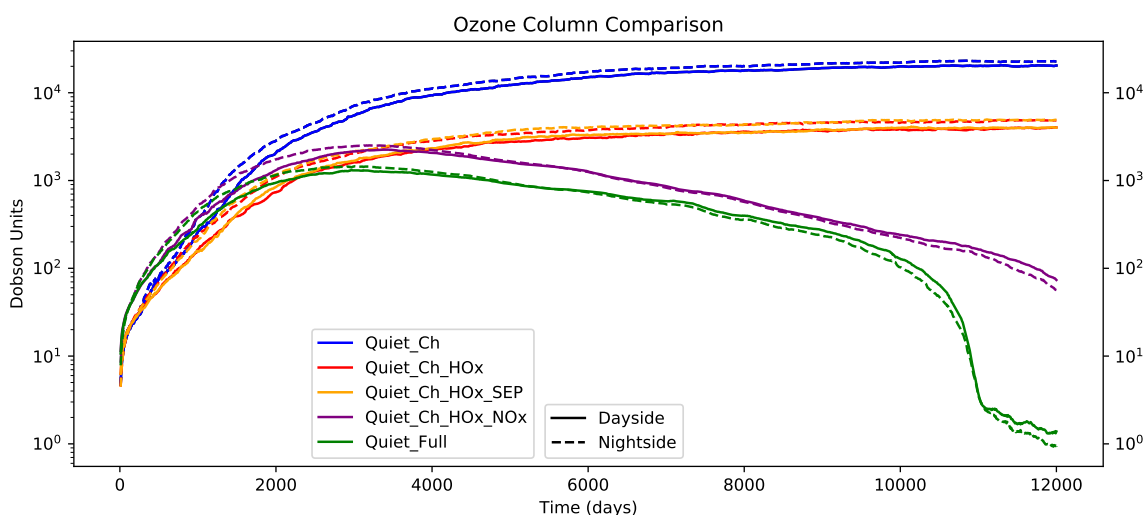
Figure 5.2: The day–side and night–side ozone columns for all five quiescent simulations, with and without SEPs.

Figure 5.3 shows the map of the ozone column for the two HO_x and NO_x simulations, and further illustrates the effects of SEPs on the ozone column. We see that the two HO_x simulations (top panels) are very similar to each other. As seen in Figure 5.2, the ozone column is not particularly affected by SEPs when only considering HO_x chemistry. When including SEPs into the NO_x chemistry in our simulations (Quiet_Ch_HOx_NOx and Quiet_Full), the ozone distribution changes drastically (the bottom panels of Figure 5.3), reducing significantly across the entire planet. Ozone is further depleted, reducing the global average ozone column from $\sim 60\,DU$ to $\sim 1\,DU$. Ozone is further depleted in the polar regions, and the night–side gyres (cold traps at high latitudes).

Figure 5.4 shows the averaged day–side and night–side vertical profiles of the ozone mole fraction for all five quiescent simulations. Once again, we see that Quiet_Ch_HOx and Quiet_Ch_HOx_SEP are effectively the same. The difference
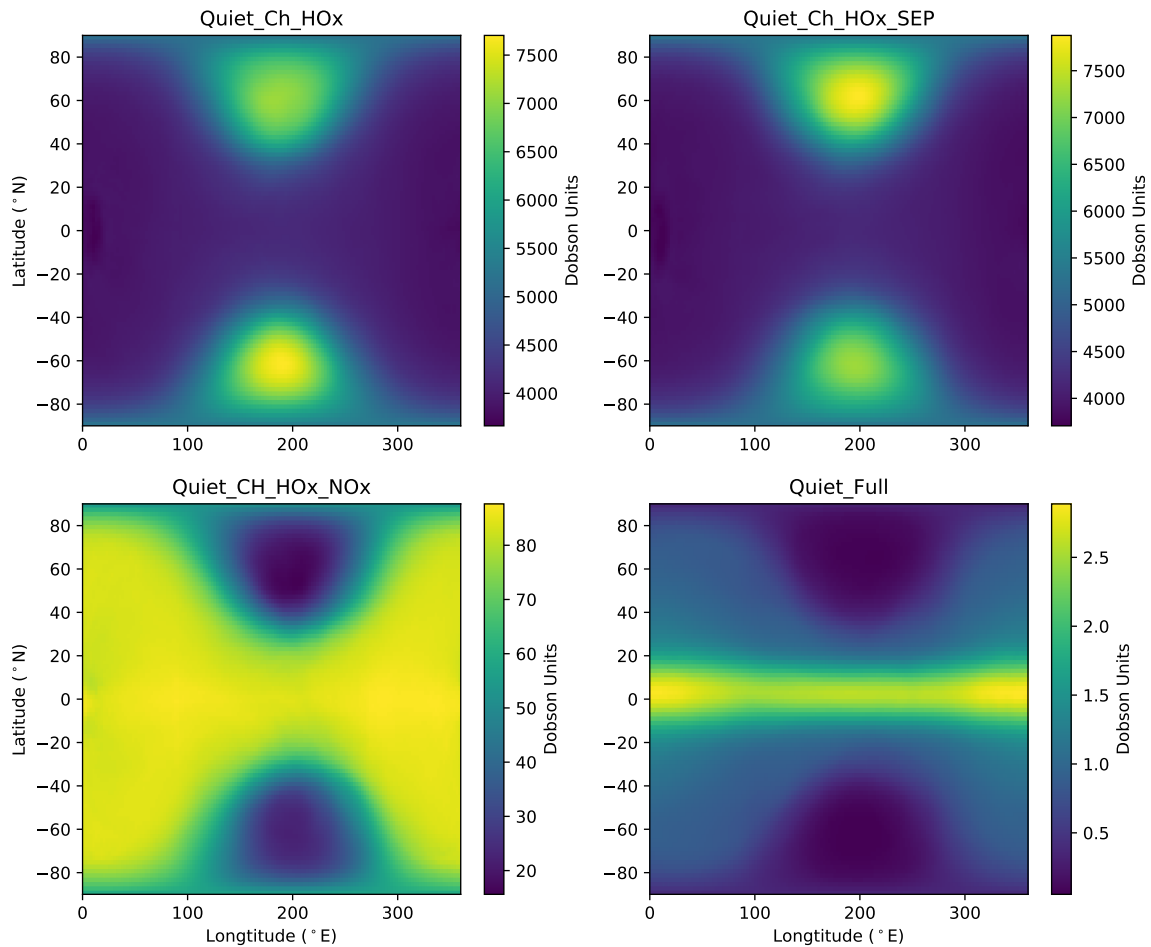
Figure 5.3: The spatial distribution of the ozone column in Dobson units, temporally averaged over the period of 11800–12000 days for the Quiet_Ch_HOx (top left), Quiet_Ch_HOx_SEP (top right), Quiet_Ch_HOx_NOx (bottom left) and Quiet_Full (bottom right) simulations from the quiescent phase. See Table 5.1 for explanation of the simulation names. The ozone distribution is significantly reduced by the addition of NO_x chemistry, and is further depleted by the inclusion of SEPs.

in ozone mole fraction between the two NO_x simulations is apparent below 50 km, but only significantly diverges below 30 km. The inclusion of SEPs has heavily depleted the lower stratosphere and the troposphere. The tropospheric abundance has been reduced from ~ 100 ppb to less than 1 ppb.
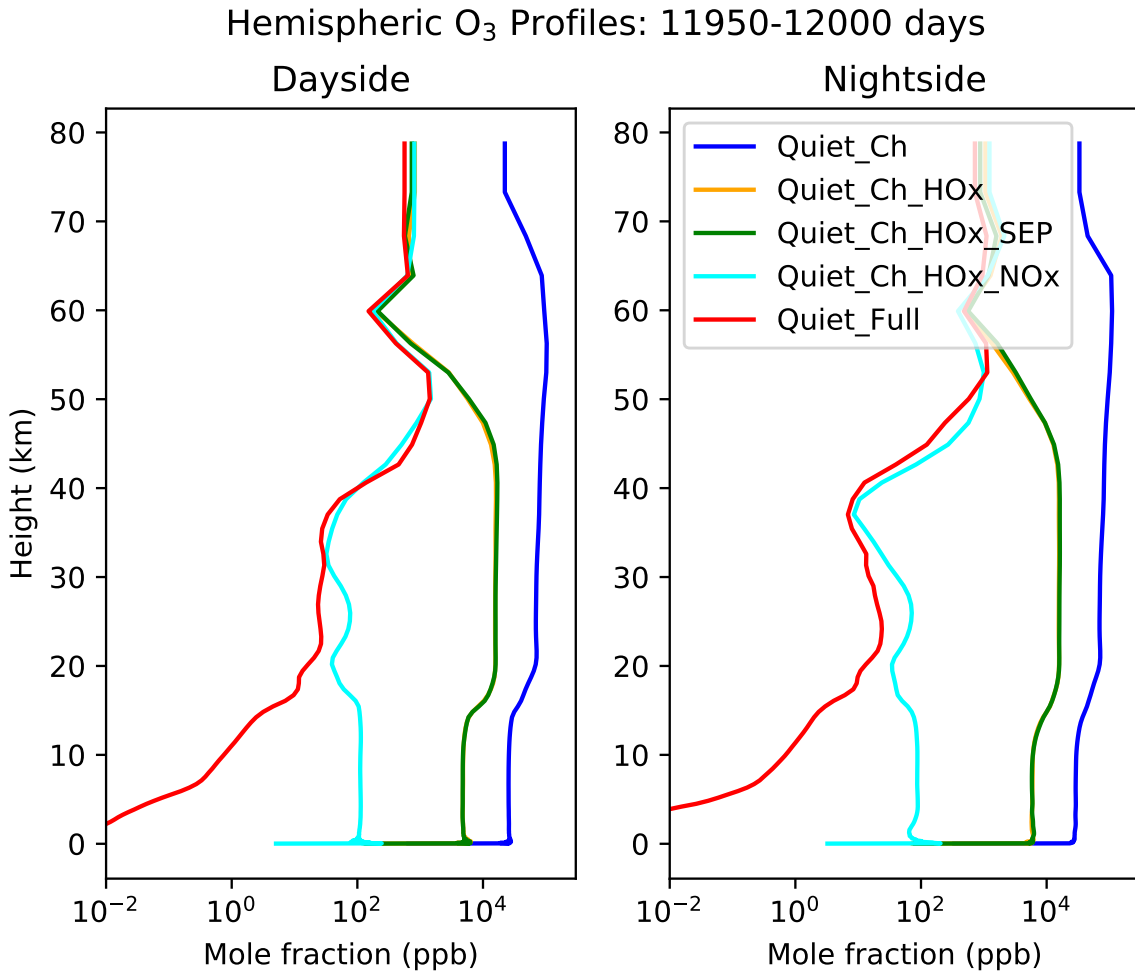
Figure 5.4: The spatially averaged vertical profile of the ozone mole fractions from the planets day–side and night–side for the five chemical networks under quiescent condition. Refer to Table 5.1 for the details of the different networks.

Figure 5.5 shows the day–side chemical lifetime (without including deposition) of ozone from the five quiescent simulations. Once again, we see that Quiet_Ch_HOx and Quiet_Ch_HOx_SEP have effectively the same chemical lifetime. The effects of SEP inclusion on NO_x chemistry are visible below 50 km, where the chemical lifetime of ozone is reduced. The tropospheric lifetime has been reduced from 5×10^4–10^5 seconds in Quiet_Ch_HOx_NOx to 3×10^4–8×10^2 seconds in Quiet_Full. The reduced chemical lifetime tells us that ozone in the lower stratosphere and troposphere is created and destroyed several times during a trip across the day–side. This has important implications for the effects of stellar flares, as will be
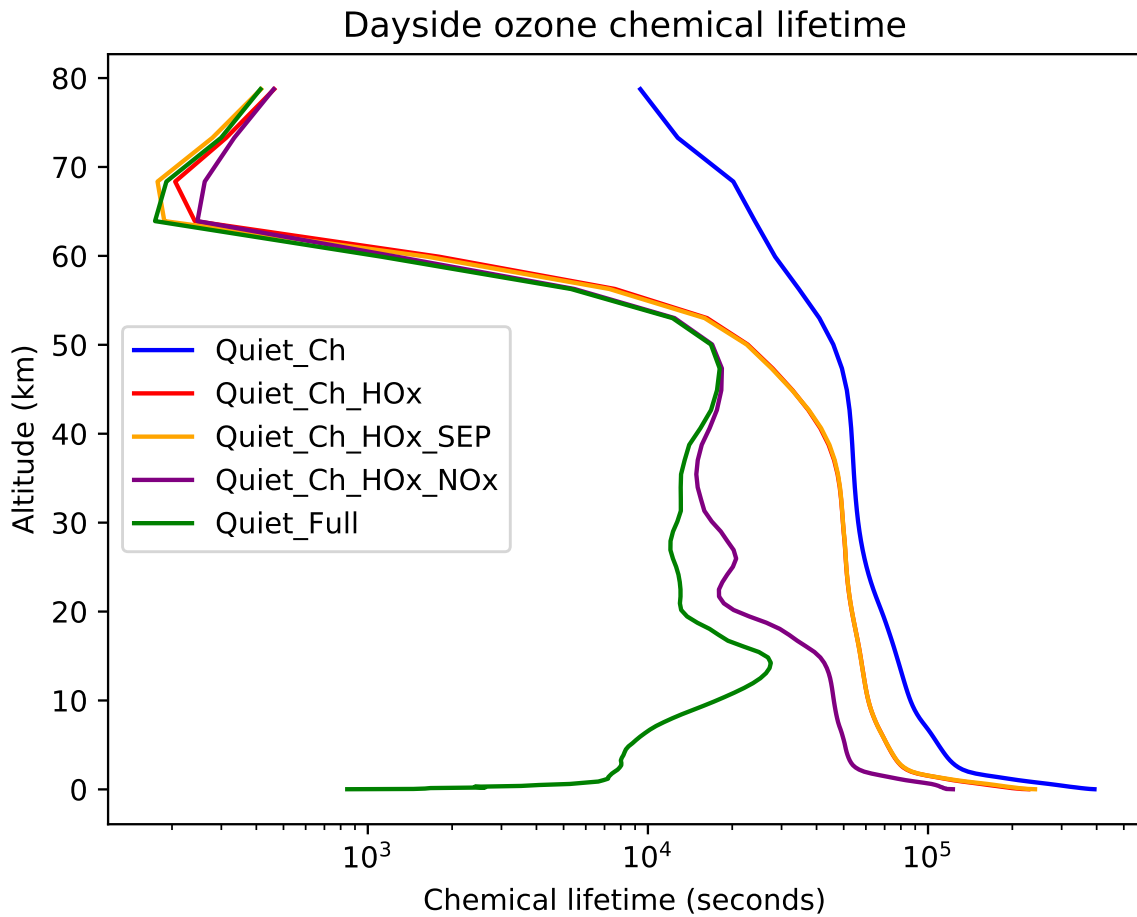
Figure 5.5: The day–side chemical life time (not including deposition) of ozone from the five quiescent simulations.

described in Section 5.3.

The reasons why SEPs have a limited effect for HO_x chemistry and a large effect for NO_x chemistry can be explained by looking at the reaction rates of HO_x and NO_x sources and how they compare to the SEP reactions. The contribution of quiescent SEPs to HO_x chemistry can be examined by comparing the reaction rates of

$$H_2O + p^+/e^- \longrightarrow H + OH,$$

$$O(^1D) + H_2O \longrightarrow OH + OH,$$

$$H_2O + h\nu \longrightarrow H + OH,$$
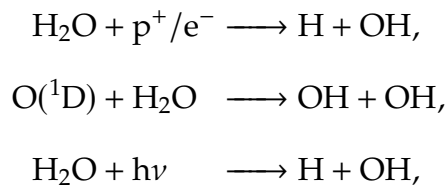
to compare the rates of how H_2O is converted into HO_x molecules between SEPs, the initial reaction of the HO_x cycle, and water photolysis. Figure 5.6 shows the reaction rates of the aforementioned reactions averaged over the day-side, using the atmospheric composition and temperature of Quiet_Full, averaged over the
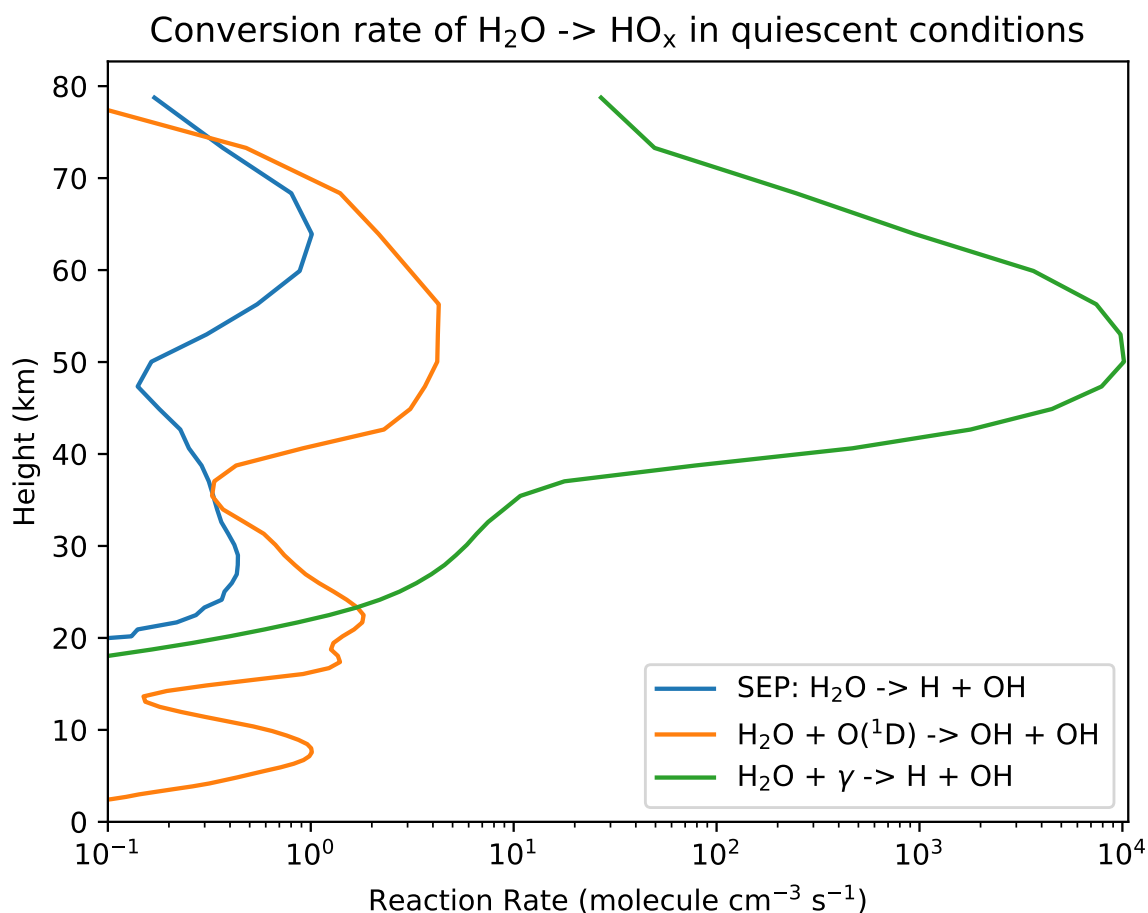
Figure 5.6: A comparison of the rate of H_2O conversion into H and OH by SEPs, photolysis, and through a reaction with $O(^1D)$.

last 50 days of the simulation. We see that the SEP reaction is much weaker than $H_2O + h\nu \longrightarrow H + OH$ at all altitudes, and only exceeds $O(^1D) + H_2O \longrightarrow OH + OH$ at high altitudes.

This only provides a small additional contribution to the amount of HO_x in the atmosphere, and causes a limited effect on the amount of ozone. This is further illustrated by Figure 5.7, which shows the day–side reaction rates of the HO_x cycle from Quiet_Ch_HOx (solid) and Quiet_Ch_HOx_SEP (dashed), which shows that the inclusion of SEPs does indeed barely change the reaction rates of any of the reactions which impact ozone concentrations.

Explaining the impact of quiescent SEPs on the NO_x chemistry is a little more complicated as the generation mechanisms for NO_x are different with and without SEPs (atomic nitrogen reacting with O_2 instead of reactions between N_2 and $O(^1D)$ with N_2O acting as an intermediary), but we can compare the generation rate of
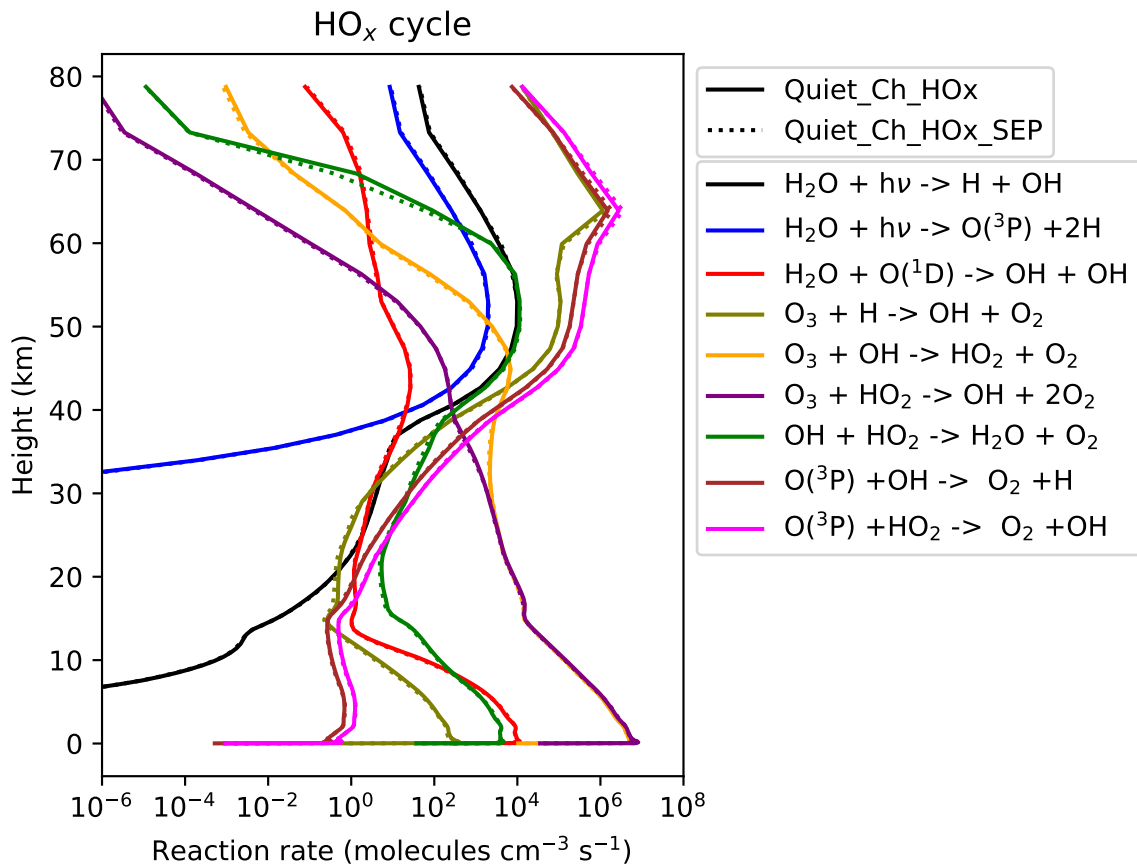
Figure 5.7: A comparison of the day–side reaction rates for HO_x chemistry with and without the effects of SEPs.

NO between the two sources, and see how that impacts ozone concentrations. The impact of SEPs on NO_x generation can be examined in two ways; by comparing the NO generation rates for the following reactions

$$O(^1D) + N_2O \longrightarrow NO + NO,$$

$$N(^4S) + O_2 \longrightarrow NO + O(^3P),$$

$$N(^4S) + NO \longrightarrow N_2 + O(^3P)$$

$$N(^2D) + O_2 \longrightarrow NO + O(^3P),$$

$$N(^2D) + N_2O \longrightarrow NO + N_2.$$
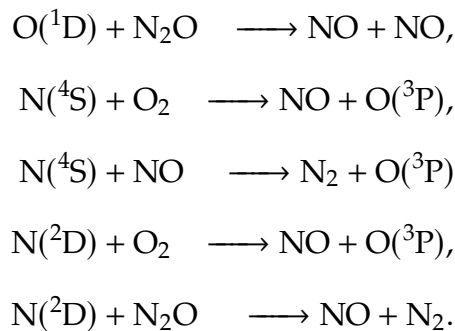
As well, the net NO production due to SEPs is also shown. This allows us to compare the two sources, as well as how $N(^4S)$ and $N(^2D)$ contribute to NO production. Figure 5.8 compares the production rate of NO for each reaction, using the same atmospheric composition/configuration as Figure 5.6 from the last 50 days of Quiet_Full, as well as comparing the rate of $O(^1D) + N_2O \longrightarrow NO + NO$

between the Quiet_Ch_HOx_NOx and Quiet_Full simulations. We see that the net production of NO due to SEPs is much larger than $O(^1D) + N_2O \longrightarrow NO + NO$ above 17 km. The quiescent SEPs create significantly more NO above 20 km. We can see that $N(^4S)$ is a very efficient destructor of NO, showing us that most of the NO generated by the $N(^2D)$ created due to SEPs is destroyed by the $N(^4S)$ created by SEPs, except at lower altitudes, where the destruction of NO due to $N(^4S)$ begins to decrease. We also see that the rate of $O(^1D) + N_2O \longrightarrow NO + NO$ for the Quiet_Ch_HOx_NOx simulation does not fall off as sharply in the troposphere, but is lower than the rate for the Quiet_Full simulation above 15 km. We attribute this to $N(^4S) + NO_2 \longrightarrow N_2O + O(^3P)$ providing an additional source of N_2O above 15 km and increasing the reaction rate. The sharp decrease in the rate for the Quiet_Full simulation is due to the lack of atomic nitrogen limiting $N(^4S) + NO_2 \longrightarrow N_2O + O(^3P)$, as well as a lack of $O(^1D)$ which is primarily derived from O_3 photolysis. The Quiet_Ch_HOx_NOx simulation has more ozone in the troposphere, and has a higher rate of ozone photolysis which provides more $O(^1D)$. This is especially important as the source of N_2O in the Quiet_Ch_HOx_NOx simulation is $O(^1D) + N_2 + M \longrightarrow N_2O + M$, so an increase in ozone photolysis will increase the amount of both of the reactants of $O(^1D) + N_2O \longrightarrow NO + NO$.

We can then look at how this impacts ozone by looking at how ozone destruction has changed as well as how the abundances of NO_x species have changed. This is shown in Figure 5.9 which shows a comparison of the day–side reaction rates of the NO_x cycle, and Figure 5.10, which compares the number densities of the chemical species involved in the reactions shown in Figure 5.9. We see a large increase in the rate of $NO + O_3 \longrightarrow NO_2 + O_2$ which is now much stronger, especially considering that the reduction in the amount of ozone directly impacts the reaction rate (as it depends on $[NO][O_3]$. Correspondingly, we see a large increase in the amounts of NO and NO_2 below 20 km.
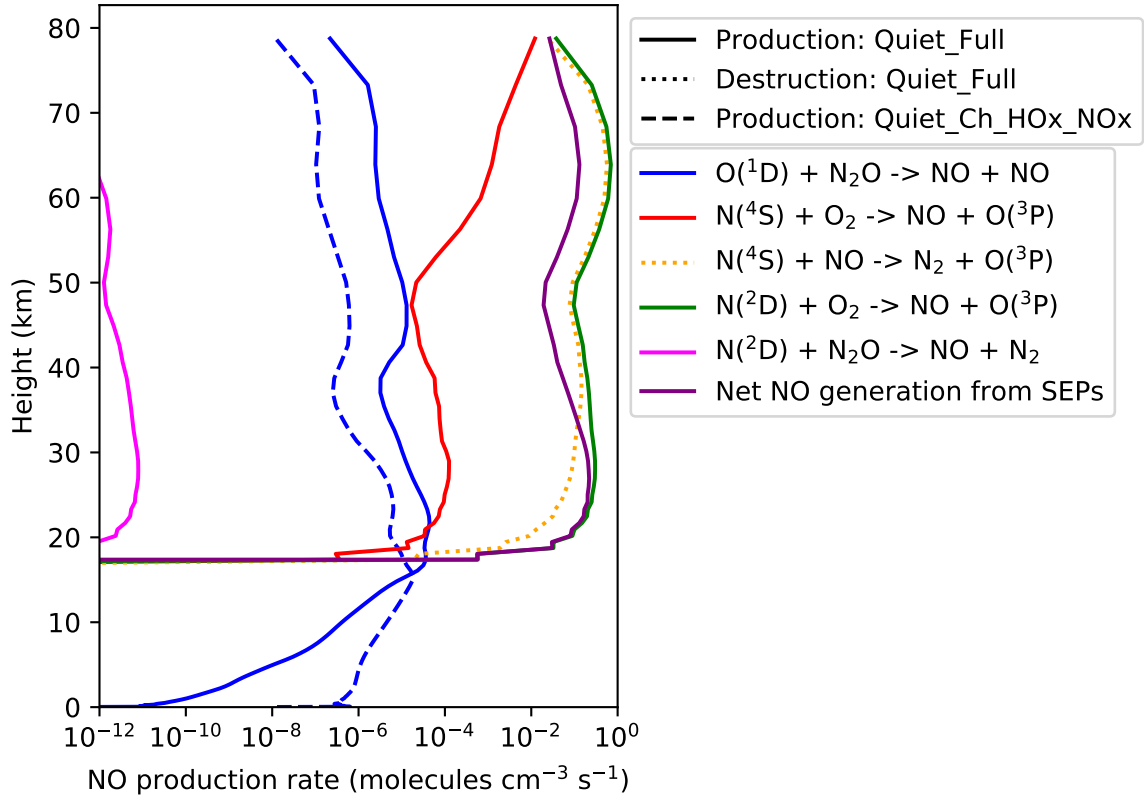
Figure 5.8: The reactions controlling the production and destruction of new NO in quiescent conditions in the Quiet_Ch_HOx_NOx and Quiet_Full simulations.
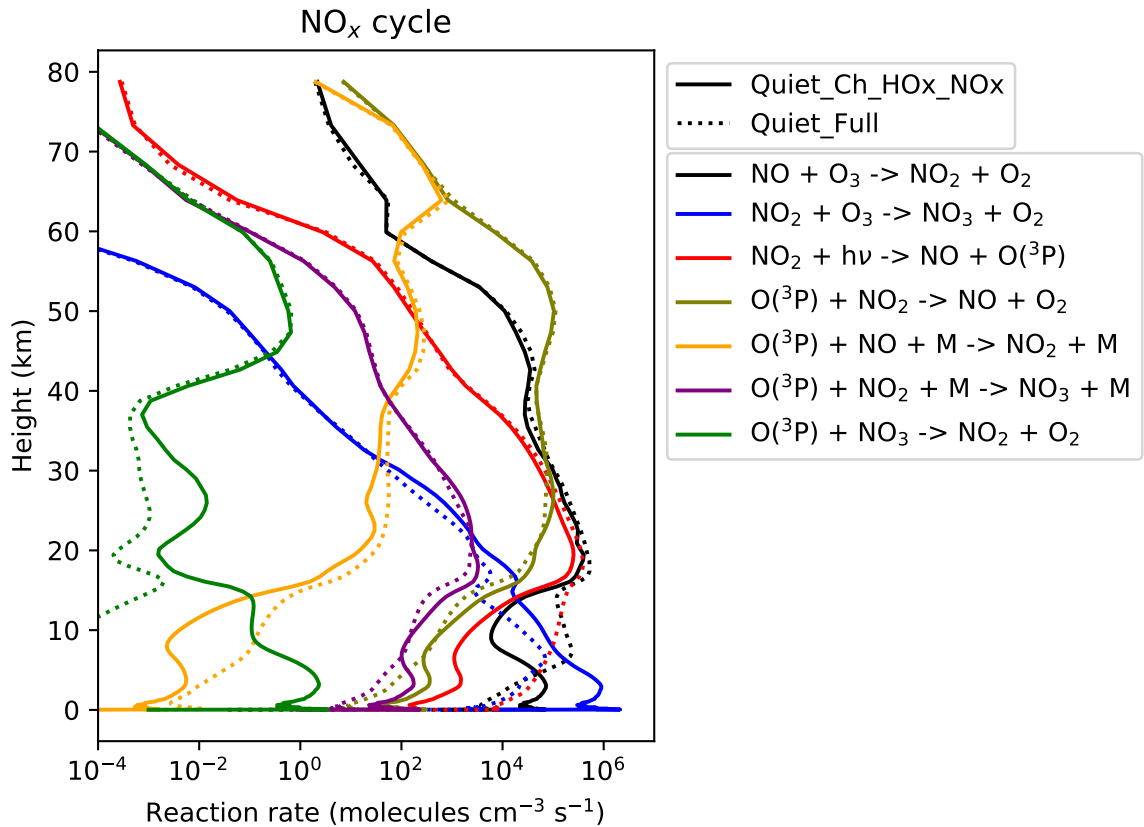
Figure 5.9: A comparison of the day–side reaction rates for NO_x chemistry with and without the effects of SEPs.

Chemical species relevant to ozone chemistry
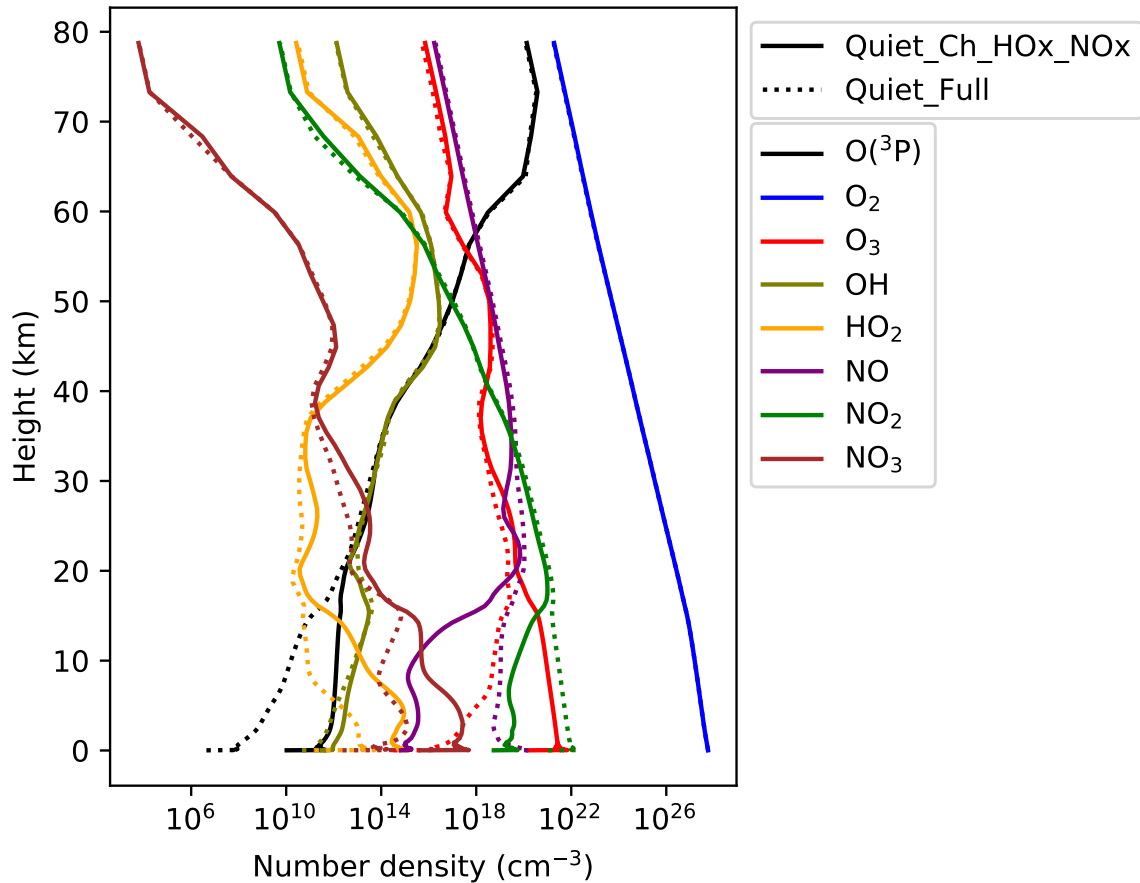
Figure 5.10: A comparison of the day–side number densities for several species involved in NO_x chemistry with and without the effects of SEPs.

The Chapman cycle and HO_x cycle reactions are relatively straightforward. The ozone loss reactions are all much weaker at low altitudes in the Quiet_Full simulation compared to the Quiet_Ch_HOx_NOx simulation, once again reflecting the lack of ozone at lower altitudes. Now that we have explored all of the quiescent simulations, we have an understanding of how the chemical networks behave for this planet, as well as how quiescent SEPs contribute to the atmospheric composition. We can proceed to simulating the impact of flares and CMEs.

5.3 Flaring

The main focus of this work is to explore the impact of a flaring M dwarf star on the climate of an 'Earth-like' terrestrial, tidally–locked, exoplanet. Therefore, in this section we focus on our three simulations including flares, namely Flare_UV (full chemistry but omitting CMEs), Flare_Full (full chemistry and CMEs) and
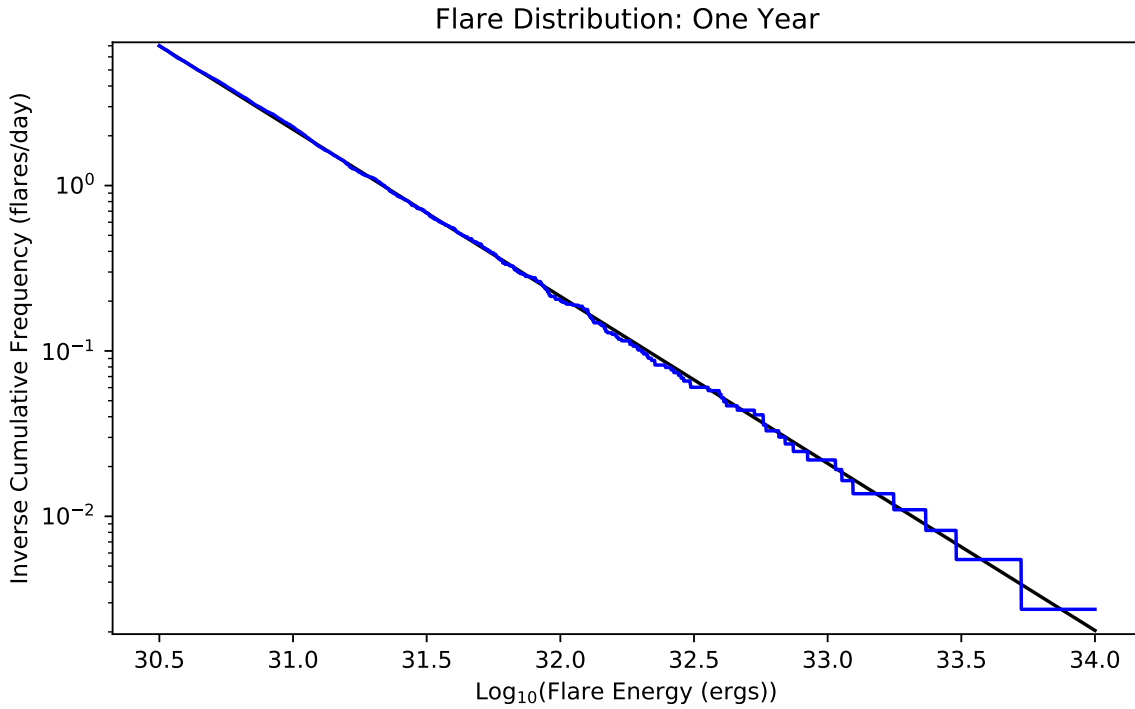
Figure 5.11: The inverse–cumulative–frequency (in flares/day) of flare energy from a one year sample (blue line) as compared to the analytic distribution (black line).

Mean_flaring (full chemistry, a constant mean flaring spectrum and quiescent levels of SEPs), using our Control (full chemistry but quiescent spectrum and SEP profile) as a reference.

5.3.1 Flare and CME generation

Using the Inverse Transform Sampling technique discussed in Section 4.4.1, a sample of flares and CMEs were generated for the period of a single year of simulation. However, the sample of flares from a period of a single year could have significant inter–annual variability, and differ considerably from the analytic distribution. Therefore, samples of flares from a one year period were generated $\approx 10^6$ times and the sample which best matched the distribution was used in this work (i.e. the sample of flares with the minimum l^2-norm when comparing the occurrence-flare energy distribution from the sample to the analytic distribution) shown in Figure 5.11. We note that the choice was made to force the one year samples to include a 10^{34} erg flare with an associated CME that occurs 60 days into the simulation. This was done in order to observe the impacts of a maximum strength flare and CME, the results of which are discussed in the following section.

5.3.2   Results

We can begin with the changes in ozone that have happened due to flares. Figure 5.12 shows the day–side (solid) and night–side (dashed) mean ozone columns during the flaring section of the simulation for the four cases, as well as CME onset times. We find that the impact of the stellar flare irradiation we have constructed is to increase the global averaged total column of ozone in the atmosphere from $\approx 1\,\mathrm{DU}$ (at the end of Quiet_Full) to $\approx 15-20\,\mathrm{DU}$ (the range of values over the last 50 days of the simulations with flares), as the day–side and night–side columns have similar values. During a flare the UV increases substantially and increases O_2 photolysis generating additional atomic oxygen. The increase in atomic oxygen drives the growth of ozone via $O_2 + O(^3P) + M \longrightarrow O_3 + M$. The destruction of ozone by photolysis or through additional HO_x and NO_x increases during a flare as well, but does not increase enough to offset the significant growth of ozone. The net effect of the flare causes the amount of ozone on the day–side to increase rapidly (the largest flares capable of creating an ozone column of >75 DU), and slowly decrease once the flare has ended. This is due to ozone on the day–side being destroyed or being transported onto the night–side. The enhancement of night–side ozone is due to the advection of ozone from the day–side. The difference in the peak day–side ozone column and peak night–side ozone column (with the flare and CME on day 60 being a good example, where the day–side ozone column peaked at 75-80 DU, while the night–side column peaked at 40 DU) demonstrates that a large fraction of ozone created during a flare is destroyed quickly, before it can be transported to the night–side. Both the Flare_UV and Flare_Full simulations exhibit very similar behaviour. The average ozone column is quite insensitive to the inclusion of CMEs, only reducing the average ozone column by a small amount. This is attributed to a lack of additional HO_x and NO_x created via Reactions R84-R86. Both of the quiescent and CME ion pair production rate profiles used in this work (see Figure 4.7) rapidly decline below 35 km (which has a pressure on the day–side of $\sim 100\,\mathrm{Pa}$), and are reduced to 0 below 15 km ($\sim 7000\,\mathrm{Pa}$). As the ionisation rate declines, the SEPs are less important
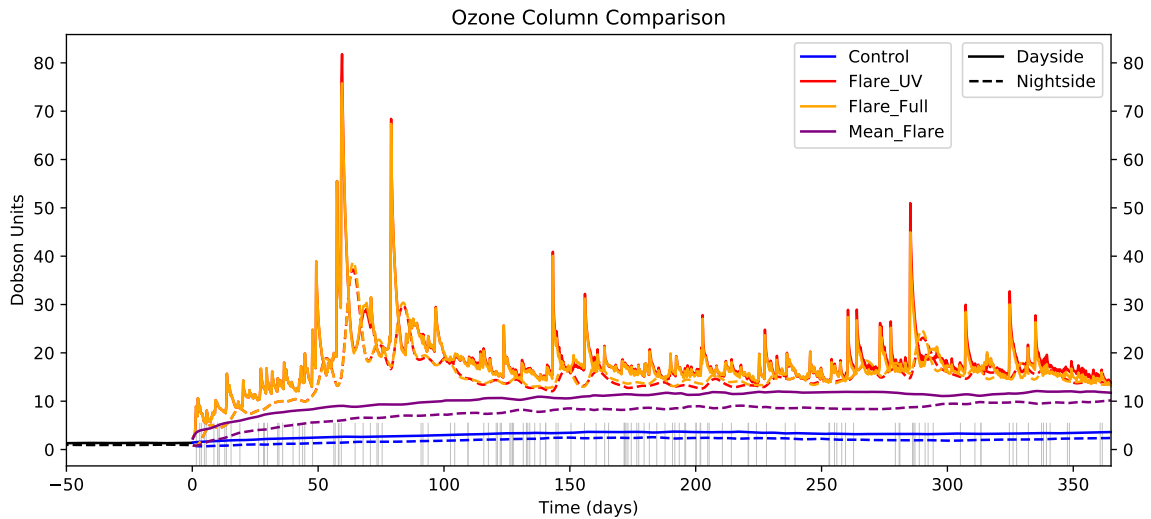
Figure 5.12: The hemispherically averaged mean ozone column of the day–side and night–side from the flaring simulations used in this work as described in Table 5.1. CME onset times have been marked in gray.

and generate less HO_x and NO_x, which results in ozone below 35 km not being heavily affected by CMEs, and only being strongly affected by the increased UV from the flare. Figure 5.12 demonstrates that the ozone column is perturbed from a non-flaring state, and that the inclusion of CMEs does not produce a significant change in the global amount of ozone. A 10^{34} erg flare with an accompanied CME occurred on day 60 of the simulation, and during the peak of this flare the global mean ozone column increased from 20 DU to 45 DU. To view an animation of the evolution of the ozone column for the first 30 days of the simulations, please view Supplementary Figure 1 (external link), which is available online at the Open Research Exeter Repository (ORE) entry for this thesis, or here.

These results differ significantly from the results reported by Chen et al. (2021) and Tilley et al. (2019), which see a reduction in the ozone column due to flares and CMEs. This is the opposite result to this work, and should be explained. I believe this can be attributed to several factors, particularly to how SEPs and CMEs are included in their work. Chen et al. (2021) includes SEPs which are scaled by flare strength similarly to my work, but they apply the scaled SEPs as daily averages. This is in contrast to this work which applies the scaled SEPs during the flare. This will increase the effect of CMEs substantially in their work. As well, they do not incorporate CME impact probability, so every CME impacts the planet. In

Section 4.6.1 I found that the impact probability of a CME for the simulated planet was 6%. By not taking this into account, this will exaggerate the impact of CMEs compared to this work which will translate to a stronger impact of SEP reactions, and a negative impact on the amount of ozone.

It does not appear that Tilley et al. (2019) incorporates quiescent SEPs into their chemistry calculations. As seen in the differences between Quiet_Ch_HOx_NOx and Quiet_Full, the inclusion of quiescent SEPs can cause a large reduction in the amount of ozone. The impact of CMEs would be much stronger on a planet which has more ozone, and this might explain the trends observed by Tilley et al. (2019).

I would suggest that this merits some future work in the form of a review and comparison of all inputs and techniques used in these works to determine what methodology or model differences have resulted in the observed difference. This would be a good companion to the review I propose in Section 3.3.9.

We can analyse the changes in chemical reactions and abundances to inform us about how flares have impacted this work. We can look at how the Chapman cycle, HO_x chemistry, and NO_x chemistry change during flares. To do this, we will be using data taken during the 10^{34} erg flare that occurred on day 60 of the flaring simulation. The CME (of maximum strength) from this flare impacted the planet, so we can compare how the changes to SEPs change the chemistry, despite having only a limited long-term impact on the ozone column. The results shown in the following figures will be broadly applicable to every flare and CME which occurred during the simulation. We can begin with showing changes in chemical abundances.

Figure 5.13 shows the number densities of chemical species directly relevant to ozone chemistry under the initial quiescent conditions, and during the 10^{34} erg flare. We see that the amount of $O(^3P)$ is heavily increased during the flare, driven by higher O_2 and ozone photolysis rates. The amount of ozone has increased below 55 km from the quiescent values, which is consistent with the increase of the

Chemical species relevant to ozone chemistry
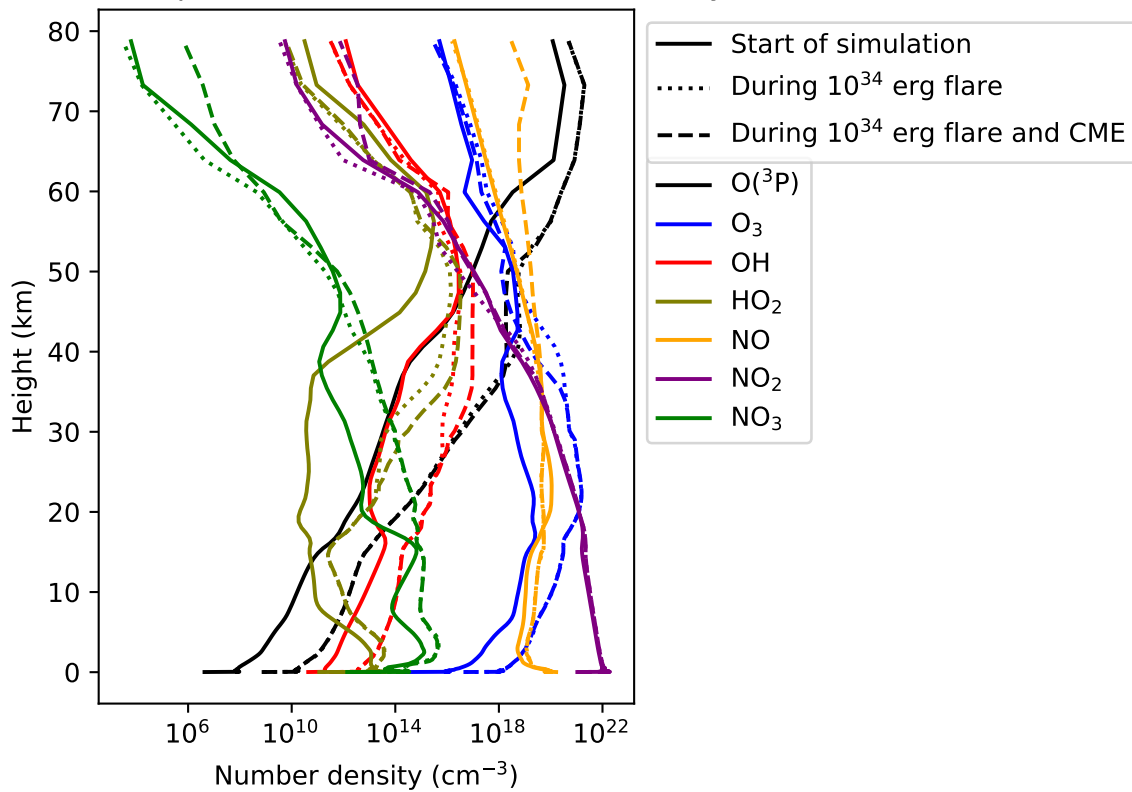
Figure 5.13: Day–side number density profiles of several chemical species connected to ozone chemistry.

ozone column seen in Figure 5.12. We see that between 35–50 km the ozone number density in the Flare_Full simulation is lower than the data from the Flare_UV simulation, showing the effect of the increased amount of SEPs. The amounts of OH and HO_2 have increased due to flares, with CMEs causing them to further increase between 20–50 km. We do not see an appreciable change in the amount of NO_2, but we do see a change in NO. Below 40 km we do not see a large impact due to CMEs on the amount of NO, as both the Flare_UV and Flare_Full simulations show similar profiles. Above 40 km we see that CMEs have heavily increased the amount of NO, whereas flares have not significantly affected NO. NO_3 remains a minor constituent, and is increased by flares. Once again, we see that CMEs only have a significant impact above 40 km.

We can examine the three main portions of the chemical network to see how they have evolved. Figure 5.14 shows the changes in the Chapman cycle reactions during the 10^{34} erg flare. We see a large increase in O_2 and ozone photolysis of at least several orders of magnitude. The increased availability of atomic oxygen has
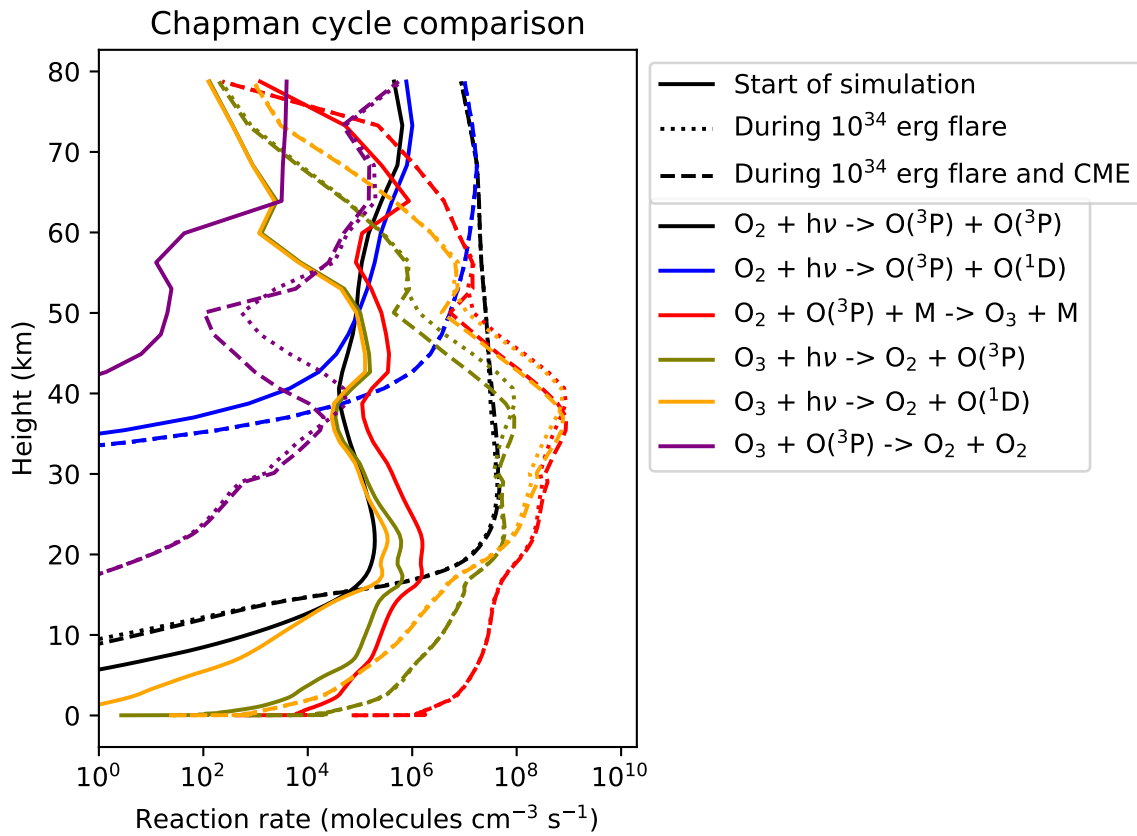
Figure 5.14: Reactions rates of the Chapman cycle during a flare and quiescent conditions.

resulted in an increase in ozone formation.

The changes in HO_x chemistry are shown in Figure 5.15. We see an overall increase in the reaction rates, with only limited differences caused by the CME. The HO_x cycle termination reaction $OH + HO_2 \longrightarrow H_2O + O_2$ now exceeds $OH + O_3 \longrightarrow HO_2 + O_2$ and $HO_2 + O_3 \longrightarrow OH + O_2 + O_2$ between 30–65 km, whereas during quiescent conditions this was only true from 45–70 km. We see that HO_x is more likely to be used to destroy itself than directly destroy ozone. The conversion of atomic oxygen into molecular oxygen, $O(^3P) + OH \longrightarrow O_2 + H$ and $O(^3P) + HO_2 \longrightarrow O_2 + OH$ is now much stronger, with these reaction rates being the largest reaction rates above 25 km. These reactions do not directly destroy ozone, but instead destroy one of the reactants which form ozone. The rates of ozone loss are much lower than the rates of $O_2 + O(^3P) + M \longrightarrow O_3 + M$ seen in Figure 5.14, so these reactions remain a relatively minor loss process for ozone for most altitudes.

The contribution of SEPs to HO_x generation is shown in Figure 5.16, which compares the SEP reaction to water photolysis and $H_2O + O(^1D) \longrightarrow OH + OH$.
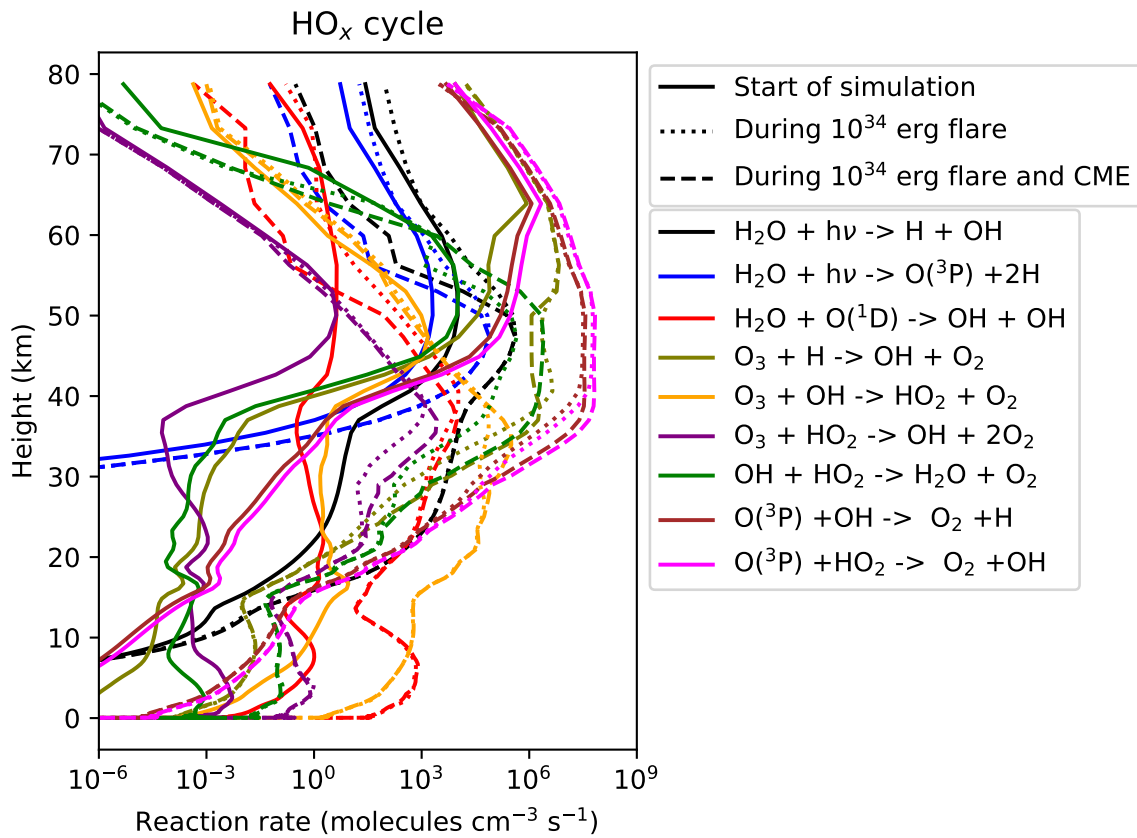
Figure 5.15: Reactions rates of HO_x chemistry during a flare and quiescent conditions.

During the CME, we can see that the SEP reaction is now the dominant source of HO_x, except at low altitudes, where $H_2O + O(^1D) \longrightarrow OH + OH$ remains the larger source of HO_x instead of water photolysis. The other two reactions show interesting behaviour, where below 49 km both flaring simulations are similar, but at high altitudes the Flare_Full simulation has lower rates than the Flare_UV simulation, and even has lower rates than the quiescent conditions at the start of the simulation. The decrease in the rates, especially the water photolysis rates, suggest that the SEPs have heavily depleted the amount of water at high altitudes.

The changes to NO_x chemistry are seen in Figure 5.17. We see that $NO + O_3 \longrightarrow NO_2 + O_2$ remains a major loss process for ozone, with NO–NO_2 cycling being quite rapid, and comparable to the ozone production rate seen previously in Figure 5.14. Once again, we see that the strengthening of the SEP reactions due to CMEs do not have a significant impact on reaction rates below 30 km.

Figure 5.18 compares all NO_x generation sources during the 10^{34} erg flare. We see
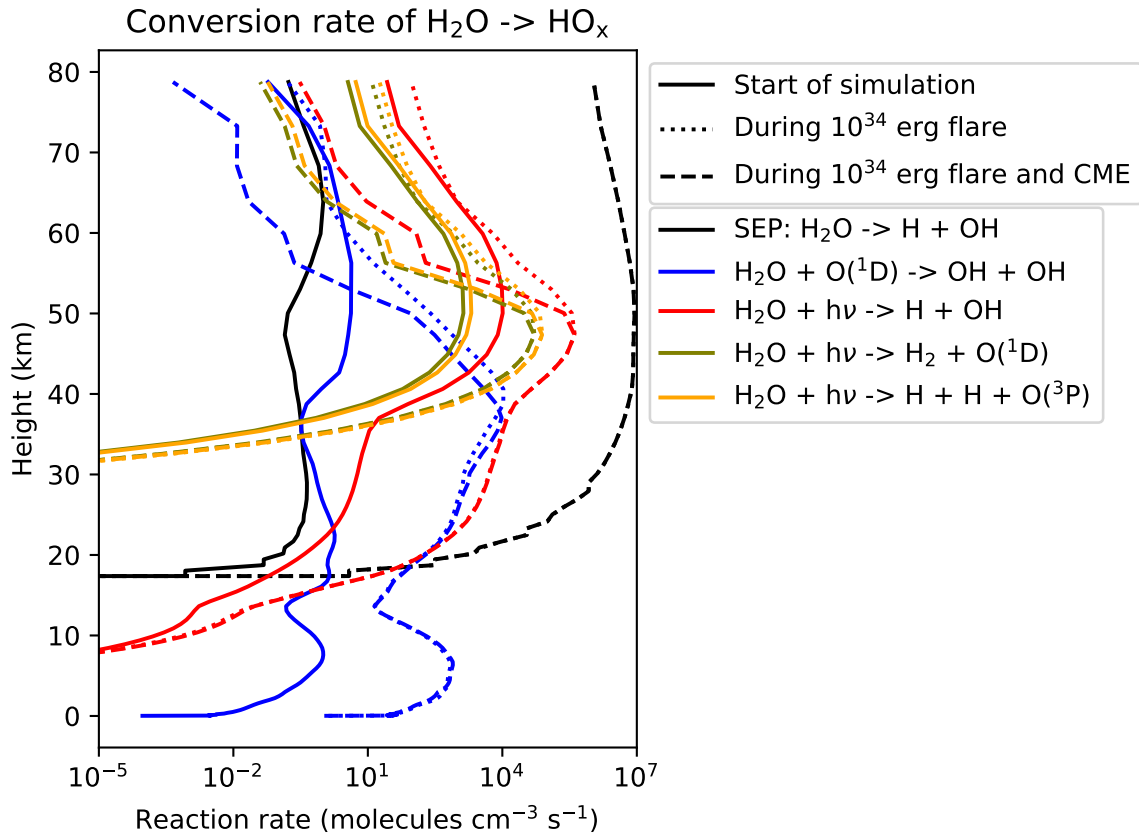
Figure 5.16: A comparison of the sources of new HO_x during the 10^{34} erg flare.
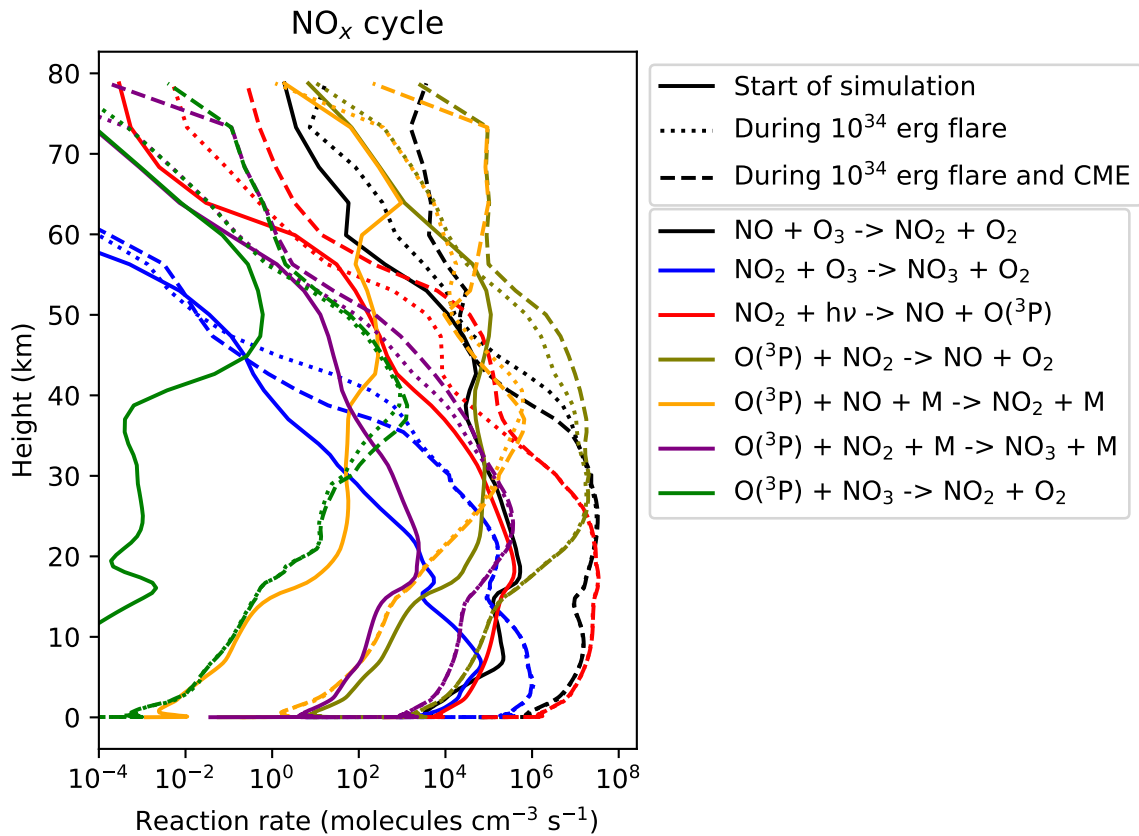
Figure 5.17: Reactions rates of NO_x chemistry during a flare and quiescent conditions.
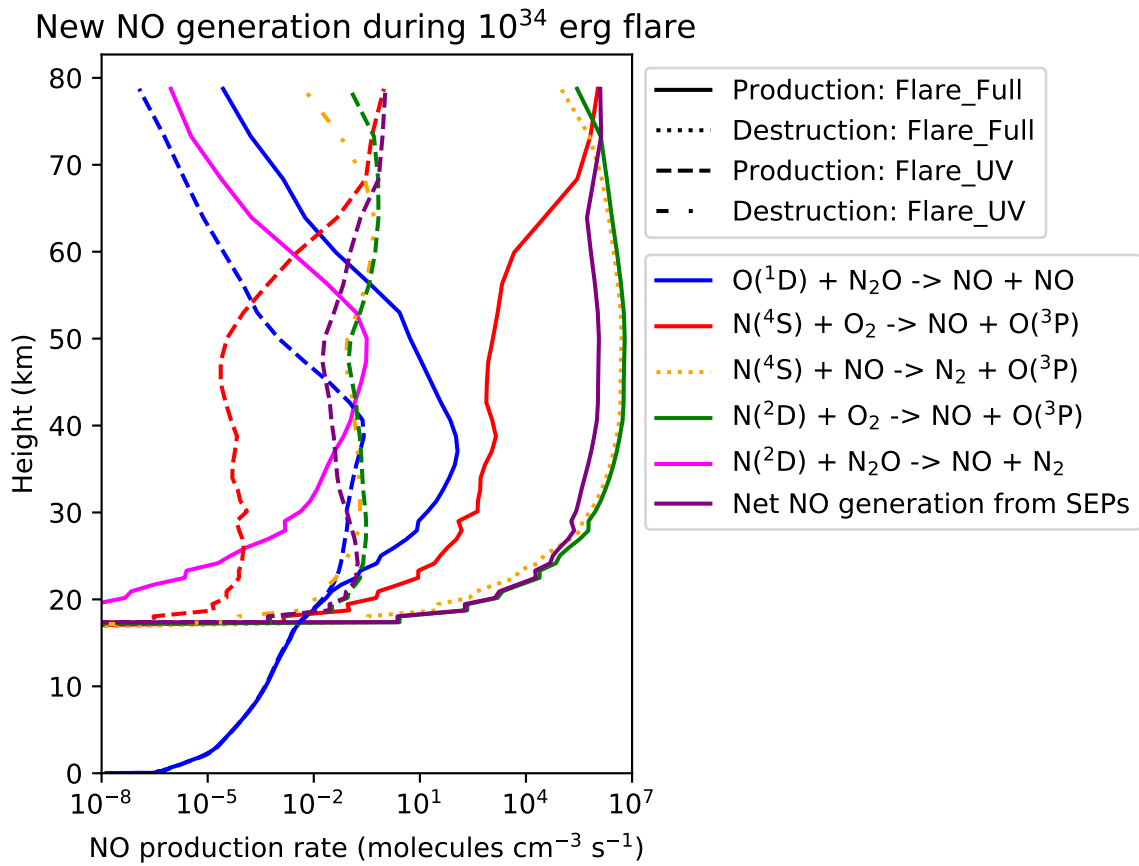
Figure 5.18: A comparison of the sources of new NO during the 10^{34} erg flare.

that for the Flare_UV simulation, at 40 km $O(^1D) + N_2O \longrightarrow NO + NO$ is comparable to the quiescent SEPs induced reactions, which themselves remain unchanged from the rates shown in Figure 5.8. The SEP induced reactions have been increased by approximately 6 orders of magnitude above the quiescent values. We see that despite SEPs significantly increasing the amount of NO generation, this does not translate to a significant impact on ozone concentrations over the long term, as this does not translate to a significant difference in the ozone column between the Flare_UV and Flare_Full simulations.

Figure 5.19 shows the spatially averaged day–side and night–side mole fractions of ozone as a function of altitude for the Control, Flare_UV and Flare_Full simulations, temporally averaged over the last 50 days of the simulation. The impact of the flares, and also the SEPs is clear. An ozone layer between 20-25 km (hereafter referred to as the lower ozone layer) has developed. This is also present in the quiescent simulation but is much smaller. The ozone layer between 45-55 km (hereafter referred to as the upper ozone layer) from the Flare_Full simulation has
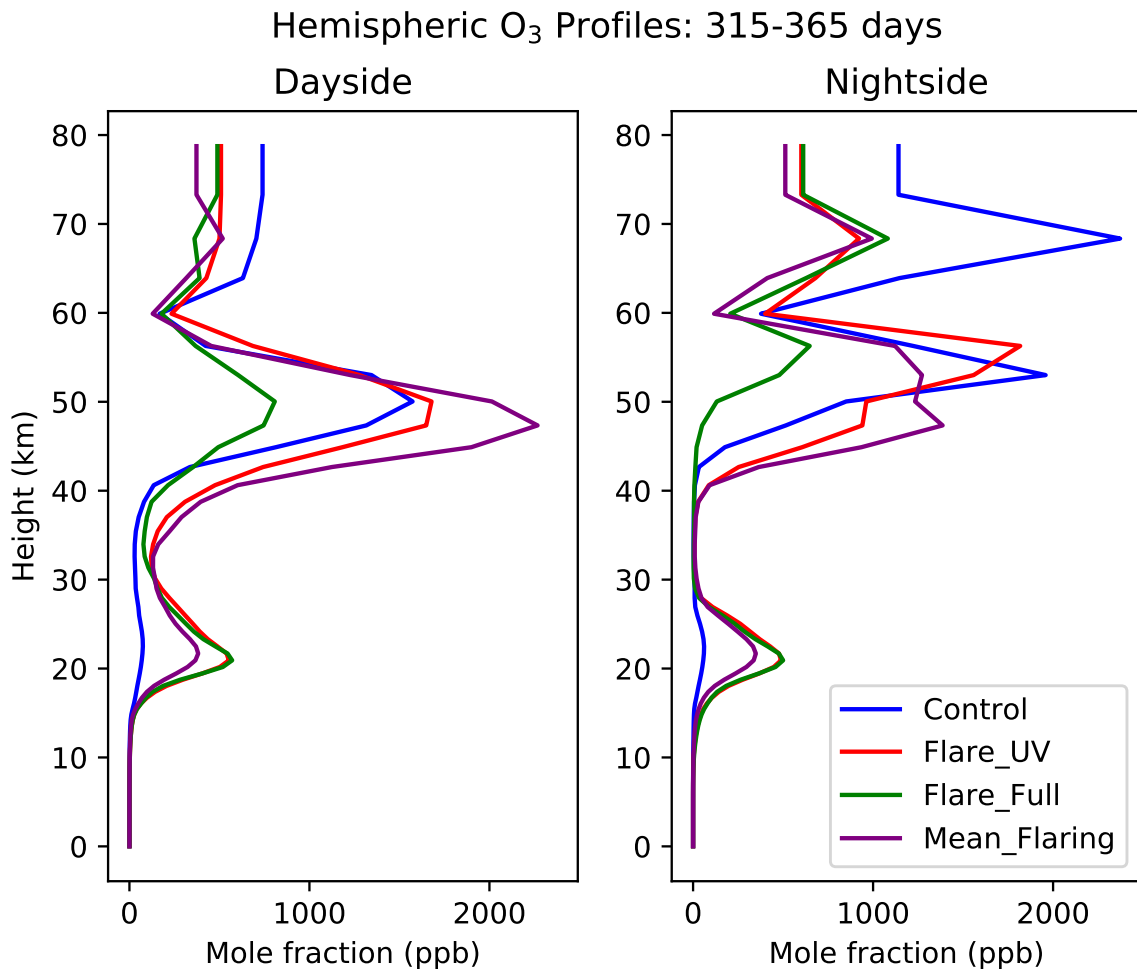
Figure 5.19: The spatially averaged vertical profile of the ozone mole fractions from the planet's day-side and night-side for the Control, Flare_UV, Flare_Full, and Mean_flaring simulations, averaged over the last 50 days of the simulations. The impacts of the stellar flares are seen in the generation of an ozone layer around 20–25 km. The impact of the CMEs is seen in the depletion of ozone above 35 km.

been depleted relative to the Flare_UV simulation. The depletion is due to the increased amount of NO which was generated by the CMEs. The impact of the CMEs on ozone concentration is found to have negligible long-term effects below 35 km, as the SEP-induced ionisation rapidly declines in strength below 35 km and generates less HO_x and NO_x at those altitudes as a result.

Figure 5.20 (top) shows the zonal (east–west) average of ozone mole fraction on the planets day–side and night–side, temporally averaged over the last 50 days of the simulation period as compared to the control simulation without flares (left). The impact of flares is readily seen in the enhancement of ozone around the equatorial jet between 20-25 km (the lower ozone layer), CMEs were found to have negligible effects at this altitude. In the upper ozone layer between 45-55 km, we see that
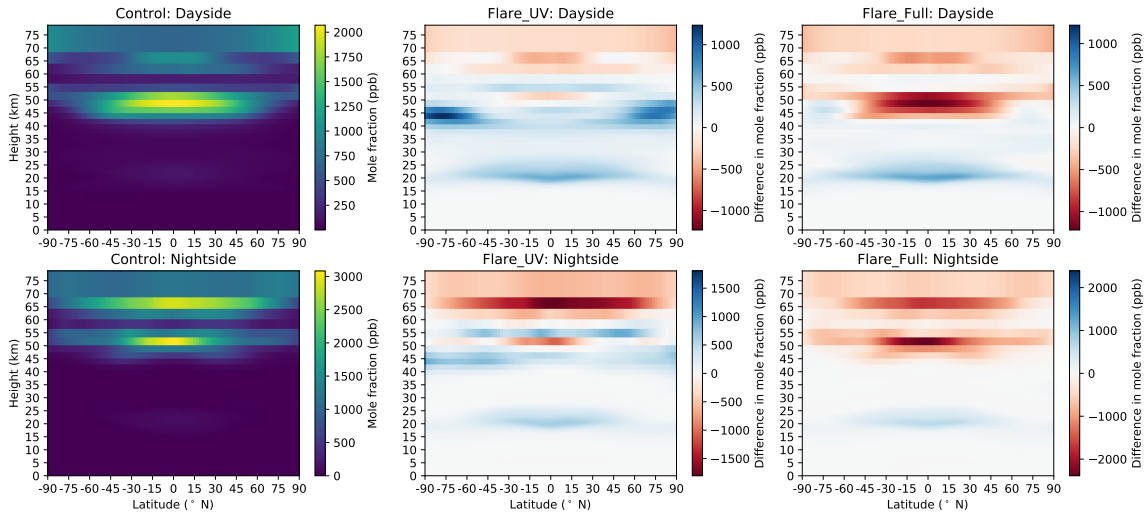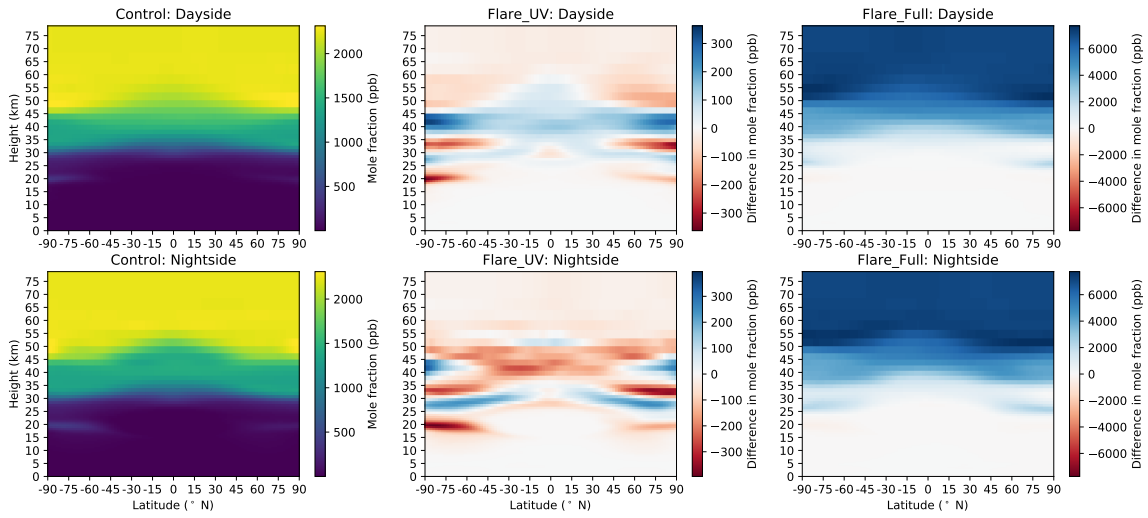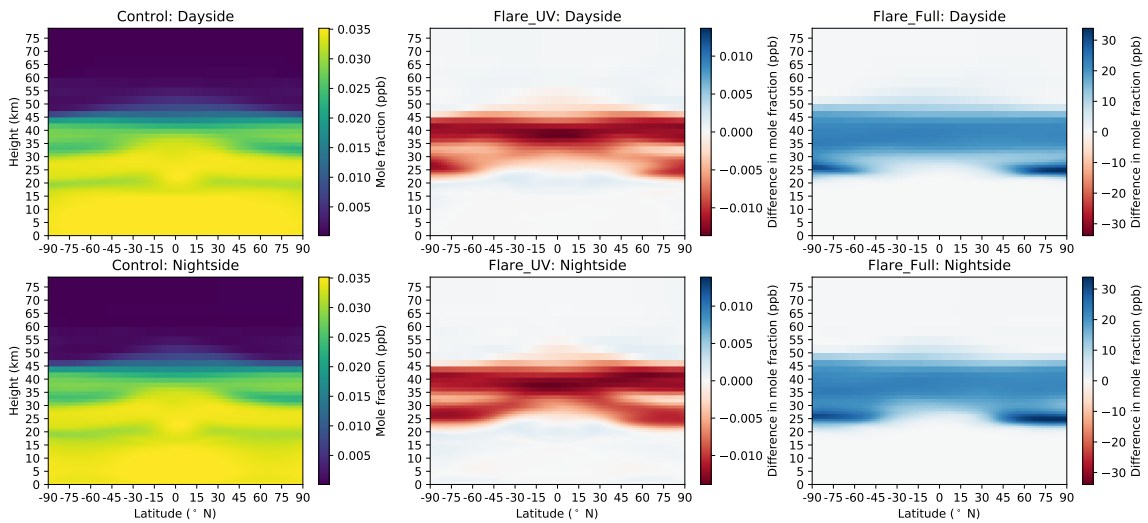
Figure 5.20: Zonal means of the ozone (top), NO (centre), and N$_2$O (bottom) mole fraction on the day-side (top row for each molecule) and the night-side (bottom row for each molecule) of the planet for the quiescent Control (left), and differences in ozone mole fraction from the control from Flare_UV (centre) and Flare_Full (right), temporally averaged over the last 50 days of the runs.
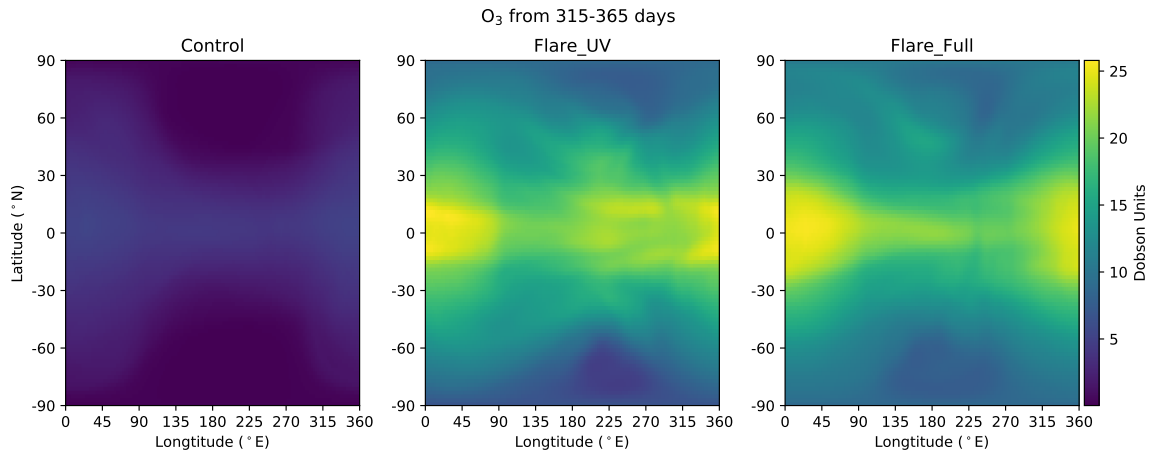
Figure 5.21: The spatial distribution of the ozone column (DU) for Control, Flare_UV, and Flare_Full averaged over the last 50 days of the simulations. The addition of flares have significantly increased the amount of ozone in the atmosphere. Ozone is concentrated in the equatorial regions and has a larger presence on the day-side.

flares extend the upper ozone layer into the polar regions. In contrast, we see that the CMEs deplete the upper ozone layer. This is also clear in the spatial distribution of the ozone column shown in Figure 5.21 (which is also temporally averaged over the last 50 days), for the flaring and control simulations. Figure 5.21 (centre and right columns) shows that the enhanced ozone column is largest in the tropics, due to oxygen photolysis being strongest in the sub-stellar region and the ozone carried by the equatorial jet.

The flares also induce long–term changes in the concentrations of several nitrogen–containing species. The SEPs due to CMEs create a large enhancement of NO and N_2O in the stratosphere. For NO, Figure 5.20 (middle) shows that NO responds to flares and CMEs very differently at different altitudes. The CMEs have lead to an increase in the amount of NO above 30 km by a factor of 3–4, from 1–2.3 ppm to 9.5 ppm. This increase is due the following reactions, with the first one being controlled by the SEPs,

$$N_2 \longrightarrow N(^2D) + N(^2D),$$

$$N(^2D) + O_2 \longrightarrow NO + O(^3P).$$
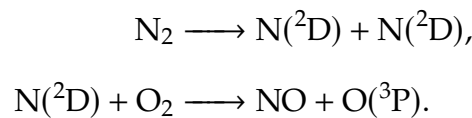
Figures 5.20 (bottom) show the impacts of the stellar flares on N_2O. These figures
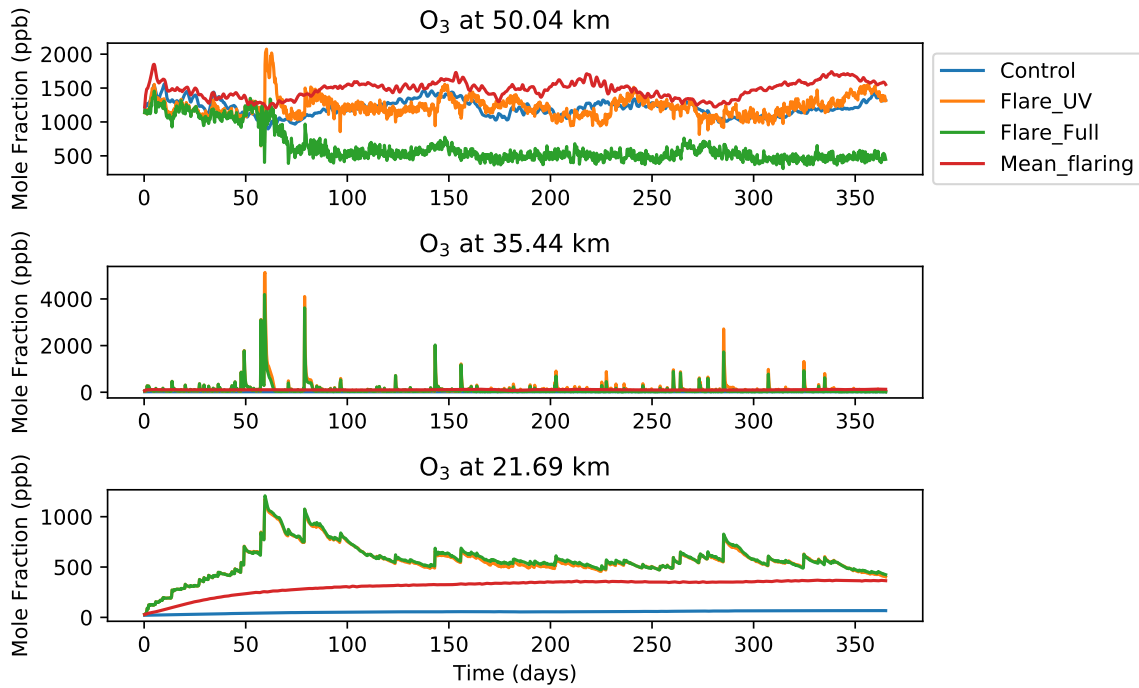
Figure 5.22: The globally averaged mole fraction of ozone in the lower ozone layer (bottom row), mid stratosphere (middle row), and the upper ozone layer (top row).

show that the UV irradiation causes minimal changes in the mole fraction of N_2O, but the SEPs have induced a very large increase between 25-50 km. We attribute this to

$$N_2 \longrightarrow N(^4S) + N(^4S),$$

$$NO + O_3 \longrightarrow NO_2 + O_2,$$

$$N(^4S) + NO_2 \longrightarrow N_2O + O(^3P),$$
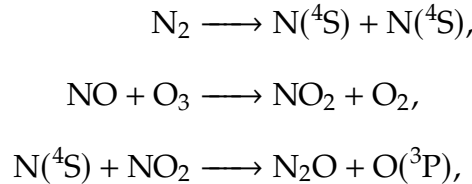
as the SEPs cause significantly more $N(^4S)$ and NO_2 (via the creation of additional NO) to be generated, which would enhance this reaction and generate more N_2O.

Figures 5.22–5.24 shows the temporal evolution of the globally averaged mole fraction of ozone, NO, and N_2O at several heights, chosen to sample three regions seen in Figure 5.19; the upper ozone layer, the mid-stratosphere, and the lower ozone layer. We see that different regions of the atmosphere respond to flares and CMEs in very different ways in our simulations. The impact of flares and CMEs on each molecule will be discussed individually. Figure 5.22 shows the

146
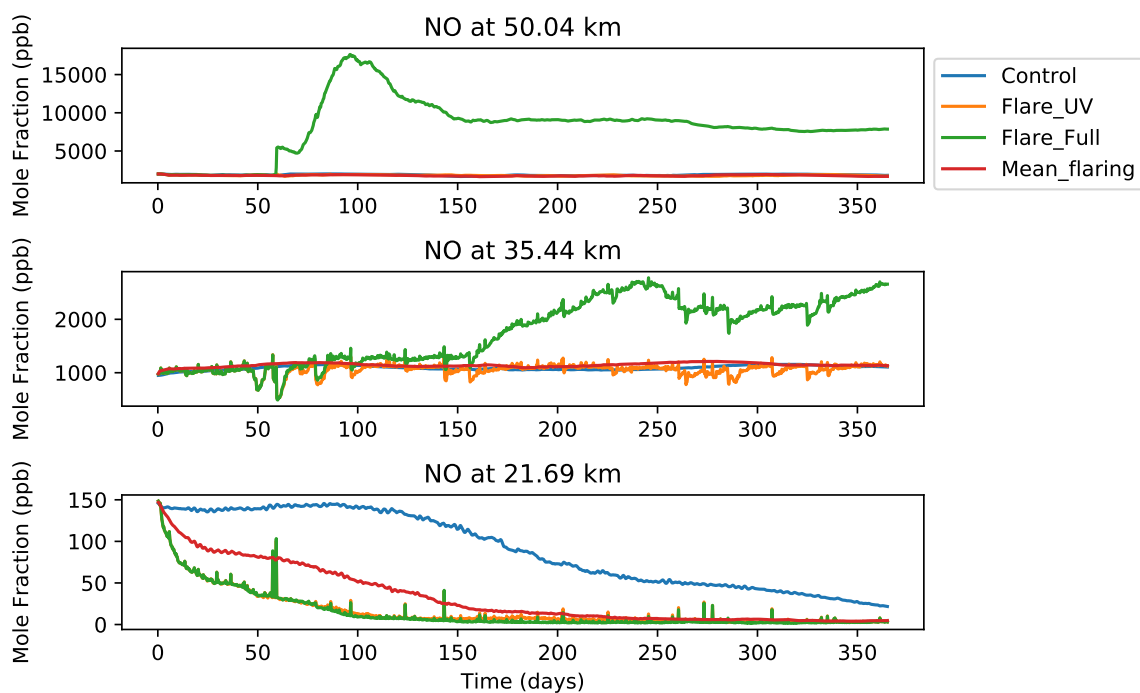
Figure 5.23: The globally averaged mole fraction of NO in the lower ozone layer (bottom row), mid stratosphere (middle row), and the upper ozone layer (top row).
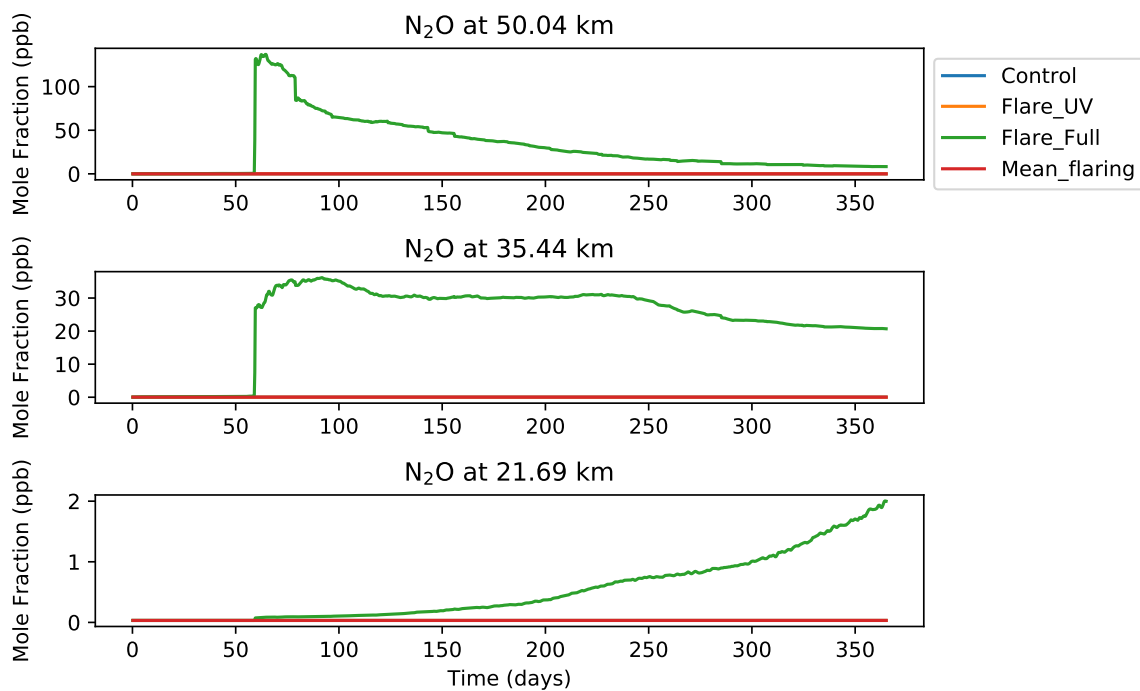
Figure 5.24: The globally averaged mole fraction of N_2O in the lower ozone layer (bottom row), mid stratosphere (middle row), and the upper ozone layer (top row).

evolution of the globally averaged mole fraction of ozone. The lower ozone layer rapidly grows from ~25 ppb to a concentration of 400-500 ppb which is perturbed by stellar flares. The abundance of ozone in the mid-stratosphere region is quite sensitive to the flares and shows rapid increases and decreases in ozone concentration. The impact of the SEPs is also quite visible, but not long lasting, as the ozone abundance rapidly decreases after the end of the flare. The abundance of ozone from the Mean_flaring simulation remains below the values observed in the flaring simulations, but the result at the end of all simulations is similar.

The upper ozone layer shows little change (compared to Control) in concentrations due to flares (aside from the 10^{34} erg flare on day 60 of the simulation which has a short–lived increase of 750 ppb relative to Control), but does show a response to CMEs, causing the upper ozone layer to reduce in concentration from ~ 1250 ppb to 500 ppb. A long–lived change in the ozone concentration is visible after the 10^{34} erg flare and maximum strength CME impacts the planet on day 60 of the Flare_Full simulation. We see that the upper ozone layer in the Flare_Full simulation stays at a lower ozone concentration and does not recover towards the other simulations, even during periods of relatively quiet activity such as the period between days 340-365 of the simulation, at least over the duration of these simulations. The abundance of ozone from the Mean_flaring simulation is enhanced compared to Flare_UV, telling us that while the short-term effects of flares do not individually change the upper ozone layer, the temporally–resolved stellar flares are important to include to accurately model the evolution of the upper ozone layer. Comparing the results from the flaring simulations to those reported by Chen et al. (2021) (their Figure 3), we see qualitatively similar results for the long term trend of ozone at this altitude, where both show a long-term depletion of ozone.

This is also similar to the recent work simulating the super-Earths GJ 832 c and GJ 581 c by Louca et al. (2022) who reported temporary enhancement of ozone at similar altitudes as our lower ozone layer and depletion of ozone at a similar

height to our upper ozone layer.

As seen in Figure 5.23, in the lower stratosphere NO experiences temporary increases due to the flares (and only minimal responses to CMEs) and rapidly returns to the concentrations it was at before the flare began. At mid altitudes, we see that NO shows a negative response to stellar flares (as it depletes during a flare and recovers afterward) but does have a positive response to CMEs, eventually leading to a long-term enhancement in concentration. We attribute this to the creation of NO at high altitudes, which is transported to lower altitudes. At high altitudes, we see that NO shows little to no response to flares, but shows a very strong response to CMEs. The peak enhancement increases the concentration by a factor of 9, reaching 18 ppm before decreasing to 8-9 ppm which is maintained for the rest of the simulation, albeit slowly decreasing. This was not solely caused by the 10^{34} erg flare and CME that occurred on day 60 of the simulation (although the impact is clearly noticeable through a very rapid increase in concentration from 2-5 ppm on the bottom figure) but by a series of weaker flares. This indicates that the largest flares are not the major cause of changes in NO. Instead the cumulative impacts of the weaker flares and CMEs are the main driver in the changes of NO concentration. We do see that the results from the Mean_flaring do mostly agree with the Flare_UV simulation.

Figure 5.24 shows that the additional atomic nitrogen generated by CMEs is able to temporarily enhance N_2O concentrations up to 100 ppb at high altitudes in our simulations. This is above the levels of N_2O seen in Segura et al. (2003) in simulations of Earth-like atmospheres including surface fluxes of N_2O. On Earth, N_2O is mostly produced by biological activity and is thought to be a biosignature (Segura et al., 2003). Our results, however, show that care must be taken when interpreting enhanced N_2O as an indicator of biotic processes. Comparing our results to Chen et al. (2021), we find that our results differ significantly. Chen et al. (2021) report N_2O abundances significantly higher than found in our results, with a peak in N_2O mixing ratio of 10^4 ppb during their flare peak, almost two orders

of magnitude higher than our results. This, in part, may well be due to the pre–flare conditions also having a significantly higher abundance than in our case, and should be investigated in future work, beyond the scope of this work (this future work is described in Section 6.2). Overall, however, our results and those of Chen et al. (2021) exhibit similar qualitative behaviour.

5.4 Planetary Habitability

The effect of flares on the potential habitability of these planets can be checked in two ways. We can examine the surface temperature, as well as look at the surface radiation environment. This allows us to check whether the additional heating from the additional UV radiation released by flares is enough to raise the surface temperature to uninhabitable levels, as well as examine whether the surface UV is raised to amounts where it may be impossible for surface–based life (that is similar to Earth–based life) to survive. Figure 5.25 shows the day–night temperature profiles for different stages during the flaring simulations: the start of the simulations, during a 10^{34} erg flare, the end of the flaring simulations, and the end of the Mean_flaring simulation. These serve to check whether the additional UV from the flares cause the surface temperature to change significantly. As can be seen, this is not the case, during the flare, despite increasing the temperature at high altitudes immensely with the topmost level having a day–side temperature over 1000 K (not shown), the additional UV radiation from the flare causes minimal heating below 45 km. Any differences due to the presence of CMEs were seen to be negligible in both quiescent and flaring conditions. The temperature profiles from the end of the Mean_flaring simulation are seen to be small, but have caused a small reduction in the near-surface temperatures on the day–side compared to the start of the simulation. We can conclude that flares (with or without CMEs) do not have an appreciable effect on the surface temperature of the planet, in our simulations.

Looking at the surface radiation environment tells us how habitable the planet
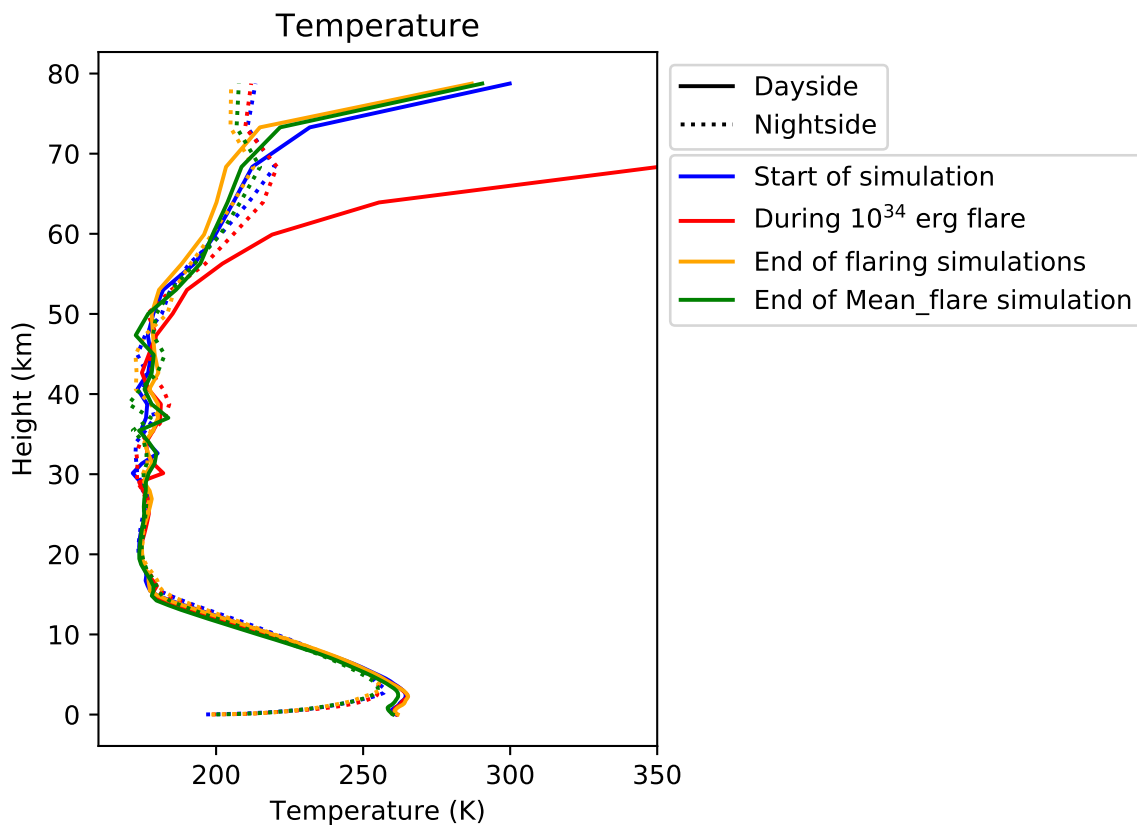
Figure 5.25: The day–side and night–side temperature profiles at different stages during the simulation: the start of the simulations, during a 10^{34} erg flare, the end of the flaring simulations, and the end of the Mean_flaring simulation.

would be for surface–based life. As UV radiation is harmful to life, a significant increase in the surface UV radiation environment would suggest that any surface–based life on these planets would be unlikely to establish itself (unless it could evolve some form of adaptation to the increased UV).

In order to observe the surface radiation environment, I created UM simulations with high–resolution radiative transfer (covering a wavelength range of 0.5 nm–505.5 nm with 500 bands with a width of 1 nm) describing quiescent conditions and the conditions of the Flare_UV and Flare_Full simulations at the peak of a 10^{34} erg flare, to see any changes in the quiescent environment due to flares and how the increase of ozone due to the flares (and other changes in the atmospheric composition) have affected the surface UV.

5.4.1 A lack of wet deposition and nitric acid

There is one caveat that must be discussed regarding concentrations of nitric acid (HNO_3). Due to a lack of wet deposition parameterisation, a very large buffer of HNO_3 has been created. Figure 5.26 shows the large concentrations of HNO_3 that are built up within the troposphere during the quiescent simulations, around 43 ppm, and Figure 5.27 shows that CMEs have caused the amount to increase slightly as well. This amount of HNO_3 is likely much too high, and would be significantly reduced by the inclusion of wet deposition, as seen in Chen et al. (2021), which found that HNO_3 would have a much lower abundance.
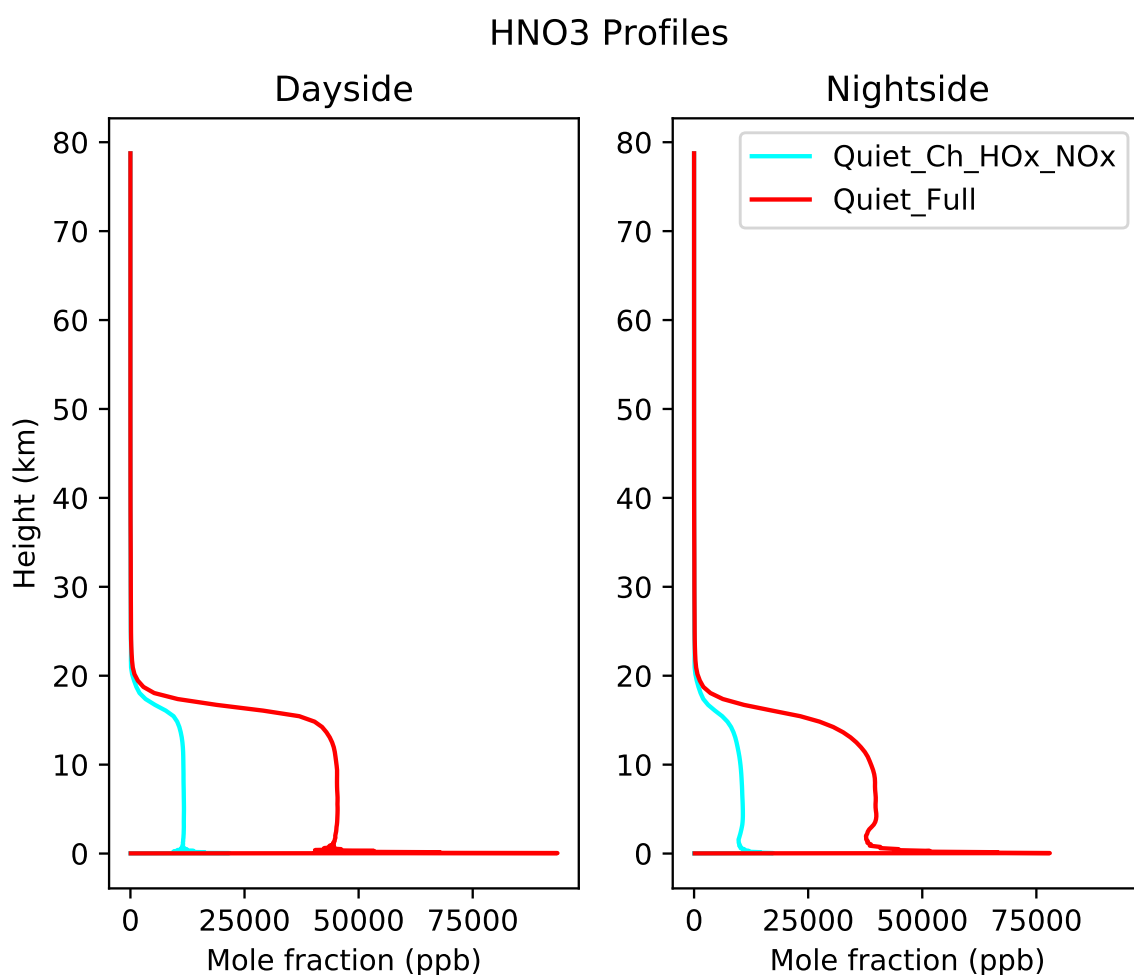
Figure 5.26: The hemispherically averaged vertical profile of HNO_3 from the quiescent simulations.

This is important to note because HNO_3 absorbs UV, and in the concentrations observed here, acts as a strong absorber of UV. As such, we have made the choice to present two versions of the figures presented in this section, versions with and without the contribution of HNO_3 to radiative transfer. Future work which incor-
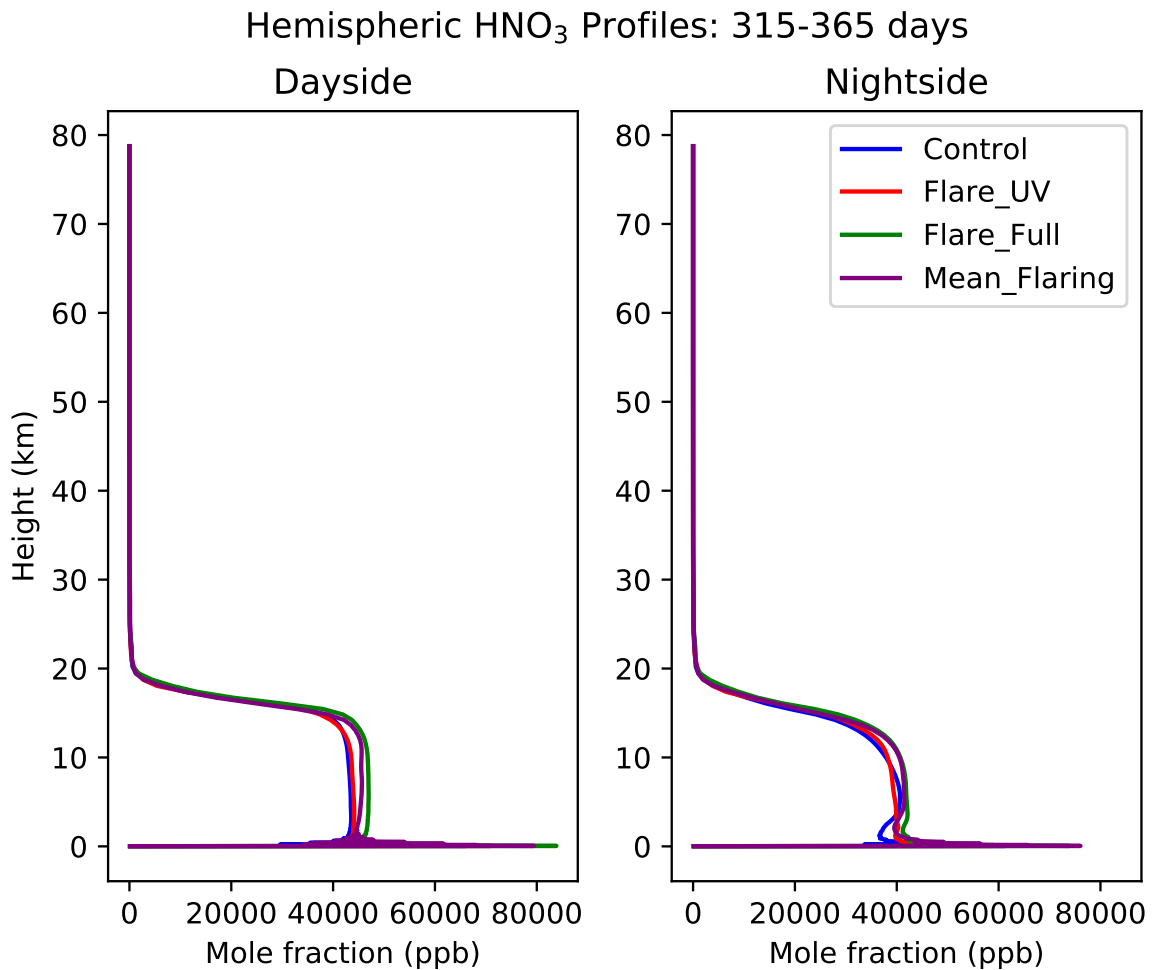
Figure 5.27: The hemispherically averaged vertical profile of HNO$_3$ from the flaring simulations.

porates wet deposition into our simulations and provides a more accurate distribution of HNO$_3$ concentrations should be performed.

However, the main conclusion of this work (stellar flares could generate a thin ozone layer) will not be changed significantly by the inclusion of wet deposition.

5.4.2 Results

Figure 5.28 shows the average day-side surface radiation environment for the Control, Flare_UV, and Flare_Full simulations under quiescent conditions (dashed) and at the peak of a 10^{34} erg flare (solid). The Control simulation is only run with quiescent conditions, but seeing what the surface UV environment in the Control simulation would have been if it was subjected to a strong flare is useful as a comparison to simulations which have already been subjected to many flares and CMEs. A reference spectrum for the Earth under quiescent conditions (American

153

Society for Testing and Materials G-173-03 reference spectra[1]) is included as well, demonstrating that our simulations result in a significantly different surface UV environment to that typically seen on Earth.

Comparing the results of the Control simulation under quiescent conditions to the quiescent Earth reference, we see that the planet receives significantly less UV–A and UV–B, but much more UV–C. The changes to the Flare_UV and Flare_Full simulations are apparent even during quiescent conditions. The changes in atmospheric composition due to stellar flares reduce the amount of UV radiation below 320 nm that reaches the planets surface. The UV–A flux is relatively unaffected, but UV–B and UV–C have been significantly reduced. This occurs for quiescent conditions and during the flare peak, the changes in atmospheric composition have added additional screening of UV which has resulted in a relatively modest decrease in UV–A (315–400 nm) and UV–B (280–315 nm), and a much larger reduction in UV–C (200–280 nm). Given the dramatic increase in the flux emitted by the star at these wavelengths during flares that can reach the surface, as seen in the Control simulation at the flare peak, this implies a stabilising feedback through the generation of a 'shielding' layer. This could have important implications for the existence of life on such planets. Interestingly, we see that the Flare_UV simulation shows a greater decrease in the surface UV than that found in the Flare_Full case. While this is most noticeable at shorter wavelengths where the surface fluxes are very low, this tells us that the species created by the CMEs cause an overall reduction in the amount of UV shielding. The amount of UV–B and UV–C which reaches the planet's surface during a flare are still much higher than that seen on Earth however, which has implications for habitability which are discussed in Section 5.4.

It should be noted that our simulations of ProxCen b have a very cloudy region around the substellar point which will reduce the average day-side surface UV drastically. Cloud formation is most prominent on the day–side around the sub-

---

[1] https://www.astm.org/g0173-03.html, spectra obtained from https://www.nrel.gov/grid/solar-resource/spectra-am1.5.html
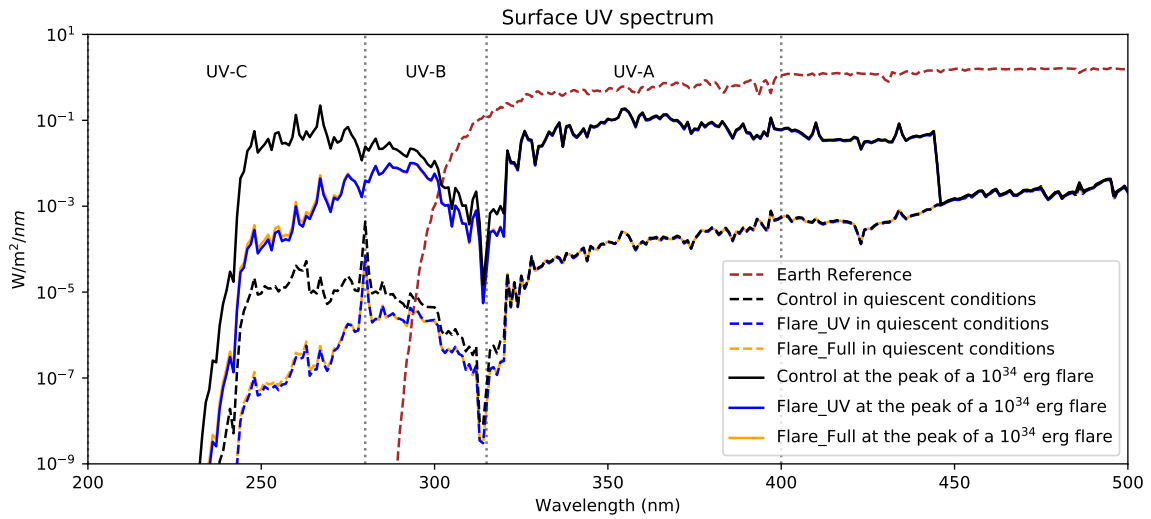
Figure 5.28: The average day-side surface UV environment under quiescent conditions and during the peak of a 10^{34} erg flare from the end of the spin-up simulation Quiet_Full (black), a run containing only stellar flares (blue), and a simulation containing both stellar flares and CMEs (orange), using the atmospheric configurations from the end of their respective simulations. A reference for the Earth under quiescent conditions is also included. The changes in atmospheric composition due to stellar flares have caused additional screening of the surface from UV radiation.

stellar point. This is due to our simulation containing a global slab ocean (Frierson et al., 2006). A slab ocean is a model where the ocean does not move (no horizontal transport), and has a fixed heat capacity (in this case a heat capacity of $10^7 \, \mathrm{J \, K^{-1} \, m^{-2}}$), representing an ocean depth of approximately 2.4 m. The presence of an ocean at the substellar point drives cloud formation, (see Sergeev et al., 2020, for more details). Figure 5.29 shows the spatial distribution of the surface UV flux on the day–side of the planet for three cases; Control, Flare_UV, and Flare_Full. This is separated into the UV–A (315-400 nm), UV–B (280–315 nm), and UV–C (200–280 nm) bands. As shown in Figure 5.28, the surface UV–A flux is not meaningfully altered by the presence of flares or SEPs. There is, however, a 50% reduction in the maximum surface UV–B flux from a peak of $2.6 \, \mathrm{W \, m^{-2}}$ to approximately $1.3 \, \mathrm{W \, m^{-2}}$, and a reduction in the maximum UV–C flux from $6.95 \, \mathrm{W \, m^{-2}}$ to $0.36 \, \mathrm{W \, m^{-2}}$, a 94.77% reduction, both of which we attribute to the increased amount of ozone. The region around the substellar point receives less UV than the areas further away from the substellar point, suggesting that this region may be affected less by stellar flares due to the large amounts of cloud. A planet with a different land–ocean configuration may behave differently in this regard as changes in the hydrological cycle from a different configuration will af-

Surface UV
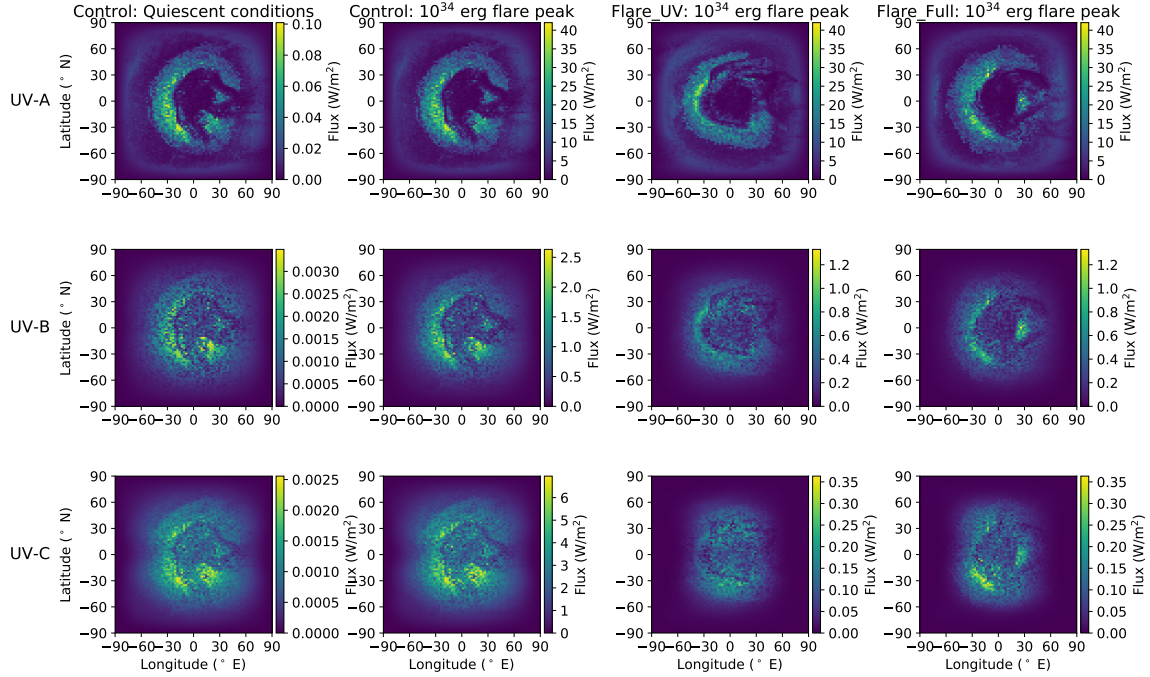
Figure 5.29: The surface UV radiation environment for the Control simulation under quiescent conditions, as well as Control, Flare_UV, and Flare_Full if they were to be subject to the peak of a 10^{34} erg flare. As seen previously in Figure 5.28, the changes in atmospheric composition due to flares have not significantly changed the UV–A flux, but have resulted in a a significant reduction in the amount of UV–B and UV–C flux.

fect the generation of clouds (Lewis et al., 2018), A planet without a large source of water (an ocean, sea, or series of lakes/swamps) in the warmer regions of the planet (in our planets case the substellar point) will have significantly less cloud formation. Fewer clouds would mean that the amount of UV which reaches the surface would increase. Likewise, if the planet was warmer or colder (due to being closer or further from its star, or the star itself being hotter or colder), the regions of the planet where clouds could form would also change. As well, changes in the land-ocean configuration and hydrological cycle will result in changes to dry deposition and wet deposition rates, further changing the atmospheric composition.

The high UV flux during a flare presents a danger for any life which may exist on the planets surface. As a proxy for examining the effects of flares on surface life, we can use the UV index. The UV index is used to measure the danger of sustained exposure to sunlight to human skin. It is calculated as

$$\text{I}_{\text{UV}} = k_{\text{er}} \int_{250\,\text{nm}}^{400\,\text{nm}} E(\lambda) S_{\text{er}}(\lambda) d\lambda, \tag{5.1}$$

156
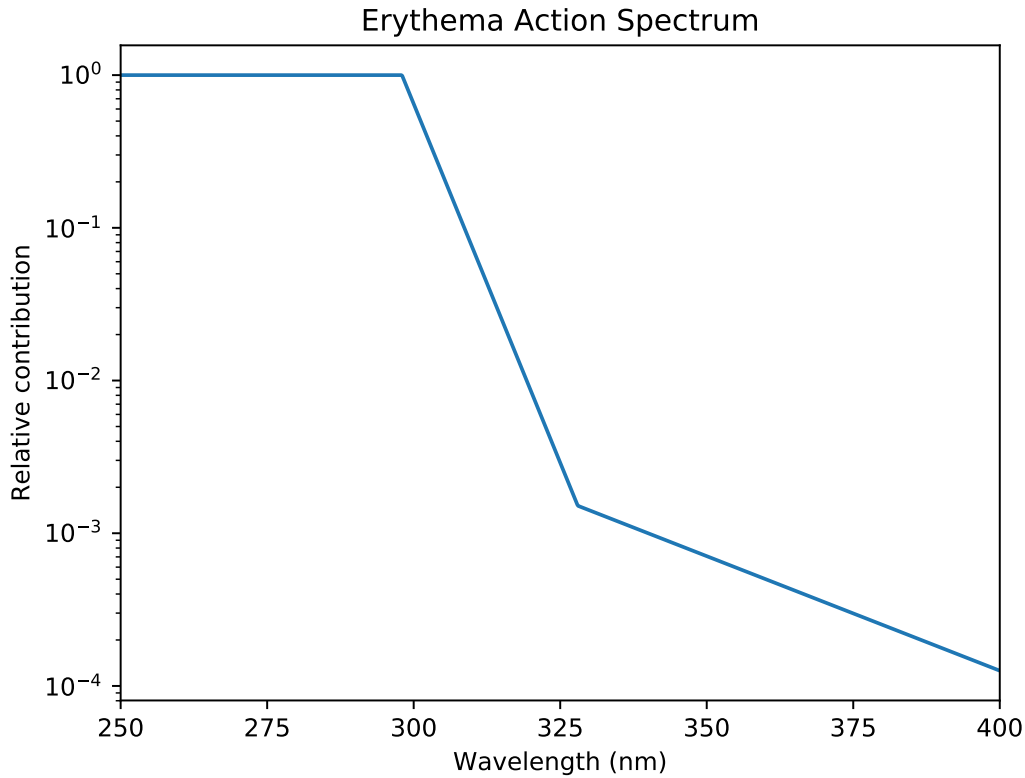
Figure 5.30: The standard erythema action spectrum.

where $E(\lambda)$ is the solar spectral irradiance, $S_{\mathrm{er}}(\lambda)$ is the erythema action spectrum, which represents the relative effectiveness of UV radiation in damaging human skin, and k_{er} is a constant of $40\,\mathrm{m^2W^{-1}}$ which was chosen so the standard range of the index is between 0 and 10 (the range of values typically seen on Earth). An idealised form of the erythema action spectrum (International Organization for Standardization standard ISO 17166:1999[2]) is described as

$$S_{\mathrm{er}}(\lambda) = \begin{cases} 1 & 250 < \lambda < 298\,\mathrm{nm}, \\ 10^{0.094(298-\lambda)} & 298 < \lambda < 328\,\mathrm{nm}, \\ 10^{0.015(139-\lambda)} & 328 < \lambda < 400\,\mathrm{nm}, \end{cases} \tag{5.2}$$

and Figure 5.30 illustrates this spectrum.

During quiescent conditions the UV index is very mild (less than 0.2 for the Control simulation, and less then 0.04 for the Flare_UV and Flare_Full simulations, due

---

[2] https://www.iso.org/obp/ui/#iso:std:iso:17166:ed-1:v2
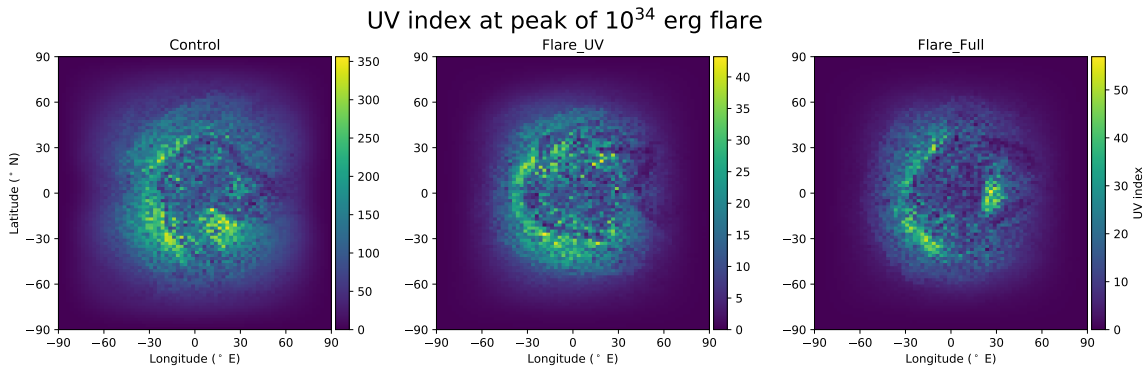
Figure 5.31: Maps of the UV index for Control, Flare_UV, and Flare_Full if they were to be subject to the peak of a 10^{34} erg flare. While the UV index is extremely high for all simulations, changes in atmospheric composition due to previous flares result in the peak UV index being reduced by ~85%.

to the increased shielding from ozone as previously described), but the UV index reaches very high values during the peak of a maximum strength flare, as shown in Figure 5.31. The Control simulation has a peak UV index of over 350. The ozone generated by previous flares has reduced the UV index to ~55, which is still extremely high, but is a reduction of ~85% from the Control simulation. Using Equation 4.8

$$\log_{10}(\nu) = -1.01 \log_{10}(E) + 31.65, \qquad \text{(4.8, revisited)}$$

indicates that flares of this magnitude occur every 500 days on average. This presents a key danger for the surface habitability of this planet, even after a shielding layer of ozone has been generated. Future research on whether life could adapt to these conditions (or arise in the first place) should be conducted.

For completeness, we can also examine versions of Figures 5.28-5.31 with the contribution of nitric acid (HNO_3) included in the calculations.

The large amount of HNO_3 in our simulations causes significant changes in the surface UV radiation environment. Figure 5.32 shows significantly smaller UV–B and UV–C fluxes which reach the planet's surface. The amount of UV–A is unchanged. The reduction in UV–C is quite important due to the potential harm to life.
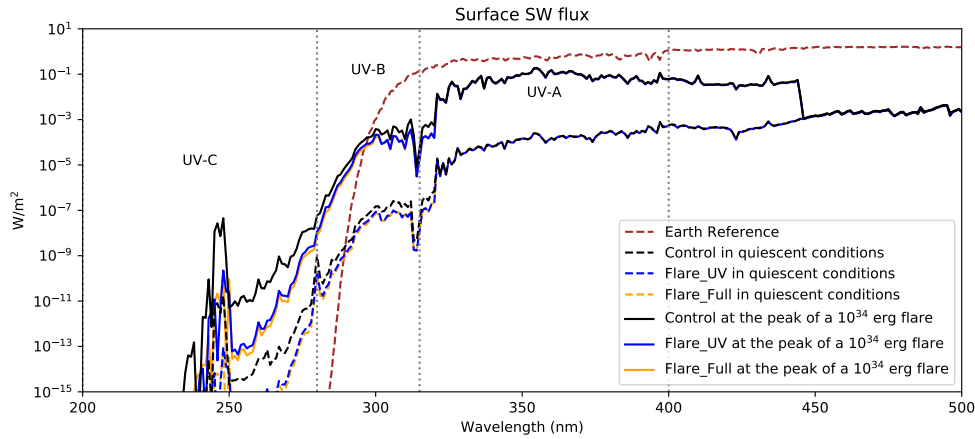
Figure 5.32: The average day-side surface UV environment under quiescent conditions and during the peak of a 10^{34} erg flare from the end of the spin-up simulation Quiet_Full (black), a run containing only stellar flares (blue), and a simulation containing both stellar flares and CMEs (orange), using the atmospheric configurations from the end of their respective simulations, including the contribution of HNO_3. The changes in atmospheric composition due to stellar flares have caused additional screening of the surface from UV radiation. The inclusion of HNO_3 has caused a significant reduction in the UV–B and UV–C fluxes.

Figure 5.33 shows the spatial distribution of the UV–A and UV–B fluxes. The flux levels of UV–C are very low in this case, where HNO_3 is not removed from the atmosphere. We observe that the additional screening caused by the changes in atmospheric composition now result in a small reduction in UV–B.

Figure 5.34 shows the UV index at the peak of a 10^{34} erg flare. The additional screening due to HNO_3's contribution causes the UV index to drop substantially. It is now very mild, and is not significantly reduced by the changes in atmospheric composition caused by flares.

5.5   Are the impacts of flaring observable?

To determine whether the impacts of stellar flares could be observable for our representation of ProxCen b, we generated a synthetic transmission spectrum for several simulations. The UM is able to output a synthetic transmission spectrum, using the method described in Lines et al. (2018) and recently updated by Christie et al. (2021). It should be noted that ProxCen b is not thought to transit (Jenkins et al., 2019). The planet we simulate is merely a planet based on the parameters of ProxCen b, with the results indicative for M dwarf hosted planets with 'Earth–

159
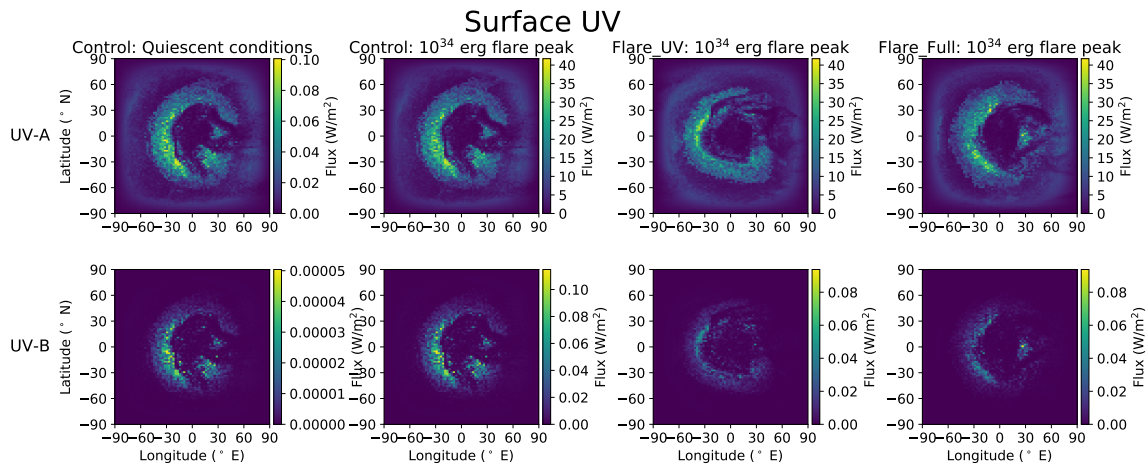
Figure 5.33: The surface UV radiation environment for the Control simulation under quiescent conditions, as well as Control, Flare_UV, and Flare_Full if they were to be subject to the peak of a 10^{34} erg flare, including the contribution of HNO_3 to radiative absorption. As seen previously in Figure 5.32, the changes in atmospheric composition due to flares have not significantly changed the UV–A flux, but have resulted in a a minor reduction in UV–B.
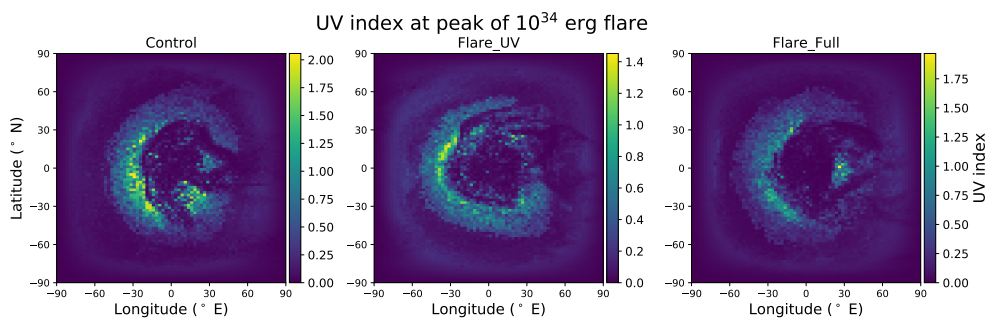
Figure 5.34: Maps of the UV index for Control, Flare_UV, and Flare_Full if they were to be subject to the peak of a 10^{34} erg flare, including the contribution of HNO_3.

like' atmospheres. As stated in Section 5.4, we think it is justified to remove the contribution of HNO_3 to the transmission spectra. This is shown in Figure 5.35, and for completeness the transmission spectrum with the contribution of HNO_3 is shown in Figure 5.36.

Figure 5.35 shows the transmission spectra (between 500 nm and 10 μm) from the previously described simulations (Control, Flare_UV, and Flare_Full). Changes in the transmission spectrum are caused by changes in atmospheric composition, temperature, and pressure. Figure 5.35 shows that the transmission spectrum is rather unchanged by the changes in the atmospheric composition due to flares or SEPs. We observe strong absorption features for NO_2 and ozone. The ozone absorption peaks at 9.5 microns are the only features altered in a noticeable fashion. The differences in these features are relatively small and are not expected to be readily discernible with current-generation instrumentation.
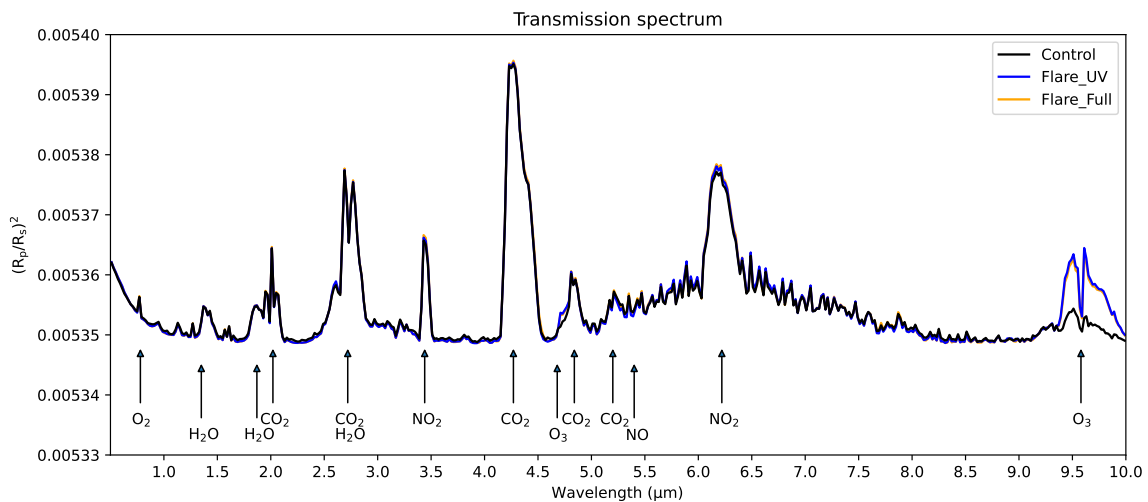
Figure 5.35: The transmission spectra for the simulated planets for 500 nm-10 μm at the end of their respective simulations. The colors refer to the same simulations as Figure 5.28.

The atmospheric composition changes due to the SEPs (a reduction of the upper ozone layer, and a significant increase in NO and N_2O) cause very small changes in the transmission spectrum, namely a slight increase in the continuum absorption in several wavelength regions, and a small increase in the NO_2 absorption feature at 6.3 microns. Figure 5.36 shows the transmission spectra with the contribution of HNO_3. We see that HNO_3 has absorption features at 5.8, 7.5, and 8.3 μm, but is otherwise quite similar to Figure 5.35.
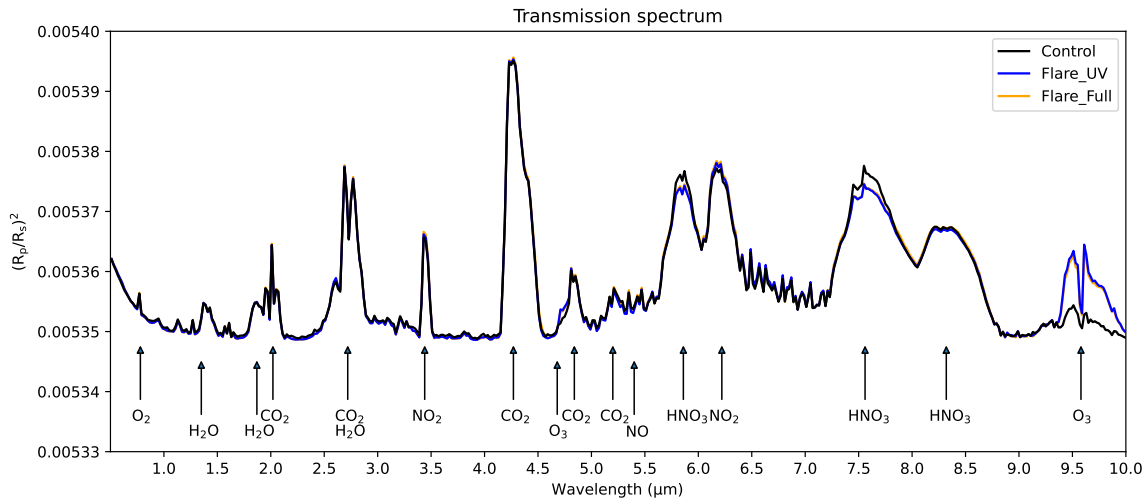
Figure 5.36: The transmission spectra for the simulated planets for 500 nm-10 μm at the end of their respective simulations including the contribution of HNO_3. The colors refer to the same simulations as Figure 5.28.

5.6 Chapter Summary

In this chapter I have described the impact of stellar energetic particles on quiescent simulations. The impact of stellar flares and coronal mass ejections has been described in detail, both in the effects on atmospheric composition, as well as the changes in the surface UV radiation environment due to the aforementioned changes in atmospheric composition. We have found that stellar flares have caused an increase in the amount of ozone in the atmosphere, which has moderately improved the planet's habitability in quiescent conditions. We find that the strongest flares cause the planet's day–side to receive very dangerous levels of UV. Coronal mass ejections were found to not have a significant long–term impact on the amount of ozone.

Chapter 6

Conclusions

In this thesis I have described how I coupled the Met Office Unified Model, a 3D general circulation model, a chemical kinetics scheme, and a photolysis scheme to create a self–consistent photochemical scheme capable of describing the interplay between atmospheric chemistry and planetary dynamics. This was done in order to further understand how stellar flares impact the planets which orbit the star.

6.1 Results

In this first application of my model, I simulated Proxima Centauri b as an indicative terrestrial aquaplanet, although the qualitative results should hold for similar targets. The simulated planet is tidally locked with an Earth-like atmosphere orbiting an M dwarf star. I incorporate Earth-based observations of ionisation caused by stellar protons to create an approximation of a quiescent stellar wind, as well as a representation of the ionisation caused by a CME which is used to approximate the effects of CMEs which result in SEPs impacting the planet's atmosphere through the creation of short-lived radical species, which induce significant changes in the atmosphere. I found that under quiescent conditions the planet maintains an extremely thin upper ozone layer at 45-55 km resulting in an average ozone column which is hundreds of times thinner than seen on Earth. I

find that the introduction of HO_x and NO_x chemistry results in the depletion of ozone globally as expected, but the depletion is strongest through the inclusion of NO_x chemistry. The depletion of ozone due to the introduction of NO_x chemistry is strongest within the night–side gyres, removing a night–side reservoir of ozone. This behavior was partially due to the choice of stellar spectra containing chromospheric emission. This highlights the need for active stellar spectra models to be considered in exoplanet climate studies as well as terrestrial climate studies.

I find that the effect of stellar flares on the planet's atmosphere is to increase the amount of ozone present in the atmosphere. A lower ozone layer is developed between 20–25 km and is transported onto the night-side through the equatorial jet. Coronal Mass Ejections are found to cause minimal changes in the total amount of ozone, but do cause a reduction in the upper ozone layer.

The increased UV radiation due to the stellar flares causes a 20 DU increase in the amount of ozone present. The ozone concentration enters a punctuated equilibrium state which is perturbed by flares to temporarily increase the ozone concentration. CMEs were found to have a limited impact on the amount of ozone. The impact of flares and CMEs is dependent on altitude. At low altitudes the ozone concentration increases from ~ 10 ppb to hundreds of ppb. At mid altitudes there is a rapid increase and decrease in ozone concentration, with the increases ranging from hundreds to thousands of ppb. At high altitudes we do not see a response due to flaring. We see a response due to CMEs which reduces the ozone concentrations by ~ 600 ppb. This reduction indicates a long-term divergence in the chemical evolution of ozone in the upper atmosphere due to CMEs.

Simulating the planet with a constant spectrum consisting of the time-averaged stellar spectra from the year-long simulation shows a mixture of agreement and disagreement with the simulation only containing flares. While the concentrations of species such as N_2O and NO broadly match, species that are more sensitive to flares (such as O_3) are quite different. This tells us that while such a spectrum can be used to model changes in atmospheric composition due to stellar flares without

needing a high-resolution time-varying stellar irradiance model, it cannot be used without caution, as it is not accurate for every species and will not capture any short-term behaviours.

The introduction of CMEs causes a significant increase in the concentration of the biosignature N_2O in the stratosphere. While this increase is not readily discernible by the current generation of instrumentation, it does highlight the need for caution if N_2O is detected in significant quantities, as I have found that stellar flares and CMEs can plausibly act as an abiotic source of N_2O.

The changes in the atmospheric composition have heavily reduced the amount of UV–B and UV–C which reaches the planets surface. While rare, during the peak of the strongest flares in this model, the surface UV–A and UV–B fluxes increase by a factor of 400 and the UV–C by a factor of 145. These results were obtained after removing the contribution of HNO_3 to radiative absorption, mimicking perfect wet deposition.

To summarise, I find that the stellar flares are inducing changes in the atmosphere to create additional shielding from UV. Essentially, the atmosphere is responding in such a way that makes the next flare less impactful, with the most significant, and potentially irreversible impacts being caused by the largest flares which are relatively common for M dwarf stars.

6.2   Future Work

The question of whether M dwarf hosted planets are habitable is a challenging one. In general, 3D exoplanet climate modelling studies can adapt complex and more 'complete' treatments developed for Earth, or develop more simplified treatments. For the former case the studies are less likely to miss important elements, and could be more accurate, however the latter approach is more amenable to interpretation and less subject to Earth–centric assumptions. In reality, to make progress the scientific community needs a range of approaches. In this work I introduce a new

model, complementary in its approach to that of Chen et al. (2021) and Braam et al. (2022) in examining ozone chemistry in 3D, but are aware that this first step motivates extensive follow–up both in terms of more extensive application of this model, and further development.

Firstly, for our current study, improvements in computational efficiency would allow us to perform longer simulations including a larger number of flares, and studying the longer term behaviour of the atmosphere. The evolution of the ozone distribution is not completely understood and initial conditions for a flaring simulation are not well constrained. Work is underway to adapt the next generation climate model of the Met Office, termed LFRic (Adams et al., 2019) to exoplanets (Sergeev et al., in prep), which will open up much larger scale computations allowing the inclusion of more physical process, improvement to higher spatial and temporal resolution and longer simulation times. In this work I have focused on a few important species, but as detailed in Appendix A.1 I track the abundances of many more species which I could explore in more detail. Additionally, I have assumed an unmagnetised planet, but could implement a spatial dependence of the SEP impacts to mimic a magnetic field topology. I have also assumed an 'Earth–like' atmospheric composition for this initial study, but varying compositions could also be studied through adaptations of the chemistry. Additionally, it is clear that 'M dwarfs' are not a uniform population, but actually a diverse set of objects so studies should be expanded to cover the spectral range more completely.

For our current model, the treatment of dry deposition should be improved beyond the simple model of Giannakopoulos et al. (1999), and give the dry deposition the capability of being used for a variety of terrain types. This would act to alter the abundance of the species listed in Section 3.1.4 including ozone, and give us the capability of simulating a much larger variety of terrestrial planets. Our models currently lack a description of wet deposition, which should be included. The inclusion of wet deposition would impact the chemistry in the troposphere, and heavily deplete NO_x reservoirs such as HNO_3. Additionally, non–LTE effects

in the upper atmosphere should be included to more accurately capture the high altitude heating, something which is essentially omitted in this work. SOCRATES is currently being upgraded to include such a treatment (Jackson et al., 2020). Furthermore, ions and aqueous interactions could be included in the chemistry, which would lead to a more complete description of the impact of stellar activity. The generation of hazes in the upper atmosphere would also likely impact the UV budget so should also be included. Hazes are likely to play a key role in, for example, the Archean Earth and analogue exoplanets (Arney et al., 2016). Finally, additional sources and sinks into the atmosphere could be included such as atmospheric escape and influx from the surface (e.g., volcanic activity).

The long–term changes in the abundances in several species as a result of the flares or SEPs suggests that the occurrence and timing of large flares or CMEs might be quite important in determining the state of the planet at the end of the simulations. This could be tested in several ways, such as increasing the length of the simulation to eliminate short-term effects, or by subjecting the planet to the same sampling of flares, but in a different order.

This model could also be adapted to the study of the Archean Earth, as mentioned with the inclusion of hazes, as well as being applied to hot Jupiters with adaptations to the chemistry and model setup (as the UM is already routinely applied to hot Jupiters to study the chemistry, e.g, Drummond et al., 2020; Zamyatina et al., 2022). In particular, I plan to adapt this model to the Archean Earth, and study exoplanet analogues of this stage in Earth's history, where the first evidence of life is found (Nisbet & Sleep, 2001).

Clearly there is much to be done to improve our understanding of the interaction between 'active' stars and the planets they host.

Appendices

Appendix A

Chemical reactions and reaction coefficients

This appendix consists of tables listing every chemical reaction used in this work, and the coefficients used to determine their reaction rates.

A.1   Chemical Species

Table A.1 lists the tracked species which are advected through the atmosphere, impact the radiative transfer calculation (alongside the other, constant abundance, background atmospheric gases, Boutle et al., 2017) and take part in the various chemical and photochemical reactions. The majority of the molecular opacities in this work were sourced from the high-resolution transmission molecular absorption database (HITRAN, Gordon et al., 2022b). Other sources include Burkholder et al. (2015) hereafter referred to as JPL2015, the MPI-Mainz UV/VIS Spectral Atlas (Keller-Rudek et al., 2013), and data from the South–West Research Institute (SWRI, Huebner & Mukherjee, 2015).

Our underlying chemistry framework (Drummond et al., 2016) has previously been coupled to the dynamics and radiative transfer, and tested, at various levels of sophistication for performance such as conservation (see Drummond et al.,

Species	Formula	Opacity data source
Molecular oxygen	O_2	HITRAN, recommended sources for wavelengths below 294 nm in Burkholder et al. (2015)
Ozone	O_3	HITRAN, JPL2015, SWRI
Molecular nitrogen	N_2	HITRAN, Fennelly & Torr (1992); Henke et al. (1993)
Carbon dioxide	CO_2	HITRAN, MPI-Mainz UV/VIS Spectral Atlas, SWRI
Atomic oxygen (ground state)	$O(^3P)$	–
Atomic oxygen (first excited state)	$O(^1D)$	–
Water	H_2O	HITRAN, MPI-Mainz UV/VIS Spectral Atlas, SWRI
Hydroxyl radical	OH	–
Hydroperoxyl radical	HO_2	JPL2015, SWRI
Molecular hydrogen	H_2	–
Atomic hydrogen	H	–
Hydrogen peroxide	H_2O_2	JPL2015, SWRI
Nitric oxide	NO	–
Nitrogen dioxide	NO_2	MPI-Mainz UV/VIS Spectral Atlas, SWRI
Nitrate radical	NO_3	MPI-Mainz UV/VIS Spectral Atlas, SWRI
Dinitrogen pentoxide	N_2O_5	MPI-Mainz UV/VIS Spectral Atlas, SWRI
Peroxynitric acid	HO_2NO_2	JPL2015, SWRI
Nitrous acid	HONO	JPL2015, SWRI
Nitric acid	HNO_3	JPL2015, SWRI
Nitrous oxide	N_2O	HITRAN, MPI-Mainz UV/VIS Spectral Atlas
Atomic nitrogen (ground state)	$N(^4S)$	–
Atomic nitrogen (excited state)	$N(^2D)$	–

Table A.1: The species tracked in our model and involved in the ozone chemistry, and the source(s) for their opacity if the species is involved with the radiative transfer.

2020; Zamyatina et al., 2022).

A.2 Bimolecular Reactions

Table A.2 contains the full list of bimolecular reactions used in this work, and the coefficients used to calculate their reaction rates.

A.3 Termolecular Reactions

Table A.3 contains the full list of termolecular formation reactions used in this work, and the coefficients used to determine their reaction rates. Table A.4 contains the termolecular decomposition reactions used in this work, and their coefficients. As they are decomposition reactions and only have a single reactant, the units of k_1 and k_2 differ from formation reactions, so they have been listed in a separate table.

Reaction	A (cm^3 molecule^{-1} s^{-1})	α	E_a/R (K)	T range (K)	Source
$O(^3P) + O_3 \longrightarrow O_2 + O_2$	8.00×10^{-12}	0	2060	220-409	JPL2019
$O(^1D) + O_2 \longrightarrow O(^3P) + O_2$	3.3×10^{-11}	0	-55	104-424	JPL2019
$O(^1D) + N_2 \longrightarrow O(^3P) + N_2$	2.15×10^{-11}	0	-110	103-673	JPL2019
$O(^1D) + CO_2 \longrightarrow O(^3P) + CO_2$	7.5×10^{-12}	0	-115	195-370	JPL2019
$O(^1D) + O_3 \longrightarrow O_2 + O_2$	1.20×10^{-10}	0	0.0	103-393	JPL2019
$O(^1D) + O_3 \longrightarrow O_2 + O(^3P) + O(^3P)$	1.20×10^{-10}	0	0.0	103-393	JPL2019
$O(^1D) + H_2O \longrightarrow OH + OH$	1.63×10^{-10}	0	-60	217-453	JPL2019
$O(^1D) + H_2 \longrightarrow OH + H$	1.20×10^{-10}	0	0	204-4210	JPL2019
$O(^3P) + OH \longrightarrow O_2 + H$	1.8×10^{-11}	0	-180	136-515	JPL2019
$O(^3P) + HO_2 \longrightarrow O_2 + OH$	3.0×10^{-11}	0	-200	229-391	JPL2019
$O(^3P) + H_2O_2 \longrightarrow HO_2 + OH$	1.40×10^{-12}	0	2000	283-386	JPL2019
$H + O_3 \longrightarrow OH + O_2$	1.40×10^{-10}	0	470	196-424	JPL2019
$H + HO_2 \longrightarrow OH + OH$	7.2×10^{-11}	0	0	245-300	JPL2019
$H + HO_2 \longrightarrow O(^3P) + H_2O$	1.6×10^{-12}	0	0	245-300	JPL2019
$H + HO_2 \longrightarrow H_2 + O_2$	6.9×10^{-12}	0	0	245-300	JPL2019
$OH + O_3 \longrightarrow HO_2 + O_2$	1.7×10^{-12}	0	940	190-357	JPL2019
$OH + H_2 \longrightarrow H_2O + H$	2.8×10^{-12}	0	1800	200-1050	JPL2019
$OH + OH \longrightarrow H_2O + O(^3P)$	1.8×10^{-12}	0	0	233-580	JPL2019
$OH + HO_2 \longrightarrow H_2O + O_2$	4.8×10^{-11}	0	-250	252-420	JPL2019
$OH + H_2O_2 \longrightarrow H_2O + HO_2$	1.8×10^{-12}	0	0	200-300	JPL2019
$HO_2 + O_3 \longrightarrow OH + O_2 + O_2$	1.0×10^{-14}	0	490	197-413	JPL2019
$HO_2 + HO_2 \longrightarrow H_2O_2 + O_2$	3.0×10^{-13}, [1]	0	-460	222-1120	JPL2019
$O(^1D) + N_2O \longrightarrow N_2 + O_2$	4.641×10^{-11}	0	-20	195-719	JPL2019
$O(^1D) + N_2O \longrightarrow NO + NO$	7.259×10^{-11}	0	-20	195-719	JPL2019
$O(^3P) + NO_2 \longrightarrow NO + O_2$	5.1×10^{-12}, [2]	0	-210	199-2300	JPL2015
$O(^3P) + NO_3 \longrightarrow NO_2 + O_2$	1.3×10^{-11}	0	0	298-329	JPL2019
$H + NO_2 \longrightarrow OH + NO$	1.35×10^{-10}	0	0	195-2000	JPL2019
$OH + NO_3 \longrightarrow HO_2 + NO_2$	2.0×10^{-11}	0	0	298	JPL2019
$OH + HONO \longrightarrow H_2O + NO_2$	3.0×10^{-12}	0	-250	276-1400	JPL2019
$OH + HNO_3 \longrightarrow H_2O + NO_3$	2.4×10^{-14}	0	-460	–	IUPAC[3]
$OH + HO_2NO_2 \longrightarrow H_2O + NO_2 + O_2$	4.5×10^{-13}	0	-610	218-335	JPL2019
$HO_2 + NO \longrightarrow NO_2 + OH$	3.44×10^{-12}	0	-260	182-1270	JPL2019
$HO_2 + NO_3 \longrightarrow OH + NO_2 + O_2$	3.5×10^{-12}	0	0	263-338	JPL2019
$N(^4S) + O_2 \longrightarrow NO + O(^3P)$	3.3×10^{-12}	0	3150	280-1220	JPL2019
$N(^4S) + NO \longrightarrow N_2 + O(^3P)$	2.1×10^{-11}	0	-100	196-3660	JPL2019
$N(^4S) + NO_2 \longrightarrow N_2O + O(^3P)$	5.8×10^{-12}	0	-220	223-700	JPL2019
$NO + O_3 \longrightarrow NO_2 + O_2$	3.0×10^{-12}	0	1500	195-443	JPL2019
$NO + NO_3 \longrightarrow NO_2 + NO_2$	1.7×10^{-11}	0	-125	209-703	JPL2019
$NO_2 + O_3 \longrightarrow NO_3 + O_2$	1.2×10^{-13}	0	2450	231-362	JPL2019
$NO_2 + NO_3 \longrightarrow NO + NO_2 + O_2$	4.35×10^{-14}	0	1335	236-538	JPL2019
$NO_3 + NO_3 \longrightarrow NO_2 + NO_2 + O_2$	8.5×10^{-13}	0	2450	298-1100	JPL2019
$N_2O_5 + H_2O \longrightarrow HNO_3 + HNO_3$	2×10^{-21}	0	0	290-298	JPL2019
$N(^2D) + O(^3P) \longrightarrow N(^4S) + O(^3P)$	3.3×10^{-12}	0	260	300-400	Herron (1999)
$N(^2D) + O_2 \longrightarrow NO + O(^3P)$	9.7×10^{-12}	0	185	200-500	Herron (1999)
$N(^2D) + N_2O \longrightarrow N_2 + NO$	1.5×10^{-11}	0	570	200-400	Herron (1999)
$N(^2D) + N_2 \longrightarrow N(^4S) + N_2$	1.7×10^{-14}	0	0	298	Herron (1999)

Table A.2: The bimolecular reactions included in the chemical network, and their coefficients.
Notes:
1. In the presence of water there is an extra corrective factor of $1 + 1.4 \times 10^{-21}[H_2O] \exp(2200/T)$.
2. Integrated rate constant for both association and dissociation.
3. We only use k_1 from the expanded rate coefficient to account for temperature dependence.

Reaction	k_1 (cm^6 molecule^{-2} s^{-1})	α_1	β_1 (K)	k_2 (cm^3 molecule^{-1} s^{-1})	α_2	β_2 (K)	Source
O(^{3}P) + O$_2$ + M $\longrightarrow$ O$_3$ + M	6.1×10^{-34}	-2.4	0	–	–	–	JPL2019
HO$_2$ + HO$_2$ + M $\longrightarrow$ H$_2$O$_2$ + O$_2$ + M	2.1×10^{-33}, [1]	0	-920	–	–	–	JPL2019
H + O$_2$ + M $\longrightarrow$ HO$_2$ + M	5.3×10^{-32}	-1.8	0	9.5×10^{-11}	0.4	0	JPL2019
OH + OH + M $\longrightarrow$ H$_2$O$_2$ + M	6.9×10^{-31}	-1	0	2.6×10^{-11}	0	0	JPL2019
O(^{1}D) + N$_2$ + M $\longrightarrow$ N$_2$O + M	2.8×10^{-36}	-0.9	0	–	–	–	JPL2019
O(^{3}P) + NO + M $\longrightarrow$ NO$_2$ + M	9.1×10^{-32}	-1.5	0	3.0×10^{-11}	0	0	JPL2019
O(^{3}P) + NO$_2$ + M $\longrightarrow$ NO$_3$ + M	3.4×10^{-31}	-1.6	0	2.3×10^{-11}	-0.2	0	JPL2019
OH + NO + M $\longrightarrow$ HONO + M	7.1×10^{-31}	-2.6	0	3.6×10^{-11}	-0.1	0	JPL2019
OH + NO$_2$ + M $\longrightarrow$ HNO$_3$ + M	1.8×10^{-30}	-3	0	2.8×10^{-11}	0	0	JPL2019
HO$_2$ + NO$_2$ + M $\longrightarrow$ HO$_2$NO$_2$ + M	1.9×10^{-31}	-3.4	0	4×10^{-12}	-0.3	0	JPL2019
NO$_2$ + NO$_3$ + M $\longrightarrow$ N$_2$O$_5$ + M	2.4×10^{-30}	-3	0	1.6×10^{-12}	0.1	0	JPL2019

Table A.3: The termolecular reactions included in the chemical network, and their coefficients (see Table A.4 for decomposition reactions).
Note:
1. In the presence of water there is an extra corrective factor of $1 + 1.4 \times 10^{-21}$[H$_2$O] exp(2200/T).

Reaction	k_1 (cm^3 molecule^{-1} s^{-1})	α_1	β_1 (K)	k_2 (s^{-1})	α_2	β_2 (K)	Source
N$_2$O$_5$ + M $\longrightarrow$ NO$_2$ + NO$_3$ + M	1.3×10^{-3}	-3.5	11000	9.7×10^{14}	0.1	11080	IUPAC
HO$_2$NO$_2$ + M $\longrightarrow$ HO$_2$ + NO$_2$ + M	4.1×10^{-5}	0	10650	6.0×10^{15}	0	11170	IUPAC

Table A.4: The termolecular decomposition reactions included in the chemical network, and their coefficients.

A.4 Photolysis

The complete list of photolysis reactions we include in our model is given in Table A.5. Several of the photolysis reactions are described in the main document but are repeated here for completeness. Refer to Chapter 3 for a discussion of the development, inclusion, and effects of these reactions.

A.5 Stellar Proton Forcing

The development and impact of SEPs in a quiescent context is discussed in Section 4.5. The impact of SEPs during flares is discussion in Section 5.3.2 and the complete list of reactions we include in our model is given in Table A.6. The reactions caused by SEPs are described in the main paper, but repeated here for completeness.

Photolysis	Threshold wavelength (nm)	Quantum yield source
$O_2 + h\nu \longrightarrow O(^3P) + O(^3P)$	242.3	JPL2019
$O_2 + h\nu \longrightarrow O(^3P) + O(^1D)$	175	JPL2019
$O_3 + h\nu \longrightarrow O(^3P) + O_2$	1180	JPL2019
$O_3 + h\nu \longrightarrow O(^1D) + O_2$	411	JPL2019
$HO_2 + h\nu \longrightarrow OH + O(^3P)$	438	Assumed to be 1
$HO_2 + h\nu \longrightarrow OH + O(^1D)$	259	Assumed to be 1
$H_2O + h\nu \longrightarrow H + OH$	242	JPL2019
$H_2O + h\nu \longrightarrow H_2 + O(^1D)$	175	JPL2019
$H_2O + h\nu \longrightarrow H + H + O(^3P)$	129	JPL2019
$H_2O_2 + h\nu \longrightarrow OH + OH$	557	JPL2019
$H_2O_2 + h\nu \longrightarrow H + HO_2$	329	JPL2019
$NO_2 + h\nu \longrightarrow NO + O(^3P)$	422	JPL2019
$NO_3 + h\nu \longrightarrow NO_2 + O(^3P)$	7320	JPL2019
$NO_3 + h\nu \longrightarrow NO + O_2$	640	JPL2019
$N_2O + h\nu \longrightarrow N_2 + O(^1D)$	336	JPL2019
$N_2O_5 + h\nu \longrightarrow NO_3 + NO_2$	1255	JPL2019
$N_2O_5 + h\nu \longrightarrow NO_3 + NO + O(^3P)$	298	JPL2019
$HONO + h\nu \longrightarrow OH + NO$	579	Assumed to be 1
$HNO_3 + h\nu \longrightarrow NO_2 + OH$	581	Assumed to be 1
$HO_2NO_2 + h\nu \longrightarrow HO_2 + NO_2$	1207	JPL2019
$HO_2NO_2 + h\nu \longrightarrow OH + NO_3$	726	JPL2019

Table A.5: The list of photolysis reactions (channels) used in the chemical network, and the threshold wavelength for each reaction.

Reaction	Production efficiency
$H_2O + p^+/e^- \longrightarrow H + OH$	2
$N_2 + p^+/e^- \longrightarrow N(^4S) + N(^4S)$	0.55
$N_2 + p^+/e^- \longrightarrow N(^2D) + N(^2D)$	0.7

Table A.6: The list of reactions caused by stellar proton (or stellar energetic particles, SEPs) forcing used in the chemical network and the total amount of molecules produced per ion pair for each reaction.

Bibliography

Adams S., et al., 2019, Journal of Parallel and Distributed Computing, 132, 383

Allard F., Hauschildt P. H., 1995, The Astrophysical Journal, 445, 433

Alvarado-Gómez J. D., Drake J. J., Cohen O., Fraschetti F., Garraffo C., Poppen-häger K., 2022, Astronomische Nachrichten, 343, 1

Amundsen D., 2015, PhD thesis, University of Exeter

Amundsen D. S., Bara I., Tremblin P., Manners J., Hayek W., Mayne N. J., Acreman D. M., 2014, Astronomy and Astrophysics, 564, A59

Amundsen D. S., et al., 2016, Astronomy & Astrophysics, 595, A36

Anglada-Escudé G., et al., 2016, Nature, 536, 437

Archibald A. T., et al., 2020, Geoscientific Model Development, 13, 1223

Arney G., et al., 2016, Astrobiology, 16, 873

Atkinson R., et al., 2004, Atmospheric Chemistry and Physics, 4, 1461

Barber R. J., Tennyson J., Harris G. J., Tolchenov R. N., 2006, Monthly Notices of the Royal Astronomical Society, 368, 1087

Barnes R., 2017, Celestial Mechanics and Dynamical Astronomy, 129, 509

Barton E. J., Yurchenko S. N., Tennyson J., 2013, Monthly Notices of the Royal Astronomical Society, 434, 1469

Batalha N. E., et al., 2017, Publications of the Astronomical Society of the Pacific, 129, 064501

Belov A., Garcia H., Kurt V., Mavromichalaki H., Gerontidou M., 2005, Solar Physics, 229, 135

Benz A. O., Güdel M., 2010, Annual Review of Astronomy and Astrophysics, 48, 241

Berglund M., Wieser M. E., 2011, Pure and Applied Chemistry, 83, 397

Bernath P. F., 2020, Journal of Quantitative Spectroscopy and Radiative Transfer, 240, 106687

Berntsen T. K., Isaksen I. S. A., 1997, Journal of Geophysical Research: Atmospheres, 102, 21239

Bochanski J. J., Hawley S. L., Covey K. R., West A. A., Reid I. N., Golimowski D. A., Ivezić Ž., 2010, The Astronomical Journal, 139, 2679

Borucki W. J., et al., 2010, Science, 327, 977

Boutle I. A., Mayne N. J., Drummond B., Manners J., Goyal J., Hugo Lambert F., Acreman D. M., Earnshaw P. D., 2017, Astronomy & Astrophysics, 601, A120

Boutle I. A., Joshi M., Lambert F. H., Mayne N. J., Lyster D., Manners J., Ridgway R., Kohary K., 2020, Nature Communications, 11, 2731

Braam M., Palmer P. I., Decin L., Ridgway R. J., Zamyatina M., Mayne N. J., Sergeev D. E., Abraham N. L., 2022, Monthly Notices of the Royal Astronomical Society, 186, 227

Brasseur G. P., Jacob D. J., 2017, Modeling of Atmospheric Chemistry. Cambridge University Press, doi:10.1017/9781316544754, https://www.cambridge.org/core/product/identifier/9781316544754/type/book

Burkholder J. B., et al., 2015, Chemical Kinetics and Photochemical Data for Use in Atmospheric Studies, Evaluation No. 18, http://jpldataeval.jpl.nasa.gov

Burkholder J. B., et al., 2019, Chemical Kinetics and Photochemical Data for Use in Atmospheric Studies, Evaluation No. 19, `http://jpldataeval.jpl.nasa.gov/`

Campargue A., Mikhailenko S., Lohan B. G., Karlovets E., Mondelain D., Kassi S., 2015, Journal of Quantitative Spectroscopy and Radiative Transfer, 157, 135

Carrington R. C., 1859, Monthly Notices of the Royal Astronomical Society, 20, 13

Chang W. L., Bhave P. V., Brown S. S., Riemer N., Stutz J., Dabdub D., 2011, Aerosol Science and Technology, 45, 665

Chapman S., 1930, The London, Edinburgh, and Dublin Philosophical Magazine and Journal of Science, 10, 369

Charbonneau D., Brown T. M., Noyes R. W., Gilliland R. L., 2002, The Astrophysical Journal, 568, 377

Chen H., Wolf E. T., Kopparapu R., Domagal-Goldman S., Horton D. E., 2018, The Astrophysical Journal, 868, L6

Chen H., Zhan Z., Youngblood A., Wolf E. T., Feinstein A. D., Horton D. E., 2021, Nature Astronomy, 5, 298

Christensen U. R., Holzwarth V., Reiners A., 2009, Nature, 457, 167

Christie D. A., et al., 2021, Monthly Notices of the Royal Astronomical Society, 506, 4500

Cliver E. W., Dietrich W. F., 2013, Journal of Space Weather and Space Climate, 3, A31

Davenport J. R. A., 2016, The Astrophysical Journal, 829, 23

Davenport J. R. A., et al., 2014, The Astrophysical Journal, 797, 122

Davies T., Cullen M. J. P., Malcolm A. J., Mawson M. H., Staniforth A., White A. A., Wood N., 2005, Quarterly Journal of the Royal Meteorological Society, 131, 1759

Demory B.-O., et al., 2016, Nature, 532, 207

Des Marais D. J., et al., 2002, Astrobiology, 2, 153

Drummond B., 2017, PhD thesis, University of Exeter

Drummond B., Tremblin P., Baraffe I., Amundsen D. S., Mayne N. J., Venot O., Goyal J., 2016, Astronomy & Astrophysics, 594, A69

Drummond B., Mayne N. J., Baraffe I., Tremblin P., Manners J., Amundsen D. S., Goyal J., Acreman D., 2018a, Astronomy & Astrophysics, 612, A105

Drummond B., et al., 2018b, The Astrophysical Journal Letters, 855, L31

Drummond B., Mayne N. J., Manners J., Baraffe I., Goyal J., Tremblin P., Sing D. K., Kohary K., 2018c, The Astrophysical Journal, 869, 28

Drummond B., et al., 2020, Astronomy & Astrophysics, 636, A68

Dumusque X., 2016, Astronomy & Astrophysics, 593, A5

Dumusque X., et al., 2017, Astronomy & Astrophysics, 598, A133

Eager J. K., et al., 2020, Astronomy & Astrophysics, 639, A99

Edwards J., Slingo A., 1996, Quarterly Journal of the Royal Meteorological Society, 122, 689

Ehhalt D., et al., 2001, in , Climate Change 2001: The Scientific Basis. Cambridge University Press, Cambridge, United Kingdom and New York, NY, USA, Chapt. 4, pp 239–287

Evans T. M., et al., 2016, The Astrophysical Journal, 822, L4

Evans T. M., et al., 2017, Nature, 548, 58

Fauchez T. J., et al., 2021, The Planetary Science Journal, 2, 106

Fauchez T. J., et al., 2022, The Planetary Science Journal, 3, 213

Fennelly J., Torr D., 1992, Atomic Data and Nuclear Data Tables, 51, 321

France K., et al., 2016, The Astrophysical Journal, 820, 89

Fraser P., 1997, Australian Meteorological Magazine, 46, 185

Frierson D. M. W., Held I. M., Zurita-Gotor P., 2006, Journal of the Atmospheric Sciences, 63, 2548

Gebauer S., Grenfell J., Stock J., Lehmann R., Godolt M., von Paris P., Rauer H., 2017, Astrobiology, 17, 27

GharibNezhad E., Shayesteh A., Bernath P. F., 2013, Monthly Notices of the Royal Astronomical Society, 432, 2043

Giannakopoulos C., Chipperfield M. P., Law K. S., Pyle J. A., 1999, Journal of Geophysical Research: Atmospheres, 104, 23761

Gillon M., et al., 2017, Nature, 542, 456

Gopalswamy N., 2004, in , The Sun and the Heliosphere as an Integrated System, 1 edn, Springer Dordrecht, Chapt. 1, pp 201–251, doi:10.1007/978-1-4020-2831-1_8, http://link.springer.com/10.1007/978-1-4020-2831-1_8

Gopalswamy N., Yashiro S., Xie H., Akiyama S., Aguilar-Rodriguez E., Kaiser M. L., Howard R. A., Bougeret J., 2008, The Astrophysical Journal, 674, 560

Gordon I., et al., 2022a, Journal of Quantitative Spectroscopy and Radiative Transfer, 277, 107949

Gordon I., et al., 2022b, Journal of Quantitative Spectroscopy and Radiative Transfer, 277, 107949

Gorman M. N., Yurchenko S. N., Tennyson J., 2019, Monthly Notices of the Royal Astronomical Society, 490, 1652

Gorshelev V., Serdyuchenko A., Weber M., Chehade W., Burrows J. P., 2014, Atmospheric Measurement Techniques, 7, 609

Grenfell J. L., 2018, in , Handbook of Exoplanets. Springer International Publishing, Cham, pp 3159–3172, doi:10.1007/978-3-319-55333-7_68, http://link.springer.com/10.1007/978-3-319-55333-7_68

Gulev S., et al., 2021, in , Climate Change 2021: The Physical Science Basis. Cambridge University Press, Cambridge, United Kingdom and New York, NY, USA, Chapt. 2, pp 287–422, doi:10.1017/9781009157896.004

Günther M. N., et al., 2020, The Astronomical Journal, 159, 60

Hawley S. L., Pettersen B. R., 1991, The Astrophysical Journal, 378, 725

Hawley S. L., Davenport J. R. A., Kowalski A. F., Wisniewski J. P., Hebb L., Deitrick R., Hilton E. J., 2014, The Astrophysical Journal, 797, 121

Henke B., Gullikson E., Davis J., 1993, Atomic Data and Nuclear Data Tables, 54, 181

Herron J. T., 1999, Journal of Physical and Chemical Reference Data, 28, 1453

Huebner W., Mukherjee J., 2015, Planetary and Space Science, 106, 11

Jackman C. H., McPeters R. D., 2004, in No. 141, Solar Variability and Its Effects on Climate. American Geophysical Union, pp 305–319, doi:10.1029/141GM21, https://onlinelibrary.wiley.com/doi/10.1029/141GM21

Jackson D. R., et al., 2020, Journal of Space Weather and Space Climate, 10, 18

Jenkins J. S., et al., 2019, Monthly Notices of the Royal Astronomical Society, 487, 268

Johns-Krull C. M., Valenti J. A., 1996, The Astrophysical Journal, 459, 95

Joshi M., Haberle R., Reynolds R., 1997, Icarus, 129, 450

Joy A. H., Humason M. L., 1949, Publications of the Astronomical Society of the Pacific, 61, 133

Kaltenegger L., Traub W. A., Jucks K. W., 2007, The Astrophysical Journal, 658, 598

Kasting J. F., Whitmire D. P., Reynolds R. T., 1993, Icarus, 101, 108

Keller-Rudek H., Moortgat G. K., Sander R., Sörensen R., 2013, Earth System Science Data, 5, 365

Khodachenko M. L., et al., 2007, Astrobiology, 7, 167

Kitadai N., Maruyama S., 2018, Geoscience Frontiers, 9, 1117

Kochukhov O., 2021, The Astronomy and Astrophysics Review, 29, 1

Krnavek L., Simpson W. R., Carlson D., Domine F., Douglas T. A., Sturm M., 2012, Atmospheric Environment, 50, 349

Lacis A. A., Oinas V., 1991, Journal of Geophysical Research, 96, 9027

Lavail A., Kochukhov O., Wade G. A., 2018, Monthly Notices of the Royal Astronomical Society, 479, 4836

Lefèvre M., Turbet M., Pierrehumbert R., 2021, The Astrophysical Journal, 913, 101

Lewis N. T., Lambert F. H., Boutle I. A., Mayne N. J., Manners J., Acreman D. M., 2018, The Astrophysical Journal, 854, 171

Li G., Harrison J. J., Ram R. S., Western C. M., Bernath P. F., 2012, Journal of Quantitative Spectroscopy and Radiative Transfer, 113, 67

Li H. Y., Tennyson J., Yurchenko S. N., 2019, Monthly Notices of the Royal Astronomical Society, 486, 2351

Lindemann F. A., Arrhenius S., Langmuir I., Dhar N. R., Perrin J., McC. Lewis W. C., 1922, Trans. Faraday Soc., 17, 598

Lines S., et al., 2018, Monthly Notices of the Royal Astronomical Society, 481, 194

Lopez E. D., Fortney J. J., 2014, The Astrophysical Journal, 792, 1

Lopez-Hilfiker F. D., Constantin K., Kercher J. P., Thornton J. A., 2012, Atmospheric Chemistry and Physics, 12, 5237

Louca A. J., Miguel Y., Tsai S.-M., Froning C. S., Loyd R. O. P., France K., 2022, Monthly Notices of the Royal Astronomical Society

Madhusudhan N., Nixon M. C., Welbanks L., Piette A. A. A., Booth R. A., 2020, The Astrophysical Journal, 891, L7

Manners J., Edwards J. M., Hill P., Thelen J.-C., 2022, SOCRATES (Suite Of Community RAdiative Transfer codes based on Edwards and Slingo) Technical Guide., https://code.metoffice.gov.uk/trac/socrates

Marcy G., Butler R. P., Fischer D., Vogt S., Wright J. T., Tinney C. G., Jones H. R. A., 2005, Progress of Theoretical Physics Supplement, 158, 24

Matthes K., et al., 2017, Geoscientific Model Development, 10, 2247

Mayne N. J., Baraffe I., Acreman D. M., Smith C., Wood N., Amundsen D. S., Thuburn J., Jackson D. R., 2014a, Geoscientific Model Development, 7, 3059

Mayne N. J., et al., 2014b, Astronomy and Astrophysics, 561, 1

Mayor M., Queloz D., 1995, Nature, 378, 355

McKemmish L. K., Masseron T., Hoeijmakers H. J., Pérez-Mesa V., Grimm S. L., Yurchenko S. N., Tennyson J., 2019, Monthly Notices of the Royal Astronomical Society, 488, 2836

McNamara S. M., et al., 2019, Environmental Science & Technology, 53, 8057

Meadows V. S., 2017, Astrobiology, 17, 1022

Meadows V. S., et al., 2018, Astrobiology, 18, 133

Muheki P., Guenther E. W., Mutabazi T., Jurua E., 2020, Astronomy & Astrophysics, 637, A13

Mullan D. J., 2010, The Astrophysical Journal, 721, 1034

National Academies of Sciences, Engineering, and Medicine 2021, Pathways to Discovery in Astronomy and Astrophysics for the 2020s. The National Academies Press, Washington, DC, doi:10.17226/26141

Nisbet E. G., Sleep N. H., 2001, Nature, 409, 1083

O'Connor F. M., et al., 2014, Geoscientific Model Development, 7, 41

Owens A., Conway E. K., Tennyson J., Yurchenko S. N., 2020, Monthly Notices of the Royal Astronomical Society, 495, 1927

P. Loyd R. O., et al., 2016, The Astrophysical Journal, 824, 102

Patel B. H., Percivalle C., Ritson D. J., Duffy C. D., Sutherland J. D., 2015, Nature Chemistry, 7, 301

Patrascu A. T., Yurchenko S. N., Tennyson J., 2015, Monthly Notices of the Royal Astronomical Society, 449, 3613

Pecaut M. J., Mamajek E. E., 2013, The Astrophysical Journal Supplement Series, 208, 9

Perryman M., 2011, The Exoplanet Handbook, first edn. Cambridge University Press, Cambridge, doi:10.1017/CBO9780511994852, https://www.cambridge.org/core/product/identifier/9780511994852/type/book

Polyansky O. L., Kyuberis A. A., Zobov N. F., Tennyson J., Yurchenko S. N., Lodi L., 2018, Monthly Notices of the Royal Astronomical Society, 480, 2597

Porter H. S., Jackman C. H., Green A. E. S., 1976, The Journal of Chemical Physics, 65, 154

Powner M. W., Gerland B., Sutherland J. D., 2009, Nature, 459, 239

Rajpurohit A. S., Reylé C., Allard F., Homeier D., Schultheis M., Bessell M. S., Robin A. C., 2013, Astronomy & Astrophysics, 556, A15

Rajpurohit A. S., Allard F., Rajpurohit S., Sharma R., Teixeira G. D. C., Mousis O., Kamlesh R., 2018, Astronomy & Astrophysics, 620, A180

Reid G. C., 1986, in Sturrock P. A., Holzer T. E., Mihalas D. M., Ulrich R. K., eds, , Physics of the Sun: Volume III: Astrophysics and Solar-Terrestrial Relations. Springer Netherlands, Dordrecht, pp 251–278, doi:10.1007/978-94-009-5255-3_7

Ribas I., Gregg M. D., Boyajian T. S., Bolmont E., 2017, Astronomy & Astrophysics, 603, A58

Ricker G. R., et al., 2014, Journal of Astronomical Telescopes, Instruments, and Systems, 1, 014003

Ridgway R. J., et al., 2022, Monthly Notices of the Royal Astronomical Society, 518, 2472

Rivlin T., Lodi L., Yurchenko S. N., Tennyson J., Le Roy R. J., 2015, Monthly Notices of the Royal Astronomical Society, 451, 634

Rogers L. A., Seager S., 2010, Astrophysical Journal, 712, 974

Rugheimer S., Kaltenegger L., Segura A., Linsky J., Mohanty S., 2015, The Astrophysical Journal, 809, 57

Seager S., Kuchner M., Hier-Majumder C. A., Militzer B., 2007, The Astrophysical Journal, 669, 1279

Segura A., Krelove K., Kasting J. F., Sommerlatt D., Meadows V., Crisp D., Cohen M., Mlawer E., 2003, Astrobiology, 3, 689

Segura A., Walkowicz L. M., Meadows V., Kasting J., Hawley S., 2010, Astrobiology, 10, 751

Sergeev D. E., Lambert F. H., Mayne N. J., Boutle I. A., Manners J., Kohary K., 2020, The Astrophysical Journal, 894, 84

Sergeev D. E., et al., 2022, The Planetary Science Journal, 3, 212

Showman A. P., Wordsworth R. D., Merlis T. M., Kaspi Y., 2013, in , Comparative Climatology of Terrestrial Planets. University of Arizona Press, Chapt. 12, doi:10.2458/azu_uapress_9780816530595-ch12, http://muse.jhu.edu/books/9780816599752/9780816599752-20.pdf

Shulyak D., et al., 2019, Astronomy and Astrophysics, 626, 1

Simpson W. R., Frieß U., Thomas J. L., Lampel J., Platt U., 2018, Geophysical Research Letters, 45, 9987

Solomon S. C., 2005, Journal of Geophysical Research, 110, A10306

Solomon S., Rusch D., Gérard J., Reid G., Crutzen P., 1981, Planetary and Space Science, 29, 885

Sousa-Silva C., Seager S., Ranjan S., Petkowski J. J., Zhan Z., Hu R., Bains W., 2020, Astrobiology, 20, 235

Syakila A., Kroeze C., 2011, Greenhouse Gas Measurement and Management, 1, 17

Tan X., Showman A. P., 2020, The Astrophysical Journal, 902, 27

Tilley M. A., Segura A., Meadows V., Hawley S., Davenport J., 2019, Astrobiology, 19, 64

Tolchenov R., Tennyson J., 2008, Journal of Quantitative Spectroscopy and Radiative Transfer, 109, 559

Tremblin P., Amundsen D. S., Mourier P., Baraffe I., Chabrier G., Drummond B., Homeier D., Venot O., 2015, The Astrophysical Journal, 804, L17

Tremblin P., Amundsen D. S., Chabrier G., Baraffe I., Drummond B., Hinkley S., Mourier P., Venot O., 2016, The Astrophysical Journal, 817, L19

Troe J., 1983, Berichte der Bunsengesellschaft für physikalische Chemie, 87, 161

Turbet M., Leconte J., Selsis F., Bolmont E., Forget F., Ribas I., Raymond S. N., Anglada-Escudé G., 2016, Astronomy & Astrophysics, 596, A112

Turbet M., et al., 2018, Astronomy & Astrophysics, 612, A86

Turbet M., et al., 2022, The Planetary Science Journal, 3, 211

Upadhyay A., Conway E. K., Tennyson J., Yurchenko S. N., 2018, Monthly Notices of the Royal Astronomical Society, 477, 1520

Venot O., Rocchetto M., Carl S., Hashim A. R., Decin L., 2016, The Astrophysical Journal, 830, 77

Visscher C., Lodders K., Fegley Jr. B., 2006, The Astrophysical Journal, 648, 1181

Wakeford H. R., et al., 2017, Science, 356, 628

Walters D., et al., 2019, Geoscientific Model Development, 12, 1909

Wesely M., 1989, Atmospheric Environment (1967), 23, 1293

Winters J. G., et al., 2019, The Astronomical Journal, 157, 216

de Wit J., et al., 2018, Nature Astronomy, 2, 214

Wolszczan A., Frail D. A., 1992, Nature, 355, 145

Wood N., et al., 2014, Quarterly Journal of the Royal Meteorological Society, 140, 1505

Xu J., Mohanakumar K., Guo D., Liu Y., Yue J., 2017, Technical report, Stratospheric Processes and Their Role in Climate, http://www.sparc-climate.org/publications/sparc-reports/. SPARC, doi:10.1155/2017/3482462, http://www.sparc-climate.org/publications/sparc-reports/

Yashiro S., 2004, Journal of Geophysical Research, 109, A07105

Yashiro S., Akiyama S., Gopalswamy N., Howard R. A., 2006, The Astrophysical Journal, 650, L143

Yates J. S., Palmer P. I., Manners J., Boutle I., Kohary K., Mayne N., Abraham L., 2020, Monthly Notices of the Royal Astronomical Society, 492, 1691

Youngblood A., et al., 2016, The Astrophysical Journal, 824, 101

Yurchenko S. N., Blissett A., Asari U., Vasilios M., Hill C., Tennyson J., 2016, Monthly Notices of the Royal Astronomical Society, 456, 4524

Yurchenko S. N., Sinden F., Lodi L., Hill C., Gorman M. N., Tennyson J., 2018a, Monthly Notices of the Royal Astronomical Society, 473, 5324

Yurchenko S. N., Williams H., Leyland P. C., Lodi L., Tennyson J., 2018b, Monthly Notices of the Royal Astronomical Society, 479, 1401

Yurchenko S. N., Al-Refaie A. F., Tennyson J., 2018c, Astronomy & Astrophysics, 614, A131

Zamyatina M., et al., 2022, Monthly Notices of the Royal Astronomical Society, 519, 3129